Advanced Electrodes and Electrolytes For Long-Lived and High-Energy-Density Lithium-Sulfur Batteries

by

Quanqun Pang

A thesis

presented to the University of Waterloo

in fulfillment of the

thesis requirement for the degree of

Doctor of Philosophy

in

Chemistry

Waterloo, Ontario, Canada, 2017

Examining Committee Membership

The following served on the Examining Committee for this thesis. The decision of the Examining Committee is by majority vote.

External Examiner	Donald Siegel Associate Professor
Supervisor	Linda F. Nazar Professor
Internal Member	Pavle Radovanovic Associate Professor
Internal-external Member	Michael Pope Assistant Professor
Other Member(s)	Vivek Maheshwari Associate Professor

AUTHOR'S DECLARATION

I hereby declare that I am the sole author of this thesis. This is a true copy of the thesis, including any required final revisions, as accepted by my examiners.

I understand that my thesis may be made electronically available to the public.

Abstract

The increasing demand on renewable but intermittent energy and the need for electrified transportation place great emphasis on energy storage. Lithium-sulfur (Li-S) batteries are promising systems due to the high theoretical energy density and natural abundance of sulfur. This thesis presents a thorough investigation on strategies to confine the polysulfides and to build long-lived and high-energy-density Li-S batteries. A series of sulfur host materials and a class of sparingly solvating electrolyte are presented.

Chapter 3 presents an approach to confine polysulfides within a cobalt sulfide material, which exhibits both metallic conductivity and high polysulfide adsorptivity. First-principles calculations and X-ray photoelectron spectroscopy studies consistently demonstrate the coupled interaction between the ionic components of cobalt sulfide and lithium polysulfides. The interconnected nanosheets form 3D networks and enable high sulfur loading electrodes with stable cycling. Chapter 4 presents a novel dual-doping strategy on porous carbon for effective binding of polysulfides. The N and S heteroatoms respectively bond with the Li cations and S anions in the polysulfide. The synthesis is based on liquid-crystal driven self-assembly of bio-sustainable cellulose nanocrystals.

Chapter 5 reports a light-weight graphitic carbon nitride material that incorporates high concentration of active N-doping sites for polysulfide binding. Excellent long-term cycling performance of the sulfur electrode is achieved with only 0.04% capacity fading per cycle over 1500 cycles. Chapter 6 further reports a comprehensive strategy on coupling a hybrid sulfur host with an *in-situ* cross-linked binder in order to construct high loading electrodes while using a low electrolyte volume. Alternative stacking of graphitic carbon

nitride and graphene offers both Li-N based adsorption for polysulfide and high electronic conductivity. Benefiting from the high elasticity of the cross-linked binder, crack-free high loading electrodes are fabricated at an electrolyte/sulfur ratio of 3.5:1 (µl:mg).

Chapter 7 presents a comprehensive study on the ACN_2-LiTFSI-TTE electrolyte with sparing solubility for polysulfides at elevated temperature. A quasi-solid state reaction is demonstrated by the distinct Li-S voltage profiles and sulfur/lithiu sulfide phase evolution as probed by *operando* XRD measurements. This discovery will inspire further studies into modifying the local structure of electrolytes to control the reaction pathways of dissolution-precipitation electrochemistry.

Acknowledgements

I would like to send my sincere gratitude to my supervisor, Dr. Linda F. Nazar, for her tremendous support and guidance in the past five years of my graduate career. It was a wonderful time to study, do research and dig into the science in this group. I have learned how to think, propose ideas, work thoughtfully from her. I would also like to thank Dr. Dipan Kundu and Dr. Xiao Liang for their help and guidance in my early career. I would also like extend my gratitude to my PhD committee: Dr. Pavle Radovanovic, Dr. Vivek Maheshwari, Dr. Eric Prouzet, Dr. Germán Sciaini, Dr. Michael Pope for their guidance on my research. Furthermore, I would like to thank my undergraduate supervisors, Dr. Yunhui Huang, Dr. Zhaohui Wang, Dr. Yue Shen for bringing me into this challenging but wonderful world of electrochemical batteries.

I would like first to say thank you to my Mom and Dad. Thank you for bringing me up and supporting me through my studies and life in the past two and half decades. You may not know how I felt to study away from home and you may not see what I have been experiencing every day, but I know you always love me and support me. I can never express how much I love you! To my big sister and big brother, Ting and Chao, I want to say thank you, for taking care of me and our Mom and Dad. Without you, I would never be able to finish this thesis.

I would like to thank my beautiful fiancée, Zhenna, for what you have done in the past 7 years and 9 months. Your love and companion has made me through the difficult times.

I would also like to thank my colleagues in this great group for all the nice moments and scientific discussions: Guang, Marine, He, Xiaoqi, Chun Yuen, Abhi, Laidong, Robert,

Brian, Elahe, Yverick, Scott, Ivan, Erika, Kavish, Fabien, Patrick and Guerman! I would also thank my dear friends in Chemistry, Biwu, Juntao, Zihe, Wenhu, Zhicheng, for making my life so enjoyable in Waterloo!

Dedication

I would like dedicate this thesis to my family, my Mom and my Dad, my brother and my sister, my fiancée, for their tremendous support. I love you all!

Table of Contents

List of Figures

List of Tables

List of Abbreviations

ACN	Acetonitrile
BET	Brunauer-Emmett-Teller
BO	Born-Oppenheimer
CDC	Cellulose-derived carbon
CE	Coulumbic efficiency
CMC	Carboxymethyl cellulose
CNC	Cellulose nanocrystal
CNT	Carbon nanotube
CTAB	Cetyltrimethyl ammonium bromide
CV	Cyclic voltammetry
DFT	Density functional theory
DME	Dimethoxymethane
DMF	Dimethylformamide
DMSO	Dimethyl sulfoxide
DN	Gutmann donor number
DOL	1,3-dioxolane
DSC	Differential scanning calorimetry
G4	Tetraethylene glycol dimethyl ether
GGA	Generalized gradient approximation
EDX	Energy dispersive x-ray spectroscopy
EIS	Electrochemical impedance spectroscopy

EV	Electric vehicles
EXAFS	Extended X-ray absorption fine structure
FTIR	Fourier transform IR
HRTEM	High-resolution TEM
IR	Infrared spectroscopy
KB	Ketjen Black
LCF	Linear combination fit
LDA	Local density approximation
LIBs	Lithium-ion batteries
LICGC	Li^+ ion conductive glass ceramic
LiPS	Lithium polysulfide
Li-S	Lithium-sulfur
LiTFSI	Bis(trifluoromethanesulfonyl)imide lithium
MOF	Metal-organic framework
NC	N-doped carbon
NG	N-doped graphene
NSC	N,S dual-doped carbon
OCV	Open-circuit voltage
PAW	Projected augmented wave
PBE	Perdew-Burke-Ernzerhof
PEG	Polyethylene glycol
PR	Polyrhodanine

PSD	Pore size distribution
PVDF	Polyvinylidene fluoride
PVP	Polyvinylpyrrolidone
QSDFT	Quenched Solid State Functional Theory
RTIL	Room-temperature ionic liquid
SBR	Styrene butadiene rubber
SEM	Scanning electron microscopy
SE	Schrödinger equation
STEM	Scanning transmission electron microscopy
TEGDME	Tetraethylene glycol dimethyl ether
TEM	Transmission electron microscopy
TEOS	Tetraethyl orthosilicate
THF	Tetrahydrofuran
TGA	Thermal gravimetric analysis
TTE	1,1,2,2-tetra-fluoroethyl 2,2,3,3-tetrafluoropropyl ether
TXM	Transmission x-ray microscopy
USPP	Ultrasoft pseudopotentials
VASP	Vienna Ab initio Simulation Package
XANES	X-ray absorption near-edge structure
XAS	X-ray absorption spectroscopy
XPS	X-ray photoelectron spectroscopy
XRD	X-ray diffraction

Chapter 1 Introduction

1.1 Lithium-Based Batteries and Terminologies

The ever-growing consumption of fossil fuels and its associated environmental pollution have driven scientists to pursue renewable energies. Photovoltaic panels and fly wheels are being installed worldwide. However, to fully utilize the electricity generated by these intermittent sources, rechargeable battery systems are important, which likely enable grid-scale electric storage and electric vehicular transport.[1]

Amongst all the rechargeable battery systems that have serviced mankind for decades, lithium-ion batteries (LIBs) have dominated the commercial battery market, owing to their high cell voltage, low self-discharge rate, and stable cycling performance. [2-4] One cell usually consists of two electrodes – positive electrode and negative electrode (cathode or anode) – which are separated by the electrolyte. These battery systems – which are conventionally represented by a graphite anode and a lithium metal oxide cathode (as shown in **Figure 1.1**[5]) and rely on the Li^+ ion intercalation mechanism – have been attractive for the electric vehicle (EV) market. For a LIB using graphite and $LiCoO_2$ as the electrodes, during the discharge, the reactions occurring at the anode and cathode follows **Equation 1.1 and 1.2.**

$$LiC_6 \rightarrow Li^+ + 6C + e^- \qquad \textbf{Equation 1.1}$$

$$2\ Li_{0.5}CoO_2 + Li^+ + e^- \rightarrow 2\ LiCoO_2 \qquad \textbf{Equation 1.2}$$

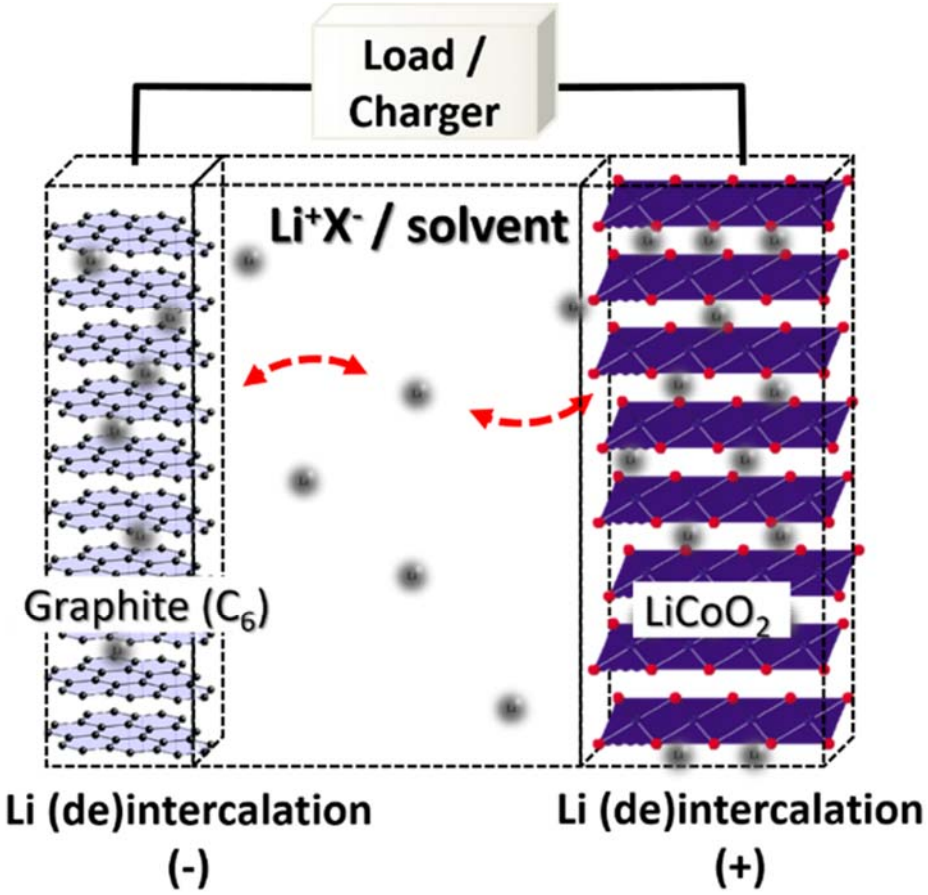

Figure 1.1 Schematic illustration of a typical lithium-ion battery that consists of layer-structured $LiCoO_2$ and graphite as the positive electrode (cathode) and negative electrode (anode), respectively. The electrolyte layer consisting of lithium salt(s) in the solvent(s) is in between the electrodes. Adapted from Ref. 5.

The operation of an electrochemical cell is driven in principle by the difference of chemical potentials of the two electrodes, where electrochemical reduction and oxidation occur separately. The two electrodes require both electronic and ionic conductivity as the electron transfer and ion transportation processes occur simultaneously on the surface of and/or within the electrodes. The electrolyte, being an ionic conductor and electrical insulator, can be either liquid or solid, rendering two type of batteries: traditional liquid-containing and all-solid-state

batteries. An electrolyte-permeable but insulating porous separator is needed for liquid electrolyte cells to avoid physical contact of the two electrodes.

Here I introduce some metrics that are widely used when evaluating the performance of a cell, including cell voltage and voltage profile, specific capacity, specific energy, energy density, rate capability and cycling life. These concepts are essential for understanding the research in this thesis.

Potential and Cell Voltage

The standard potential (E^o) of an electrode is determined by **Equation 1.3**,

$$\Delta G = -nFE^o \qquad \textbf{Equation 1.3}$$

where ΔG is the free energy change of the half reaction, n is the number of electrons involved in the half reaction and F is the Faraday's Constant. The standard cell voltage (V^o) is determined by the difference of the E^o of the two reactions. A large difference of standard potential between cathode and anode is desired for a full cell, since the output energy is the product of voltage and capacity. This potential difference has to be within the potential window of the electrolyte that is in use, in order to prevent electrolyte decomposition (reduction and oxidation). The real electrode potential is, however, also dependent on other parameters such as ion concentration and temperature, as outlined in Nernst Equation. On top of this, the cell voltage measured upon discharge (charge) is lower (higher) due to the presence of overpotential, derived from some limiting kinetic factors such as mass diffusion, migration and electron conduction, (electro)chemical reactions.

Specific Capacity

The theoretical specific capacity of an electrode is one of the most important metrics, other than the standard potential. It is defined as the number of charge (electrons or ions) that

can be transferred during the complete reaction per unit of mass or volume of the electrode material. The specific capacity can be represented in either gravimetric form (mA h g^{-1}) or volumetric (mA h cm^{-3}). The specific capacity obtained for an electrode material is usually lower than the theoretical capacity due to incomplete reaction from kinetic reasons. The discharge/charge voltage profile is a plot of voltage evolution as a function of specific capacity during the galvanostatic cycling of a cell, when a constant current is applied. The profiles envelope information about the redox reactions and at what voltage they are occurring. Minimum voltage difference between discharge and charge (that is, lowest polarization) is desired for achieving high capacity, high rate capability and high energy efficiency (the ratio of dischargeable energy over charged energy).

Specific Energy and Energy Density

The total energy output from a cell is given by the product of capacity (mA h) and cell voltage (V). The specific energy and energy density is defined by the energy output per mass (W h kg^{-1}) or volume (W h L^{-1}) of materials, respectively. In some literature, they are referred to as gravimetric energy density and volumetric energy density, respectively. The two representations are preferentially used in the specific conditions; grid-scale energy storage requires high energy density, whereas EVs and portable electronics emphasize more on energy density (size of the battery in use), although specific energy is also important (weight of the battery in use). Note that the calculation of specific energy (or energy density) can base on the mass (or the volume) of one specified electrode, two electrodes or the whole cell configuration, depending on the situation. Regardless, it has to be clearly indicated for fair comparisons between systems without confusion.

Power Density/Rate Capability

The current at which a cell is operated is usually noted as a fraction of "C" rate as per the working electrode, where "1 C" corresponds to the rate (mA g^{-1}) at which the theoretical specific capacity of this material is fully discharged/charged in one hour. The capability to sustain high voltage output and specific capacity at high rates means the power density and rate capability of a cell (or electrode). In general, discharging at higher rate potentially gives higher power but generally leads to higher polarization, lower energy efficiency and lower specific capacity.

Cycling Life

Cycling life of a cell usually means the number of cycles that it can survive with specified capacity retention. It can also be represented as the capacity fading rate (%) per cycle over a specified number of cycles. For the commercialization of a cell, the cycle life is extremely important as it is pertinent to its service life. A battery that can retain 80% of the initial capacity over more than 500 cycles is desired for an EV to serve for 3 years without swamping the battery. In laboratory research, the examination of cycle life is usually performed by cycling (discharging/charging) a cell in a galvanostatic mode continuously until the capacity fades substantially, although in practice the operation conditions are more complicated (*e.g.*, operation at varied rates/power outputs; long shelf-duration).

Among all rechargeable batteries, lithium batteries have become the most widely utilized and researched due to their high specific energy and energy density and are considered to be a promising candidate to replace nickel-hydrogen or lead-acid batteries. Although sodium batteries are also under intensive research and embrace the advantage of the earth-abundance

of sodium, lithium batteries are closer to be commercialized, due to the challenges in finding appropriate and low-cost anodes and electrolytes as well as the relatively lower specific energy for sodium batteries (as compared to lithium batteries).[6]

However, the applications of these LIBs batteries have been limited due to their low specific energy and energy density (100-220 W h $kg^{-1,}$ 300-600 W h L^{-1}, achievable) and high cost.[7,8] Consequently, they do not enable a long driving range unless very large battery packs are utilized, which comes at very high cost and excess weight. Thus the goal of traveling 500 km per time of charge is still unattainable. Electrochemical systems that offer a higher capacity and energy density as well as a long life-time at lower costs are desired, but are definitely challenging to bring into practice.

1.2 Lithium-Sulfur Batteries Overview

Lithium-sulfur (Li-S) batteries, based on lithium and sulfur, are considered as one of the most promising candidates for the next-generation energy storage systems, because of their high theoretical energy density, natural abundance (thus low cost) of sulfur, low environmental concern. [5, 9-11] A conventional Li-S cell consists of a lithium metal anode and an elemental sulfur cathode in a dilute (1 M) ether-based electrolyte, as shown in **Figure 1.2a**.[12] The coupling of the high-capacity electrodes, lithium (3840 mA h g^{-1}) and sulfur (1675 mA h g^{-1}), affords an average cell voltage of 2.2 V and a theoretical specific energy of 2570 W h kg^{-1} (based on the two electrodes). The reversible conversion reaction between sulfur and lithium sulfide (Li_2S) is accompanied by a series of intermediate lithium polysulfides (Li_2S_n, $2 \leq n \leq 8$, denoted as LiPSs). The electrochemical reactions of Li-S batteries are completely different

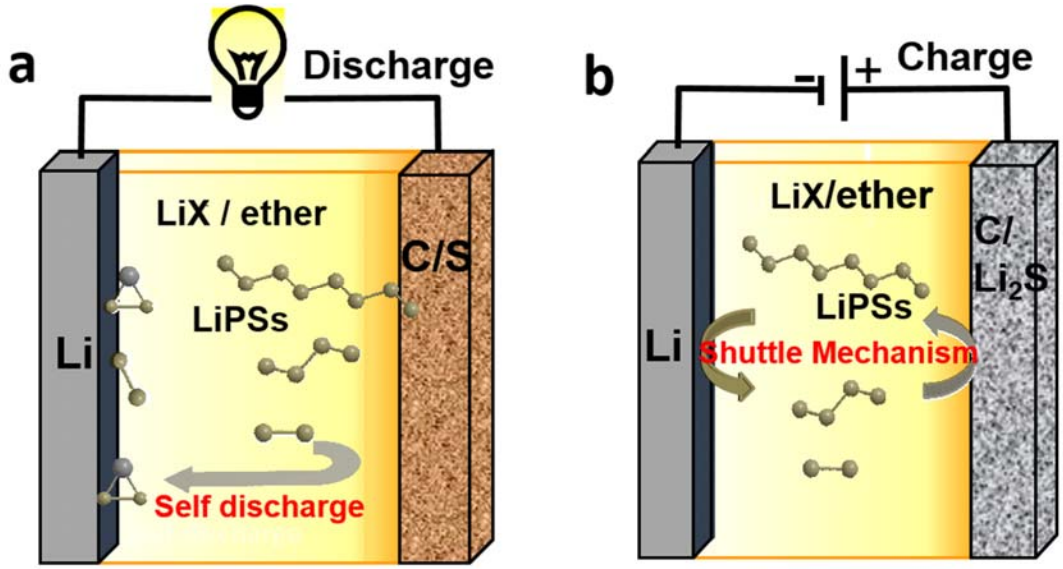

Figure 1.2 The configuration of a conventional Li-S battery using dilute ether electrolytes and the fundamental problems with using porous carbons as a sulfur host material. A Li-S cell consists of a lithium metal anode and an elemental sulfur/porous carbon mixture cathode. Physical entrapment of sulfur/polysulfides in the positive electrode by porous carbons is not sufficient to prevent dissolution and diffusion into the electrolyte. a) On discharge, diffusion of soluble LiPSs to the anode results in self-discharge *via* chemical reduction at the lithium surface. b) On charge, redox shuttling of soluble LiPSs between the electrodes gives rise to poor Coulombic efficiency and leads to precipitation of Li_2S at the exterior cathode surface. Stick-and-grey ball structures represent long and short chain LiPSs (Li_2S_8, Li_2S_4, Li_2S_2). LiX: electrolyte lithium salts. Reproduced from Ref. 12.

than the conventional LIBs because the LiPSs are soluble in the ether-based electrolytes. The seemingly simple chemistry is yet complicated and remains to be fully understood.

The charge and discharge voltage profiles of a Li-S cell using a typical electrolyte solvent (a mixture of 1,3-dioxolane (DOL) and dimethoxymethane (DME)) are shown in

bottom panels of **Figure 1.3**.[13] It is generally believed that on discharge, the high-voltage plateau at ~2.4 V corresponds to the reduction of cyclic S_8 to long-chain LiPSs (Li_2S_n with $4< n \leq 8$) and the low-voltage plateau at ~2.1 V relates to their further reduction into short-chain LiPSs ($2\leq n \leq 4$) and Li_2S. Upon charge, the long slope in the first region corresponds to the oxidation of solid Li_2S to long-chain LiPSs and the final short plateau represents oxidation to S_8. However, unlike the simple designation of the single-plateau profile for Li-ion intercalation based materials like $LiFePO_4$, this general designation for Li-S cells has not been fully evidenced and convincing. Nonetheless, *operando* studies on the sulfur speciation (during cell operation without interruption) *via* X-ray absorption near-edge structure (XANES),[13,14] UV-vis spectroscopy,[15] X-ray diffraction (XRD)[16] and transmission X-ray microscopy[17] have provided more information on the reaction mechanism of a Li-S cell.

Our group has performed *operando* XANES study on a carbon spheres-sulfur cathode in a Li-S cell.[13] The weight percentage of each sulfur component (Li_2S, S_4^{2-}, S_6^{2-} and S_8) was determined by using linear combination fit (LCF) of the *operando* XANES spectra, and their evolution during the course of charge and discharge is shown in the upper panels of **Figure 1.3**. It is observed that upon charge, Li_2S was monotonically consumed with the formation of soluble S_4^{2-} and S_6^{2-} on the first slope stage; they are then completely converted to S_8 on the second stage (**Figure 1.3a**). Upon discharge, conversion from S_8 into S_6^{2-} and S_4^{2-} occurs and ends at the supersaturation point (the knee before second plateau as shown in bottom of **Figure 1.3b**), and Li_2S formation was observed only when it reaches the middle of the second plateau.

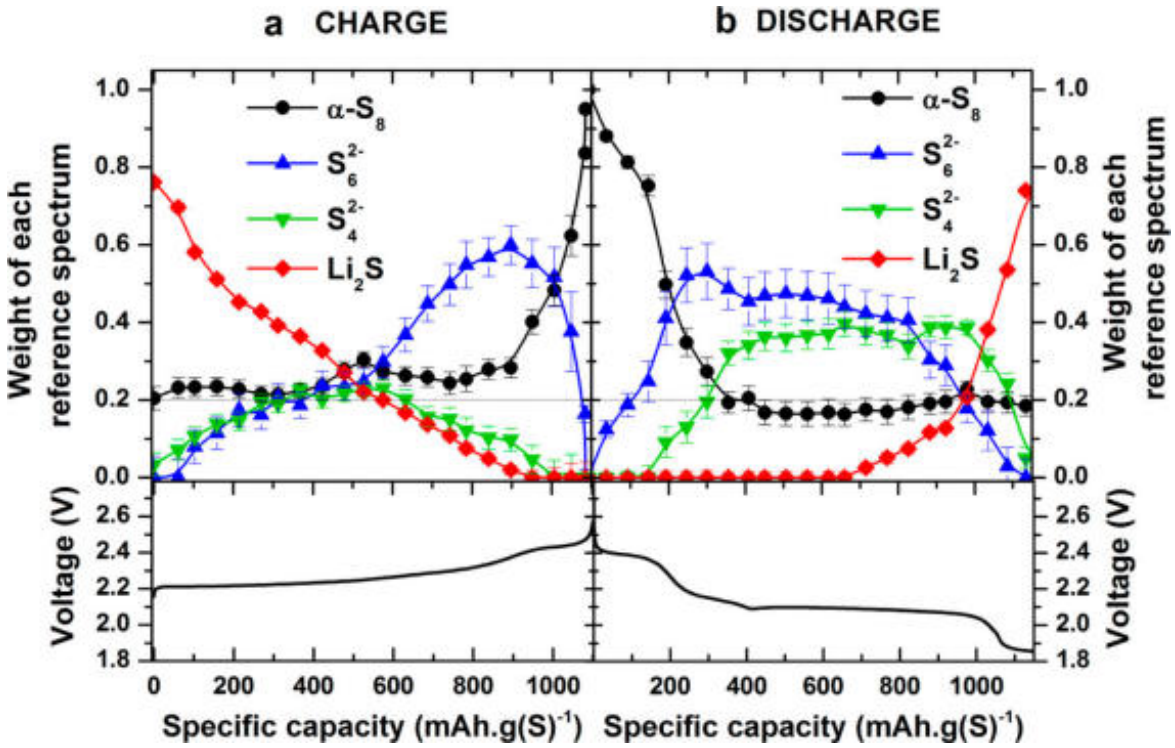

Figure 1.3 Typical charge/discharge voltage profile (bottom panels) and corresponding evolution of sulfur species (S_8, S_6^{2-}, S_4^{2-} and Li_2S) upon charge a) and discharge b) at C/10 rate. The weight of each sulfur component was determined by a linear combination fit of the *operando* XANES spectra. Reproduced from Ref. 13.

Alloin *et al.* investigated the evolution of crystalline phases, Li_2S and sulfur, using *operando* X-ray diffraction (XRD). They observed that the reduction of LiPSs into Li_2S occurs in a different reaction pathway than the oxidation of Li_2S back to LiPSs, based on the finding of a hysteresis on the evolution of Li_2S for discharge *vs.* charge; this is due to the complex equilibrium among all LiPSs in the cell. Crystalline Li_2S starts to appear at the supersaturation point on discharge (as opposed to the middle of second plateau for XANES[13]) and Li_2S is completely consumed at the end of first slope stage on charge. Interestingly, β-S_8 is formed on charge, as opposed to the starting α-S_8 phase, the reason of which is unclear, however. Other

operando techniques have also probed the formation of sulfur and/or Li_2S, but the reaction mechanisms proposed differ with respect to the cathode structures, indicating that the reaction pathway may, to some extent, depend on the cathode structure, host materials *etc*.[17]

The dissolution-precipitation transitions that are involved in the redox reactions of sulfur pose great challenges, however. Upon discharge and charge, the dissolved LiPS intermediates diffuse to the Li anode and get reduced to short-chain (poly)sulfides, which are either precipitated on the Li surface or shuttle back to the cathode. This parasitic reaction, called the polysulfide shuttle, continuously occurs in the cell unless means are provided to shut it down (**Figure 1.2a**). This process results in self-discharge, low Coulombic efficiency (CE) as well as active material loss and rapid capacity fading. This is one of the major hurdles that limit the practical realization of the Li-S batteries. Others include low sulfur utilization rate (due to the extremely low conductivity of sulfur and Li_2S), high volume expansion on discharge (from sulfur to Li_2S) and lithium anode degradation (**Figure 1.2b**).

In the next section, an overview of the various approaches to confine the polysulfides and to prevent the polysulfide shuttling process is provided. Note that protecting Li anode from dendrite formation and alleviating the consequent degradation and safety concern is another major challenge preventing the commercial applications of Li-S batteries. Overview in the area of Li anode protection is beyond the scope of this thesis and referred elsewhere.[18]

1.3 Porous Carbons to Physically Trap the Polysulfides

To solve the LiPS shuttle problem, much effort has been devoted to physical confinement of LiPSs using carbonaceous materials in the past decade. A variety of 3D porous carbon materials, including CMK-3,[19] porous hollow carbon spheres,[20-23] carbon nanotubes[24] and nanofibers,[25,26] as well as microporous carbons[27,28] have been developed to host the sulfur and

suppress the diffusion of LiPSs into the electrolyte, by retaining them in the nanostructured pores. A similar effect was also achieved by wrapping sulfur particles with 2D graphene nanosheets[29,30] or conductive polymers.[31] Work on using interlayer carbon paper has been shown to be effective in inhibiting the diffusion of polysulfide to the lithium anode.[32] The porous architecture enables these carbon interlayers to act as a pseudo current-collector providing good electronic conductivity as well as a layer for polysulfide retention.[33] Along with suppressing the polysulfide shuttle, these carbonaceous materials provide additional electron conduction and pathways for electrolyte and Li^+ ion diffusion, resulting in improvement in the cycling performance of Li-S batteries. Comprehensive reviews on nanostructured carbon host materials are provided in some publications.[34,35]

However, Li-S cell cathodes made from non-polar carbonaceous hosts still generally suffer from rapid capacity fading over long-term cycling (> 200 cycles). This is fundamentally because the very weak interactions between the non-polar carbon and the polar LiPSs species can only spatially confine the LiPSs and limit their diffusion. Eventually, the LiPSs still migrate out of the cathode host upon long-term cycling (**Figure 1.2a,b**). This causes not only loss of active materials, but also unspecific deposition (detachment) of discharged products and the associated cathode passivation and deterioration. Therefore, materials with stronger adsorption/binding for LiPSs and new mechanisms of the adsorption require exploring in achieving stable long-term cycling performance for the Li-S cell.

1.4 Chemical Approaches to Adsorb the Polysulfides

A wide spectrum of studies has been reported on developing sulfur host materials with strong chemical binding for LiPSs along with mechanistic investigation into the underlying principles of these materials. Utilizing chemical adsorption – rather than solely relying on the high surface

area or pore structure of the host materials as in the case for the physical confinement – benefits from the strong interaction between the host materials and LiPS species. Li-S batteries with improved cycling stability have been achieved by using these materials in the cathodes.

1.4.1 Polar-Polar Chemical Interaction with the Polysulfides

Lithium polysulfides are inherently polar molecules and do not engage in strong interaction with typical non-polar carbons. Therefore, various approaches based on a stronger polar-polar interaction with LiPSs have been utilized, mostly using modified carbonaceous materials and metal oxides.

Owning to graphene oxide's (GO) high surface area and its ability to chemically interact with the sulfur/polysulfide species, it has been one of the most studied functionalized carbon materials used as sulfur hosts. Ji *et al.* has prepared a GO based sulfur electrode by chemically depositing a nanosized sulfur layer onto the GO nanosheets.[36] Carbon K-edge X-ray absorption spectroscopy (XAS) studies revealed a strong chemical interaction between sulfur and the GO functional groups along as well as formation of C-S bonds (**Figure 1.4a,b**). Another study using various spectroscopy techniques, including X-ray photoelectron spectroscopy (XPS) and X-ray emission spectroscopy, provides a comprehensive understanding into the electronic structure and chemical bonding of GO-S composite.[37] A follow-up study by the same group reported a Li-S cell with greatly improved cycling performance (0.039 % capacity fading per cycle over 1500 cycles) enabled by further modification with cetyltrimethyl ammonium bromide (CTAB) along with an ionic liquid-based electrolyte and an elastomeric binder

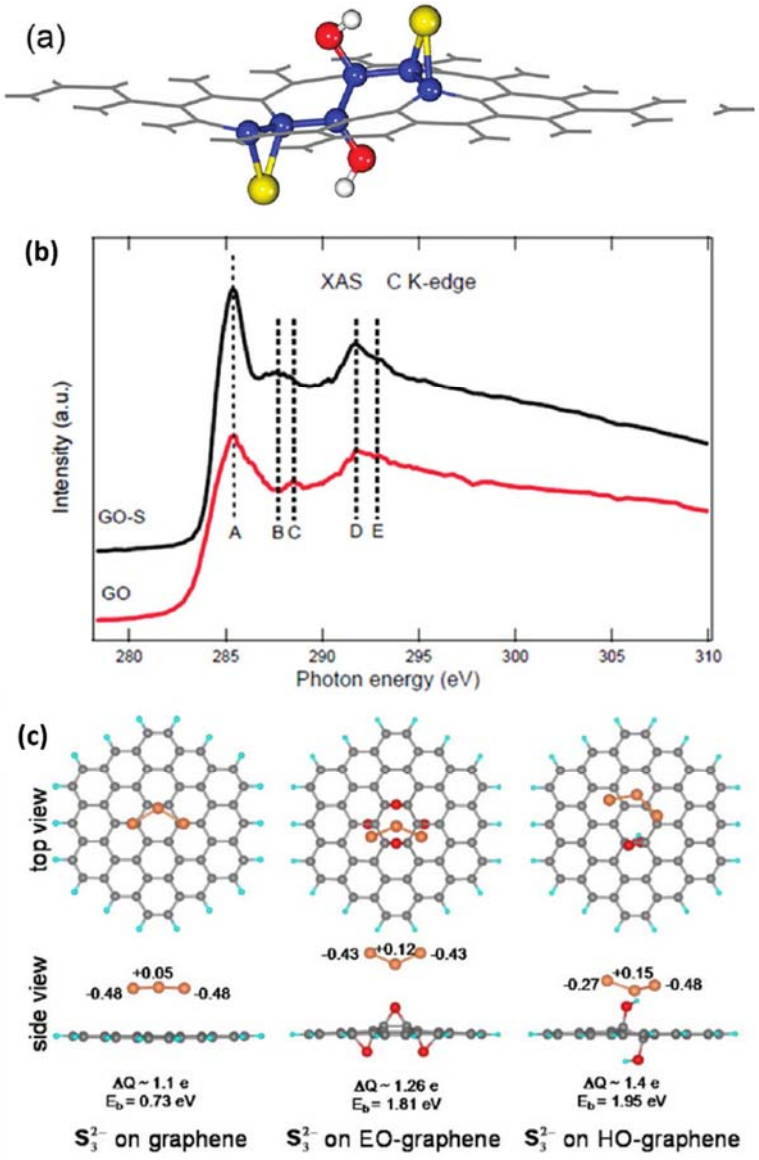

Figure 1.4 a) Representative pattern of GO immobilizing S_8. Yellow, red, and white balls denote S, O, and H atoms, respectively, while the others are C atoms; b) C K-edge XAS spectra of GO and GO-S nanocomposites after heat treatment in Ar at 155 °C for 12 h. Reproduced from Ref. 36. c) Geometry configuration (side and top view) of S_3^{2-} on graphene, EO-graphene, and HO-graphene surfaces via DFT calculations, with the electron exchange and binding energy values shown. Reproduced from ref. 39.

system.[38] CTAB, a polar ionic surfactant, affords additional binding of outer-layer sulfur and is suggested to be one of the reasons for the improvement in capacity fading. These early studies focused mostly on probing the interaction of GO with sulfur rather than polysulfides.

A thorough study on polysulfide binding with the inherent GO functional groups by density functional theory (DFT) calculations was carried out by Zhou *et al*.[39] Compared to pristine graphene, the functionalized graphene shows much greater binding energy with S_3^0, S_3^-, S_3^{2-} moieties (S_3^{2-} binding is shown in **Figure 1.4c**). The calculations demonstrated that the hydroxyl groups are bound more strongly than epoxy groups, and that polysulfide anion species (S_3^-, S_3^{2-}) exhibit stronger binding than neutral S_3^0 molecules. This was ascribed to the induced asymmetric charge distribution over the S_3^{2-} that causes a greater polarization and stronger electrostatic interactions between S_3^{2-} and functionalized graphene.

However, GO exhibits a much lower conductivity than graphene due to the presence of the oxygenated groups. Doping carbon with nitrogen is an alternative method to enhance the chemisorption towards LiPSs without compromising the conductivity to the same degree.[40] Song *et al.* has introduced a mesoporous N-doped carbon with high surface area (824 $m^2 g^{-1}$).[41] Excellent capacity retention of 95% over 100 cycles was achieved, which was ascribed to the improved chemical adsorption for LiPSs from N-doping (**Figure 1.5a**). The strong interaction with LiPSs was probed using pair distribution function analysis on the polysulfide contacted N-doped carbon, although the assignments of these peaks are not completely clear (**Figure 1.5b**). Other studies have also introduced N-doped graphene or porous hollow nanospheres to confine LiPSs.[42-45]

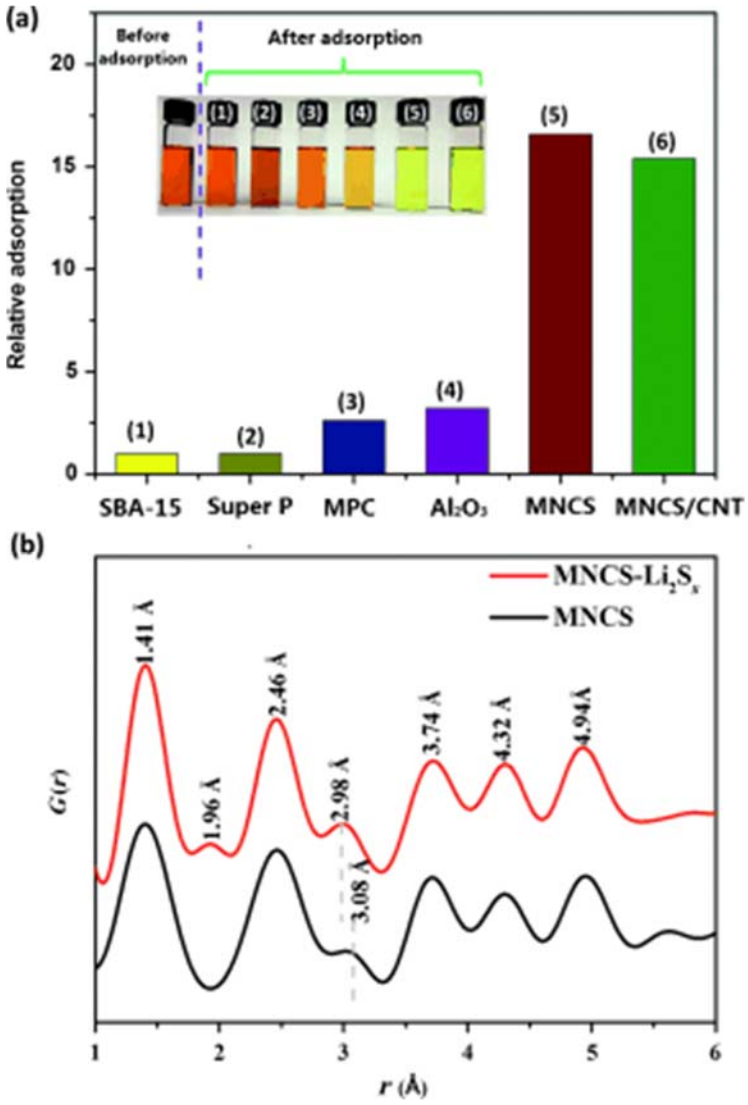

Figure 1.5 a) Comparison of the relative polysulfide adsorption for various adsorbents: SBA-15 mesoporous silica, Al_2O_3 nanoparticles, carbon black (Super P), mesoporous carbon (MPC), and nitrogen-doped mesoporous carbon (MNCS and MNCS/CNT). Inset: Photographs of a polysulfide solution before and after exposure to the different adsorbents. (b) PDF profiles of MNCS and MNCS–Li_2S_n. Reprinted from Ref. 41.

A comprehensive DFT calculation study on pyridinic and quaternary nitrogen in doped carbon by Peng *et al.* provides important insights into the underlying mechanism for

polysulfide binding (**Figure 1.6**).[46] It was found that the positive Li^+ ions bind directly to the electron-rich pyridinic N that possesses a lone electron pair, whereas for the quaternary N, Li^+ ions are prone to bind to the neighboring carbon atoms due to the distribution of N-donated electrons in the delocalized π-system. In short, this coupled interface is related to the electron donating/accepting behavior between polysulfides and the N-doped carbon.

Grafting amphiphilic polymers on carbon materials represents another approach in this category. This concept was first adopted by Zheng *et al.* by coating a polyvinylpyrolidone (PVP) layer onto carbon nanofiber walls.[47] Transmission electron microscopy (TEM) analysis showed that the PVP coating can alleviate the Li_2S detachment from the CNF walls upon discharge (**Figure 1.7a,b** *vs.* **e,f**). The improved polysulfide binding was further confirmed by a DFT calculation showing a Li^+-O (in pyrolidone) interaction. Ma *et al.* introduced another facile method to incorporate nitrile-containing molecules into carbon/sulfur composite by alkoxy-silane grafting. It was calculated that amine and imidazolium chloride molecules exhibit higher LiPS binding energy than polyacrylonitrile.[48] Amino groups have also been covalently bonded to a graphene oxide substrate.[49] The authors demonstrated not only the binding ability of polysulfides with amino groups, but also that of the amino groups onto the graphene oxide substrate.

Metal oxides, in contrast to carbon materials, are intrinsically polar materials that can strongly interact with polar polysulfide species. No further surface modification is needed for such interfacial adsorption. In the early stage of their application in sulfur cathodes, metal

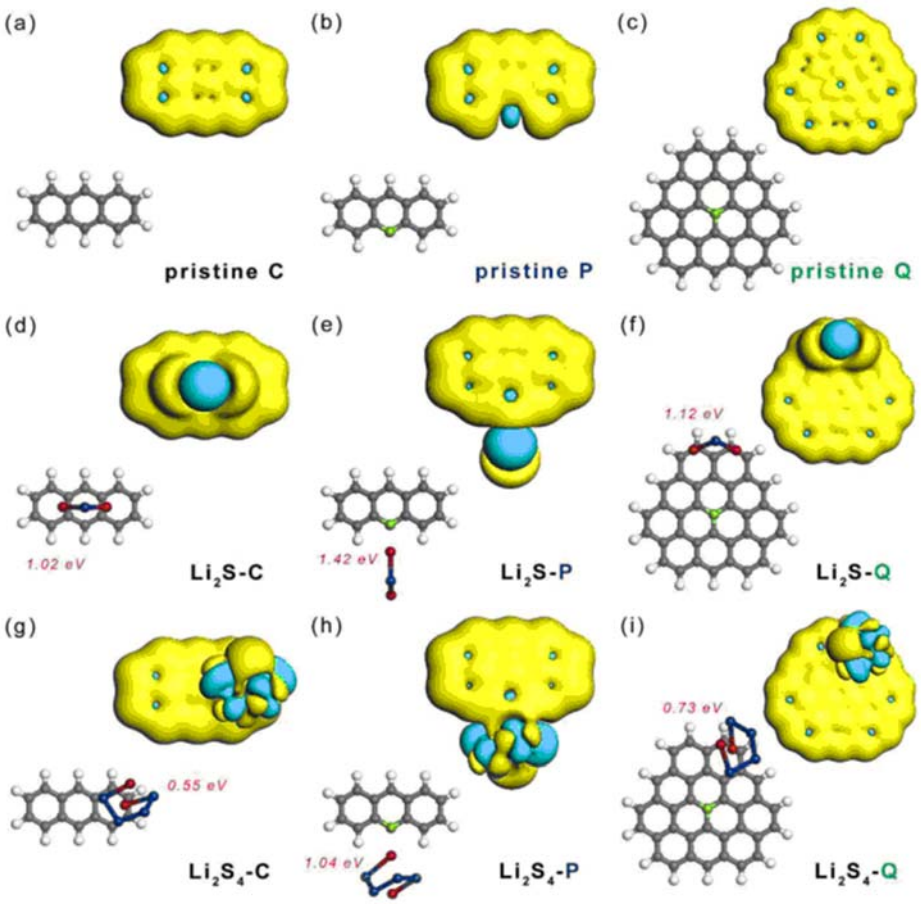

Figure 1.6 First-principles calculation of carbon host-sulfur guest interactions, showing the optimized molecular configuration and corresponding deformation charge density. Molecules and charge density of a) pristine carbon, b) pyridinic-N doped, and c) quaternary-N doped carbon, and corresponding pair with d-f) Li_2S and g-i) Li_2S_4. In the molecular configurations, the numbers represent the binding energy between host and guest while the hydrogen, lithium, carbon, nitrogen, and sulfur atoms are denoted as spheres in white, red, dark grey, green, and blue, respectively. In distribution of deformation charge density, donation/acceptance of electron is denoted as light yellow/cyan respectively. Reproduced from Ref. 46.

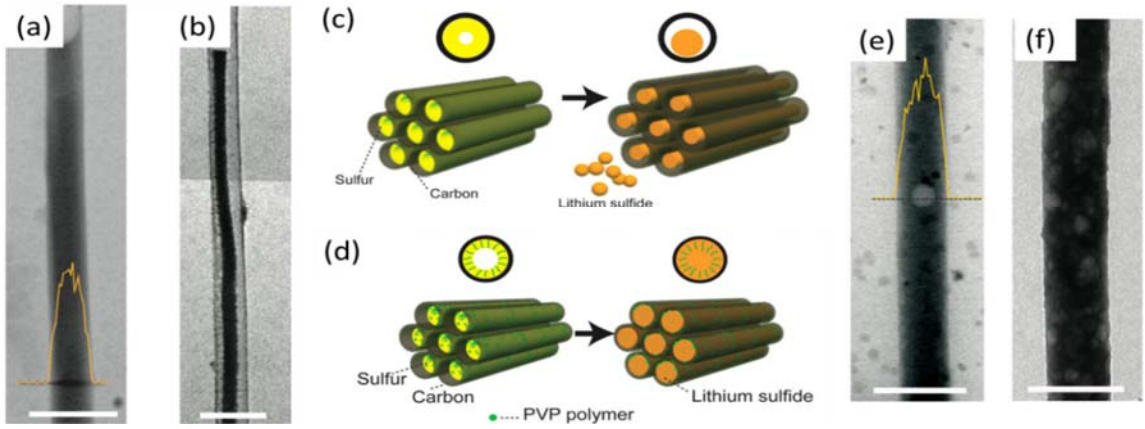

Figure 1.7 TEM images of the CNF encapsulated sulfur cathodes without a,b) and with e,f) PVP modification before discharge a,e) and after full discharge to 1.7 V b,f). The yellow lines represent the EDX counts of the sulfur signal along the dark line. The scale bars are all 500 nm. Schematics of the sulfur cathodes without c) and with d) PVP modification before and after discharge. Adapted from ref. 47.

oxides were used only as additives due to their very poor conductivity. $Mg_{0.6}Ni_{0.4}O$ and Al_2O_3 nanoparticles (~50 nm) were used as adsorbent additives in carbon/sulfur composites and improved Coulombic efficiency, initial discharge capacity, and cycling stability.[50,51]

Metal oxides with higher surface area or pore volume were later introduced to gain a more effective polysulfide adsorption for practical sulfur loading. Our group reported on a mesoporous silica SBA-15 with high surface area (850 $m^2\ g^{-1}$) and large pore volume (1.2 $cm^3\ g^{-1}$) as an additive for a carbon/sulfur composite.[52] Improved initial discharge capacity and cycling stability were demonstrated for an electrode with 70 wt % sulfur loading. EDX elemental analysis of the silica particles at early and late discharge stages showed that the polysulfides are preferentially absorbed in the pores of silica particles and then released upon

demand for further reduction. This reversible adsorption mechanism is important for non-conductive reservoirs.

Evers *et al.* have also probed the interaction between an α-TiO_2 surface and Li_2S_6 using Fourier transform infrared (FTIR) and Raman spectroscopy analysis (**Figure 1.8**).[53] When the Li_2S_6 was synthesized in the presence of α-TiO_2, a new band at 541 cm^{-1} appeared in the FTIR spectrum, corresponding to formation of a S-Ti-O bond. As well, the peak shift in the Raman spectra indicates an altered chemical environment around the titanium oxide surface following the adsorption of Li_2S_6. These observations represent the first spectroscopic evidence for the chemical interactions between polar oxides and polysulfides.

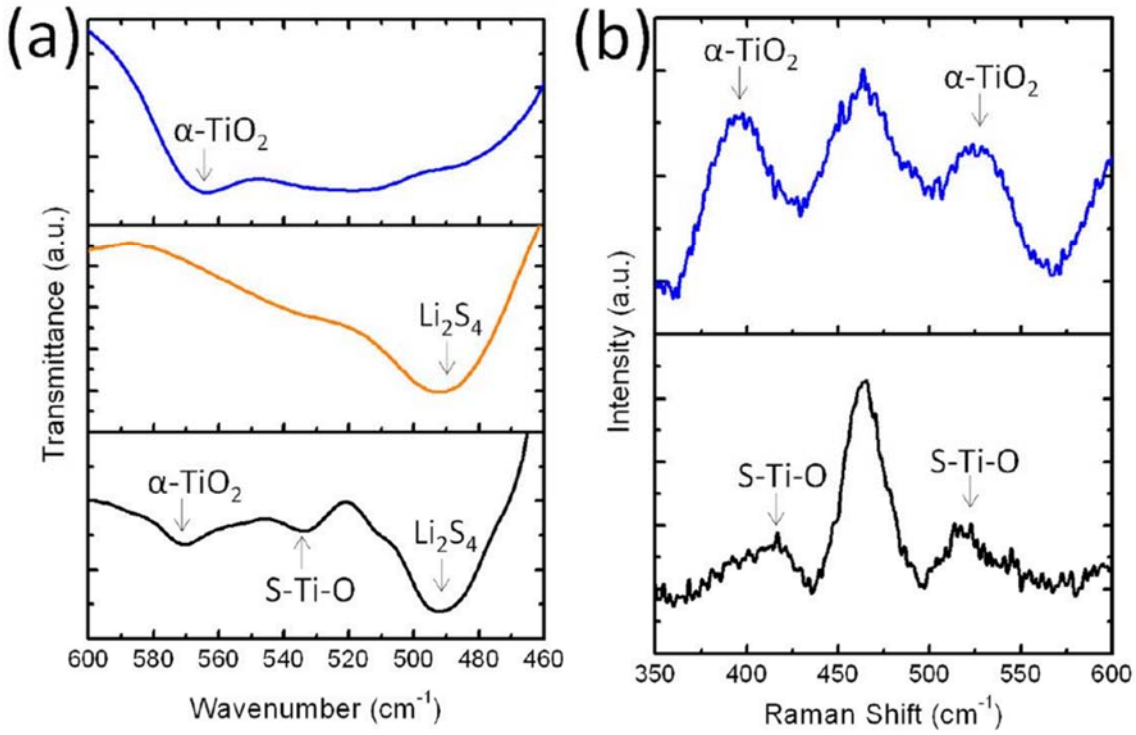

Figure 1.8 a) FTIR spectra of α-TiO_2 (top, blue), Li_2S_4 (middle, orange), and α-TiO_2/Li_2S_4 (bottom, black); b) Raman spectra of α-TiO_2 (top, blue) and α-TiO_2/Li_2S_4 (bottom, black). Peaks characteristic of the material are highlighted with arrows. Reproduced from Ref. 53.

Other than being used as additives, metal oxides have also been employed as coated layers on carbon/sulfur composites or sulfur particles.[54 - 56] Our group coated CMK-3/S composite particles with a thin oxide (SiO_x, VO_x) layer through a surface initiated growth method.[54] The thin oxide coating layer functions not only as a physical barrier towards LiPS diffusion, but also a polar/hydrophilic layer to chemically adsorb the LiPSs. Using a more sophisticated nanostructure design, Seh *et al.* coated amorphous TiO_2 onto sulfur nanoparticles to create a yolk-shell structure. This cathode material yielded a long-life Li-S battery with 0.033% capacity fading per cycle over 1000 cycles.[55] Although the chemical interaction of LiPSs with metal oxides was not directly mentioned in either report, it is believed this was one of the major contributions to the improved cycling performance using metal oxides. Another interesting work by Xiao *et al.* demonstrated the use of a hybrid TiO_2/graphene interlayer between the sulfur cathode and the separator, as a polysulfide reservoir layer.[57] The TiO_2 nanoparticles anchored between the graphene sheets chemically bind the dissolved polysulfides, while the graphene conducts electrons to reactivate them. In addition, mesoporous TiO_2 has also been used directly as a sulfur host, demonstrating improved cycling performance.[58,59]

As the underlying drawbacks of the highly insulating nature of these metal oxides hinders their overall electrochemical performance, our group has developed a bifunctional sulfur host material – nanostructured Ti_4O_7 – which combines metallic conductivity with a strong chemical binding ability for LiPSs (**Figure 1.9a**).[60,61] The high surface area Ti_4O_7 (290

$m^2 \cdot g$) is shown to adsorb more LiPSs than the non-polar carbon materials, as indicated by the color fading after Ti_4O_7 adsorption (**Figure 1.9 b,c**).

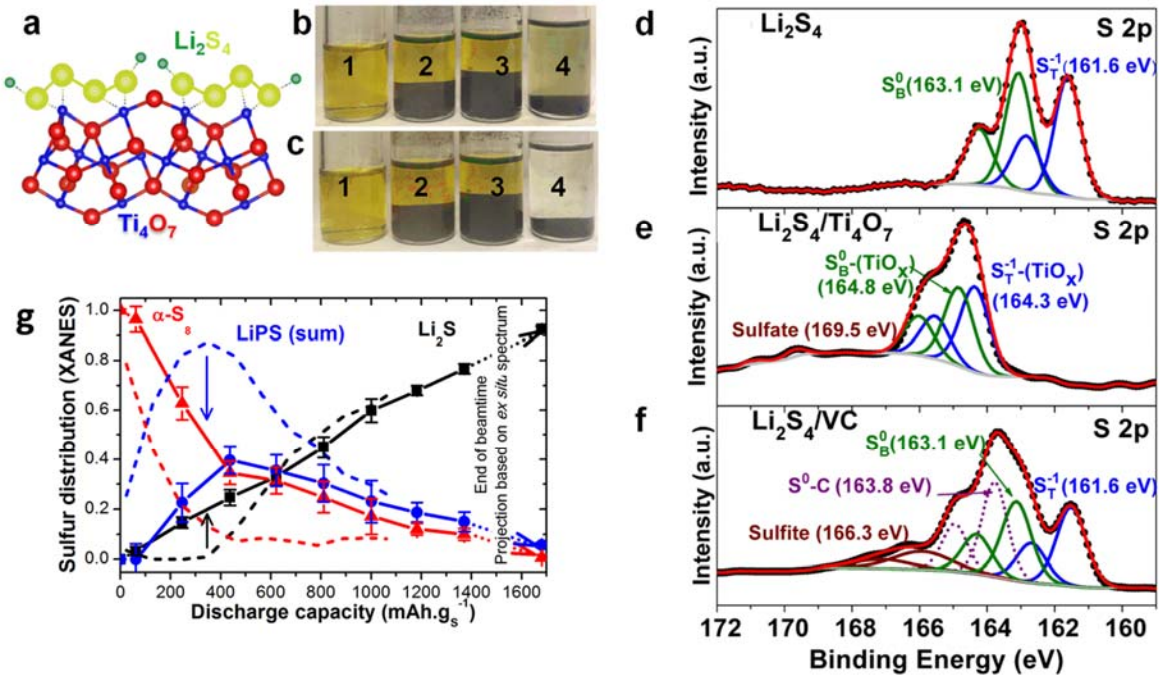

Figure 1.9 a) A schematic showing the electron density transfer between Li_2S_4 and TiO_x (yellow = S, green = Li, blue = Ti, red = O). b,c) Sealed vials of a Li_2S_4/THF solution (1), and after contact with graphite (2), VC carbon (3) and Ti_4O_7 (4), b) immediately upon contact and c) after 1 h stirring. d–f) High-resolution XPS S 2p spectra of d) Li_2S_4, e) Li_2S_4/Ti_4O_7 and f) Li_2S_4/VC (black dotted line = experimental data, red line = overall fitted data, solid/dotted lines in other colours = fitted individual components). g) The evolution of sulfur species (S_8, LiPS, L_2S) as calculated by fitting XANES spectra for Ti_4O_7/S-6 (solid lines, symbols) compared with VC/S-6 (dashed lines) showing the much lower concentration of LiPS in solution. (Black = Li_2S; blue = LiPS, shown as the sum of Li_2S_6 and Li_2S_4; red = elemental S_8.) Reproduced from Ref. 60.

The underlying mechanism of the chemical interaction between LiPS and Ti_4O_7 was probed by analyzing S 2p XPS spectra of the materials before and after contact (**Figure 1.9d-f**). The two $2p_{3/2}$ components of pristine Li_2S_4, at 161.6 and 163.1 eV, correspond to the terminal and bridging sulfur atoms (S_T^{-1} and S_B^0), respectively. Upon contact of Li_2S_4 with Ti_4O_7, the two sulfur components shift to higher binding energies by 2.7 and 1.7 eV, respectively, indicating the polarization of electrons away from the terminal and bridging sulfur atoms to the Ti_4O_7 surface.

Different from an insulating TiO_2 host where the trapped LiPSs cannot engage in redox behavior, on the metallic surface of Ti_4O_7 the electron transfer to chemically bounded LiPSs is enhanced, resulting in surface-mediated deposition of the discharged product Li_2S. This was evidenced by the significantly lowered concentration of LiPS intermediates in the *operando* cell and the much earlier precipitation of Li_2S than in the case of carbon electrodes, as probed by *operando* XANES (**Figure 1.9g**). This conclusion was further supported by the conformal deposition of Li_2S onto the Ti_4O_7 host, and the two-fold lowered charge-transfer resistance on the discharged electrode, as compared with carbon electrode. Tao *et al.* has also studied the Ti_4O_7 material and provided understanding of LiPSs binding *via* DFT calculations.[62] Using the Ti_4O_7 (1−20) surface as an test substrate, the optimized geometry indicated that the small sulfur lusters S_n (x=1,2,4) are preferentially bonded to low coordinated Ti sites.

1.4.2 Lewis Acid-Base Interaction with Polysulfides

The lone electron pairs of the polysulfide anion, S_n^{2-}, render it a soft Lewis base. Sulfur host materials that have Lewis acid characteristics, in principle, are able to interact strongly with LiPSs and thus trap them within the hosts.[63] Examples of these materials are metal-organic frameworks (MOFs) and *MXene* phases.

Beyond porous carbons, MOFs represent another class of host materials with high surface area and tunable porosity.[64] Because of this, some MOFs, including ZIF-8[65,66] and MIL-101(Cr)[67], were used directly as a host material to encapsulate sulfur/polysulfides, and showed promising cycling performance. More importantly, MOFs can trap the soluble polysulfides owing to their binding to the transition metal ions and the functional groups. A Li-S battery using a porous Cr-based MOF, MIL-100(Cr), achieved a remarkable increase in the capacity retention.[68] Aside from the LiPS confinement in the meso- and micropores, the improvement also benefits from the oxygen rich surface groups, which provides additional adsorptivity *via* chemical interactions.

Zheng *et al.* introduced the Ni-based metal organic framework (Ni-MOF), $Ni_6(BTB)_4(BP)_3$, as a sulfur host; very significant improvement in cycling stability was achieved.[63] Besides the LiPSs confinement in the pores of the Ni-MOF, the soluble LiPSs are further immobilized by the Lewis acid-base interaction. The Lewis acidic Ni(II) center is inclined to coordinate with a soluble S_n^{2-} anion (soft Lewis base, as axial ligand), through which LiPSs can be effectively captured within the cathode, as shown in **Figure 1.10.** High capacity retention of 89 % was demonstrated after 100 cycles at a rate of 0.1 C. The Lewis acid-base interaction between the open metal sites of the MOF and sulfur was also reported for HKUST-1, in which the Cu(II)–S interactions in the composite result in the S 2*p* peaks shifted to lower energies.[69]

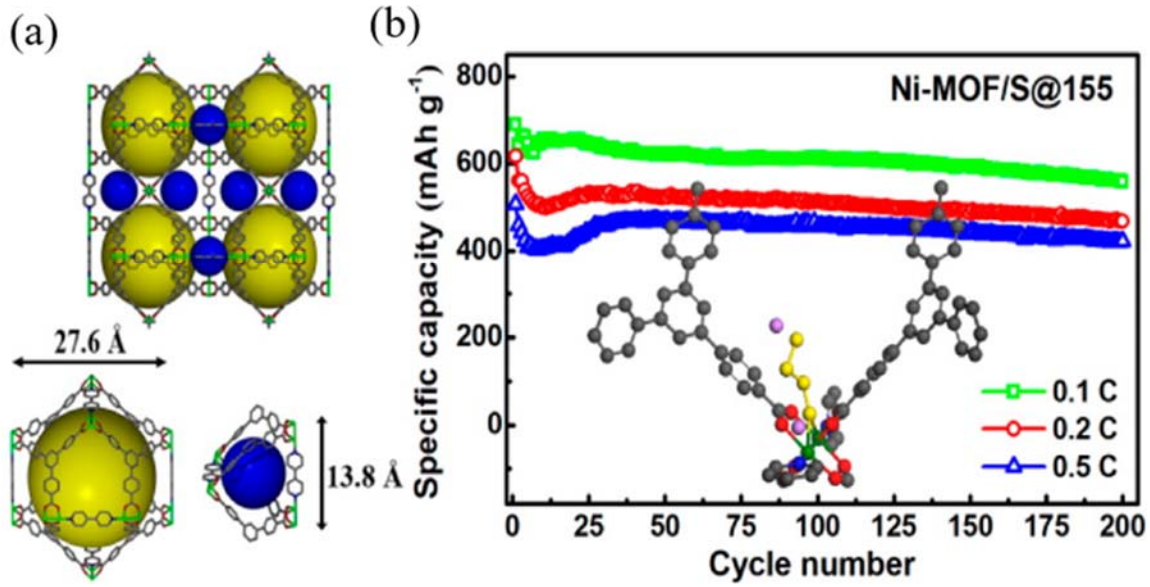

Figure 1.10 a) Crystal structure of Ni-MOF, $Ni_6(BTB)_4(BP)_3$; b) cycling performances of Ni-MOF/S composite at various rates; the inset scheme shows the interaction between polysulfides and Ni sits in Ni-MOF. Reproduced from Ref. 63.

In spite of their good polysulfide adsorptivity, the MOFs are highly electronically insulating hosts, resulting in low sulfur utilization, and poor rate performance of Li–S cells. Our group reported a class of sulfur host materials — delaminated *MXene* phases (**Figure 1.11a,b**) — that capitalize on a combination of inherently high conductivity and a highly active two-dimensional surface to chemically bind LiPSs.[70] The existence of metal-sulfur bonding, S-Ti-C, at the interface as determined by XPS analysis, is suggestive of strong interaction and chemisorption of LiPSs onto the Lewis acid Ti sites, as shown in **Figure 1.11c**. These active centers also provide multiple Li_2S nucleation sites. This effectively mitigates the dissolution of LiPSs into the electrolyte and results in very good cycling performance with a capacity fading rate of 0.05% per cycle. Some other family members of the *MXene* phases having good

LiPSs absorptivity as well as high conductivity have also been demonstrated to be highly promising candidates for high performance Li-S batteries.[71]

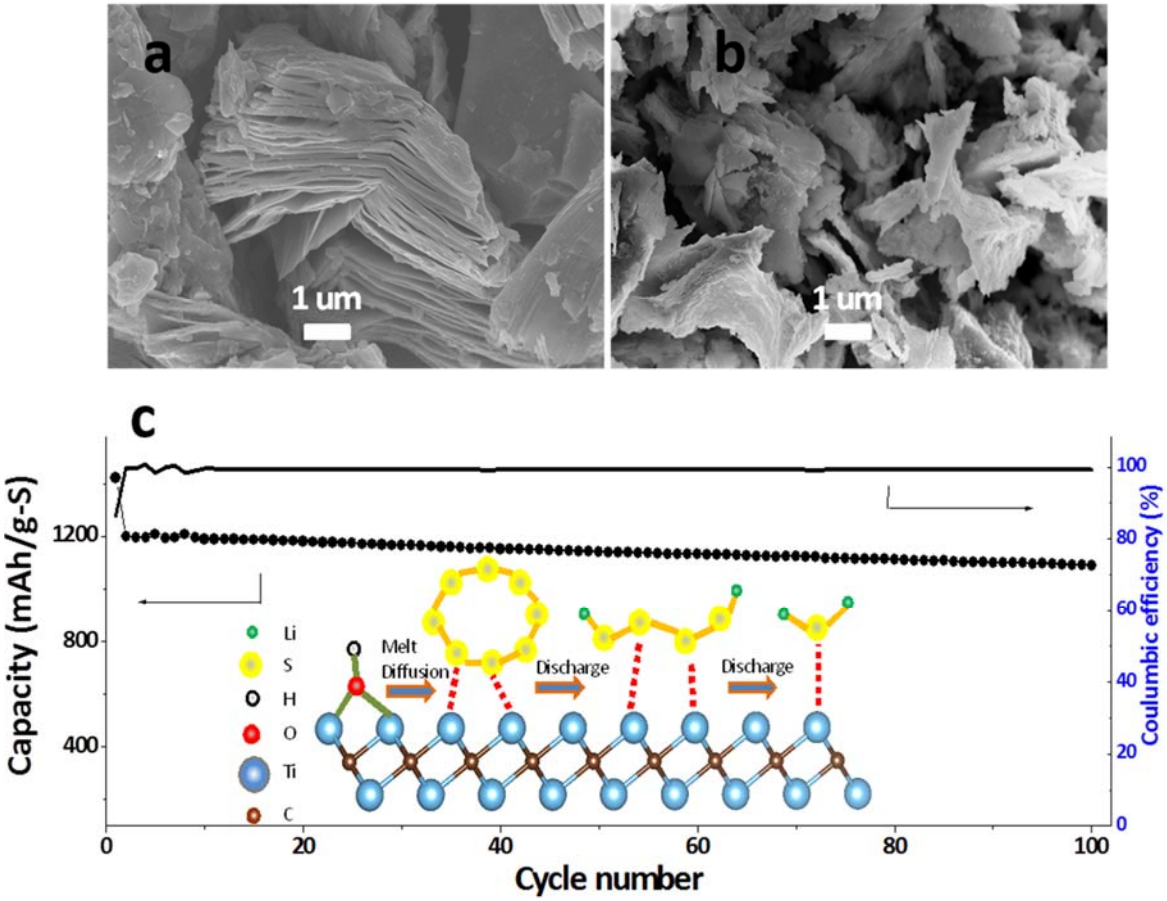

Figure 1.11 SEM images of a) exfoliated Ti_2C *MXene* and b) delaminated *MXene* sheets and c) the corresponding cycling performance of S/Ti_2C composite. Inserted scheme c) shows the Lewis acid-base interaction of Ti_2C MXene with sulfur species. Reproduced from Ref. 70.

1.4.3 Thiosulfate-Polythionate Conversion to Trap Polysulfides

The previously discussed interaction between the host materials and LiPSs rely on surface affinity, either from polar-polar interactions or Lewis acid-base interactions. Our group has

reported that δ-MnO_2 nanosheets chemically trap LiPSs by a unique mechanism – thiosulfate-polythionate conversion – that has its foundation in the "Wackenroder reaction" reported for aqueous sulfur species over a century ago.[72,73] We demonstrated that this mechanism originates from a redox reaction between MnO_2 and the LiPSs formed on discharge.

The XPS evidence shows that the surface Mn(IV) oxidizes the S_n^{2-}, thereby forming Mn(II) in the process and decorating the MnO_2 nanosheet surfaces with functional $S_2O_3^{2-}$ groups. These species anchor 'higher-order' S_n^{2-} ($n > 4$) by catenating them into the S-S bond in the thiosulfate ($[O_3S\text{-}S]^{2-}$) to form polythionate complex of the type $[O_3S\text{-}S_n\text{-}S]^{2-}$, leaving insoluble 'lower-order' polysulfides in electrical contact with the MnO_2 host, as shown in **Figure 1.12a-b**.[72] This curtails active mass loss during the discharge/charge process, suppresses the polysulfide shuttle and provides a good interface for the Li_2S deposition, resulting in a Li-S battery with long cycling (up to 2000 cycles; **Figure 1.12c**).

The high LiPSs adsorptivity of MnO_2 contributes to a low self-discharge rate of only 5% irreversible capacity loss over 3 days' shelf time. This is far superior to that of materials with low affinity for LiPSs (e.g. Super P carbon, which exhibits a 42% loss under the same conditions).[74] Furthermore, the thiosulfate-*polythionate* conversion may also account in part for the excellent properties of another Li-S host material, GO, based on observation of the same thiosulfate and polythionate groups on the GO surface after contact with polysulfides.[72]

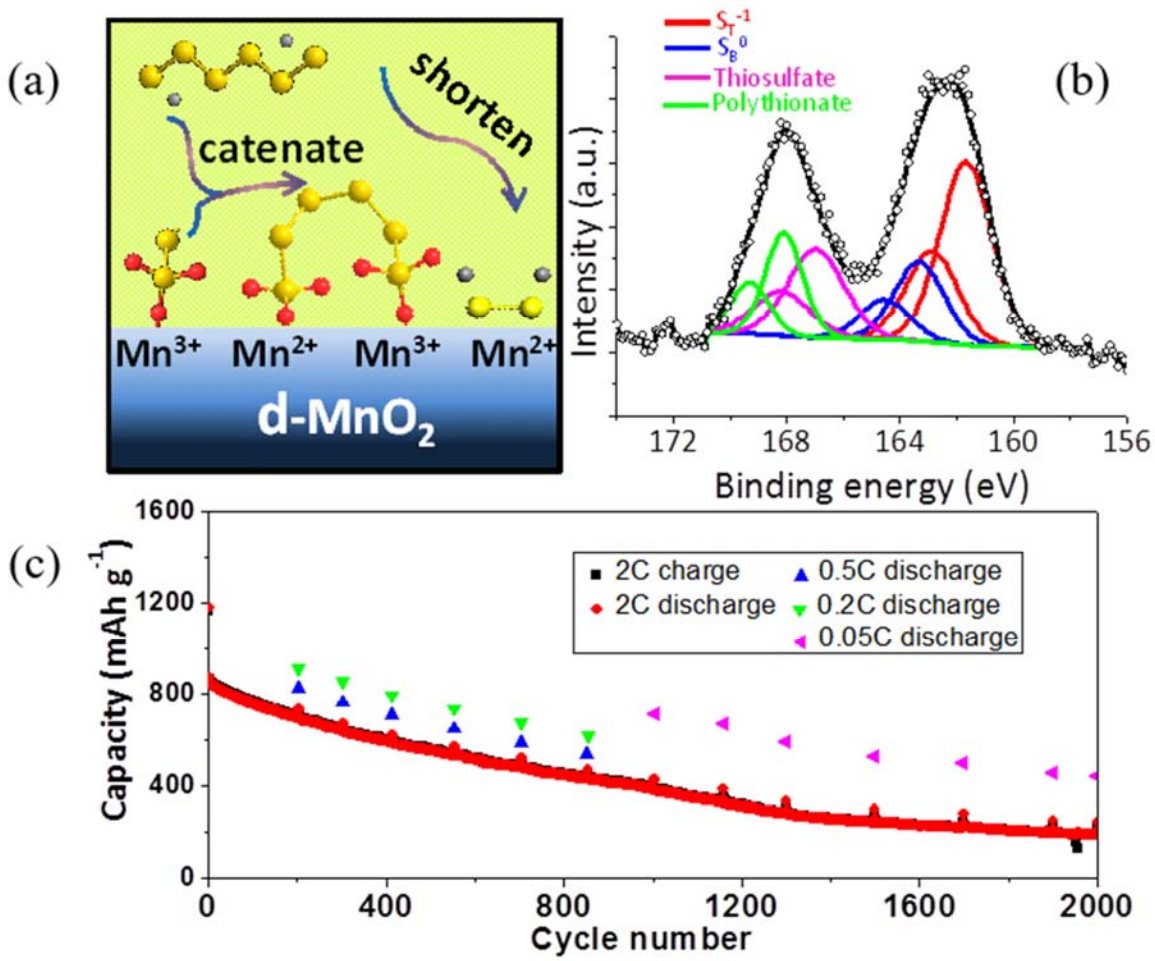

Figure 1.12 a) A schematic showing entrapment of soluble polysulfides by the MnO_2 nanosheet surface via the thiosulfate-polythionate conversion; b) high resolution S 2p spectrum of Li_2S_4 after contact with MnO_2, showing the appearance of thiosulfate and polythionate; c) long-term cycling performance of the 75S/MnO_2 composite. Reproduced from Ref. 72.

1.5 Nonsolvent Electrolytes to Suppress Polysulfide Solubility

In order to overcome the LiPS dissolution/shuttle problem, studies have also been conducted to the development of new electrolytes with suppressed LiPS solubility. The dissolution of LiPSs, like any other Li salts, relies in part on the solvation of Li^+ cations and the counter

anions. Electrolyte solutions with lower electron donor ability are less able to solvate Li^+ ions and thus can suppress the LiPS solubility, as compared to conventional dilute ether-based electrolytes (**Figure 1.13**). Reported "nonsolvent" electrolytes include amide-based room-temperature ionic liquids (RTILs) and solvates of Li salts, mostly lithium bis(trifluoromethane) sulfonimide (LiTFSI), in conventional solvent systems.

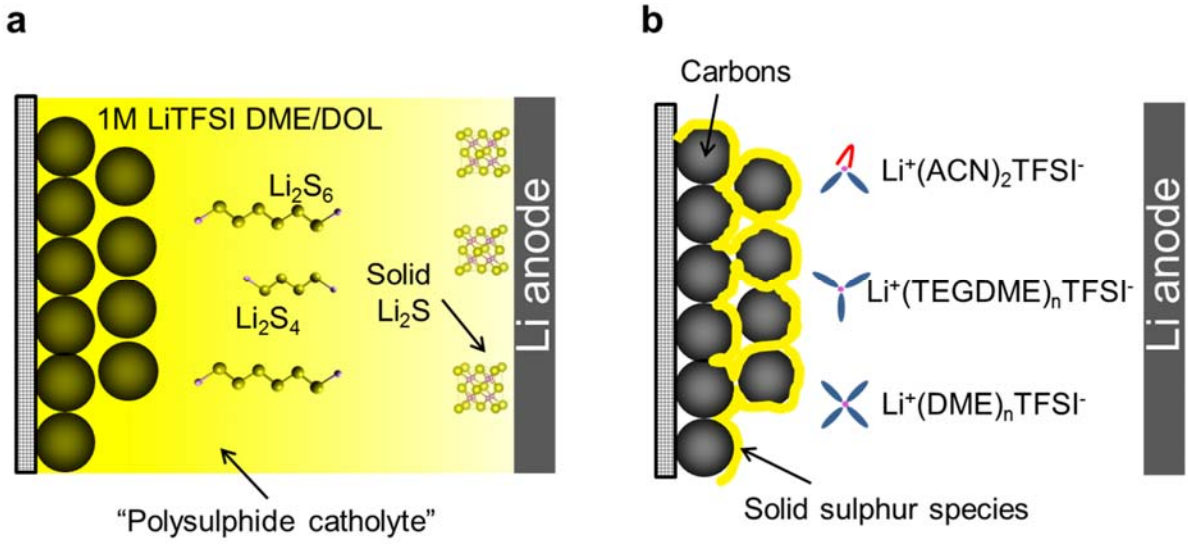

Figure 1.13 Concept of using nonsolvent compared with conventional ether-based electrolytes. The nonsolvents are exemplified by ionic solvates: TEGDME-LiTFSI, DME-LiTFSI and $(ACN)_2$-LiTFSI. a) In a conventional electrolyte, polysulfides are dissolved, activating cross-over to and reduction on the Li anode to form insulating Li_2S layer. b) In nonsolvent electrolytes, polysulfides are formed but largely in the solid state, confined within the cathodes; the Li anodes are likely to be free of sulfide layer. The extremely low solubility of the polysulfides in these non-solvent systems arises from the strong complexation of solvent molecules with Li^+ (or/and $TFSI^-$), leaving little free solvent available for polysulfide solvation.[12]

RTILs, consisting of coordinated cations and anions, are well known for their high electrochemical stability, non-flammability and non-volatility. Lacking any free solvent molecules, the donor ability of RTILs is solely dependent on the anionic component, which is related to the LiPS solubility.[75] LiPSs have much lower solubility in a RTIL with a low Gutmann donor number (DN) of *ca.*10 kcal mol^{-1} than one with a DN of *ca.*20 kcal mol^{-1}.[75] Other RTILs with amide anions also show suppressed polysulfide solubility.[75] The intrinsic drawback with these RTILs is their poor rate capability due to their low Li^+ ion diffusion coefficient and Li^+ transference number.

The design of a non-solvent electrolyte based on super-concentrated organic solvents is promising. Adding a high concentration of Li salts into ether solvents can decrease the ability to solvate extra lithium species, *i.e.*, LiPSs. The concept was first explored in a glyme–Li equimolar complex (**Figure 1.13b**).[76] Glyme is favourable for the solvation of Li^+ ions due to its Lewis-basic oxygen atoms, especially for long chain glymes such as TEGDME (noted as G4).[76] Since both $[Li(G4)]^+$ and $[TFSI]^-$ behave as discrete ions, LiPS dissolution is mitigated. Glyme-Li salt equimolar complex also shows RTIL-like behaviour such as high thermal stability, low volatility, and a wide electrochemical window. Similar solvation properties were reported for highly concentrated salt DME/DOL electrolytes (up to 7 M).[77] Most of the solvent molecules coordinate with the Li^+ cations, leading to low LiPS solubility. These electrolytes showed promising results for the Li–S system, especially in terms of Coulombic efficiency. Interestingly, however, for both the G4 and DME based solvate electrolytes, the discharge curves of Li-S cells using carbon-sulfur cathodes resemble the two-plateau curve of conventional dilute (1 M) electrolytes, indicating unaltered sulfur speciation pathway.

Our group has reported an electrolyte based on an $(ACN)_2$-LiTFSI complex, in which two moles of acetonitrile (ACN) molecules are coordinated to one mole of Li^+ cations, which form counter ion pairs with $TFSI^-$ anions (**Figure 1.13b**).[78] Two benefits are the suppressed electrolyte reaction with lithium metal and the extremely low LiPS solubility. To lower the viscosity and enhance the ionic conductivity, 1,1,2,2-tetra-fluoroethyl 2,2,3,3-tetrafluoropropyl ether (TTE) was added as a co-solvent. The TTE is too fluorinated to participate in Li^+ solvation, and therefore minimizes LiPS solubility, which is first described for glymes.[79] A combination of *operando* XANES at the S K-edge and electrochemical studies demonstrated that LiPSs are indeed formed in these ACN complexed electrolytes. The very limited dissolution and mobility of LiPSs in the electrolyte strongly affect the speciation and polysulfide equilibria, resulting a one sloping plateau discharge curve and enhanced capacity close to the theoretical value.

Note that these polysulfide non-solvent based electrolytes generally exhibit relatively low ionic conductivity - due to the high viscosity and thus high mass transport resistance - limiting the rate capabilities and energy efficiency during cycling.

1.6 First-Principles Computations for Li-S Batteries

It is beneficial to understand some metrics in battery research using computational studies, such as the electrode potential, materials interactions, electrolyte/electrode interfacial reactions/stability, ion diffusion properties, *etc*. Experimental techniques including XPS, infrared and Raman spectroscopies have been routinely used to probe the chemical interaction between LiPSs and sulfur hosts.[53,55,60,62] Computational studies based on first-principles calculations can provide very valuable metrics regarding the strength of the interaction based on binding energies.

First-principles calculation (*ab initio* in *Latin*) is a computation approach that starts with the very basic nature of matters, that is, they are made of atoms and atoms are made of positively charged nuclei and negatively charged electrons. Describing the interactions of the constituent electrons and nuclei of a system as accurately as possible would enable us to understand and predict the materials behavior, that is, their physical and chemical properties. Here the introduction of computations for solid state materials, or the narrow meaning of condensed matters by physics, is presented.

Many aspects of solid state material properties are highly dependent on their electronic structure. Increasing the accuracy and precision of computational methods is crucial for successful theoretical modeling of the electric, magnetic and optical properties. Over the last decades, the outstanding progress achieved in first-principles calculations has led to the capability of building strong correlation between theoretical and experimental data. The foundation of this progress was laid by density functional theory. DFT is a branch of first-principles calculations that relies on the electron density to describe the functionals, as opposed to molecule orbitals, valence bonding, for example.

1.6.1 Overview of Density Functional Theory

The foundation for first-principles calculation is to solve the non-relativistic time-independent Schrödinger equation (SE, **Figure 1.4**), which describes the quantum property of atoms and molecules.

$$\widehat{H}\Psi = E\Psi \qquad \textbf{Equation 1.4}$$

where $\widehat{H}$ is the Hamiltonian operator describing the system, Ψ is the wavefunction, that is, a set of solutions (eigenstates) of the Hamiltonian, and E is the energy of the system, that is, the

corresponding eigenvalues. The Hamiltonian operator is composed of the following components shown in **Equation 1.5**,

$$\widehat{H} = T_e(r) + T_N(R) + V_{eN}(r,R) + V_{NN}(R) + V_{ee}(r) \qquad \textbf{Equation 1.5}$$

where R and r is the spatial coordinates of nuclei and electrons in the system, respectively. $T_e(r)$ and $T_N(R)$ are the kinetic energy of electrons and of nuclei, and $V_{eN}(r,R)$, $V_{NN}(R)$, $V_{ee}(r)$ are the electron-nuclei, the nuclei-nuclei and electron-electron interactions, respectively.

An explicit solution for the SE can only be obtained for simply systems such as the hydrogen atom or ideal harmonic oscillator. When describing solid state materials, which involves many nuclei and electrons in the system (many-body system), it is practically impossible to find the analytical solutions to the SE. Approximations that intake semi-empirical or empirical parameters are thus needed to solve these equations in a numeric manner. DFT is a successful method that has developed reasonable approximate solutions to the SE over the past decades, and gives a reasonable prediction of the ground state (eigenstates and eigenvalues) and other relevant properties of the system.

1.6.2 Born-Oppenheimer Approximation

Exact solution to **Equation 1.5** requires solving the nuclei and electrons simultaneously, which is analytically impossible. With much lower mass than the nuclei, electrons respond much more rapidly to the changes in the surrounding potentials than nuclei can (that is, not on the same time scale). Therefore, the wavefunction can be described in two components, describing nuclei and electrons separately, based on the so-called Born-Oppenheimer (BO) approximation

(**Equation 1.6**). This decoupling has greatly reduced the computation costs for DFT and enabled its development.

$$\Psi(r, \mathrm{R}) = \Psi(\mathrm{r})\, \chi(\mathrm{R}) \qquad \textbf{Equation 1.6}$$

where $\Psi(\mathrm{r})$ is the component for electrons, and $\chi(\mathrm{R})$ is for nuclei.

With the BO approximation, the SE equation can then be solved in two successive steps. First, with the positions of all nuclei fixed, all electrons in the system relax and find the ground state based on the potentials present, the so-called electronic step. Therefore, during the electronic steps, the SE can be rewritten as **Equation 1.7**.

$$\widehat{H}_e \Psi_e = E_e \Psi_e \qquad \textbf{Equation 1.7}$$

where $\widehat{H}_e$, Ψ_e and E_e is the version for electrons.

Then the positions of the nuclei in the system can be updated based on the potential energy surface of the electronic ground state, the so-called ionic step. The program goes through the two step iteratively until certain accuracy has been achieved for the SE equation. The total energy E_{tot} are then the sum of energy of electrons and nuclei.

$$E_{tot} = E_e + E_N \qquad \textbf{Equation 1.8}$$

Note that the variational principle states that by minimizing the expectation value of the energy, $E(\Psi)$ with respect to the electron wavefunction Ψe, we can obtain the ground state wavefunction Ψ_0 and the ground state energy $E_0 = E(\Psi_0)$.

1.6.3 Hohenberg-Kohn-Sham Theorems

Solving the electron wavefunctions (Ψ_e) for the many-body system is computationally difficult and expensive. Hohenberg-Kohn theorem greatly simplifies the problem by introducing the

electron density, $\rho(r)$, which is a central quantity of DFT calculation. It is defined as a function of individual wavefunctions as in **Equation 1.9**.

$$\rho(r) = 2\sum_i \Psi_i^*(r)\Psi_i(i) \qquad \textbf{Equation 1.9}$$

Hohenberg- Kohn theorem states that the particle density $\rho_0(\boldsymbol{r})$ uniquely determines the energy, wavefunction and other properties of the system ($\boldsymbol{E}$=$\boldsymbol{E}[\rho(\vec{r})]$ **Equation 1.10**). This theorem is significant in that it simplifies the many-body problem (3N dimensions) to an electron density problem that relies on only 3 spatial coordinates. This greatly saves the computation requirements to a practical level.

$$E = E[\rho(\vec{r})] \qquad \textbf{Equation 1.10}$$

Kohn-Sham theorem reveals that the functional $E[\rho(\vec{r})]$ will have the lowest energy if and only if the electron density is the true ground state electron density, $\rho_0(\vec{r})$ (**Equation 1.11**)

$$\frac{\delta E[\rho(\vec{r})]}{\delta\rho(\vec{r})}\Big|_{\rho(\vec{r})=\rho_0(\vec{r})} = 0 \qquad \textbf{Equation 1.11}$$

The ground-state energy functional with respect to the electron density is then expressed as in **Equation 1.12**. We can solve for the exact electron density if we can find the minimum of the energy functional.

$$E(\rho) = T_e(\rho) + V_{ext}(\rho) + V_H(\rho) + E_{ex}(\rho) \qquad \textbf{Equation 1.12}$$

where $T_e(\rho), V_{ext}(\rho), V_H(\rho),\ E_{ex}(\rho)$ represent the kinetic energy of electrons, external potential energy, Hartree-Fock potential energy and electron exchange-correlation energies. We have the explicit expressions for all terms except the exchange-correlation functional $E_{ex}(\rho)$. It represents the exchange interaction and correlation interaction between electrons as

well as some other effects such as self-interaction correction terms. Therefore, the accuracy and reliability of the calculations are thus strongly dependent on the choice of the exchange-correlation functionals.

1.6.4 Exchange-Correlation Functionals for DFT

Finding the exact form or an optimized form of the exchange-correlation functional has been the major topic for DFT development. Currently there are several approaches to approximate the $E_{ex}(\rho)$, two of which are widely used: the local density approximation (LDA) and the generalized gradient approximation (GGA). LDA defines the exchange-correlation functional by using the local density of the quantum Monte-Carlo simulated uniform electron gas. The exact form of LDA is known, where the electrons are balanced by a positive background charge distribution. LDA is the basis of all other approximate exchange-correlation functionals.[80] In addition to the electron density, GGA takes into account of the gradient of the electron density, $\nabla\rho(\boldsymbol{r})$, to simulate the non-homogeneous distribution of electrons.[81] Other more complex approximations and hybrid approximations, are also available.

1.6.5 Periodic Systems and Plane-Wave Basis Set

Crystalline solids have periodically repeating structure; computations on these systems can be greatly simplified by calculating only one supercell (one or multiple unit cells) and then expanding to the whole crystals to derive the material properties. DFT calculations of periodic systems obeys the Bloch theorem (**Equation 1.13**).

$$\psi_{\mathbf{k}}(\boldsymbol{r}) = \exp(i\mathrm{kr})\, u_{\mathrm{k}}(r) \qquad \textbf{Equation 1.13}$$

where k is the wavevector in the reciprocal space of the crystal and $u_{\mathrm{k}}(r)$ is a periodic function of the periodicity of the crystal. The exponential term $\exp(i\mathrm{kr})$ describes a typical plane wave function; therefore, plane wave basis set is an ideal and natural choice for such periodic system with boundary conditions. The rapid switching between coordinate and momentum spaces in such basis set can be performed *via* fast Fourier transform.

Therefore, the solving of SE can be performed for each k independently. The electron density is then constructed by integrating all possible k values. Attention should then be paid to the selection of k-point grids in the reciprocal space of the primitive cell (the first Brillouin Zone), as appropriate to converge and be accurate while with the lowest computation cost possible.

The number of plane waves included in the basis set is determined by the preset cut-off energy, dictated by their kinetic energy. The cut-off energy is introduced to truncate wavefunctions with high kinetic energies. A high cut-off energy could yield more accurate results, if possible, but is much more computationally expensive. The selection of a proper cutoff energy requires attention when performing DFT calculations.

1.6.6 Pseudopotentials

The core electrons are tightly bound to the nuclei and their strong interaction (with electrons and nuclei) requires very high cutoff energy and excessive plane waves basis in the DFT calculations. Furthermore, mostly only valence electrons are important for the derivation of physical and chemical properties of materials. Including the core electrons is thus computationally very expensive and unnecessary. Therefore, the complicated effects of motion of core electrons and its nucleus are usually approximated by pseudopotentials. In this way, the high-energy core electrons can be substituted by the frozen core, that is, the electron density

of core electrons is replaced by an effective density. The pseudopotential approach enables the use of much lower energy cutoff as well as less basis wavefunctions for solving the SE.

1.7 Summary

A variety of approaches have been utilized to chemically bind LiPSs. Modifications of pristine carbons that invoke graphene oxide, N-doped carbons or grafted amphiphilic polymers have the advantages of being light-weight, high surface area materials, but the mechanical and chemical stability of these modified materials over long-term cycling are under-investigated. Polar-polar interaction with LiPSs realized by using metal oxides has been shown to improve the cycling performance. In particular, the demonstrated surface-controlled polysulfide redox and Li_2S deposition behavior on a conductive and polar surface provides an exciting perspective for not only conventional "contained" cathodes but also catholyte-type Li-S cells. The strategy of using an efficient polysulfide transfer mediator, thiosulfate and polythionate is promising towards long-life Li-S batteries. Modifying the electrolyte so as to suppress the polysulfide solubility from the source also provides an unique avenue to achieve the same purpose.

Along with the significant progress in increasing the life time of Li-S batteries is the low total areal sulfur loading on the electrode, often less than 2 mg cm^{-2}. This remains one of the major hurdles that needs to be solved in order to maintain the advantageous high energy density of Li-S cells. Three-dimensional carbonaceous supports, such as free-standing CNT paper or reduced GO sponges with advanced electrode configurations have shown progress in achieving sulfur loadings up to 20 mg cm^{-2}.[82] The free-standing thick carbonaceous electrodes do not require the use of other inactive components such as carbon additives or polymeric binders. However, these porous carbon frameworks contain significant amount of void space, which

leads to high electrolyte/sulfur ratio and thus low energy density. With increasing areal sulfur loading, the cell capacity typically degrades faster than that of a lower loading cell upon long-term cycling. This may be related to the lengthened electrolyte penetration path, cathode structure collapse due to large volume expansion, increased parasitic reactions of largely dissolved LiPSs with lithium anode, and increased anode/cathode resistance.

1.8 Motivation and Scope of this Thesis

As discussed in the aforementioned introduction and summary, it is essential to effectively confine the polysulfides *via* chemical adsorption, so as to inhibit their shuttling and control the deposition of Li_2S and sulfur within the cathode. Exploring new cathode materials with these properties are of paramount importance in the Li-S field in order to narrow down the optimal avenue towards long-lived and high capacity Li-S batteries. In addition, smart architecture of the cathode − not only the host materials, but also the binder − is vital to realize Li-S batteries with high areal loading, low electrolyte volume, and thus high energy density. Finally, it is not stressed enough that finding new electrolytes (other than the conventional dilute gylme based) that control polysulfide solubility while offering good rate capability is an under-researched pathway to the ultimate goal and should be explored.

Based on these motivations, this thesis features a comprehensive study of approaches in confining lithium polysulfides and preventing their shuttling with an ultimate goal of fabricating long-life and high energy density Li-S batteries. These includes investigation on various classes of sulfur host materials, form metal sulfides to doped carbons and carbon nitride, with a focus on understanding of their chemical interaction with polysulfides, and further efforts on sparingly solvating electrolytes with an effort to reveal the sulfur reaction

mechanism. First-principles computational studies in this thesis have shed light on the mechanism of interaction of lithium polysulfides with various class of host materials.

Chapter 1 is a general introduction and overview of pertinent research that has been undertaken in the past few years on Li-S battery cathodes and electrolytes. Part of this chapter (Sections **1.1, 1.2, 1.3** and **1.4**) is adapted from Q. Pang, X. Liang, C.Y. Kwok, L.F. Nazar, Review - The importance of chemical interactions between sulfur host materials and lithium polysulfides for advanced lithium-sulfur batteries. *J. Electrochem. Soc.,* **2015**, 162, A2567; Copyright © 2015, The Electrochemical Society; or from (Section **1.5**) Q. Pang, X. Liang, C.Y. Kwok, L.F. Nazar, Advances in lithium–sulfur batteries based on multifunctional cathodes and electrolytes. *Nat. Energy,* **2016***,* 1, 16132; Copyright © 2017, Macmillan Publishers Limited.

Chapter 2 describes the research experimental methods and characterization techniques that are employed in this thesis. This chapter is partly (Sections **2.2.3** and **2.3.3**) adapted from E. Talaie, P. Bonnick, X. Sun, Q. Pang, X. Liang, L.F. Nazar, Methods and protocols for electrochemical energy storage materials research. *Chem. Mater.*, **2017**, 29, 90; Copyright © 2017, American Chemical Society.

Aiming at exploring the application of conductive metal sulfides in Li-S cathodes, **Chapter 3** describes metallic and polar Co_9S_8 used as a sulfur host material, and thoroughly discusses its chemical interaction with polysulfides. This work has been published as: Q. Pang, D. Kundu, L.F. Nazar, A graphene-like metallic cathode host for long-life and high-loading lithium-sulfur batteries. *Mater. Horiz.,* **2016**, 3,130; Copyright © 2016, The Royal Society of Chemistry.

A departure from using the relatively heavy metal compounds as sulfur hosts leads to the study shown in **Chapter 4**, which demonstrates a biomaterial derived N,S dual-doped

porous carbon that enables long-lived Li-S batteries. The synergistic binding effect from N and S atoms shows superior performance than purely N-doped carbon. This work has been published as: Q. Pang, J. Tang, H. Huang, X. Liang, C. Hart, K.C. Tam, L.F. Nazar, A nitrogen and sulfur dual-doped carbon derived from polyrhodanine/cellulose for advanced lithium–sulfur batteries. *Adv. Mater.,* **2015**, 27, 6021; Copyright © 2015, WILEY-VCH Verlag GmbH & Co. KGaA, Weinheim.

In light of the limitation of low heteroatom doping concentration for the conventional doped carbon materials as shown in **Chapter 4**, **Chapter 5** shows the application of a light-weight graphitic carbon nitride material, with a high N concentration (up to 53.5 at%), which results long-lived Li-S batteries. This work has been published as: Q. Pang, L.F. Nazar, Long-life and high areal capacity Li-S batteries enabled by a light-weight polar host with intrinsic polysulfide adsorption. *ACS Nano*, **2016**, 10, 4111; Copyright © 2016 American Chemical Society.

Based on the host material introduced in **Chapter 5** and with a goal of fabricating high energy density Li-S batteries, **Chapter 6** describes a comprehensive approach by using a light-weight bifunctional composite host material, combined with an *in-situ* cross-linked polymeric binder. This approach allows slurry-processed cathodes with high areal sulfur loading up to 14.9 mg cm^{-2}. This work has been published as: Q. Pang, X. Liang, C.Y. Kwok, J. Kulisch, L.F. Nazar, A comprehensive approach towards stable lithium-sulfur batteries with high volumetric energy density. *Adv. Energy Mater.,* **2016**. DOI: 10.1002/aenm.201601630; Copyright © 2016, WILEY-VCH Verlag GmbH & Co. KGaA, Weinheim.

Chapter 7 describes a completely different approach than **Chapter 3-6**, which relies on the application of a sparingly soluble electrolyte made from ACN_2:LiTFSI solvate in Li-S

battery. The sparing solvating feature and improved kinetics at elevated temperatures directs a different reaction pathway and results high sulfur utilization.

Chapter 8 concludes the entire thesis and provides some thoughts on Li-S batteries.

Chapter 2 Experimental and Computational Methods

This thesis employs a combination of experimental characterizations and computational techniques. Techniques in the field of electrochemistry measurements, physical and chemical characterizations and first-principles calculations are presented in this Chapter, including the fundamental principles and experimental parameters.

2.1 Electrodes and Electrolytes Preparation

Li-S cell cathodes can be made from the charged species (elemental sulfur) or the discharged species (Li_2S). In this thesis, the sulfur cathodes were all based on elemental sulfur that is thermally infiltrated into the host materials, the so-called "melt-diffusion" process. Typically, sulfur was first mixed with the host material by hand grinding at desired ratios. The mixture was then loaded into a pressing die and gently pressed to spatially confine the sulfur. The loaded die was then heated at 155 ^oC under atmosphere for 12 hours, during which the sulfur melts and exhibits the lowest viscosity. The final active material was obtained after hand grinding into powder.

The electrodes were prepared by mixing the active materials (composites of host material and sulfur), binder, and carbon additive at specified ratio (wt%, 8:1:1 or 8.5: 0.5: 1) in the solvent (dimethylformamide (DMF), or a mixture of DMF and deionized water). The slurry was obtained by mixing using Thinky® mixer or hand grounding. The slurry was then cast on carbon coated aluminum foil or carbon paper (AvCarb P50, FuelCell Earth), by drop-casting or doctor blading. The electrodes were then dried at 60 ^oC for overnight before cell assembly.

The electrolyte used for electrode studies in **Chapter 3-6** is 1 M LiTFSI and 2 wt% of $LiNO_3$ in a mixed solvent of DOL/DME (1:1, v/v), purchased from BASF. The electrolyte without $LiNO_3$ was prepared by dissolving 1 M LiTFSI in DOL/DME (1:1, v/v). The sparingly soluble electrolytes used in **Chapter 7** are prepared by dissolving LiTFSI in the solvents, acetonitrile, tetrahydrofuran (THF) or TEGDME at specific molar ratio by vigorous stirring. All the electrolyte preparation was conducted inside the glovebox. The LiTFSI salt was dried at 120 ºC in vacuum for 48 hours before use. The solvents were dried in molecule sieves or active alumina before use. Further details are referred to **Chapter 7**.

The Li-S cells were assembled using 2325 coin cells inside the glovebox. Li metal strip was used as the anode and specified amount of electrolyte was used. Precise control of the electrolyte volume is necessary as that affects the electrochemical performances of the Li-S cells. Celgard® 3501, made from microporous polypropylene monolayer membrane, was used as the separator.

2.2 Electrochemistry Methods

2.2.1 Galvanostatic Discharge/Charge

Galvanostatic cycling refers to the electrochemical cycling method where a constant current is applied to a cell until a certain amount of charge has been passed or a voltage cut-off has been reached. In the field of battery research, usually a negative current forces discharge and a positive current forces charge of a cell. This technique is realized by using a galvanostat station, which is a controlling and measuring device capable of forcing the current through a cell in coulometric titration constant, regardless of the resistance of the cell loaded (R_L). The main feature that enables a galvanostat is its nearly infinite internal resistance (R_I), that is, extremely high with respect to the loading resistance, and a rather high voltage to generate current.

Galvanostatic cycling is one of the most important and widely used electrochemical characterization techniques for research in Li-S battery and even all types of batteries. On one hand, it mimics the battery operating conditions in practice, where a constant power is desired (assuming voltage is constant in this region). On the other hand, it presents a way to understand the maximum number of Li^+ charges that can be stored (depleted) into (from) the electrodes, and the potential that these Li^+ storing/depleting processes occurs. Through this we can learn the specific capacity (charge multiplied by time, per mass/volume) of an electrode and de-convolute the thermodynamics/kinetic information about these processes.

A curve that plots the voltage response as a function of specific capacity is usually used to present the basic electrochemistry, as shown in **Figure 2.1**, using Li-S battery as an example. We can learn, for instance, the discharge consists of two stages (voltage plateaus), where the sulfur speciation occurs with the different free energy change (that is, different thermodynamics). Generally, a flat voltage plateau indicates a two-phase reaction and a slope voltage profile indicates a one-phase reaction (solid-solution, *e.g.*).

In this thesis, galvanostatic cycling was conducted using a BT2000 battery cycler (Arbin Instruments) at specified C rates within a proper voltage window. *Operando* XRD experiments shown in **Chapter 7** is based on measurements during galvanostatic cycling of the cell, where the crystalline phases at each stage of lithiation can be observed and quantified.

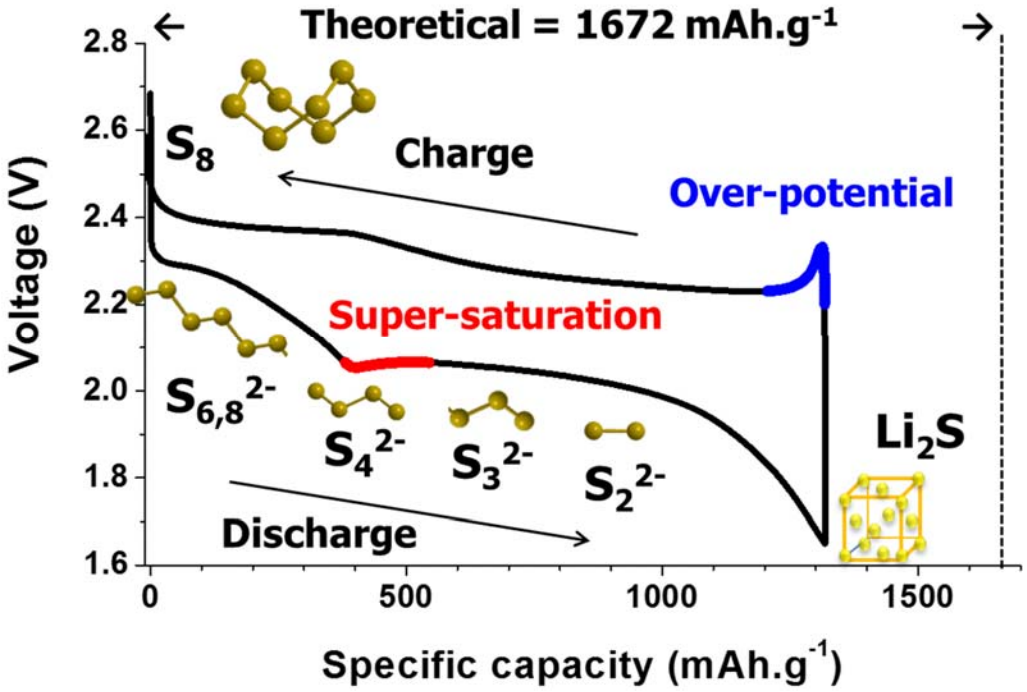

Figure 2.1 A representative discharge/charge voltage profile of Li-S batteries that base on conventional dilute glyme electrolytes, with the lower curve being discharge and the upper curve being charge. Super-saturation region (red) at the discharge and the over-potential (blue) at the charge are indicated. The representative sulfur species at each stage are indicated , although their evolution or even existence is still in debate. [5]

2.2.2 Galvanostatic Intermittent Titration Technique

Understanding the equilibrium thermodynamics and the chemical diffusion kinetics of an electrochemical cell is essential to evaluate an electrode material. Galvanostatic intermittent titration technique (GITT) is a technique useful to retrieve both thermodynamics and kinetics parameters.

In a typical GITT experiment, a constant current pulse is applied for a short period of time, followed by open circuit rest for another specified period of time. This process is repeated until no charge can be passed or the "equilibrium" potential of the cell reaches the cut-off voltage. During a negative current pulse (discharge), the potential quickly experiences an *iR* drop, where *R* consists of the charge transfer resistance R_{ct} and the uncompensated resistance R_{un}. Then the potential responds to the galvanostatic discharge pulse, either decreasing or remaining constant. When the current pulse is switched off, *i.e.*, during the open circuit relaxation, the composition in the electrode tends to homogenize by mass diffusion and/or chemical dispropotionation/equilibration. Therefore, the potential first suddenly increases by *iR*, and then it slowly increases until the electrode is in its equilibrium state (*i.e.,* when dE/dt ~ 0) reaching the open circuit potential. Then, the galvanostatic pulse is applied again, followed by current interruption. This sequence is repeated until the battery is fully discharged. During the charge pulse, the opposite holds.

Theoretically the equilibrium potential obtained for discharge and charge at the same lithiation stage would superimpose. However, in practice, it is likely to take very long time to reach equilibrium and therefore, the longer rest period, the closer we can get to the equilibrium potential. An important concern of GITT experiment is that the potential response derives from an indistinguishable superimposition of the cathode and anode. Therefore, a three-electrode cell is preferred in order to isolate the working electrode. For Li-S battery that uses clean Li metal as the anode, however, the resistance and chemical non-equilibrium at the anode side can be neglected for simplicity.

Of another importance for GITT experiment is the determination of Li^+ ion diffusion coefficient at varied stages of lithiation. For intercalation-based electrodes, the voltage

equilibration at open circuit period reflects the kinetics about the Li^+ ion diffusion. The chemical diffusion at each step can be calculated using **Equation 2.1**.

$$D = \frac{4}{\pi}\left(\frac{IV_M}{nFS}\right)\left[\left(\frac{dV}{dx}\right)/\left(\frac{dV}{d\sqrt{t}}\right)\right]^2 \qquad \textbf{Equation 2.1}$$

where I is the current, V_M is the molar volume of the host lattice, n is the number of charge of the mobile ion, F is Faraday's constant, S is the electrochemically active surface area, dV/dx is the slope of the equilibrium voltage curve at the initial value of x, and $dV/d\sqrt{t}$ is the slope of the V *vs.* $\sqrt{t}$. Further detail of the analysis principle is referred to Ref. 83 .

However, for Li-S batteries, calculation of Li^+ diffusitivity is not feasible due to the fact that in catholyte-type cells, polysulfides anions are both soluble in electrolyte other than Li^+ cations and thus contribute to the equilibration; and the widely used high surface area of the highly porous carbon hosts undermines the validation of **Equation 2.1**. Some details on determination of Li^+ and polysulfide anion diffusitivity is referred to Ref. 84.

2.2.3 Electrochemical Impedance Spectroscopy

A high impedance in an electrochemical cell can cause large overpotentials (the difference between the equilibrium and measured potentials), low energy efficiency, low rate capability, and can increase the risk of thermal runaway. It is important to examine and understand the evolution of impedance at each state of discharge/charge and over long-term cycling. Generally, there are three sources of voltage drop: ohmic loss, charge transfer or activation polarization, and concentration polarization. Electrochemical impedance spectroscopy (EIS) is a widely used tool to diagnose the impedance of an electrochemical system by recording the current response to an applied potential at varying frequencies. Since the response of an electrochemical system, such as a Li-ion cell, is very non-linear, the impedance is investigated

in a perturbative manner where an AC voltage of 1-10 mV (with frequencies between 1 mHz – 1M Hz) on top of the controlled DC voltage (usually OCV) is applied.

Among various ways to present the spectrum, the so-called *Nyquist* plot is commonly used in the battery field by plotting the negative of the imaginary part of impedance versus the real part for different frequencies. The Nyquist plot usually consists of one or more semicircles at high frequencies (which are charge transfer processes) followed by a spike at low frequencies (which is diffusion towards/away from the surface, *i.e.,* "Warburg" impedance). Note that symmetric axes (same axis scale) should always be used for the Nyquist plot in order to convey the information presented by the shape of the plot.

EIS data are commonly analyzed by fitting the curve with an equivalent electrical circuit model to understand the contribution from each interface or bulk process. Most of the circuit elements are common electrical elements such as resistors, capacitors, and inductors. Each element in the model should have a physical basis in the electrochemistry of the system and the number of elements should be minimized to be physically meaningful. Any curve can be fit perfectly by using a large enough number of elements (variables), but such a fit would likely be meaningless. Practically, there can be a number of interfacial diffusional process (charge transfer) on both electrodes of a cell. This can cause error in interpreting different processes as they may occur in an overlapping range of frequency resulting a depressed semicircle, so a three-electrode design as discussed above is preferred. For porous electrodes with high surface area, it raises the issue of distinguishing multiple contact resistance and the mass diffusion process; a pelletized electrode with minimized surface area will be useful for this case.

In this thesis, EIS measurements on two-electrode Li-S cells were carried out on VMP3 potentiostat/galvanostat station with EIS/Z capabilities (Bio-Logic Science Instruments). For EIS measurements, the DC voltage was maintained at open-circuit voltage and an AC voltage of 5 or 10 mV in amplitude was applied with a frequency of 200 kHz - 20 mHz.

2.3 Physical and Chemical Characterizations

2.3.1 Powder X-ray Diffraction

X-ray diffraction (XRD) is the most commonly used technique to identify phase composition and to analyze crystal structures. "Bragg's Law" is used to explain the appearance of a diffracted pattern through interference of X-ray coming out of the crystal planes, as shown in **Equation 2.2**.

$$n\,\lambda = 2d\ sin\,\theta \qquad \textbf{Equation 2.2}$$

where θ is the angle between incident X-ray beam and the parallel planes, λ is the X-ray wavelength, and *d* represents crystallographic planes, as shown in **Figure 2.2**. When parallel X-ray beams are diffracted by neighboring parallel planes with a distance of *d*, the beam going into a deeper plane travels an extra distance of $2d\ sin\ \theta$. When the Bragg's law is satisfied, the two parallel beams will be in phase after being diffracted and there will be a diffracted pattern (observable intensity of reflected X-ray). Therefore, with this θ known, *d* can be calculated and assigned to one plane index. A series of the θ detected will give a whole pattern including all plane indices that satisfied the Bragg's Law.

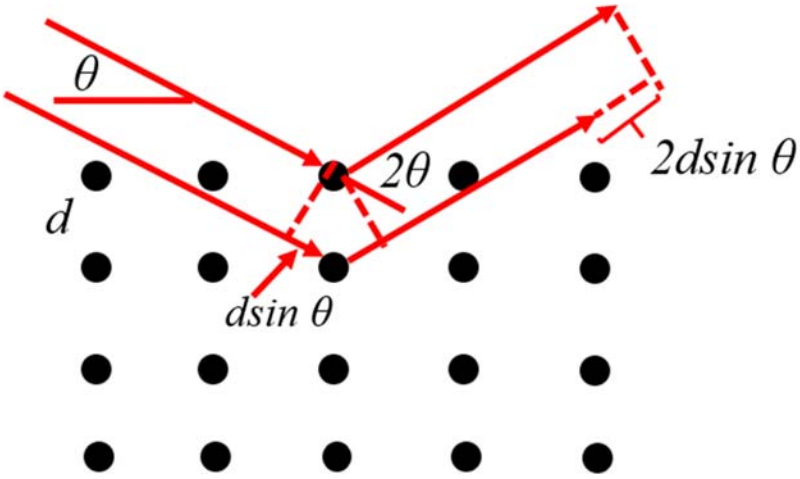

Figure 2.2 Schematic illustration of Bragg's law, where the black dots represents the atom and the red solid line is the X-ray.

Bragg's law is applicable to powder XRD. When an X-ray beam of a specific wavelength λ hits a finely ground sample which contains plenty of small crystals, there has to be a fraction of these crystals that has planes orientated with one Bragg angle for the diffraction to occur. When rotating the sample stage with respect to the incident beam, a pattern containing all characteristic diffractions can be recorded. XRD patterns are unique for compounds in terms of crystal structures and components. With the help of a comprehensive database, the phase component along with crystal structures of a sample can be identified.

In **Chapter 3-6** of this thesis, XRD is mainly used to identify crystalline phases and the patterns were collected on Bruker D8-Advance powder X-ray diffractometer operating at 40 kV and 30 mA and using Cu-Kα radiation (λ=0.15405 nm). Samples were loaded on a zero-background silicon holder. In the *operando* XRD experiments in **Chapter 7**, the diffraction patterns were collected continuously while the cell was in operation (galvanostatic cycling) without interruption. A series of XRD patterns were collected and from these we can learn the evolution of the crystalline phases, recognize either phase transformation or structure evolution

(*e.g.* ion intercalation) over discharge and charge. *Operando* XRD was performed using a PANalytical Empyrean diffractometer using Cu-K_α radiation and outfitted with a PIXcel detector. The experiments were performed using a home-made Swagelok-type cell with a glassy-carbon window for X-ray penetration. The diffraction patterns were collected in Bragg–Brentano geometry.

2.3.2 X-ray Photoelectron Spectroscopy

X-ray Photoelectron Spectroscopy (XPS), also known as electron spectroscopy for chemical analysis, is based on the principle of photoelectronic effect. Photoelectrons refers to electrons that are emitted from the ground state (of inner shell) of atoms upon photon radiation, which is X-ray in this case. When the atom receives energy, it gets excited from the ground state, where core electrons are emitted away from the atom and into the vacuum. The energy transition during this process can be described as **Equation 2.3**,

$$E_{binding} = hv - E_{kinetic} - \phi \qquad \textbf{Equation 2.3}$$

where $E_{binding}$ represents the binding energy of the electron that is ejected, $E_{kinetic}$ represents the kinetic energy of the photoelectron after emission, hv represents the X-ray energy, and ϕ is the work function specific to the spectrometer and irrespective of the sample. The spectrometer probes the kinetic energy and the number of photoelectrons. So with the hv known for an X-ray, the binding energy can be calculated, together with quantification of the intensity.

Additionally, XPS is carried out in ultra-high vacuum so as to avoid the energy interference from gas collisions with photoelectrons. Using X-ray with a sufficiently high energy, a spectrum of (the intensities as a function of binding energy) containing all electrons

emitted (photoelectrons and Auger electrons) can be obtained. Each element has its characteristic peaks, except hydrogen and helium. More important for XPS is that it is capable of providing chemical state information of an element, because binding energy that reflects the electronic structure relies on the exact chemical environment it finds itself.

The XPS acquisition in this thesis was performed by using a multi-technique ultra-high vacuum Imaging XPS Microprobe system (Thermo VG Scientific ESCALab 250) equipped with a hemispherical analyser (of 150 mm mean radius). Data were collected with a pass energy of 20 eV for the core-shell spectra, with the takeoff angle (defined as the angle between the substrate normal and the detector) fixed at 0 degree. A monochromatic Al Kα (1486.6 eV), 150 W X-ray source with 0.5 mm circular spot size and non-monochromatic Al Kα source from twin anode were used for conductive and non-conductive materials, respectively. The samples were transported to the XPS chamber under Ar, and transferred into chamber quickly, in order to prevent air contamination.

All spectra were fitted with Gaussian-Lorentzian functions and a Shirley-type background. For S 2p spectra with $2p_{3/2}$ and $2p_{1/2}$ doublets, a splitting of 1.2 eV, a peak area ratio of 2:1 ($2p_{3/2}$:$2p_{1/2}$) and equal full width half maximum was applied. The binding energy values were all calibrated using the C 1s peak at 284.8 eV.

2.3.3 X-ray Absorption Spectroscopy

The X-ray absorption spectroscopy (XAS) is a widely used technique to determine the electronic structure and atomic geometric/bonding information of matter.[85] It is performed using synchrotron radiation sources that depend on the energy ranges required. The element specific spectrum is obtained by plotting the absorption coefficient as a function of photon energy (eV) and generally consists of three regions: the pre-edge, X-ray absorption near-edge

structure and extended X-ray absorption fine structure (EXAFS), as shown in **Figure 2.3a**. The first two regions correspond to the excitation of core electrons to free orbitals and thus provide information on the electronic states; the last region appears due to the scattering of the ejected photoelectrons with the neighboring atoms and thus encapsulates bonding information. It is worth noting that XAS is a bulk (microns or tens of microns size) technique rather than a surface characterization technique, which is useful to reveal the electrochemical reactions of the bulk electrode.

It is useful to examine the phase evolution of the electrode materials during discharge/charge of the cell. Valuable information can be obtained by examining the electrodes *ex-situ* by dissembling the cells at the varied state of charge. However, since the electrochemical reactions always proceed in a non-equilibrium fashion and may not be uniform across the electrodes, *ex-situ* measurements may not reflect the exact speciation during galvanostatic experiments. Therefore, *operando* characterizations are required.

I have used *operando* XAS to examine the sulfur speciation in sparingly solvating electrolyte for Li-S cells in the Advanced Photon Source (Chicago, USA) as shown in **Chapter 7**. The typical windowed coin cell set-up for the *operando* experiments is shown in **Figure 2.3b**. Thin Aluminized Kapton^{TM} film was used in the cell design for the penetration of X-rays. The electrodes were prepared by coating slurry on porous carbon papers and were placed in the cell facing the window for maximum beam penetration.[13]

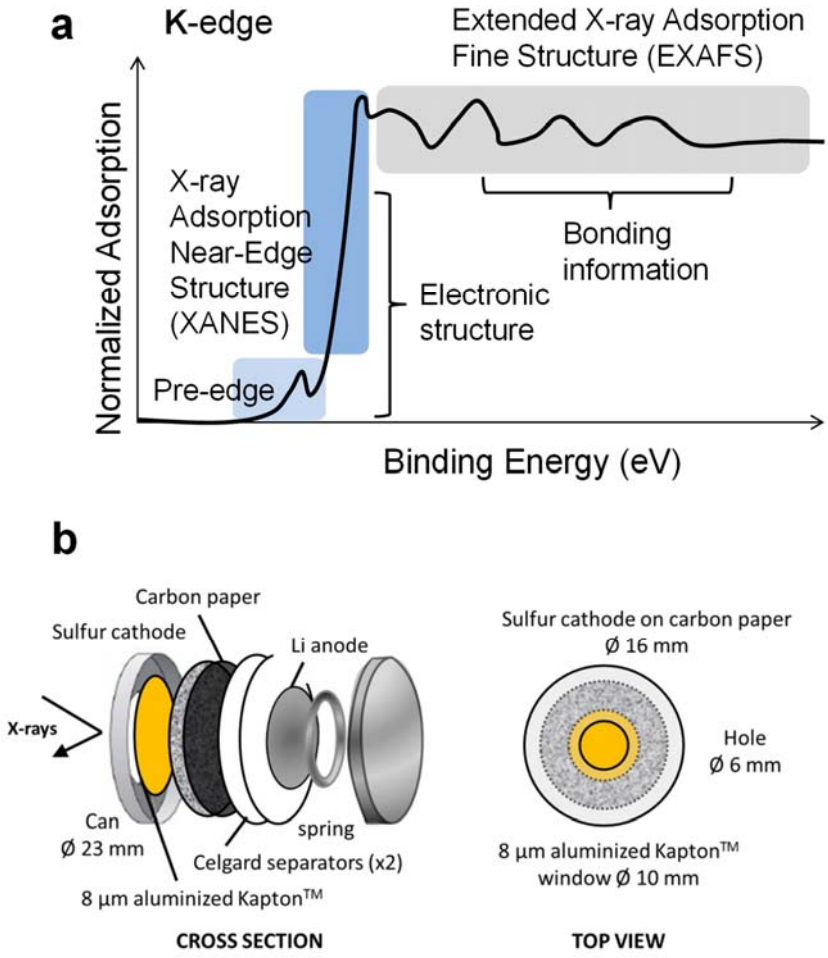

Figure 2.3 a) A scheme showing an example XAS spectrum that consists of three regions. b) The scheme showing the design of the windowed coin cell for *operando* XAS measurements, as reproduced from Ref. 13.[83]

2.3.4 Scanning Electron Microscopy

Scanning electron microscopy (SEM) is an important tool to visualize the micro/nanostructure morphology and the distribution of elements of the surface of a solid sample. In an SEM instrument, a focused beam of the primary electrons with high energy (up to 40 keV) hits the specimen surface, generating secondary electrons, back-scattered electrons, transmitted electrons, and characteristic X-rays (fluorescence), as shown in **Figure 2.4** Scheme They are probed by specialized detectors.

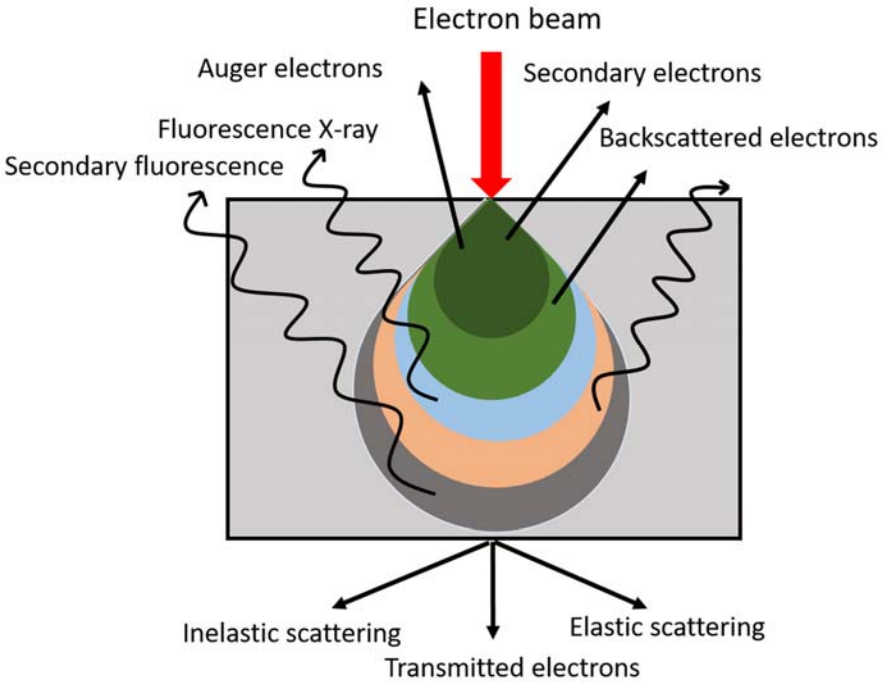

Figure 2.4 Scheme showing different types of signals (electrons and photons) emitted from different parts of the interaction volume for SEM.

Due to the repeated random scattering and absorption of primary electrons, their interaction with sample atoms occurs only within a certain depth, which is called the interaction volume (**Figure 2.4**). The secondary electrons are generated by inelastic scattering of primary

electrons by the electrons of the specimen and thus are of relatively low energy. They are generated at a lower depth and reveal surface morphology. Backscattered electrons are high-energy electrons that are reflected or backscattered by elastic scattering. They are element specific; heavy elements (high atomic number) backscatter electrons more strongly than light elements (low atomic number), thus they appear brighter in the image, making backscattered imaging excellent at chemical composition distribution. When secondary electron is generated, a shell electron with relatively low binding energy is excited leaving a hole behind. Consequently, one electron from outer shell has to jump into the hole of low energy, during which the excessive energy can be released by emitting X-rays (fluorescence). The energy of the X-ray depends on the orbital energies involved and thus this is used for identifying element for energy dispersive X-ray spectroscopy (EDX). As a semi-qualitative technique, EDX elemental mapping can provide information on the distribution of specified elements over the area scanned.

SEM imaging and EDX measurements in this thesis were carried out either on a Zeiss LEO 1530 field or Zeiss Ultra Plus field emission SEM. Secondary electron mode was used for the purpose of imaging.

2.3.5 Transmission Electron Microscopy

Transmission electron microscopy (TEM) utilizes a beam of electrons with even higher energy (200 keV) and shorter wavelength ($\lambda = 0.025$Å) that is on the scale of atom diameter, so TEM images can have much higher resolution, even able to see the atomic structure. TEM relies on the transmission of electron beam through an ultra-thin specimen and their interaction with the specimen as it passes through.

The emission source can be a tungsten filament or a lanthanum hexaboride (LaB_6) source. Manipulation of the electron beam is performed using two physical effects, magnetic fields and electrostatic fields. The use of magnetic fields allows for the formation of a magnetic lens of variable focusing power. Electrostatic fields cause the electrons to be deflected through a constant angle. The coupling of two deflections in opposing directions allows the beam path to shift, which is essential to scanning TEM (STEM).

Imaging for TEM is fundamentally based on various types of contrast formation. The most commonly used mode for TEM users (including this thesis) is the bright field imaging mode. In this mode the contrast formation can be considered to form directly by occlusion and absorption of electrons in the specimen. Thicker specimen regions or regions with heavy elements will appear darker, while regions with no sample will appear bright. The image can be assumed to be a simple two dimensional projection of the specimen down the optic axis.

Diffraction contrast is the principle for dark-filed imaging. In the case of a crystalline sample whereby the electron beam undergoes Bragg scattering, the electrons are dispersed into discrete locations in the back focal plane. Therefore, crystalline phases will appear bright while amorphous materials and wherever no sample scattering occurs will appear dark.

High-resolution TEM (HRTEM), also known as phase contrast can assist in investigating the crystal structure. When utilizing a field emission source, the images are formed due to differences in phase of exiting electron waves, which is caused by specimen interaction. Image formation is given by the complex modulus of the incoming electron beams. HRTEM allows for direct imaging of the atomic structure.

TEM samples were imaged on JEOL 2010F TEM/STEM operating at 200 KeV for this thesis.

2.3.6 Raman and Infrared Spectroscopies

Raman spectroscopy and Infrared Spectroscopy are both based on interaction of photons with the vibrational, rotational or other low-frequency modes of a molecule. They are capable of detecting the chemical bonding and the chemical environment of a molecule, but based on two different principles. Raman spectroscopy is based on the inelastic scattering of photons, while infrared is based on the absorption of infrared photons.

The Raman effect of photons describes the condition when photons interact with the polarizable electron density, the chemical bonds of the molecule and the environment it finds itself. Specifically, a photon excites the molecule that is in either the ground rotational/vibrational state or an excited state, resulting in the molecule being in a virtual energy state for a short period of time. At the same time, the photon is then inelastically scattered, which can be of either lower (Stokes) or higher (anti-Stokes) energy than the incoming photon. The difference in energy between the original state and the resulting state leads to a shift in the wavelength of the scattered photon from the excitation wavelength. This is what give rise to the identification function of Raman spectroscopy.

Infrared spectroscopy (IR) relies on the absorption of photons of infrared wavelength by the vibration/rotation of a molecule, and Fourier transform IR (FTIR) refers to the technique that relies on the Fourier transformation to convert the raw data into the actual spectrum. As with all absorption spectroscopy techniques, the IR can be used as the fingerprint of a chemical, functional group or bond. The principle is that when the incident photon interacts with a molecule at the ground vibrational state, it can be absorbed by the molecule, resulting the transition from the ground state to an excited state. Therefore, only photons with certain wavelength, characteristic of the molecule, can be absorbed at the so-called resonant frequency,

making IR a fingerprint technique. The resonant frequencies are related to the strength of the bonds and the mass of the atoms, as well as the normal modes of the motions.

There are three main processes by which a molecule can absorb radiation, based on the type of the energy levels for transition, each of which involves an increase of energy level. The first route involves a rotational transition within one vibrational energy level. The second is a vibrational transition within one electronic energy level, upon absorption of quantized energy. The third involves transition of electrons energy state, as exemplified in the XAS technique in **2.3.3**. The energy levels of transition can be generally rated in the following order: electronic > vibrational > rotational. The infrared portion of the electromagnetic spectrum is usually divided into three regions; the near- (14000–4000 cm^{-1}), mid-(4000–400 cm^{-1}) and far- infrared (400–10 cm^{-1}). The energy of mid-IR radiation is usually within the vibrational regions of molecules and is used in this thesis.

A criterion for IR absorption is a net change in dipole moment of a molecule as it vibrates or rotates. Therefore, molecules like S_8 or O_2 are IR-inactive. However, there is no such requirement for Raman spectroscopy.

Raman spectroscopy in this thesis was performed on a LabRam HR system (HORIBA Jobin Yvon) using 633 nm laser irradiation. Samples were placed on a glass slide for measurement. FTIR spectra were obtained using a Bruker Tensor 37 spectrometer. Sample powders were ground with HBr for pellet preparation.

2.3.7 Thermogravimetric Analysis

Thermal gravimetric analysis (TGA), combined with differential scanning calorimetry (DSC), is a technique that measures the changes in physical and chemical properties of a material as a function of temperature. By increasing the temperature in a linear manner, the mass change

and thermal flow from sample (calculated by comparison with the reference) can be recorded. The thermal decomposition temperature, reaction/oxidation of the materials, and phase transformation can thus be obtained.

In this thesis, the TGA was mainly used to determine the weight percentage of sulfur, by using the weight loss between 200-400 ºC, where sulfur evaporates. TGA analysis was conducted at a heating rate of 10 °C/min under a N_2 flow, using a TA Instruments SDT Q600.

2.3.8 Porosity and Surface Area Determination

Surface area, pore volume and pore size distribution (PSD) were determined on a Quantachrome Autosorb-1 instrument. Samples were degassed at 180 ºC on a vacuum line before measurement, except for sulfur containing samples, degassing at 50 ºC was used to prevent the vaporization of sulfur. Nitrogen adsorption/desorption isotherms were collected at 77 K in liquid nitrogen bath. A N_2 adsorption isotherm is the plot of volume of nitrogen adsorbed on the surface of sample as a function of the relative pressure in the sample chamber. It can provide information on the surface area and type of pore size. During the measurement, the sample is loaded into a quartz tube and evacuated first. Nitrogen gas is periodically introduced into the sample tube and adsorbed on the surface of the sample at desired pressures. The amount of N_2 adsorbed can be obtained by comparison to the balance tube.

In this thesis, the surface area was determined from Brunauer-Emmett-Teller (BET) method from multi-point analysis and the total pore volume (porosity) was calculated from the volume of nitrogen adsorbed at a relative pressure (P/Po) of 0.99. The PSD was calculated using either Barrett-Joyner-Halenda (BJH) method or quenched solid state functional theory (QSDFT) method.

2.3.9 Electronic Conductivity Measurement

Electronic conductivity of the samples was measured on a Jandel four-point probes connected with RM3000 test unit. The four-point probing technique utilizes two pairs of electrodes, that is, current-carrying and voltage-sensing electrodes. The two outer current-carrying electrodes enable a current flow over the resistor sample and the two inner voltage-sensing electrodes measure the exact voltage drop. Its advantage over conventional two-point probe is that the additional voltage-sensing electrodes exclude the voltage drop from the measuring wires.

To measure the conductivity of the powder samples, the powders were pressed to pellets. The Jandel instrument reads the sheet resistance R_s in ohm square (Ω□) and the thickness d (cm) is measured by a micrometer, so the bulk conductivity σ (S cm^{-1}) can be given as in **Equation 2.4**.

$$\sigma = \frac{1}{R_S\, d} \qquad \textbf{Equation 2.4}$$

2.3.10 Polysulfide Adsorptivity Determination

Polysulfide adsorptivity was evaluated by electrochemical titration, which determines the amount of residual LiPS in solution after contact with the respective host cathode materials as detailed in a previous report.[74] Sample solutions were prepared by stirring a known mass of in a known concentration of Li_2S_4 in TEGDME. The mixtures were stirred overnight and after centrifugation, the supernatant was collected. The supernatant was used for oxidation titration. The actual adsorption was determined by extrapolation from a calibration curve using standard materials (see details in Ref. 74). The adsorptivity was then calculated by subtracting the starting amount with adsorption amount. All procedures were performed in an argon-filled glovebox.

Solid powder Li_2S_4 was synthesized by reacting elemental sulfur and lithium superhydride ($LiEt_3BH$) with desired ratio in anhydrous THF for one hour inside the glovebox. Excess THF solvent was removed by applying vacuum under room temperature and the precipitates were retrieved by washing with toluene, followed by vacuum drying. [74]

2.4 First-Principles Calculations

2.4.1 Introduction of VASP

The Vienna Ab initio Simulation Package, known as VASP, is a plane wave based code to perform first-principles calculations. Basically, the procedure of setting up VASP calculations includes the creation of four input files with fixed names: INCAR, POSCAR, KPOINTS and POTCAR. Calculation parameters such as cut-off energy, smearing strategy, ionic relaxation approach, accuracy and algorithms are described in the INCAR file. A simplified INCAR is shown below as an example. A POSCAR file contains data about a system geometry and starting configuration coordinates, while k-points are stored in a KPOINTS file. Pseudopotentials and electron exchange-correlation functionals used for calculations are saved in a POTCAR file. After the calculation is done, the results sorted in several output files (OUTCAR, CHCAR, WAVECAR, *etc*.).

SYSTEM = Co_9S_8	# Give the name of the calculation.
ISTART = 0	# Start job: begin 'from scratch'. Initialize the wavefunctions according to the flag INIWAV, if it exists.
ICHARG = 2	# Take superposition of atomic charge densities for initial charge density.

NWRITE = 1	# Only write the eigenvalues, charge density, stress of the ionic steps.
ENCUT = 500.0	# Cut-off energy is set at 500 eV based on the pseudopotential elected.
EDIFFG=-0.01	# Break condition for ionic relax loop: all forces are smaller than 0.01.
ISMEAR = 0	# Use Gaussian smearing for partial occupancy for each wavefunction basis. Guassian smearing is mostly used for insulator of large supercell (or low k-points); for metals, use Methfessel-Paxto scheme.
SIGMA = 0.2	# Determines the width of the smearing in eV.
LREAL= Auto	# For PAW pseudopotential, projection done in real space, and optimization of projection operators is automatic.
ALGO=F	# The algorithm for electronic minimization: Fast, use Davidson scheme for initial phase and RMM-DIIS scheme for the rest of steps.
NSW = 350	# Specify the max. number of ionic steps relaxed.
POTIM = 0.5	# Serves as a scaling constant for the forces.
IBRION = 2	# Use the conjugate gradient algorithm for ion update and movement.

2.4.2 Computation Parameters

Two types of pseudopotentials are commonly used: ultrasoft pseudopotentials (USPP), projected augmented wave (PAW) pseudopotentials. In this work, PAW pseudopotentials were used for all calculations.[86] The Perdew-Burke-Ernzerhof (PBE) version of the generalized gradient approximation (GGA) were applied to describe the electronic exchange correlation effect.[87] The cut-off energy is chosen depending on the requirement from the pseudopotential files of all elements and the calculation speed, while ensuring the plane wave basis set to

converge. K mesh was selected based on convergence test, which includes the Γ-point. Generally, for slab calculations, the number density of k-point along each direction of the Brillouin Zone needs to be roughly the same. The conjugate-gradient algorithm was used for ionic relaxation. The supercells were built as large as to avoid interaction between neighboring cells, while being small to keep low cost. For fair comparisons between different systems, parameters need to be the same, such as supercell size, k-mesh points, cut-off energy, accuracy controlling, pseudopotential, exchange-correlation functionals and algorithms.

For multi-layer slab construction, a portion of the bottom layers was fixed during relaxation while the top layers were allowed to fully relax. A vacuum layer of certain thickness was used in the vertical direction of the slab, in order to avoid the interaction between the layer and its images. This requires convergence test ahead. Polysulfides of varied chain-length were employed as the adsorbates. Usually, multiple starting geometries of the substrate-polysulfide systems were attempted and compared, in order to find the lowest local minimum energy point of the system. The binding energy (E_b) of polysulfide on the substrates is defined as

$$E_b = (E_{sub} + E_{ps} - E_{sub+ps})$$

where E_{sub}, E_{ps} and E_{sub+ps} represent the ground-state energies of the substrate, the polysulfide and substrate- polysulfide. A larger positive value means a greater binding ability.

Chapter 3 A Metallic Sulfide Based Host for Long-Lived Li-S Batteries

3.1 Introduction

Addressing the polysulfide adsorption and controlling the deposition of Li_2S is an important avenue to commercialize Li-S batteries.[88 - 90] As mentioned in **Chapter 1**, initially nanostructured carbons with sophisticated pore structures were used to provide electron conductivity and physical entrapment of the LiPSs. Introducing hosts that exhibit chemical interactions with LiPSs such as graphene oxides,[36,38,39] N-doped carbons[40,41] has greatly improved electrochemical performance, although achieving high doping concentration and high conductivity in doped carbons is challenging.[91] Conductive Magnéli phases (Ti_4O_7), indium tin oxide and MXene phases have been reported to promote the surface polysulfide redox reaction and spatially control the electro-deposition of Li_2S.[60,62,70,] Layered semiconducting TiS_2 has been added to sulfur cathodes.[92] TiS_2 was also used to coat Li_2S particles in order to alleviate polysulfide leakage into the electrolyte;[93] however, in this report, prolonged cycling of high-loading electrodes (>50 cycles) or long-term cycling of low-loading electrodes (>400 cycles) was not reported.

In this Chapter, I describe a strong chemical interaction to confine LiPSs within a graphene-like Co_9S_8 nanosheet material that exhibits both metallic conductivity and hierarchical porosity. The thermal stability and electronic conductivity of cobalt sulfides are superior to most other metal sulfides.[94-96] Amongst these, Co_9S_8, a member of the Pentlandite family, a high-temperature peritectic phase in the Co-S phase diagram,[97] exhibits a particularly high room temperature conductivity of 0.29×10^3 S cm^{-1}.[98] It has been previously synthesized

by low-temperature solvothermal techniques,[99,100] but these processes require long reaction time at elevated temperature, and yield conventional large crystallites.

A rapid and scalable microwave solvothermal approach is utilized for the synthesis of a unique graphene-like Co_9S_8 with interconnected nanosheets forming 3D networks. Dr. Dipan Kundu completed the synthesis of the graphene-like Co_9S_8. In contrast to electrodes consisting of individualized Li_2S particles coated with metal sulfides,[93] the 3D network structure enables high sulfur loading electrodes with stable cycling. First-principles calculations and spectroscopic studies consistently demonstrate the coupled interaction of Co_9S_8 with Li_2S_n that relies on S_n^{2-}-$Co^{\delta+}$ and Li^{+}-$S^{\delta-}$ (of Co_9S_8) binding. It is shown that with these intrinsic active sites, the as-synthesized Co_9S_8 exhibits far superior LiPSs adsorptivity than "gold-standard" carbon materials, enabling electrodes with stable cycling behavior.

3.2 Experimental Approaches

3.2.1 Synthesis of graphene-like Co_9S_8

Microwave treatment utilizes a solvent dipole-microwave interaction and leads to rapidly superheated regions triggering rapid nucleation and growth of particles.[101] In this work a rapid and scalable microwave solvothermal method was used for the synthesis of high surface area Co_9S_8.

In a typical procedure, 3- 4 mmol cobalt chloride ($CoCl_2.6H_2O$) and an equivalent amount of thioacetamide (C_2H_5NS) were dissolved in 50 ml of water-triethylenetetramine mixture (2:3 v/v) and transferred to a Teflon™ vessel. The sealed vessels were fitted to a rotor equipped with temperature and pressure sensors. The rotor was then placed in a rotating platform for uniform heating in an Anton Parr microwave synthesis system (Synthos 3000).

The system temperature was raised to 160 °C in 10 minutes and maintained for 90 minutes. The preset temperature was maintained automatically by continuous adjustment of the applied power (limited to 800 W). The as-synthesized product was thoroughly washed with copious amounts of water, followed by acetone, and dried at 60°C for 24 hrs.

The Co_9S_8 sulfur composite was prepared via a melt-diffusion method with 75 wt% of sulfur (denoted as Co_9S_8 /S75). The Co_9S_8 powder was mixed with sulfur in the desired ratio and heated under ambient atmosphere at 155 $^{\circ}$C for 12 hours. The VC/S75 composite was prepared by the same route.

3.2.2 Synthesis of Li_2S_4 /Co_9S_8 for XPS Studies

Li_2S_4 was synthesized via the reaction of S_8 with lithium superhydride ($LiEt_3BH$) in the desired ratio in anhydrous THF at room temperature for 1 h inside an argon glovebox. The resulting solid was washed with toluene and vacuum dried. To prepare the Li_2S_4 /Co_9S_8 for XPS studies, the Co_9S_8 powder (20 mg) was added to a Li_2S_4 solution (0.8 mg ml^{-1}) in DME, which was stirred for 6 hours, and then centrifuged. The solid was recovered and vacuum dried at room temperature. All procedures were carried out in the glovebox.

3.2.3 Electrochemical Measurements

Electrodes with 1.5 mg cm^{-2} sulfur loading were prepared by mixing sulfur composites with Super P and PVDF binder in DMF in a weight ratio of 8: 1: 1. Super P carbon was utilized to aid in electrolyte wetting of the electrode. For the preparation of thick electrodes with high loading, sulfur composites with Super P, graphene (ACS Materials), styrene butadiene rubber (SBR) aqueous binder, and carboxymethyl cellulose (CMC) binder were dispersed with a

weight ratio of 80: 6: 4: 3: 7 in a mixture solvent of deionized water and DMF (2:1 v/v). The slurry was doctor-blade coated onto carbon paper (AvCarb P50) to prepare the cathodes. The electrodes were dried at 60 °C overnight.

Coin cells 2325 were assembled with a lithium foil anode and an electrolyte comprising 1 M LiTFSI and 2 wt% of $LiNO_3$ in a mixture of DME and DOL (v/v = 1:1) inside the glovebox. The cells were operated in a voltage window of 1.8-3.0 V. A slightly larger voltage window was used for higher-rate studies (1.7-3 V and 1.6-3 V for 1C and 2C rates, respectively).

3.2.4 Computational Methods

The first-principles calculations were performed using the plane wave-based VASP code. [86,87] PAW pseudopotentials and the Perdew-Burke-Ernzerhof (PBE) version of the GGA were applied to describe electron-ion interactions and the electronic exchange correlation effect. Spin-polarized calculation was employed. The van de Walls forces were included for comparison with non-included calculations. A cut-off energy of 400 eV was used for the plane wave basis set to ensure convergence.

The Li_2S, Li_2S_2 and Li_2S_4 were employed as the representative lithium polysulfides. A four-layer slab model with the two bottom layers frozen was applied to model the three Co_9S_8 surfaces. A two-layer 6×6 slab with the bottom layer frozen was use for graphite, so that Co_9S_8 and carbon were close in supercell volume. A vacuum layer of 20 Å was used in the vertical direction to avoid the interaction between the layer and its images. The conjugate-gradient algorithm was used for ionic relaxation. The binding energy (E_b) of Li_2S_n on the substrates is defined as

$$E_b = E_{sub} + E_{ps} - E_{sub+ps}$$

where E_{sub}, E_{ps} and E_{sub+ps} represent the ground-state energies of the substrate, Li_2Sn and substrate-Li_2S_n. A larger positive value means a greater binding ability.

3.3 Physical Characterizations of Co_9S_8

This distinctive microwave-assisted synthesis condition results in the formation of a long-range nanosheet structure of Co_9S_8 with a large pore volume. The XRD pattern (**Figure 3.1a**) can be indexed to cubic Co_9S_8 (F*m-3m*) with a lattice parameter of 9.930 Å (ICSD database #23929). A small amount of $Co_{1-x}S$ was also detected.

The SEM images in **Figure 3.1b, c** reveal an interconnected nanosheet structure, which gives rise to hierarchical porosity (see below). It is believed that the sheets may result from binding of the triethylenetetramine solvent molecules onto specific Co_9S_8 crystallographic planes *via* Lewis acid-base (Co-N) chelation, leading to preferential growth along certain directions. This effect is even more pronounced by the rapid heating and nucleation under microwave conditions, which is known to direct specific particle morphologies[102] - so that here, a long-range nanosheet structure is formed. Such a 3D network is critical for maintaining the electrode integrity and thus allowing stable cycling for thick high-loading electrodes as discussed below.[41,103]

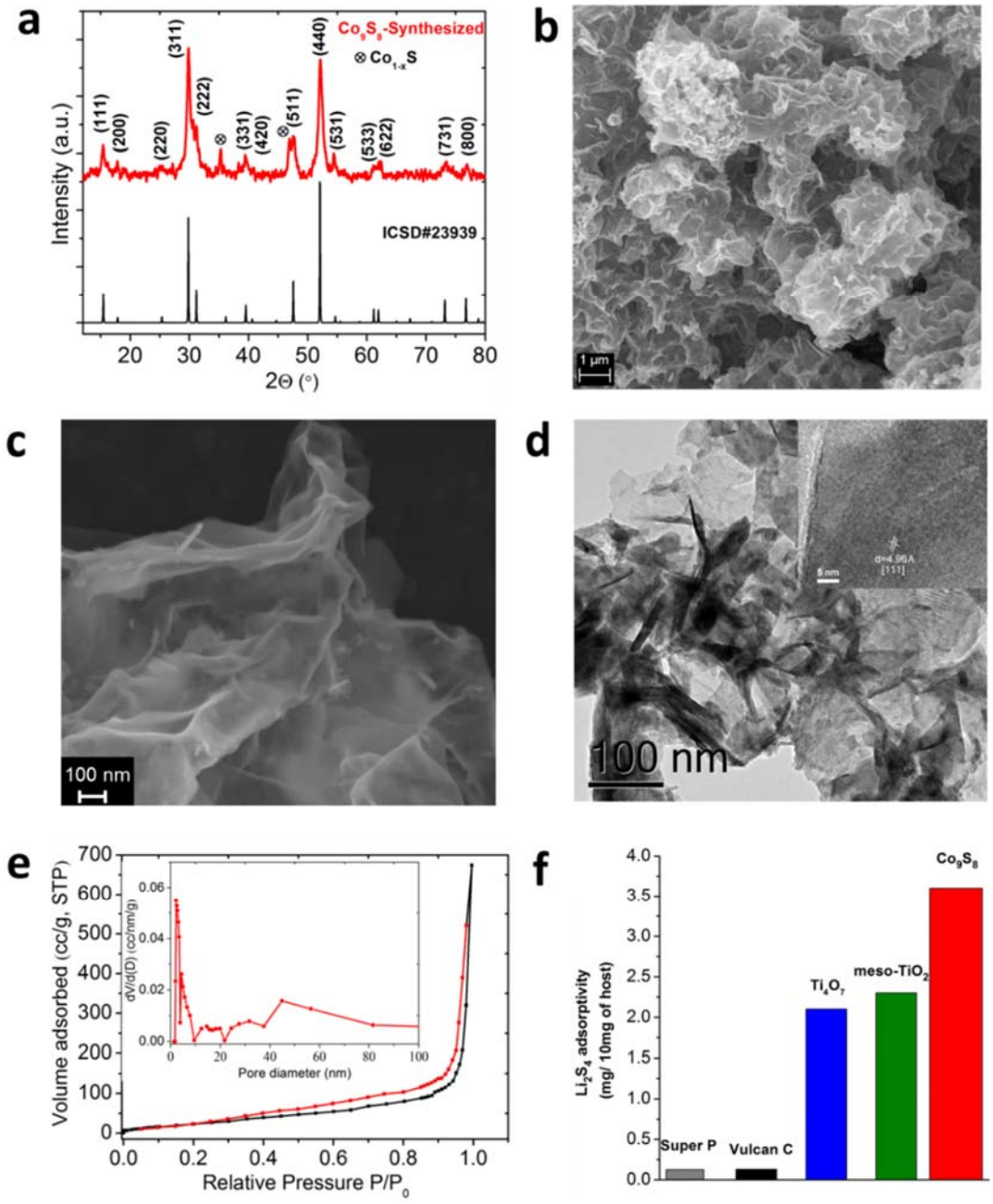

Figure 3.1 a-e) Physical characterization of the graphene-like Co_9S_8: a) XRD pattern with indexed reflections, b,c) low- and high-magnification SEM images, d) TEM image (inset: HRTEM) and e) N_2 adsorption/desorption isotherm (inset: BJH pore size distribution). f) The Li_2S_4 adsorptivity of the Co_9S_8 measured by electrochemical titration, compared to meso-TiO_2, nanostructured Ti_4O_7, Vulcan™ carbon and Super P carbon.

The thin graphene-like structure is evident in the TEM image shown in **Figure 3.1d**. The HRTEM image of a single sheet shows lattice fringes with an interplaner spacing that corresponds to the (111) plane of cubic Co_9S_8. N_2 absorption/desorption analysis (**Figure 3.1e**) indicated a high BET surface area of 108 $m^2 g^{-1}$ and a very large pore volume of 1.07 $cm^3 g^{-1}$. A broad pore size distribution by BJH method was observed, with the majority in the range of 1.2 - 10 nm and the remainder distributed over 10 - 80 nm, indicating a texture incorporating micro-, meso-, and macropores. This high surface area and pore volume along with the hierarchical porosity are vital to exert its high intrinsic LiPS adsorptivity and to enhance electrolyte penetration across the thick electrodes.

The LiPSs adsorptivity of Co_9S_8 was quantitatively evaluated by electrochemically titrating the residual polysulfide remaining in a LiPS solution after long contact with the Co_9S_8 host.[104] This is compared with traditional nonpolar carbons (Super P and Vulcan™ Carbon), a commercial mesoporous TiO_2 (meso-TiO_2), and nanostructured metallic Ti_4O_7[60] as shown in **Figure 3.1f**. Li_2S_4 was employed as the representative polysulfide. Vulcan Carbon (VC, 260 $m^2 g^{-1}$) adsorbs only 0.15 mg of Li_2S_4 per 10 mg of material. The meso-TiO_2 (272 $m^2 g^{-1}$) and Ti_4O_7 (290 $m^2 g^{-1}$) adsorb twenty fold of this amount, as reported previously.[104] However, the as-synthesized Co_9S_8 - despite possessing about one-third the surface area (108 $m^2 g^{-1}$) - adsorbs 50% more than either oxide. This demonstrates that Co_9S_8 has over five times the intrinsic LiPS adsorptivity (*i.e.* surface area normalized) of the titanium oxides.

3.4 Computation on the Chemical Interaction with Polysulfides

To understand the nature of the chemical interaction of Co_9S_8 with LiPSs, first-principles calculations based on DFT were performed. Three representative surfaces that exhibit different surface Co/S ratios, (002), (202) and (008) were selected, in order to qualitatively evaluate the

contribution of surface Co atoms and S atoms in binding LiPSs. The (002) and (202) surfaces have a Co/S ratio of 1:4, 5:4 respectively and (008) is terminated entirely with Co atoms (**Figure 3.2**).[105] A four-layer slab model (with the bottom two layers fixed) was employed, where all three surface slabs contain the same number of total atoms. Non-polar graphitic carbon was used as a comparison, employing a two-layer graphite slab so that all substrates

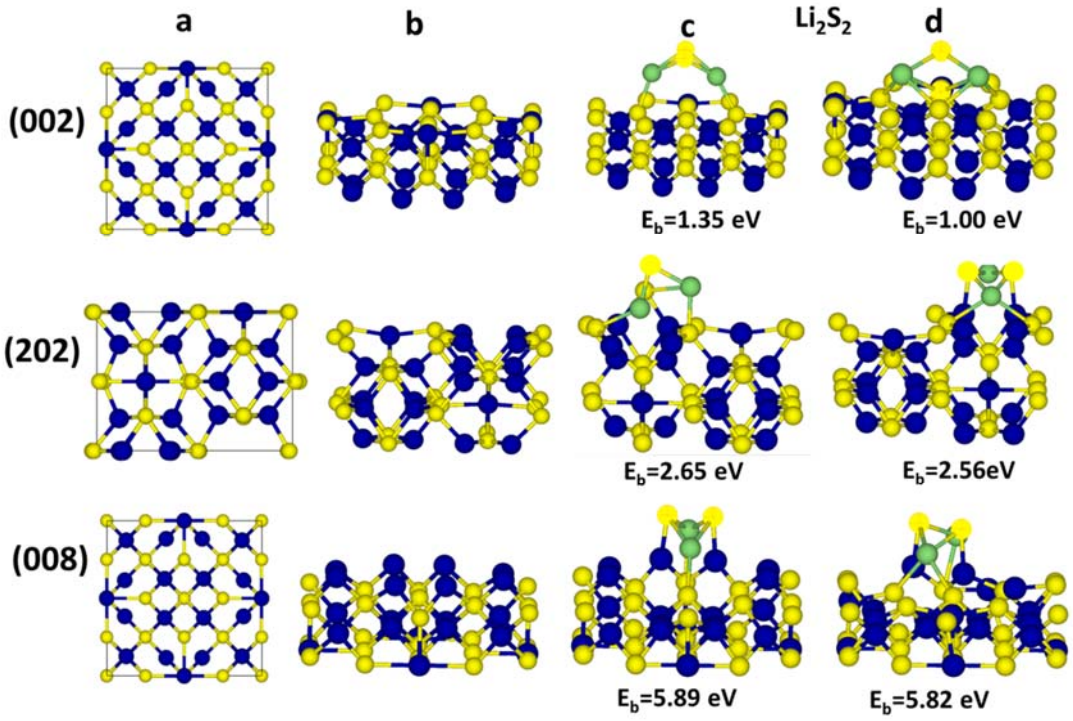

Figure 3.2 a) Top views and b) bird-views of the fully relaxed geometry of the substrate slabs (*i.e.* without Li_2S_2) after first-principles relaxation for the three surfaces of Co_9S_8; c, d) two representative meta-stable configurations of Li_2S_2 binding on the surfaces, with their binding energy value labelled. Brown, blue, green and yellow 3D spheres represent C, N, Li and S (of Co_9S_8) atoms, respectively and 2D yellow circles represent S in Li_2S_2. In this calculations, three or more different starting geometries were used for geometry optimizations and this usually yields multiple local minima, from which the lowest was used.

have supercell sizes of very close in size. The short-chain Li_2S_2, together with long-chain Li_2S_4 and the end-member Li_2S [106,107] were used to represent the LiPS molecules.

The fully relaxed geometries of Li_2S_2 binding for the surface slabs were calculated. **Figure 3.3** presents the geometry with the lowest free energy and **Figure 3.2c,d** present two representative fully relaxed geometries but with slightly higher free energy, calculated from different starting geometries.

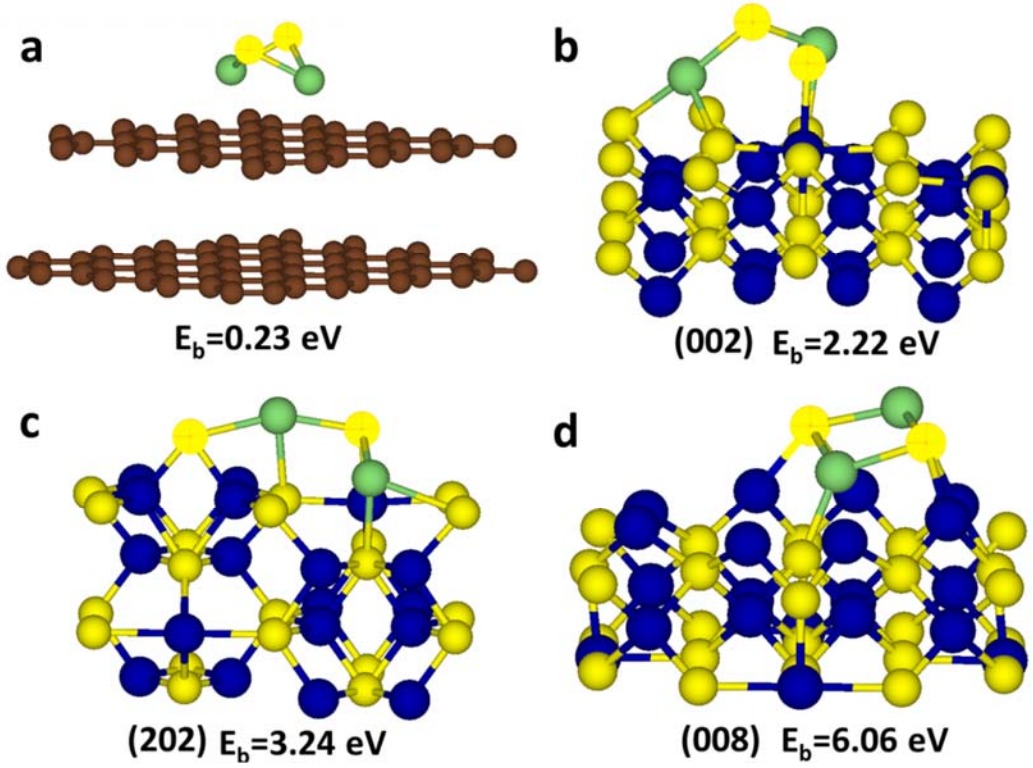

Figure 3.3 The most stable Li_2S_2 binding configuration after full relaxation by first-principles calculations for the a) double-layer graphitic carbon, and four-layer Co_9S_8 b) (002), c) (202) and d) (008) surface slabs with the corresponding binding energy values labeled. Brown, blue, green and yellow 3D spheres represent C, N, Li and S (of Co_9S_8) atoms, respectively and 2D yellow circles represent S of Li_2S_2.

The absence of any specific bonding between Li_2S_2 and the graphite substrate leads to a low binding energy of 0.23 eV, which arises from the van der Waals (VDW) interaction (**Figure 3.3a**).[107] In contrast, Li_2S_2 adsorbed on the Co_9S_8 surfaces exhibits slightly distorted geometries compared to the free Li_2S_2 molecule, indicating a strong interaction (**Figure 3.3b-d**). In all three cases, there is strong evidence for both S_2^{2-}-$Co^{\delta+}$ and Li^{+}-$S^{\delta-}$ (in Co_9S_8) binding, with binding energies above 2 eV. For example, on the (002) surface (**Figure 3.3b**), the Li atom prefers to bond with the three available neighboring sulfur (in Co_9S_8) atoms; and on the (008) surface (**Figure 3.3d**), the sulfur atoms (in Li_2S_2) prefer to bond with the Co atoms. In contrast to the previously reported observation of only Li-S (Li-O) binding between Li_2S_n and layered metal sulfide (oxide),[107] here strong synergistic binding effect from both metal and sulfide ions was observed. It is believed that this strong coupled interaction for binding LiPSs and the high surface area of the nanostructured Co_9S_8 contribute to its superior LiPSs binding capability.

Table 3.1 Summary of binding energy for different polysulfides on the surface of graphite and three Co_9S_8 surfaces (Li_2S_2-VdW indicates the result including VDW in the calculation).

E_b (eV)	Graphite	Co_9S_8 (002)	Co_9S_8 (202)	Co_9S_8 (008)
Li_2S	0.60	2.74	3.41	3.96
Li_2S_2	0.28	2.26	3.29	6.06
Li_2S_4	0.65	1.71	1.56	4.10
Li_2S_2-VdW	0.94	3.24	4.17	6.93

As reported by Zhang et al.,[107] VDW forces are important for studying the interaction of polysulfides (and sulfur) with substrates, especially for carbon surface. The VDW correction was thus included in the calculation, with the binding energy values summarized in **Table 3.1**. With VDW forces included, the binding energy of Li_2S_2 with all substrates increase by 0.65~1.00 eV, which demonstrate the VDW does play a role in binding polysulfides. And also, it is noted that the contribution of VDW in the total binding energy is greater for non-polar graphite (70%) substrate than the Co_9S_8 substrate (30%, 21%, 13% for the three surfaces respectively). For the binding of long-chain Li_2S_4, the binding of Li^+ to S of Co_9S_8, and that of terminal S to Co (if available) dominate the interaction, whereas the bridging sulfur participates only on the Co-rich surface (008) **(Figure 3.4b)**. It is observed that the binding energy values of long-chain Li_2S_4 are relatively smaller than that of short-chain Li_2S_2, consistent with what is reported in Ref. 107**.** Greater binding of Li_2S onto Co_9S_8 surface than graphite is also noted, as seen in **Figure 3.4a**.

Furthermore, the binding energy of 2.22 eV for the (002) surface (Co/S= 1:4) increases to 3.24 eV for the (202) surface (Co/S= 5:4) and further to 6.06 eV for the purely Co-terminated (008) plane that presents cobalt atoms only in tetrahedral coordination, which are under-coordinated at the surface. The correlation suggests that the Co-S interaction may play a more significant role in binding LiPSs than the Li-S interaction, as the three substrates have a similar supercell size and number of atoms. The binding energy observed here is amongst the highest reported for a lithium sulfide on a host surface, for example, exceeding that of Li_2S_2 on Ti_4O_7 (4.1 eV),[62] or on TiS_2 (3.5 eV).[107] This finding enables a better understanding on the interaction mechanism for metal sulfide/oxides and provides guidance on fabricating host materials

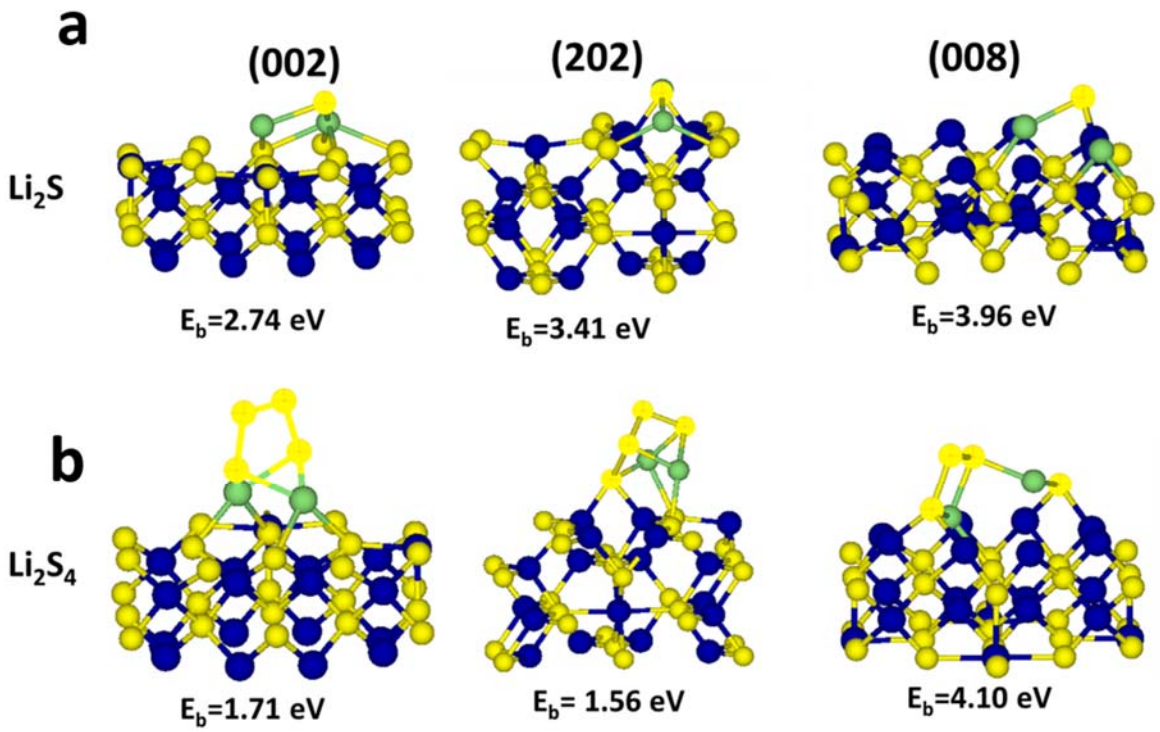

Figure 3.4 The fully relaxed binding geometry of a) Li_2S and b) Li_2S_4 molecules on the three Co_9S_8 surface substrates after first-principles calculation, with their binding energy value labelled. Brown, blue, green and yellow 3D spheres represent C, N, Li and S (of Co_9S_8) atoms, respectively and 2D yellow circles represent S in lithium polysulfides.

3.5 XPS on the Chemical Interaction with Polysulfides

XPS has proven to be effective in probing the changes of chemical environments at the interface.[60,62] To further probe the underlying principles for the superior LiPSs adsorptivity for Co_9S_8, XPS studies were performed on the Co_9S_8-Li_2S_4 solid powder retrieved from the titration experiment described above.

In the Li 1s spectrum of pristine Li_2S_4, a single component is observed at 55.4 eV (**Figure 3.5a**). Upon contact with Co_9S_8, this component shifts 0.5 eV towards lower binding

energy (54.9 eV), suggesting a strong chemical interaction that results in electron transfer from the Co_9S_8 surface to the Li ions (**Figure 3.5b**). In the Co $2p_{3/2}$ spectrum, pristine Co_9S_8 exhibits two components (778.3 eV and 780.9 eV) corresponding to two types of cobalt that occupy distinct lattice sites (octahedral and tetrahedral sites, respectively), with another broad Co 2p satellite peak (shown in purple **Figure 3.5c**).[108,109] Upon contact with Li_2S_4, the Co $2p_{3/2}$ spectrum also shifts overall towards lower binding energy (**Figure 3.5d**), indicating electron

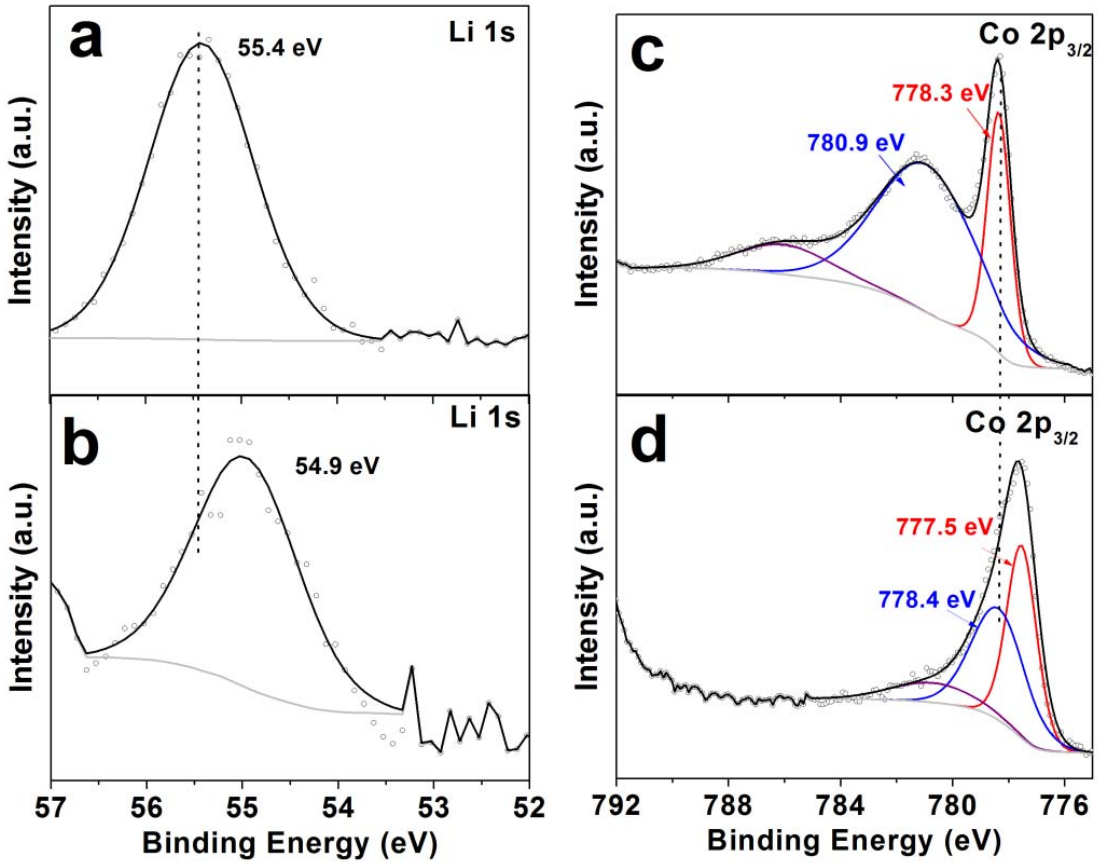

Figure 3.5 High-resolution XPS spectra of a, b) Li 1s and c, d) Co $2p_{3/2}$ regions for a) pristine Li_2S_4, c) pristine Co_9S_8, and b, d) Co_9S_8-Li_2S_4. Black circles and solid lines represent the experimental and overall fitted spectra, respectively.

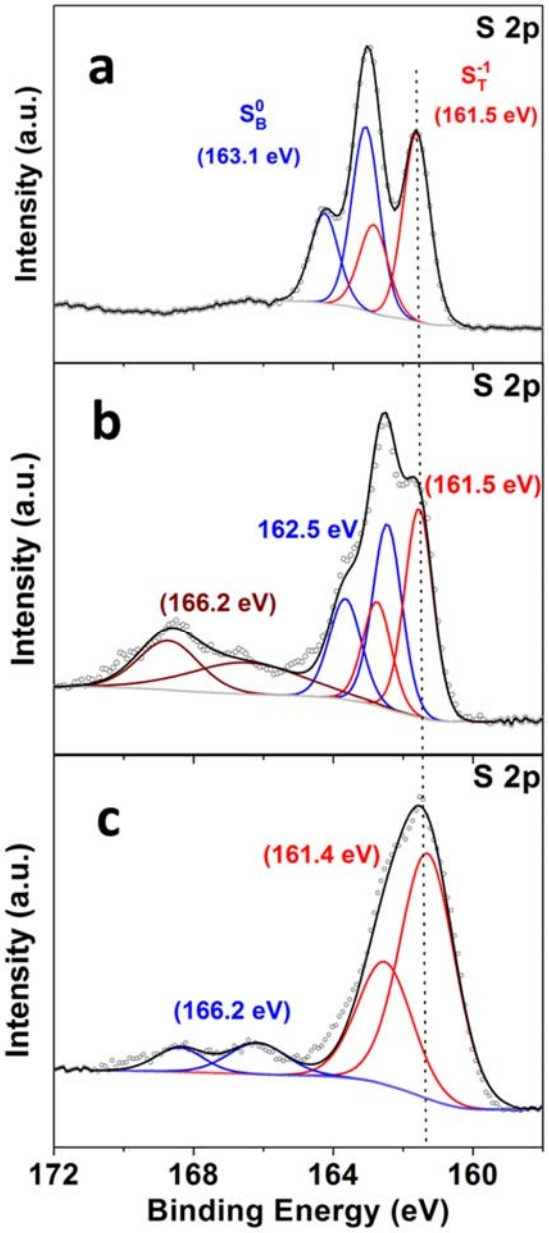

Figure 3.6 High-resolution S 2p XPS spectra of a) the pristine Li_2S_4, b) the pristine Co_9S_8 and c) the Co_9S_8-Li_2S_4 composite. Only the value of $2p_{3/2}$ is noted for each distinct component. The S 2p spectrum of Co_9S_8-Li_2S_4 is fit with two sulfur components. The peak at 161.4 eV includes multiple sulfur species, whereas the peak at 166.2 eV derives from the oxidation species in Co_9S_8.

transfer from Li_2S_4 molecules to the Co atoms. The tetrahedrally coordinated Co site shifts by 2.5 eV, about a factor of three more compared to the octahedral Co site, as expected, owing to its greater interaction based on the calculations shown above for the (008) surface (**Figure 3.3d**). This observation may extend to other transition metals. [110]

It is believed that coupled electron transfer occurs (namely $S_2^{2-} \rightarrow Co^{\delta+}$ and $Li^{+} \rightarrow S^{\delta-}$ (in Co_9S_8)), since the opposite configuration (*i.e.* $S_2^{2-} \rightarrow S^{\delta-}$, $Li^{+} \rightarrow Co^{\delta+}$) would be hindered by electrostatics. In addition, the interaction of Li_2S_4 and Co_9S_8 led to the broadening of the S 2p spectrum of the Co_9S_8-Li_2S_4, suggesting contributions from different chemical states (**Figure 3.6**), although no obvious peak shifts were observed for the S 2p components compared with the pure Co_9S_8 or Li_2S_4. Due to the presence of multiple and overlapping sulfur components, further de-convolution of the S 2p spectra was not attempted. Overall, it is shown that the synergistic interactions that exist on the Co_9S_8-Li_2S_4 interface by XPS studies, that are consistent with the first-principles calculations.

3.6 Electrochemistry of Thin Electrodes

Sulfur cathodes based on Co_9S_8 were fabricated to investigate the benefits of its high LiPS adsorptivity, high conductivity and the interconnected nanosheet structure on the cycling stability of Li-S cells. Sulfur composites with a sulfur content of 75 wt%, Co_9S_8/S75, were prepared by melt-diffusion and the weight fraction was confirmed by TGA analysis (**Figure 3.7a**). The SEM image in **Figure 3.7b** shows that sulfur is evenly distributed over the Co_9S_8 sheets and no large sulfur particles are evident, promising good electrolyte infiltration and good electronic contact to the host. As a comparison, sulfur electrodes based on VC carbon were also prepared (VC/S75, see **Figure 3.7c**).

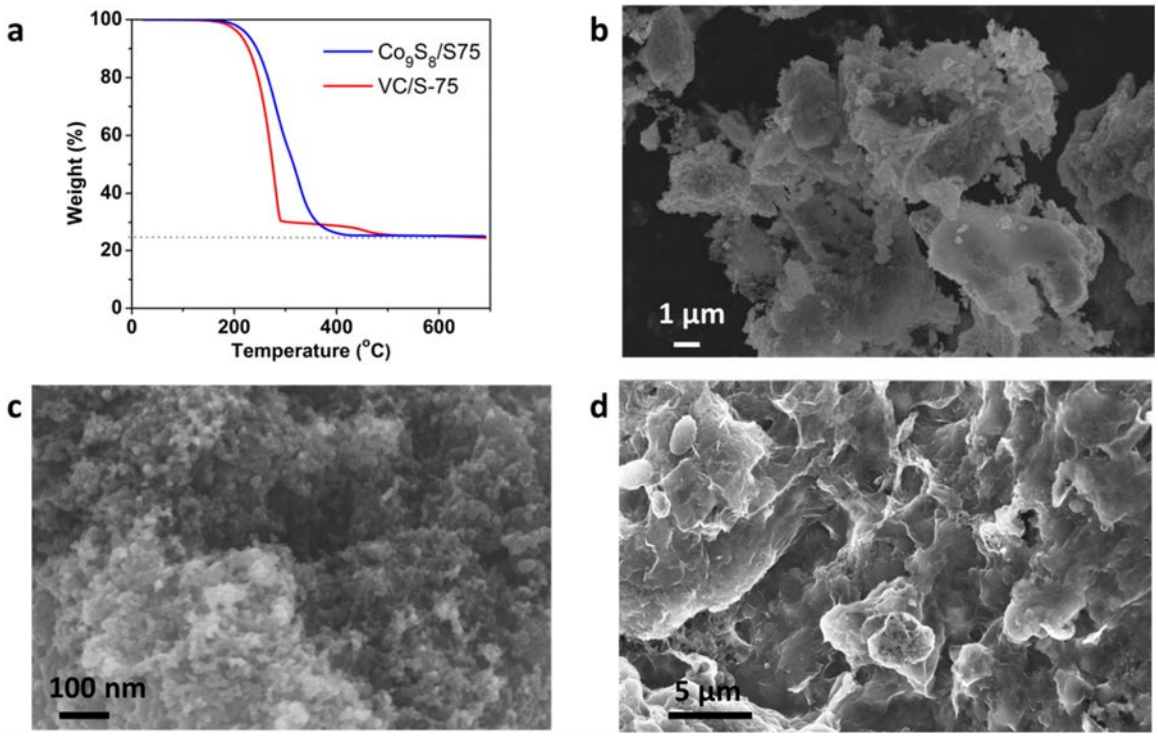

Figure 3.7 a) TGA curve of Co_9S_8/S-75 and VC/S-75 under an Ar flow with a ramp rate of 10 °C/min; representative SEM images of b) the Co_9S_8/S-75 composite, c) VC-S75 composite, d) the high-loading thick Co_9S_8/S-75 electrode surface.

Li-S Cells with a typical sulfur loading of 1.5 mg cm^{-2} and an electrolyte/sulfur (E/S) ratio of 15: 1 (µL/mg) were first examined to enable comparison with previously published work;[60,62,93] high-loading electrodes with up to 4.5 mg cm^{-2} are described in the next section. All Li-S cells were initially cycled at a C/20 rate for conditioning before cycling at higher rates. Sulfur-free cells were built with pure Co_9S_8 cathodes and lithium metal anodes to exclude the electrochemical contribution from Co_9S_8. The Co_9S_8 exhibits only capacitive behavior as indicated by its sloping profile, corresponding to a capacity of only 15-35 mA h g^{-1} in the typical Li-S voltage window (data not shown).

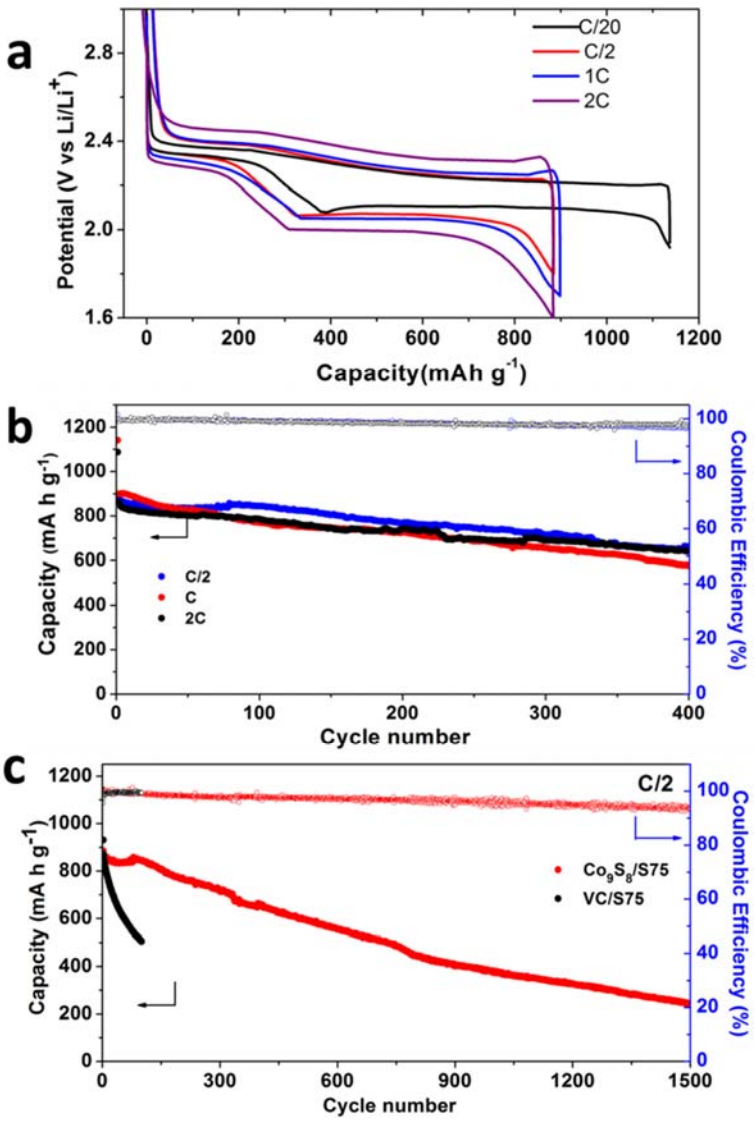

Figure 3.8 The cell voltage profiles of Co_9S_8/S75 electrodes at various C rates; b) prolonged cycling showing the discharge capacity retention of Co_9S_8/S75 electrodes at C/2, 1C and 2C rates over 400 cycles; d) the long-term cycling performance of Co_9S_8/S75 and VC/S75 electrodes at a C/2 rate under identical conditions. The Coulombic efficiency is shown on the right y-axis.

The voltage profiles of the Co_9S_8/S75 electrodes at various C rates are shown in **Figure 3.8a**. High discharge capacities of 1130, 890, 895, and 863 mA h g^{-1} were achieved at C/20, C/2, 1C and 2C rates, respectively. It is noteworthy that virtually no capacity decrease was observed upon a rate increase from C/2 to 2C, indicating highly favorable power capability owing to the metallic properties of Co_9S_8. Prolonged cycling of the electrodes at all rates showed almost identical capacity retention over 400 cycles (**Figure 3.8b**). For example, at a 2C rate, a high capacity of 643 mA h g^{-1} was still obtained over 400 cycles, corresponding to 75% of the initial capacity. As shown in **Figure 3.8c,** the long-term cycling at a medium rate of C/2 demonstrates the superior capacity retention of Co_9S_8 over the carbon-based VC/S75 electrode - the Co_9S_8/S75 electrode experienced an ultralow capacity fading rate of 0.045% per cycle, whereas the capacity of the VC/S75 electrodes faded rapidly over the first 100 cycles at a rate of 0.48% per cycle.

The evolution of the impedance of the Co_9S_8/S-75 cell over cycling was investigated, as shown in **Figure 3.9**. It was observed that upon 1st cycle, the charge transfer resistance (high-frequency semi-circle) within the electrode greatly decreased (**Figure 3.9a**); over 40 cycles, the impedance showed negligible change (**Figure 3.9b**), indicating the good host/(poly)sulfide interface and the excellent conductivity of the Co_9S_8 substrate.

The higher density of the Co_9S_8 host is also beneficial. The Co_9S_8/S75 composite has a higher compact density (2.9 g cm^{-3}) than that of a typical carbon or graphene-oxide composite at the same sulfur mass loading (4.5 g cm^{-3}). Accordingly, the Co_9S_8/S75 electrode exhibits a higher volumetric energy density of 1775 Wh/L at a C/5 rate (including the whole cathode only), compared to a theoretical value of 1275 Wh/L for a carbon electrode, assuming all else is equal. The calculation detail is as below.

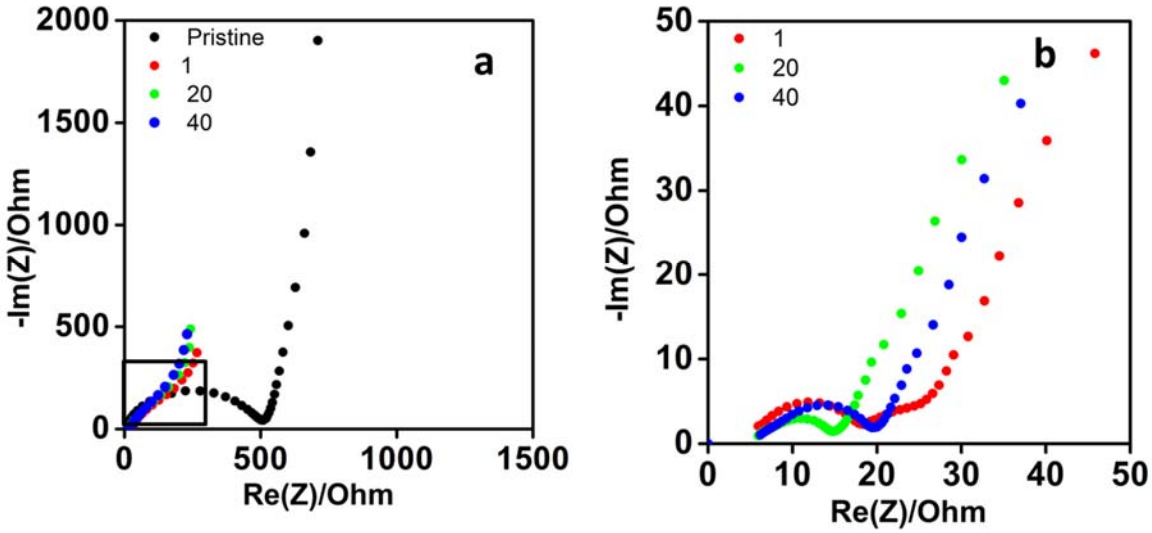

Figure 3.9 Nyquist plots of the Co_9S_8 electrodes at the pristine state and after certain number of cycles (1, 20, 40) at the discharged status; b) is the enlarged plot of the squared area in a).

The volumetric energy density of the cathode side is estimated and compared with a hypothetical graphene oxide based electrode. The assumption was made that both have the same sulfur loading (4.5 mg cm^{-2}) and areal specific capacity (2.7 mA h cm^{-2}) at a rate of C/5 (1.51 mA cm^{-2}) as in our study, with a sulfur fraction of 75 wt% in the composite. The volumetric energy density E_v can be calculated as **Equation 3.1**,

$$E_v = \frac{Q*U}{V} = \frac{Q*U}{A*d} \qquad \textbf{Equation 3.1}$$

where Q is the capacity obtained based on the cathode only, U is the average voltage of the cell (2.1 V), and d is the thickness of the cathode materials, A is the electrode area and V is the total volume of cathode. The components included are sulfur, sulfur host materials, carbon additives. The volume of polymeric binder is disregarded in this back-of-the-envelope comparison. Therefore, the total volume V is calculated as **Equation 3.2**,

$$V = V_S + V_H + V_C = A * (d_S + d_H + d_C) \qquad \textbf{Equation 3.2}$$

where V_S, V_H, V_C is the volume of sulfur, sulfur host and carbon additive, respectively. The density of sulfur, Co_9S_8, graphene oxide, and Super P is estimated at 2.07, 5.35 (crystallographic densities), 0.98 (Aldrich), 1.00 g cm^{-3} respectively.

For the Co_9S_8 based electrode:

$$d = d_S + d_H + d_C = \frac{4.5\ mg/cm^2}{2.07\ g/cm^3} + \frac{\frac{4.5}{3}\ mg/cm^2}{5.35\ g/cm^3} + \frac{\frac{4.5}{6}\ mg/cm^2}{1.00\ g/cm^3} = 0.003190\ cm = 31.90\ \mu m$$

$$E_v = \frac{Q * U}{A * d} = \frac{2.7\ mAh * 2.1\ V}{1\ cm^2 * 31.90\ \mu m} = 1777\ Wh/L$$

Similarly, for the graphene oxide based electrode:

$$d = 44.5\ \mu m, E_v = 1274\ Wh/L$$

This demonstrates that by using a higher-density sulfur host material (Co_9S_8) the cathode can achieve 40% higher volumetric energy density than the GO based cathode, although they possess the same gravimetric energy density. While this is not the volumetric energy density for a full cell, and does not take into account additional porosity needed for electrolyte egress, it simply illustrates the advantage in utilizing a denser cathode host when the same sulfur content (75 wt%) can be sustained. Furthermore, for the compact Co_9S_8 based electrode, the volume of electrolyte needed to wet the electrode would also be lower, further contributing to higher energy density.

3.7 Areal Capacity and Cycling of Thick Electrodes

Constructing high sulfur loading electrodes is critical for building a high energy density Li-S battery for practical applications such as electric vehicles. Electrodes were prepared with varied high sulfur loadings (2.5-4.5 mg cm^{-2}) to investigate the advantages of the 3D interconnected nanosheet structure of the nanostructured Co_9S_8. SBR/CMC binder and graphene carbon additives (4 wt%) were used to construct the electrodes. A low E/S ratio of

10:1 (μL/mg) was used to explore the cycling behavior at high volumetric energy density. The large-scale SEM image of the as-prepared electrodes shows a continuous surface **(Figure 3.7d)**.

Figure 3.10a shows the voltage profiles of the electrodes at a C/20 rate. Areal capacities of 2.7, 3.5 and 4.3 mA h cm^{-2} were achieved for the electrodes with 2.5, 3.5 and 4.5 mg cm^{-2} loadings, respectively. There is no obvious increase of polarization (voltage difference

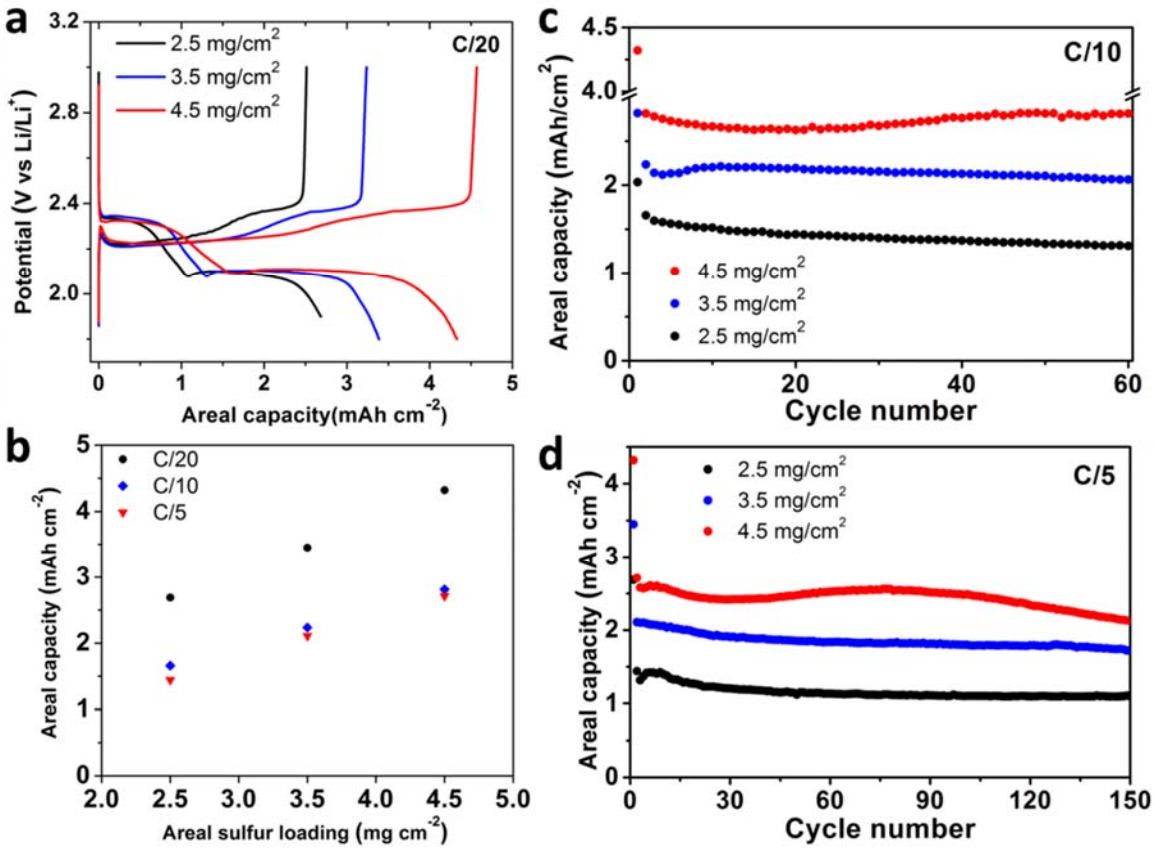

Figure 3.10 Electrochemical performance of the Co_9S_8/S75 high-loading electrodes. a) Initial-cycle voltage profiles of the electrodes with various loadings at C/20 rate; b) comparisons of the areal discharge capacity of electrodes at C/5, C/10 and C/20 rates; c) the areal discharge capacity retention of high loading electrodes at C/10 for 60 cycles; d) the prolonged cycling performance of the Co_9S_8/S75 electrodes at C/5 for 150 cycles.

between charge and discharge) upon increase of the sulfur loading, and the areal capacities obtained at C/10 and C/5 are very close (**Figure 3.10b**), indicating excellent kinetics in spite of the high sulfur loading in thick electrodes. Deep cycling of the thick electrodes at a C/10 rate shows slight capacity increase followed by very stable retention for 60 cycles (**Figure 3.10c**). Prolonged cycling at a higher rate C/5 shows a similar trend with very stable cycling over 150 cycles (**Figure 3.10d**). Although the areal capacity of 4.3 mA h cm^{-2} reported here (**Figure 3.10b, c)** is not the highest compared with some reported carbon electrodes with sophisticated cathode architecture,[41,103,111-113]these slurry-based electrodes exhibit reasonably high areal capacity, with prolonged cycling stability achieved at high sulfur loading.

3.8 Conclusion and Thoughts

In this Chapter, a scalable approach was shown to synthesize a unique high-surface-area graphene-like Co_9S_8 material with hierarchical porosity. The underlying principle is revealled for the superior LiPS adsorptivity of Co_9S_8 over carbon materials *via* a combination of first-principles calculations and XPS studies. A synergistic interaction based on $S_n^{2-} \rightarrow Co^{\delta+}$ and $Li^{+} \rightarrow S^{\delta-}$ exists between the metal sulfide host and polysulfides. Using the Co_9S_8 based sulfur composite, an ultralow capacity fading rate of 0.045% per cycle over 1500 cycles was achieved. More importantly, high sulfur loading electrodes, up to 4.5 mg cm^{-2} loading, were shown with stable cycling over 150 cycles, demonstrating their advantage in building high energy density Li-S batteries. This concept extends to other metal sulfide/oxides, and studies to find the optimal sulfur host that has both high conductivity and polysulfide adsorption are necessary.

Chapter 4 A Cellulose-Derived N, S Dual-Doped Carbon Host for Li-S Batteries

4.1 Introduction

To solve the LiPS shuttle problem, a variety of approaches have been explored, either on the electrolyte and lithium anode or on the cathode. Solid-state electrolytes[114,115]and a LiPS non-solvent liquid electrolyte[116] essentially eliminate the LiPS shuttle, but limitations on interfacial charge transfer increases the polarization and lower the energy efficiency compared to typical liquid electrolytes. Protecting the lithium anode using electrolyte additives limits side-reactions between LiPSs and lithium, leading to improved Coulombic efficiency, but the additives do not survive long-term cycling owing to their eventual consumption.[90]

It is promising to confine the LiPSs on the cathode side *via* chemical interaction using metal oxides,[52,55,60] and metal carbides (MXene phases)[70]. Despite their demonstrated remarkable LiPSs binding abilities, an ultra-high surface area for such relatively heavier (compared with carbons) metal-based hosts is required in order to take full advantage of the interactions, which pose great challenges to the synthesis. Chemical modifications of light-weight, high surface area graphene by oxidation or heteroatom-doping have shown significant potential for LiPSs confinement. Cells employing GOs coupled with an ionic liquid electrolyte and novel binders have achieved a long cycling life, for example.[36,38] The interaction between the polar oxygen groups and the LiPSs was suggested as one of the reasons for the improvement. In particular, N-doped graphene or porous carbons show substantial chemisorption of LiPSs ascribed to strong Li-N interactions, related to the electron donating property of nitrogen.[40,44,117] However, the nitrogen content in doped carbons is generally low, limiting the fraction of active sites available for chemisorption.

In this Chapter, I demonstrate a dual-doping strategy using sulfur and nitrogen atoms at a relatively high doping concentration. N and S dual-doped carbon has been previously reported to be an oxygen reduction reaction catalyst that exhibits greatly improved catalytic properties compared to non-doped carbon.[118] This is suggested to be due to its asymmetric charge density distribution; namely N bears a negative charge and S a positive charge. In our study, the interaction between LiPSs and the dual-doped carbon was examined using a combination of XPS and first-principles theoretical calculations. A greatly improved chemical interaction of the dual-doped carbon with LiPSs (electrophilic Li^+ and nucleophilic terminal S^-) compared to graphene alone is described. In addition, the dual-doped carbon exhibits a significant increase of conductivity, benefiting the power capability of a Li-S cell.

The synthesis of mesoporous carbons or graphene composites typically requires the use of exotic hard templates and/or expensive surfactants as well as high-cost polymeric carbon sources and complex procedures. Herein, a completely different route to prepare porous carbon materials is described by utilizing a low-cost biomaterial, cellulose nanocrystals (CNCs). Cellulose is the major constituent of plant cell walls and the most abundant sustainable material on the planet.[119] Cellulose nanocrystals with a nanorod morphology can be produced on the ton-scale from the acid hydrolysis of wood fibers(~$10/kg).[120,121]

In this work, the porous structure was created based on a liquid-crystal driven self-assembly of CNCs.[122] It avoids traditional nanostructured hard-templating or soft-assembly methods, and provides a promising industrial solution for utilizing sustainable cellulose materials. Moreover, the introduction of the two heteroatoms, N and S, into the carbon lattice was realized by pyrolysis of a single conjugated polymer - polyrhodanine (PR) - instead of requiring two separate sources. [118,123]

The synthesis of the precursors, PR@CNCs, part of the heat-treatment, elemental analysis was completed by Dr. Juntao Tang at Department of Chemical Engineering, University of Waterloo. I carried out part of the heat-treatment, HF etching, physical characterizations other than elemental analysis, electrochemistry measurements and computations.

4.2 Experimental Approaches

4.2.1 Synthesis of Porous Carbons

The PR coated cellulose nanocrystals precursor (denoted as PR@CNC) was synthesized by a modified process according to a previous report.[124] Cellulose nanocrystals (CelluForce Inc.) exhibit an average charge density of 0.26 mmol g^{-1}. Typically, $FeCl_3$ (45.0 mM) was added into 150 mL 0.2 wt% CNC dispersion with stirring. The mixture was introduced dropwise into the rhodanine monomer solution prepared by dissolving rhodanine monomers (45.0mM) in 150 mL deionized water. The polymerization was completed at 85 °C overnight. The PR@CNC was obtained after ultrafiltration on filter-paper membranes (100 nm pores) and rinsing with millipore-Q water until the filtered solution became colourless. Similarly, polydopamine coated CNCs, used for N single-doped carbon, was synthesized via in-situ polymerization of dopamine in the presence of tris(hydroxymethyl)aminomethane (Tris).

For the synthesis of N,S dual-doped carbon (NSC), N-doped carbon (NC) and non-doped carbon (cellulose-derived carbon, CDC), tetraethyl orthosilicate (TEOS) was added to the corresponding 3.5 wt% aqueous precursor suspension (pH=2.5) in the desired ratio. The mixture was stirred to yield a homogeneous colloidal solution, which was allowed to dry in a polystyrene Petri dish under ambient conditions. The pyrolysis was carried out at 900 °C for 6

hours under Ar flow, with a ramp rate of 2 ºC min^{-1}. The carbon materials were recovered by completely etching the silica in 5 wt% HF solutions. For synthesis of non-porous NSC (NP-NSC), the procedure was the same, except no TEOS was added in the precursor dispersion.

NSC/S-70 sulfur composite with 70 wt% of sulfur was prepared via a melt-diffusion method. The free-standing NSC film was hand ground into a powder and mixed with elemental sulfur in the desired ratio. The mixture was heated under ambient atmosphere at 155 ºC for 12 hours. The CDC/S-70 and NP-NSC/S-70 composites were similarly prepared by the same general route.

4.2.2 Electrochemical Measurements

Sulfur composites (NSC/S-70 or CDC/S-70, NP-CDC/S-70) with Super P and Kynar Powerflex binder (PVDF) were dispersed in DMF in a weight ratio of 8:1:1. The slurry was drop-cast onto carbon paper disk (2 cm^2, AvCarb P50) to prepare the cathodes. The electrodes were dried at 60 °C overnight before use.

Coin cells 2325 were assembled inside the glovebox with a lithium foil anode and an electrolyte comprising 50 µL 1 M LiTFSI and 2 wt% of $LiNO_3$ in a mixture of DME and DOL (v/v = 1:1). The electrolyte without $LiNO_3$ has same composition except that no $LiNO_3$ was added. The sulfur loading was controlled at 1.4-1.7 mg cm^{-2}. The cells were operated in a voltage window of 1.8-3.0 V at different C rates. At low rate C/20, a voltage window of 1.9-3.0 V was used and at high rate 2C, 1.7-3.0 V was used. For EIS measurements, the DC voltage was maintained at open-circuit voltage and an AC voltage of 5 mV in amplitude was applied with a frequency of 200 kHz - 20 mHz. For CV measurements, a sweep rate of 0.1 mV/s within the 1.8 -3.0V window was applied.

4.2.3 Computational Methods

The first-principles calculations were performed with the VASP code, applying pseudopotentials to describe electron-ion interactions, and the PBE version of the generalized gradient approximation (GGA) for the electronic exchange correlation effect.[86,87] A cut-off energy of 400 eV was used for the plane wave basis to ensure convergence. For modeling lithium polysulfides, Li_2S_2 was employed as a representative polysulfide. A single-layer graphene of a 6×6 supercell size was adopted as the model for non-doped carbon. The pyrrolic nitrogen and thiophene-like sulfur were used as representative dopants for the doped carbon. A vacuum layer of 16 Å was used in the vertical direction, in order to exclude the interaction between the graphene layer and its images. The k-space was sampled with a 3×3×1 k-point grid using the Monkhorst-Pack method. The conjugate-gradient algorithm was used for ionic relaxation. The binding energy (E_{bind}) of Li_2S_2 on the carbon substrate is defined as

$$E_{bind} = E_{sub} + E_{ps} - E_{sub+ps}$$

where E_{sub}, E_{ps} and E_{sub+ps} represent the ground-state energies of the carbon substrate, Li_2S_2 and carbon-Li_2S_2 composites. A larger positive value refers to a greater binding ability.

4.3 Physical Characterizations of the NSC

Carbon materials with a hierarchical pore structure were prepared from the pyrolysis of self-assembled CNCs films (**Figure 4.1a**). The CNC dispersion (1-7 wt%) exhibits lyotropic chiral nematic behavior and evaporation-induced self-assembly of the CNCs allows fabrication of an ordered nanoporous carbon.[125,126] The CNCs, used as a self-template, were first uniformly coated with polyrhodanine via *in-situ* polymerization, which provides a dual doping source for both nitrogen and sulfur. The TEM images of CNCs and PR@CNCs are shown in in **Figure 4.2a** and **b,** respectively.[121] Silica derived from the hydrolysis of TEOS was added into the

dispersion to provide a spacer between particles and avoid structural collapse upon carbonization. A free-standing film with chiral nematic (disrupted) order was then formed upon evaporation of the PR@CNC aqueous suspension (3.5 wt%). A porous carbon with N and S atoms doped mainly on the surface was obtained upon pyrolysis and etching of silica. The N single-doped carbon NC and pristine cellulose nanocrystal-derived carbon without doping CDC were fabricated in the same way using polydopamine as the doping source for NC.

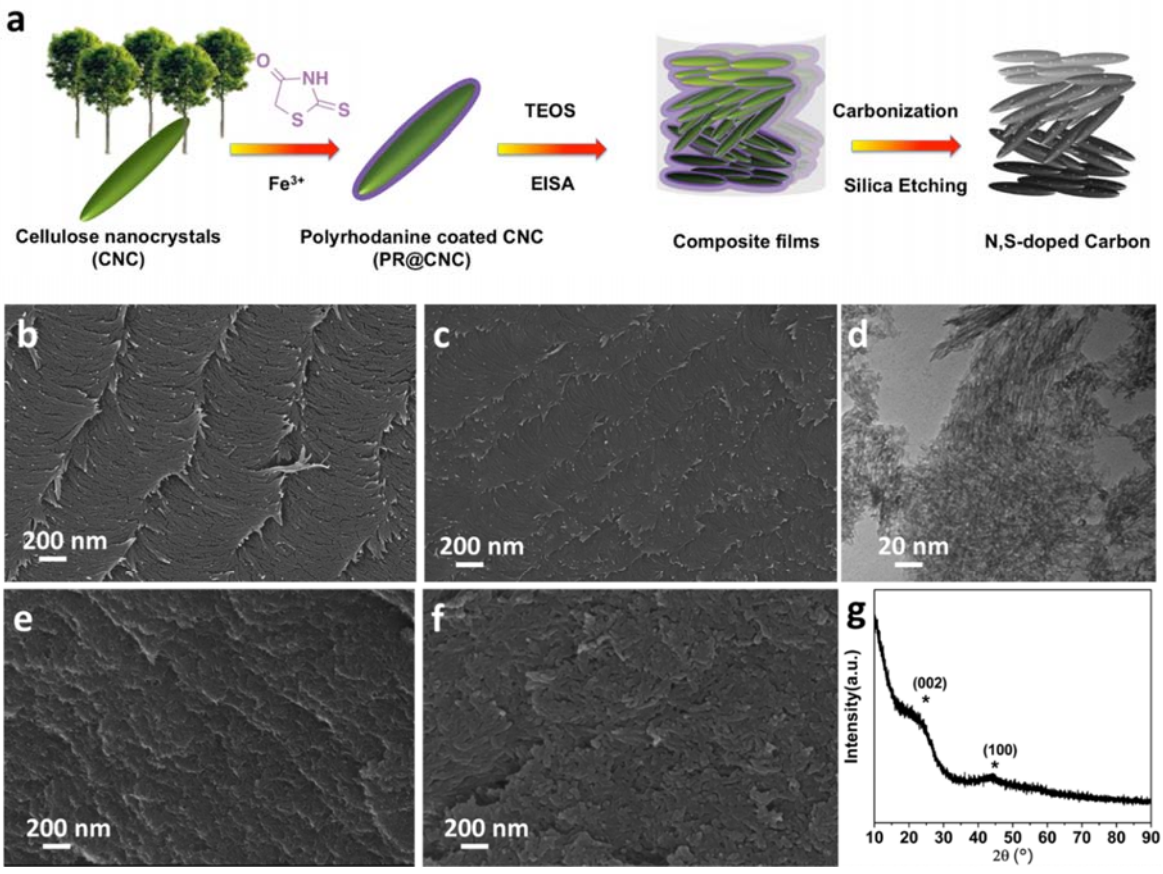

Figure 4.1 a) The schematic illustration of the synthesis of NSC; SEM images of periodic self-assembled b) CNCs and c) PR@CNC precursors for the synthesis of CDC and NSC, respectively; d) TEM and e) SEM images of NSC; f) SEM image of the NSC/S-70 composite; g) XRD pattern of the NSC.

The CNCs and PR@CNCs precursor films both exhibit a periodic structure with a chiral nematic ordered morphology, as shown by SEM images in **Figure 4.1b,c**. The self-assembly of the latter was slightly disrupted due to the decreased interparticle repulsive forces brought upon by surface modification.[127] The morphology was largely preserved upon carbonization for NSC as seen from **Figure 4.1e**. It can be seen from the TEM images (**Figure 4.1d and Figure 4.2c**) that the individual nanorods, ~5 nm in diameter and ~ 200 nm in length, are organized in a twisted periodic assembly.

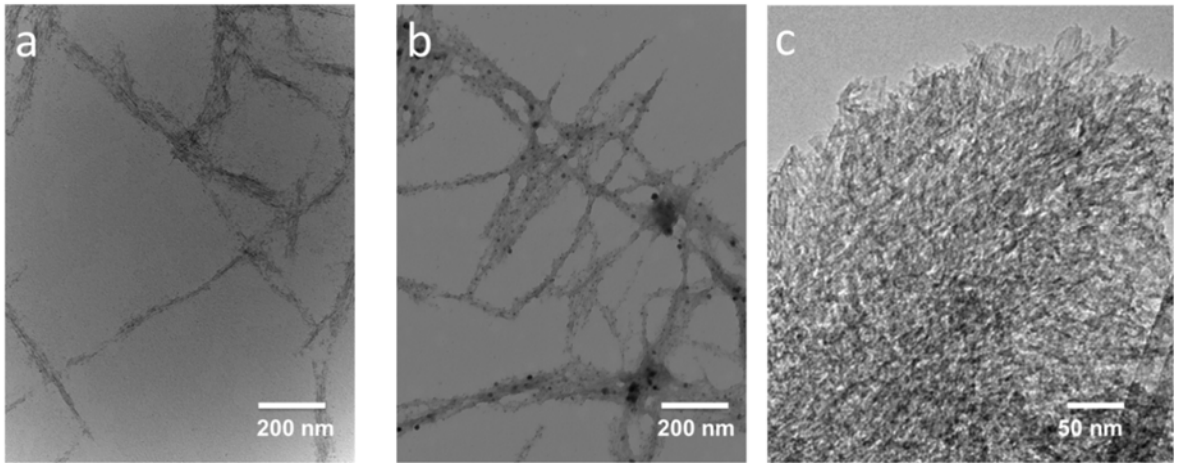

Figure 4.2 TEM images of a) pristine CNCs (with $FeCl_3$ dye) and CNC@PR (without $FeCl_3$ dye). Comparison of a) and b) shows there is a uniform distribution of PR on CNCs in the form of nanoparticles. c) TEM image of NSC, showing the arrangement of carbon nanorods.

The porosity can be tailored by tuning the PR@CNC/TEOS ratio in the precursor, resulting in four different NSC materials. The BET surface area and pore volume calculated by QSDFT method are summarized in **Table 4.1 and Figure 4.3.** The optimized NSC (NSC-1) exhibits a high BET surface area of 1200 $m^2\ g^{-1}$ and a large pore volume of 1.48 $cm^3\ g^{-1}$ and was used for this study (**Table 4.1**, **Figure 4.4a, b**). A hierarchical nano-porosity including both micropores (~ 1 nm) and mesopores (4 - 6 nm) was observed in NSC, arising from the

gas evolution upon pyrolysis of the bio-polymers and the space between self-assembled nanorods, respectively.

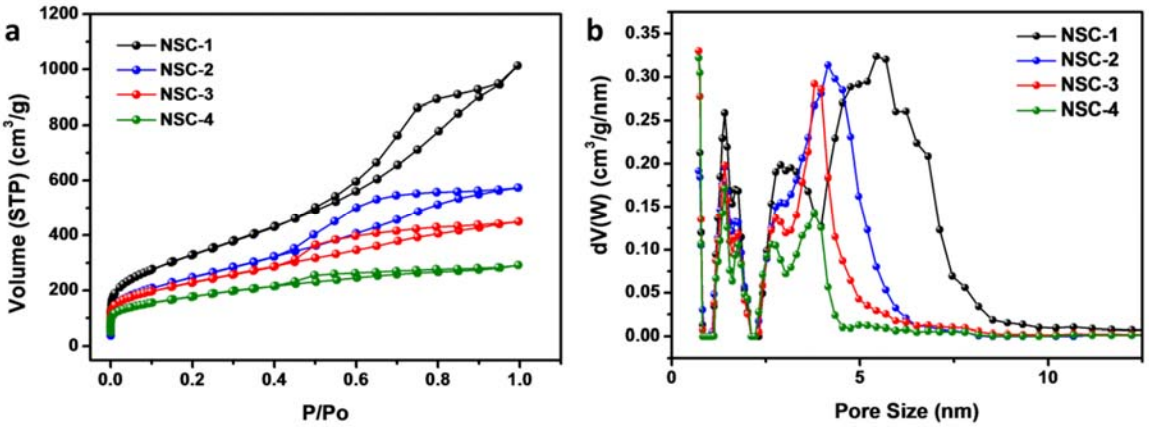

Figure 4.3 N_2 adsorption/desorption isotherms and pore size distributions of NSC materials prepared at different PR@CNCs/TEOS ratios.

It is noted that departure from this optimal ratio results in lower surface area and pore volume **Table 4.1**). A large pore volume is vital to accommodate the sulfur efficiently and allow enough void space for volume expansion, while the high surface area is important for interfacial chemisorption for LiPSs. To illustrate this point, non-porous NSC (NP-NSC), with a low surface area of 330 $m^2\ g^{-1}$ and a pore volume of 0.3 $cm^3\ g^{-1}$ (**Figure 4.4a, b)** was used as a comparison for electrochemical studies (*vide infra*). The NC and CDC exhibit comparable BET surface area of 1130 $m^2\ g^{-1}$, 1230 $m^2\ g^{-1}$ and a pore volume of 1.50 $cm^3\ g^{-1}$, 1.30 $cm^3\ g^{-1}$, respectively. A slightly smaller pore size was observed for CDC, due to the smaller size of CNC vs PR@CNC.

Table 4.1 The surface area and pore volume of NSC materials with respect to the PR@CNC/TEOS ratio.

Sample	Weight percent of PR@CNC (wt%)	BET surface area ($m^2 g^{-1}$)	Pore volume ($cm^3 g^{-1}$)
NSC-1	20	1200	1.48
NSC-2	35	905	0.82
NSC-3	45	815	0.64
NSC-4	60	620	0.40

The XRD pattern in **Figure 4.1g** exhibits three broad peaks corresponding to (002) and (100) lattice planes, suggesting that the synthesized NSC has a low degree of crystallinity. The EDX spectrum in **Figure 4.5a**, confirms the presence of nitrogen and sulfur in NSC, with an atomic concentration of 2.4% and 3.2%, respectively. As shown by EDX elemental mapping in **Figure 4.5**, N and S are homogeneously distributed throughout the carbon. Since this material is prepared *via* sintering at a temperature as high as 900 ºC, it is reasonable to conclude that the N and S are effectively doped into the graphitic lattice. This is further confirmed by Raman spectroscopy analysis. The ratio of D band (disordered carbon, 1360 $cm^{-1)}$ to G band (sp^2-hybridized graphitic carbon,1590 cm^{-1}) contributions; I_D/I_G, calculated by the integrated areas, is higher for NSC than CDC (1.23 *vs.* 1.15), suggesting the presence of more defect sites created by the N and S doping (**Figure 4.6**).[123] It is noted that the overall doping level of the two elements, N and S, reaches 5.6 at%, which is higher compared to other reports (e.g. 1.61 at% [43] or 1.5 at% [128] for N doping). This can potentially provide a higher concentration of active sites for LiPSs adsorption. The N doping concentration for NC is confirmed to be 2.2 at% by EDX.

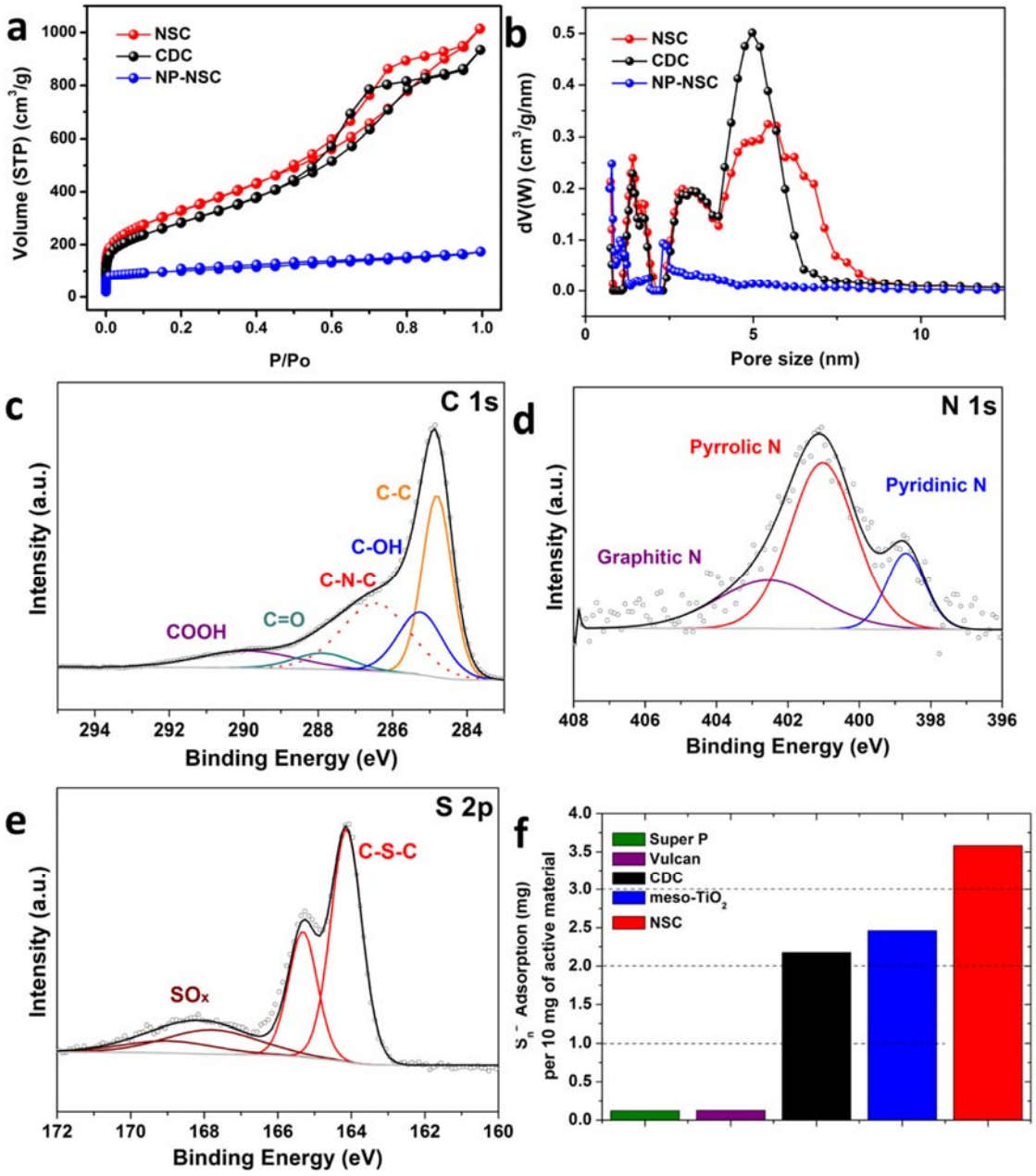

Figure 4.4 a) N_2 absorption/desorption isotherms and b) pore size distributions of CDC, NSC and NP-NSC; the high resolution (c) C 1s, (d) N 1s and (e) S 2p XPS core spectra of NSC (round circles = experimental data, black line = overall fit, solid colored lines = fitted components); f) the polysulfide adsorptivity of CDC and NSC, with Super P, Vulcan carbon, and mesoporous TiO_2.

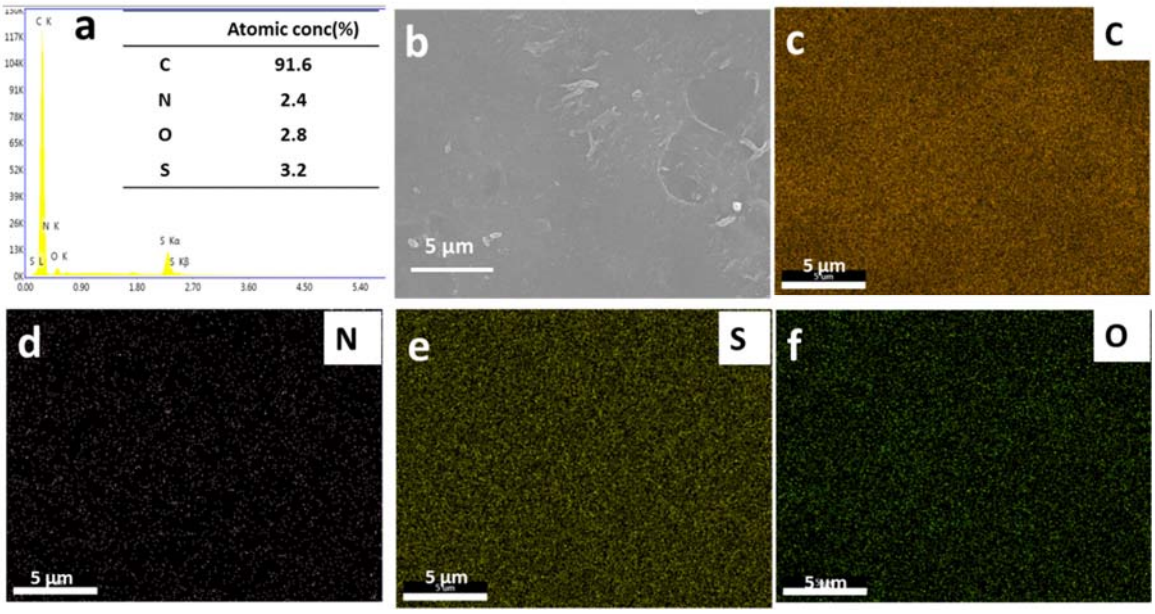

Figure 4.5 a) The EDX spectrum of NSC showing the presence of both N and S, with their atomic concentration in the inset; b-f) EDX mapping of the elements C, N, S, O in the area corresponding to b).

To investigate the chemical nature of the surface of the dual-doped carbon, XPS analysis was performed. In the high-resolution C 1s spectra (**Figure 4.4c and Figure 4.7**), both NSC and CDC display the components corresponding to C-C (284.8 eV; which also corresponds to adventitious carbon and is used as a reference), C-OH (285.2 eV), C=O (287.9 eV) and COOH (290.0 eV) species.[39,123] This suggests that both materials contain oxygen groups on the surface, which is believed to improve LiPSs' binding ability. The NSC contains an additional component with a binding energy of 286.5 eV corresponding to C-N-C species,[123] confirming the effective doping of N into carbon lattice. The N 1s spectrum of NSC reveals the chemical composition of the nitrogen environment (**Figure 4.4d**). Three components - pyridinic N, pyrrollic N and quaternary N - can be identified at 398.7 eV, 401.0 eV and 402.5

eV, respectively. [43,123] These three typical species observed in N-doped carbons have proven to contribute to LiPS binding in different ways, either by interacting with pyridinic N atoms or the neighboring carbon of quaternary N. [46]

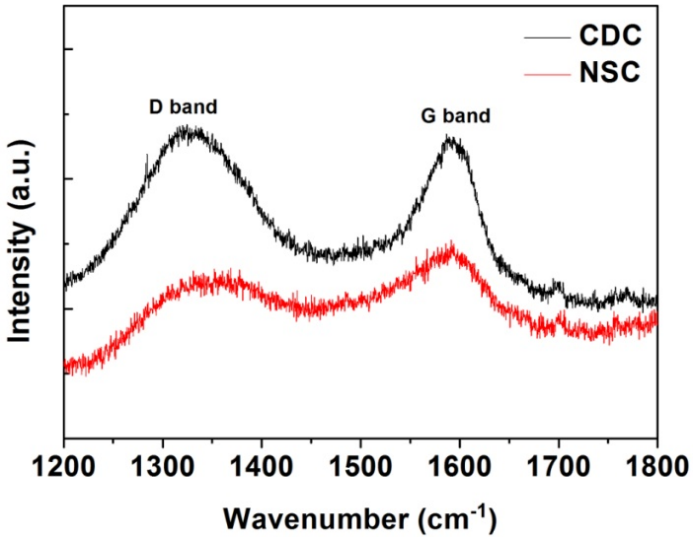

Figure 4.6 Raman spectra of CDC and NSC, showing the D and G bands.

The S 2p spectrum of NSC is shown in **Figure 4.4e.** Only the peak positions of the S $2p_{3/2}$ components of the S $2p_{3/2}/2p_{1/2}$ doublets are described, following convention. Two sulfur species are assigned to carbon-bonded thiophene-like sulfur C-S-C (164.1 eV) and highly oxidized sulfur species SO_x (167.9 eV).[118] Any possible assignment to elemental sulfur (~ 164.3 eV) can be excluded, since the material was synthesized at a high temperature. In contrast, both the N 1s and S 2p spectra of CDC indicate the absence of N and S on the surface, as seen in **Figure 4.7**. With the same pore structure but completely different surface properties, NSC, NC and CDC can thus provide an excellent platform to study the dual-doping effect on the LiPS binding capability.

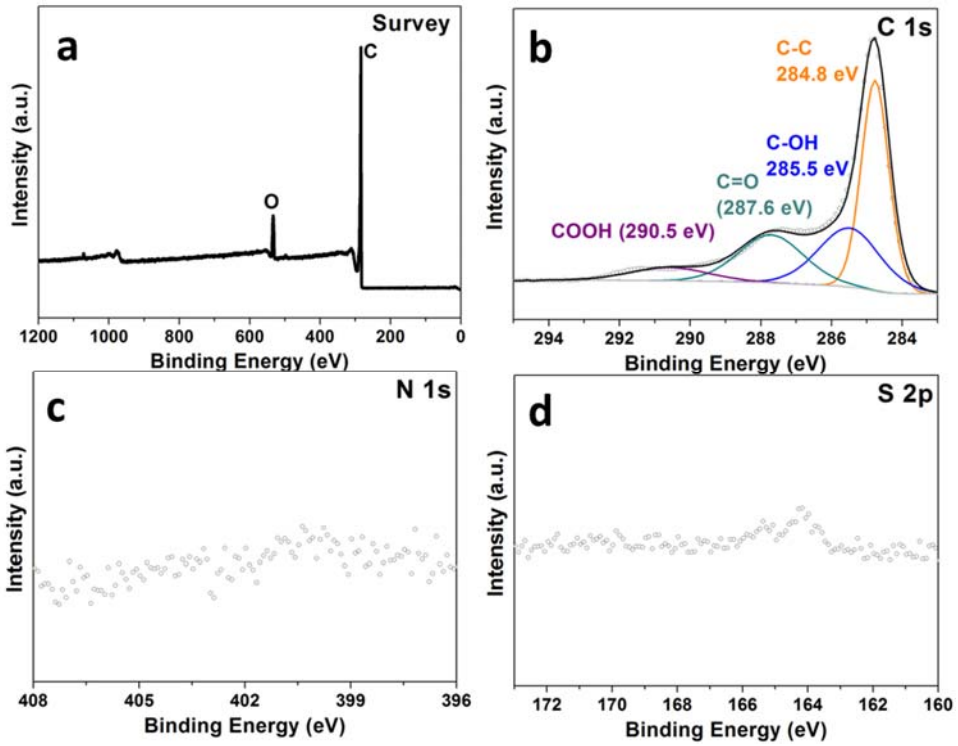

Figure 4.7 The survey a) and high-resolution b) C1s, c) N 1s and d) S 2p XPS spectra of CDC.

4.4 XPS Studies on the Chemical Interaction with Polysulfides

The adsorptivity of NSC and CDC towards LiPSs was quantitatively evaluated using an electrochemical titration method by measuring the residual LiPS remaining upon contact with the respective sulfur host materials. The polysulfide Li_2S_4 with a medium chain-length was chosen as representative of the LiPSs. The adsorptivity of NSC, CDC, commercial mesoporous TiO_2 (meso-TiO_2), VC, Super P was evaluated (**Figure 4.4f**). The CDC adsorbs ten times more Li_2S_4 than VC and Super P, and NSC can adsorb twice that of CDC. This indicates that although the oxygen functional groups contribute to Li_2S_4 binding, the N,S dual-doping is even

more effective. It is also noted that the NSC also adsorbs twice that of meso-TiO_2, indicating its superior ability in this respect compared with a highly porous oxide.

The nature of the interaction between NSC and LiPSs was studied by XPS using the solids recovered from the NSC/Li_2S_4 suspension in the titration experiment above. The Li 1s spectrum of pristine Li_2S_4 exhibits a single symmetric peak at 55.5 eV **(Figure 4.8a)**, whereas upon contact with NSC, the NSC-Li_2S_4 shows an asymmetric peak extending to higher binding energy (**Figure 4.8c**). Therefore, an additional peak with a +0.9 eV shift was fitted and attributed to the Li^+ ions interacting with doped N (Li-N), consistent with the observation for polypyrrole bonded LiPSs.[129] On the contrary, the line shape in the Li 1s spectrum of CDC-Li_2S_4 remains symmetric, indicating little Li^+ interaction (**Figure 4.8b**).

The polysulfide Li_2S_4 shows two sulfur contributions in its S 2p spectrum at 161.5 eV and 163.1 eV with a 1:1 ratio (**Figure 4.8d**), ascribed to the terminal sulfur (S_T^{-1}) and bridging sulfur (S_B^0) atoms, respectively. The S 2p spectrum of the NSC-Li_2S_4 composite sheds light on the interaction between the doped S and Li_2S_4. Compared with Li_2S_4 itself, the terminal sulfur S_T^{-1} shifts to higher binding energy by +1.4 eV, indicating a decrease in electron density on the S_T^{-1}. This was ascribed to its interaction with the positively charged dopant $S^{\delta+}$ in the NSC (Li-S_T^{-1}-$S^{\delta+}$), which is confirmed by first-principles calculations (see next section). The bridging sulfur was not fit in **Figure 4.8f**, since its binding energy region overlaps with the doped sulfur.

However, for CDC which lacks N and S dopants, the S 2p spectrum exhibited similar components as found with VC described in a previous report (**Figure 4.8e**).[60] The binding energy of both S_T^{-1} and S_B^0 in the probe molecule Li_2S_4 remained unchanged. An additional carbon-bonded S^0 species arises from the disproportionation of Li_2S_4 into S^0, favored by the

lack of interaction with the non-polar carbon surface. [60] This indicates the absence of interaction between non-doped carbon and Li_2S_4, consistent with the Li 1s spectrum.

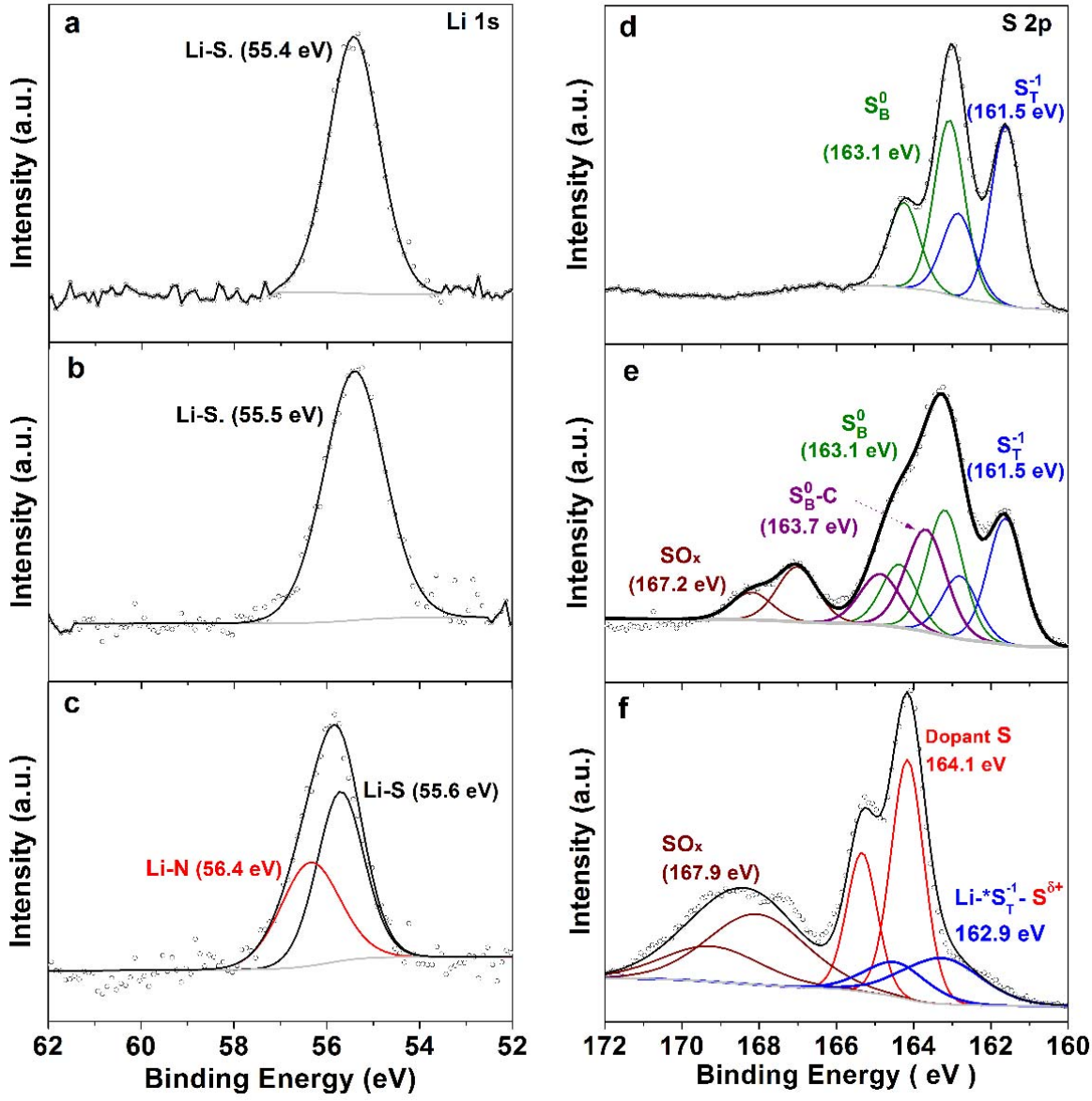

Figure 4.8 High-resolution XPS Li 1s (a-c) and S 2p (d-f) spectra of (a,d) Li_2S_4, (b,e) CDC-Li_2S_4 and (c,f) NSC-Li_2S_4.

It is noted that the new components at 160-177 eV in CDC-Li_2S_4 and NSC-Li_2S_4 are due to the thiosulfate and polythionate species formed by the redox reaction between Li_2S_4 and the oxidized carbon surfaces, as we reported for graphene oxide.[72] The N 1s spectrum and the doped sulfur region in the S 2p spectrum of NSC-Li_2S_4 do not undergo significant change. This is due to the highly delocalized electron structure of NSC, which distributes any changes in electron density over the entire lattice and smears out any observable effects in the XPS.

4.5 Computations to Understand the Chemical Interaction

To fully understand the interaction between NSC and LiPSs, first-principles calculations based on DFT were carried out. For simplicity, single layer graphene using a 6×6 supercell and a Li_2S_2 molecule were used as the models for the carbon substrate and LiPSs, respectively. In order to model the polyrhodanine doping, pyrrollic nitrogen and thiophene-like sulfur atoms were used.

The geometric configuration and charge population of the host substrates after full relaxation are shown in **Figure 4.9** and top panels of **Figure 4.10**, respectively. The non-doped graphene shows a uniform charge density distribution over the lattice (**Figure 4.9a**), whereas the pyrrolic N bears a charge of -0.81, signified by the red electron density contour curves on the N position (**Figure 4.9b, Figure 4.10b**). However, thiophene-like S exhibits a charge of +0.45 when dual-doped into the lattice, shown by the dark electron density contour curves on the S position (**Figure 4.9c**, **Figure 4.10c**).

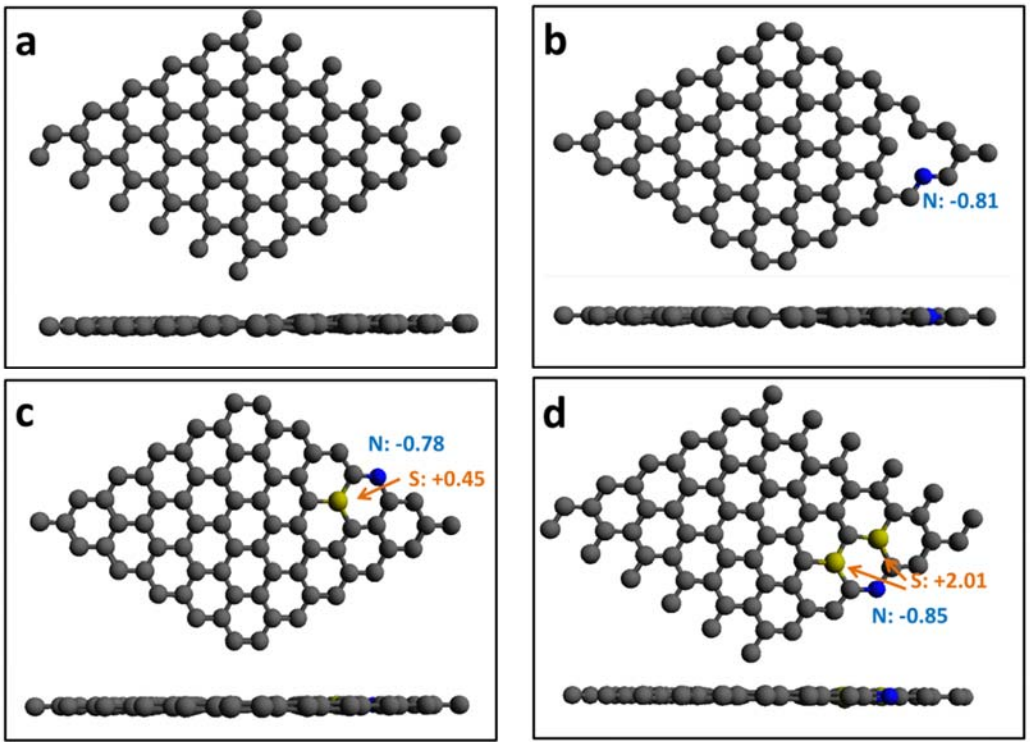

Figure 4.9 The fully relaxed structure of carbon substrates with (a) no dopant, (b) 1 N atom dopant, c) 1 N + 1 S dual-atom doping and d) 1 N + 2 S dual-atom doping (per supercell). Grey, blue, yellow balls represent C, N and S, respectively. The calculated charge population on doped N and S atoms are noted, while the balanced charge is delocalized over the whole carbon lattice.

The most stable geometric configurations of the Li_2S_2 molecule interacting with different carbon substrates are shown in **Figure 4.10** along with their binding energy values. There is no specific bonding between Li_2S_2 with non-doped graphene, resulting in a low binding energy of 0.07 eV. The results in **Figure 4.10b** indicate a favorable bonding between Li^+ and pyrrolic N (1.06 eV) and those in **Figure 4.10c and d** show highly specific bonding between the S_T^{-1} and doped $S^{\delta+}$, as evidenced by the local protrusion of doped S out of the graphene layer. The calculation indicates a binding energy (2.59 eV) of Li_2S_2 onto N, S-dual

doped carbon, which is over twice that of N-doped carbon. Furthermore, by model an S/N ratio of 2, the binding energy increases to 5.74 eV. These calculations indicate the highly favorable aspects of the N, S dual-doping strategy, with findings in full accord with XPS studies discussed above.

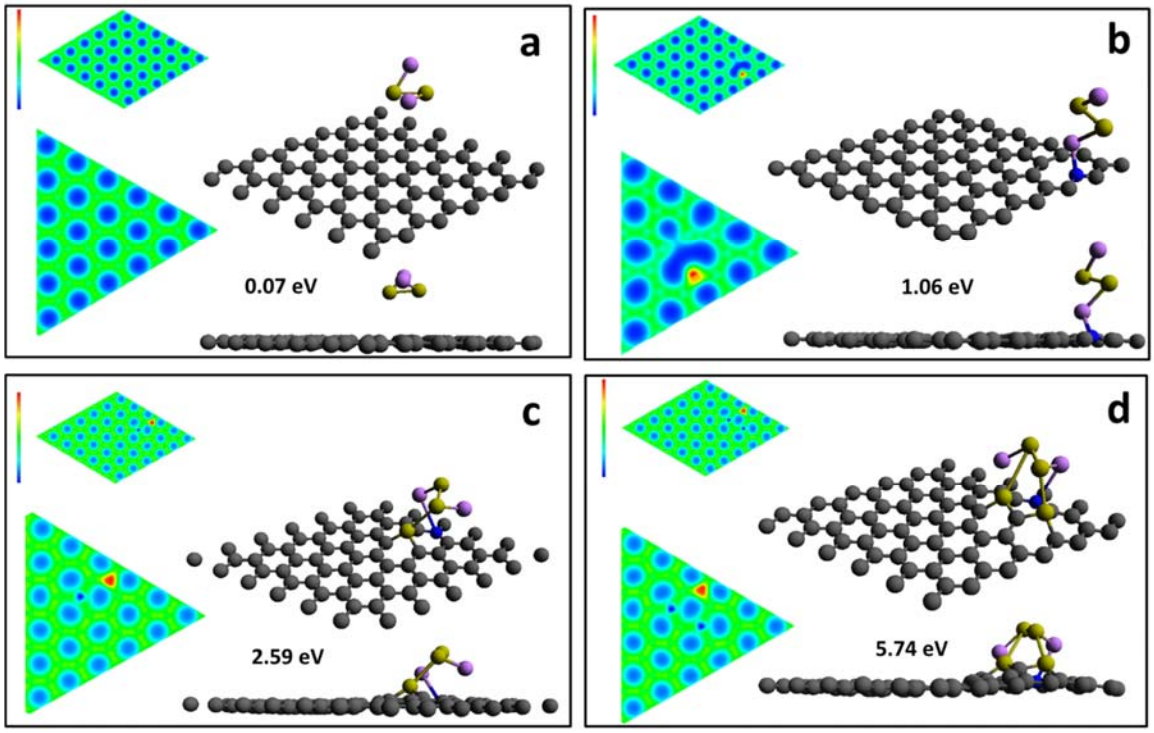

Figure 4.10 First-principles calculations illustrating the most stable Li_2S_2 binding configurations after full relaxation on carbon substrates a) with no doping and doped with b) 1 N doping, c) 1 N + 1 S and d) 1 N + 2 S per supercell (bottom right for side view); Insets on top left are the 2D deformation charge distributions of the corresponding substrates only without Li_2S_2 (red for accepting electrons, blue for donating electrons), with the magnified versions (around the heteroatoms) shown on the bottom left. Grey, blue, purple and yellow balls represent C, N, Li and S atoms, respectively.

4.6 Electrochemical Performances

To evaluate the effects of the N, S dual-doping approach on the electrochemical properties, sulfur composites with 70 wt% of sulfur were prepared via the melt-diffusion method for NSC, NC, CDC and NP-NSC. These cathodes were employed in Li-S batteries. The sulfur content was determined by TGA (**Figure 4.11**). The representative SEM images of the NSC/S-70 composites (**Figure 4.1f**) show no aggregated sulfur particles on the surface of carbon materials, indicating that sulfur was fully diffused into the pores of the carbon networks.

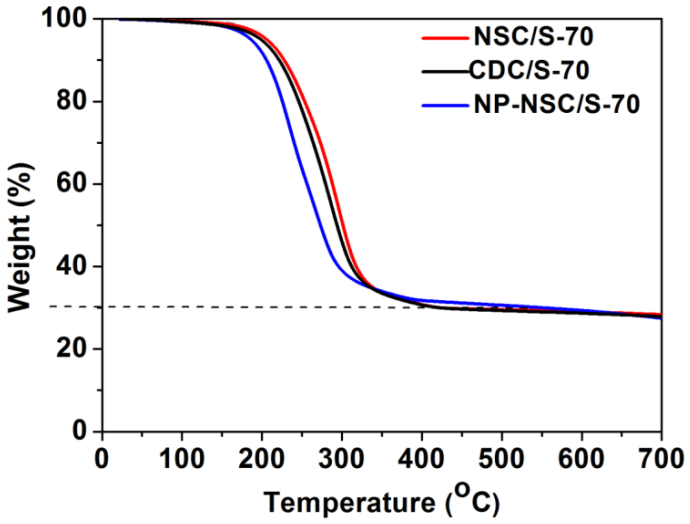

Figure 4.11 TGA curves of NSC/S-70, CDC/S-70 and NP-NSC/S-70 composites measured under a N_2 flow with a heating rate of 10 °C/min.

Substitutional doping of heteroatoms in graphitic lattices has proven to be an efficient route to improve the conductivity.[40] The bulk conductivity of NSC, measured by a four-point probe method, is an order of magnitude higher than non-doped CDC (0.78 S cm^{-1} *vs.* 0.04 S cm^{-1}). Electrochemical cells constructed with NSC as the cathode *vs.* a lithium metal anode show that the NSC host itself is not electrochemically active in the 1.8-3 V (*vs.* Li/Li^+) window, only contributing a negligible capacitive capacity of 30 mA h g^{-1} (**Figure 4.12**). This confirms

that the doped atoms, especially S, do not participate in redox activity and thus maintain their chemical integrity during the operation of a Li-S cell.

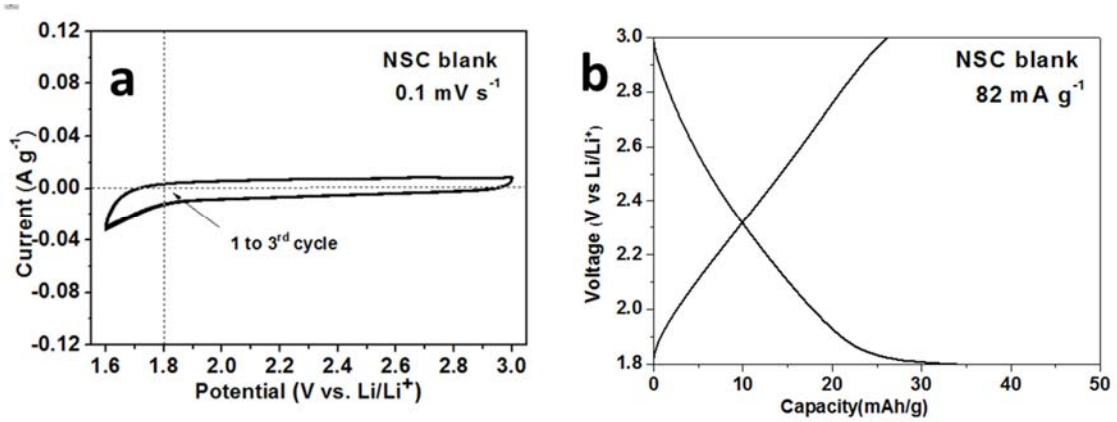

Figure 4.12 a) CV curve (1.6-3.0 V) for the first three cycles and b) voltage profile (1.8-3.0 V) at a current of 82 m A g^{-1} for the NSC blank electrode without sulfur.

Figure 4.13a shows the galvanostatic voltage profiles of Li-S cells with NSC/S-70 electrodes at various current densities. They exhibit typical two-plateau discharge curves at ~ 2.4 and 2.1 V. The overcharge in the first cycle at various rates is negligible, indicating effective inhibition of LiPS shuttle. There is very little increase in polarization upon increase of current density. The favorable redox kinetics are owed to the improved conductivity of doped carbon and the excellent interface between the NSC and LiPS intermediates; the void volume within the composite for electrolyte infiltration is an additional advantage. The NSC/S-70 electrode exhibits a high discharge capacity of 1370 mA h g^{-1}, 1280 mA h g^{-1}, 1135 mA h g^{-1} and 830 mA h g^{-1} at C/20, C/5 and C/2 and 2C rates, respectively. Long-term cycling at various rates was carried out after a conditioning cycle at C/20 (**Figure 4.13a**).

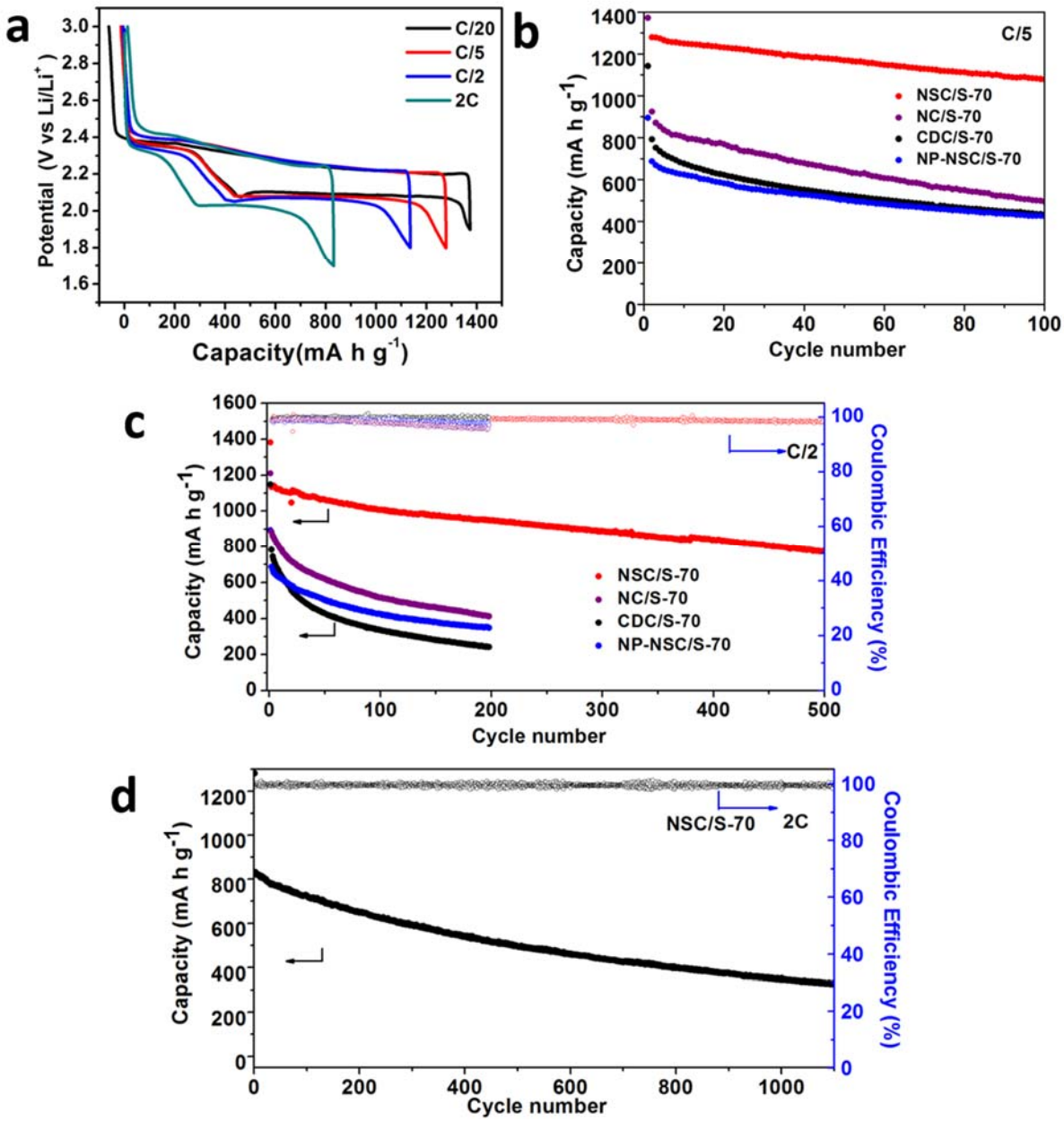

Figure 4.13 a) Voltage profiles of NSC/S-70 electrodes at various C rates b,c) the discharge capacity retention of NSC/S-70, NC/S-70, CDC/S-70 and NP-NSC/S-70 electrodes at b) C/5 and (c) C/2 rates; d) the long-term cycling performance of NSC/S-70 electrode at a high 2C rate, showing Coulombic efficiency on the right y-axis.

At C/5, the capacity of NSC/S-70 stabilized at 1080 mA h g^{-1} at 100 cycles, whereas NC/S-70 fades from 925 mA h g^{-1} to 500 mA h g^{-1} and similarly for CDC/S-70, from 800 mA h g^{-1} to 430 mA h g^{-1} (**Figure 4.13c**). This implies that compared with N-doping, the N, S dual-doping strategy greatly inhibits the LiPS shuttle. At a faster rate of C/2, the NSC/S-70 electrode was able to maintain a high capacity of 775 mA h g^{-1} even after 500 deep cycles with a low decay rate of 0.065% per cycle, whereas the capacity of NC/S-70 and CDC/S-70 faded to 420 mA h g^{-1} to 350 mA h g^{-1} over 200 cycles (**Figure 4.13b**).

The non-porous NSC based electrode (NP-NSC/S-70) also exhibited a slightly slower capacity fade than CDC/S-70, but this is not noteworthy. Compared to porous NSC/S-70, it demonstrates that the high-surface-area porous structure plays an indispensable role in LiPS binding. In order to examine the potential of NSC/S-70 for high-power storage, the electrode was subjected to high rate cycling at a 2C rate. The cell was able to retain 365 mA h g^{-1} after 1100 cycles, with an ultralow capacity fading rate of 0.052% per cycle (**Figure 4.13d)**. This performance was obtained without utilization of novel binders or electrolytes and is amongst the best for carbonaceous sulfur host materials.[38-40,43]

The estimated volumetric capacity of the electrode (including current collector) would be *ca.*120 Ah $L^{-1,}$ based on these values: sulfur specific capacity - 1370 mA h g^{-1}, sulfur loading - 1.5 mg cm^{-2}, electrode thickness - 170 μm (thickness of carbon paper is 120 μm).

To further probe the effectiveness of the chemical interaction on the suppression of the LiPS shuttle, Li-S cells without $LiNO_3$ additive in the electrolyte were also examined. Greatly alleviated first-cycle overcharge (**Figure 4.14a**) and improved average Coulombic efficiency

(~93 % *vs.* 83% for CDC/S-70) was observed for NSC/S-70 (**Figure 4.14b**), demonstrating the effect of the interfacial interaction arising from N,S dual-doping.

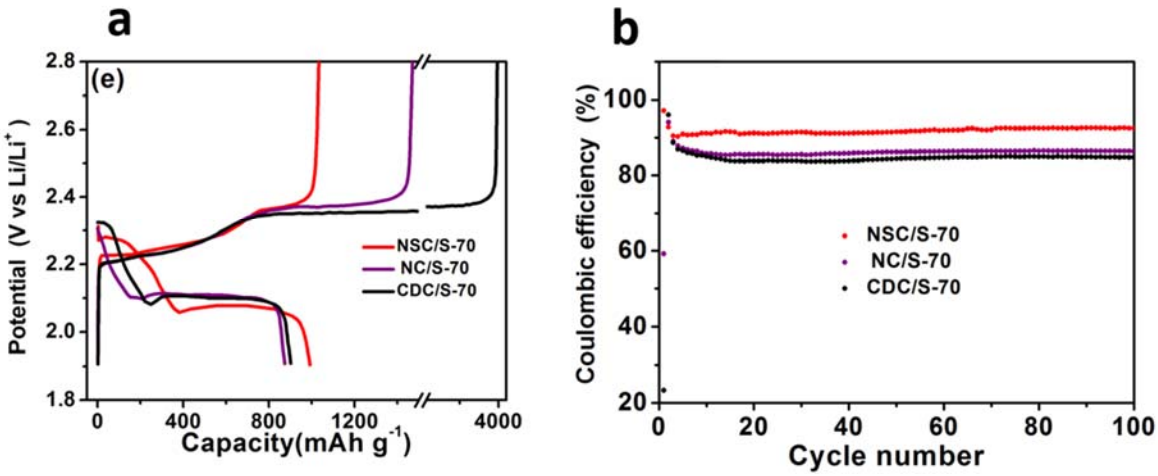

Figure 4.14 a) First-cycle voltage profiles (at a C/20 rate) and b) Coulombic efficiency evolution upon cycling (at a C/2 rate) of NSC/S-70, NC/S-70 and CDC/S-70 electrodes in cells without $LiNO_3$ additive in the electrolyte.

The evolution of positive electrode microstructure and impedance upon cycling was examined to further explore the underlying reason for the more stable cycling exhibited by NSC/S-70. The cycled cells, stopped after 500 cycles at a fully charged status, were dissembled and examined by SEM. **Figure 4.15** shows the electrode morphology of CDC/S-70 and NSC/S-70 (the small particles indicates Super P). After 500 cycles of CDC/S-70, even at a charged status, a glassy layer of Li_2S/Li_2S_2 is evident that coats the upper layers (**Figure 4.15b**). This finding indicates that the LiPS intermediates dissolve, diffuse out from the micro/mesoporous channels and randomly re-deposit on the electrode surface. It verifies that non-polar carbon surfaces are not effective in confining LiPSs over long-term cycling. On the contrary, for the NSC/S-70 electrode (**Figure 4.15d**), the morphology of individual NSC bulk

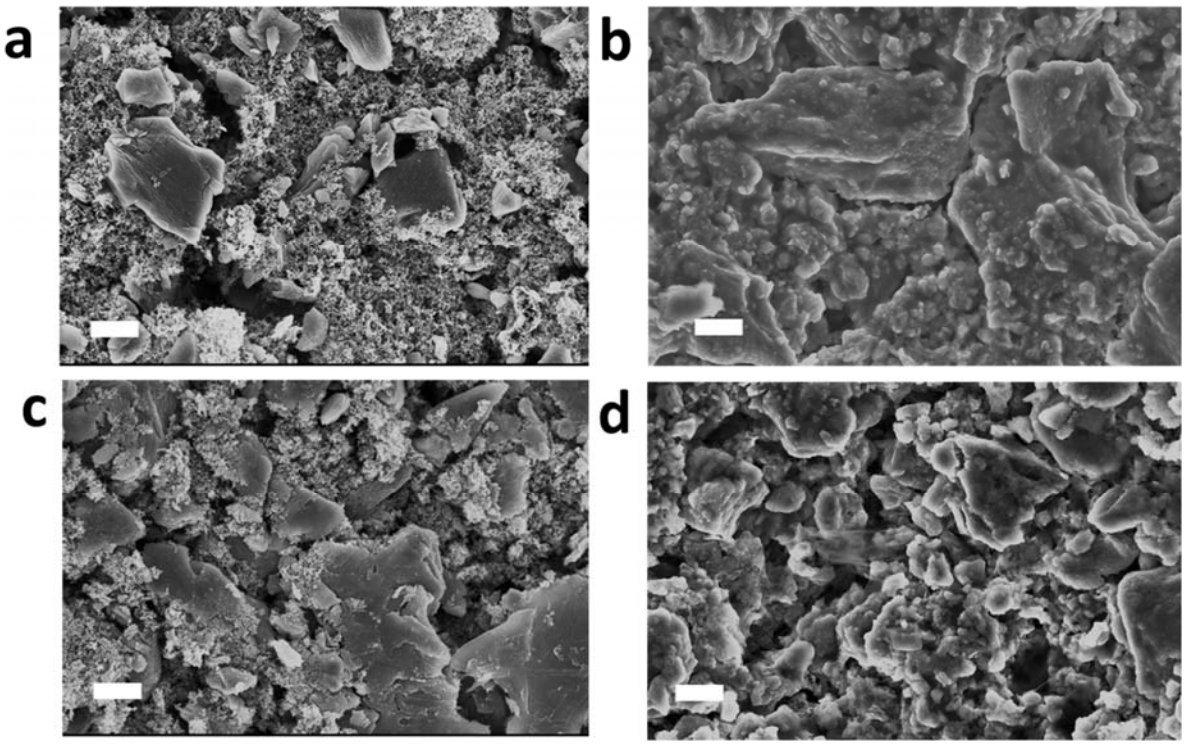

Figure 4.15 SEM images of a,c) pristine electrodes before cycling and b,d) after 500 cycles at charged status for a,b) CDC/S-70 and c,d) NSC/S-70 composites; scale bar, 5 μm. The small particles are the Super P carbon additive.

particles mixed with Super P particles is maintained, demonstrating the effective confinement of LiPSs within the porous structure.

EIS measurement at discharged status provides additional support for this conclusion (**Figure 4.16**). The charge-transfer resistance within the cathode, represented by the semicircle at high-frequency range, dramatically decreases upon first discharge and remains almost unchanged over 10 cycles. The stable charge-transfer resistance is ascribed to inhibited LiPS diffusion and/or confined Li_2S deposition over the electrode.

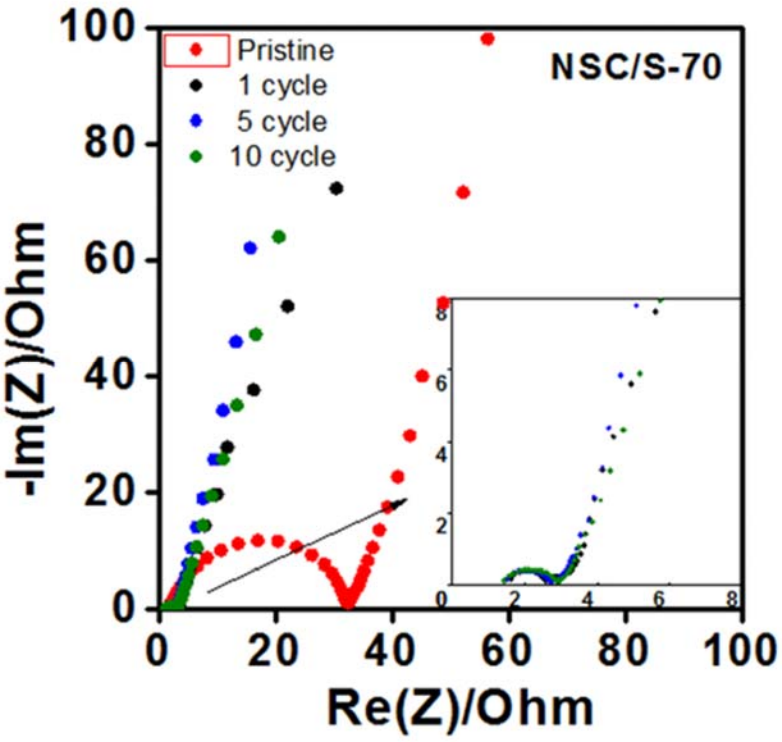

Figure 4.16 Nyquist plots for the NSC/S-70 electrodes before cycling (pristine) and over the first 10 cycles

4.7 Conclusion and Thoughts

In conclusion, nitrogen-sulfur doped nanocarbon, synthesized through the self-templating of sustainable biomaterial-derived cellulose nanocrystals, exhibits a tunable hierarchical pore structure with a high surface area. The dual-doping with N and S atoms on porous carbon greatly enhances the chemisorption of LiPSs. The XPS studies revealed a synergistic effect arising from N-Li and S-S interactions. Both Li^+ and S_n^{2-} are effectively bound to N, S dual-doped carbon, giving rise to doubled LiPS adsorptivity over N single-doped or non-doped carbons. The binding configuration was confirmed by first-principles calculations. This is the first time that a dual-doped carbon has been utilized as a sulfur host material with demonstrated

chemisorption mechanisms. Additionally, the electric conductivity of NSC is also greatly improved compared to non-doped carbon, favoring high-rate kinetics.

Using this dual-doped carbon as a sulfur host, the sulfur electrode was able to deliver a high capacity of 1370 mA h g^{-1} at C/20 and discharge/charge for 1100 cycles at 2C rate with a very low capacity fading of 0.052% per cycle. This is attributed to the high pore volume and surface area of the host that can provide sufficient active sites for chemically adsorbed LiPS.

Chapter 5 A Light-Weight Graphitic Carbon Nitride for Long-Lived Li-S Batteries

5.1 Introduction

In light of the ineffectiveness of physical interactions of non-polar carbons with polar LiPSs - researchers have explored highly modified carbon surfaces in order to more effectively adsorb the LiPSs. Examples of such materials of intrinsic light weight (low-density) include graphene oxide,[36,38] N-doped carbons,[40,46] and N,S-dual doped carbon[130] as described in **Chapter 5**. However, there is a threshold for the N concentration doped in carbon lattices (14.5 atom %).[91] The concentration that has been practically achieved is usually less than 5 %, which places a constraint on the density of active sites for LiPS adsorption.[40,41,43,46] A light-weight sulfur host material that contains a very high accessible fraction of LiPSs chemisorption sites is ideal to realize a long-life and high-loading Li-S battery.

In this Chapter, a strategy of chemically confining the LiPSs in a light-weight polar host material, graphitic carbon nitride (g-C_3N_4) is described. It is a highly ordered polymeric material consisting of continuous tri-s-triazine building blocks, with a structure analogous to layered graphite.[131] The intrinsic high charge polarity of g-C_3N_4 embraces enriched LiPS binding sites (pyridinic N) as demonstrated with first-principles calculations. This provides superior LiPS adsorptivity, which not only leads to controlled precipitation of the discharge product Li_2S upon reduction of LiPSs, but also of the charge product elemental sulfur upon oxidation.[60,62] Additionally, the polymeric nature of g-C_3N_4 allows for structural elasticity that can aid in accommodating the volume expansion upon formation of Li_2S on discharge.[132] Zhang *et al.* has reported using g-C_3N_4 and oxygenated C_3N_4 (o-C_3N_4), prepared by pyrolysis of urea and glucose, as sulfur host materials. This is a different material with a different

perspective than the approach in this Chapter. [133] For the g-C_3N_4 in their report, very low accessible surface area (73 m^2 g^{-1}) was obtained and thus led to fast capacity fading. For the o-C_3N_4, the structure is featured as carbon nitride supported oxygenated carbon, with a low N content of 15-20 wt%. Thus the stable cycling of the sulfur cathode at a lower sulfur content (56 wt%) and low areal sulfur loading was ascribed to the rich oxygen groups, instead of the pyridinic N sites. [133]

5.2 Experimental Approaches

5.2.1 Synthesis of Nanoporous g-C_3N_4

The nanoporous g-C_3N_4 was synthesized using a hard-template approach. Typically, cyanamide and Ludox (AS-30) silica nanoparticle (12 nm) colloid solutions with a cyanamide/SiO_2 weight ratio of 1: 1.5 were mixed by stirring at 60 °C for 6 hours. The as-formed dispersion was dried *in vacuo* at 60 °C for overnight to form the white composite powder. The g-C_3N_4 powder was obtained by thermal condensation of the precursor powder at 550 °C for 4 hours (4 °C/min ramping) and HF (5 wt%) etching. The sample was washed and dried at 90 ºC *in vacuo* before use. Porous N-doped carbon (NdC) was synthesized in the same way, except that polydopamine was used. Polymerization of dopamine was carried out in the presence of tris(hydroxymethyl)aminomethane (Tris) in aqueous solution at 25 °C overnight (w/w 2:1).

The g-C_3N_4/S75 sulfur composite was prepared *via* a melt-diffusion method. The g-C_3N_4 powder was mixed with elemental sulfur in the desired ratio and the mixture was heated under ambient atmosphere at 155 °C for 12 hours.

5.2.2 Electrochemistry Measurements

For the preparation of electrodes with 1.5 mg cm^{-2} sulfur loading, sulfur composites with Super P and PVDF binder were dispersed in DMF with a weight ratio of 7.5: 1.5: 1. For the preparation of electrodes with 3-5 mg cm^{-2} sulfur loading, sulfur composites with Super P, graphene (ACS Materials), SBR aqueous binder, and CMC binder were dispersed in a mixture solvent of deionized water and DMF (2:1 v/v) in a weight ratio of 8: 0.5: 0.5: 0.5: 0.5. The slurry was doctor-blade coated onto carbon paper (AvCarb P50) to prepare the cathodes. The P50 paper was used as purchased without any pre-treatment and cut into 16 cm diameter disks. The electrodes were dried at 60 °C overnight, and assembled into 2325 coin cells in an Ar-filled glovebox. A lithium foil anode and an electrolyte comprising 1 M LiTFSI in a mixture of DME and DOL (v/v = 1:1) was used. A 2 wt% of $LiNO_3$ was added for $LiNO_3$ containing electrolyte. The cells were operated in a voltage window of 1.8-3.0 V (or 1.7-3.0 V, 1.9-3.0 V, depending on rates).

5.2.3 Computational Methods

First-principles calculations were performed using the plane-wave-based VASP code. PAW pseudopotentials were applied to describe electron-ion interactions, and PBE version of the GGA was used for the electronic exchange correlation effect.[86,87] The Li_sv version PAW potential was used for Li atoms. A cut-off energy of 500 eV was used for the plane wave basis to ensure convergence. Spin-polarized calculations were employed. Li_2S, Li_2S_2 and Li_2S_4 were employed as the representative LiPSs. A single-layer graphene of a 6×6 supercell size was adopted as the platform for pristine and N-doped carbon (graphitic). Varied numbers of pyridinic nitrogen atoms per supercell (1~3) were incorporated to model the doped carbon. For

modeling g-C_3N_4, a 2×2 supercell size was used to achieve the same supercell size for both graphitic carbon and g-C_3N_4. A vacuum layer of 15 Å was used in the vertical direction in order to exclude the interaction between the layer and its images. The conjugate-gradient algorithm was used for ionic relaxation. The binding energy (E_{bind}) of Li_2S_2 on the substrates is defined as

$$E_{bind} = (E_{sub} + n\,E_{ps} - E_{sub+ps})/n$$

where E_{sub}, E_{ps} and E_{sub+ps} represent the ground-state energies of the substrate, respective polysulfide and substrate-polysulfide and n is the number of respective polysulfide employed per supercell. A larger positive value is indicative of greater binding ability.

5.3 Physical Characterizations of g-C_3N_4

Nanoporous g-C_3N_4 was synthesized by polycondensation of cyanamide (CN_2H_2) based on a hard-template approach,[131] as shown schematically in **Figure 5.1a**. Upon heat treatment of cyanamide at 550 °C, graphitic C_3N_4 is formed *via* a step-wise condensation of the melamine units with the release of NH_3 gas; g-C_3N_4 is reported to be thermally stable up to 600 °C under air. The graphitic nature of g-C_3N_4 is confirmed by its XRD pattern (**Figure 5.2a**), where the two reflections at 27.6° and 13.1° correspond to the interlayer stacking (002) and in-plane (100) repeating motifs of the tri-s-triazine network (see **Figure 5.1a**).

The chemical structure of g-C_3N_4 was confirmed by FTIR (**Figure 5.2b**). The bands at 810 cm^{-1}, 1200-1600 cm^{-1} and 3200 cm^{-1} correspond to the s-triazine units, the tri-s-triazine units and the residue surface amino groups, respectively.[134] XPS studies provide detailed information on the chemical environment of the N and C sites. The N 1s spectrum (**Figure 5.1b**) shows three N components, of which the major is pyridinic N (398.2 eV) and two others are tertiary nitrogen in N-$(C)_3$ groups (399.8 eV) and amino groups (400.8 eV). The

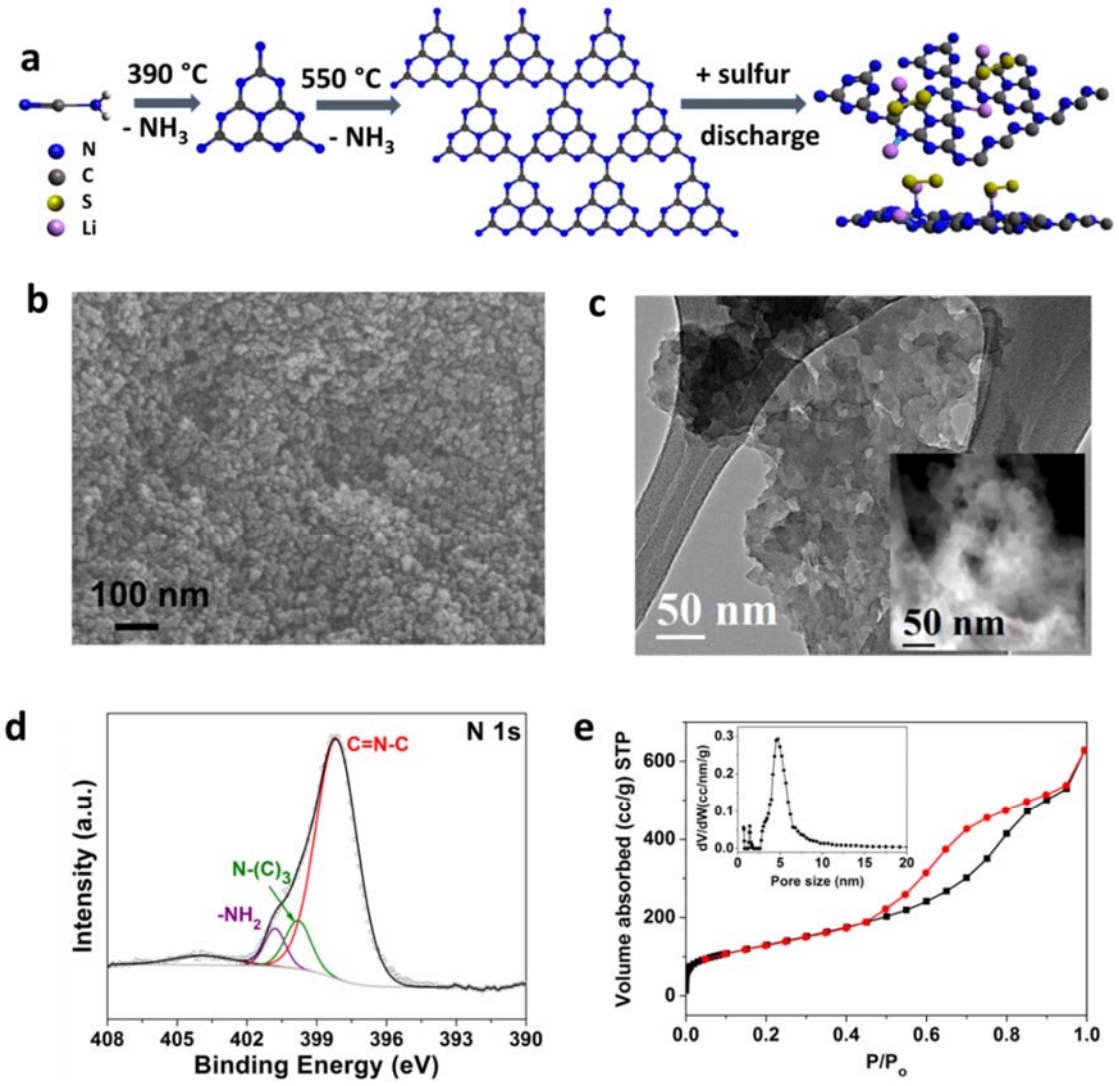

Figure 5.1 a) Schematic illustration of the synthesis of g-C_3N_4 by step-wise polycondensation from cyanamide and its interaction with lithium polysulfides as shown by first-principles calculations; b) high-resolution XPS N 1s spectrum, c) N_2 adsorption/desorption isotherm (inset: pore size distribution), d) SEM image and e) bright-field (inset: dark-field) TEM of as-synthesized g-C_3N_4.

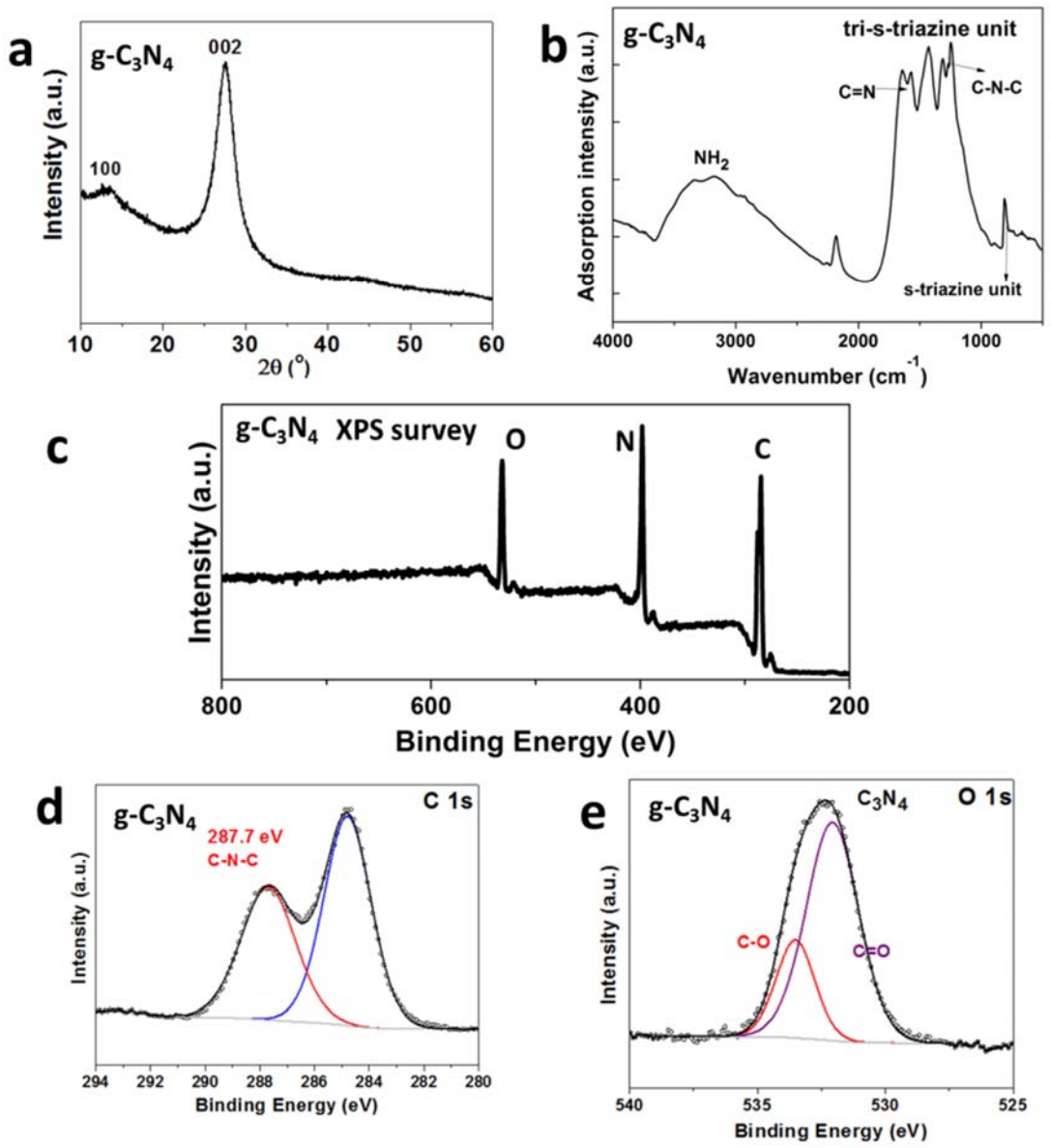

Figure 5.2 Characterization of g-C_3N_4: a) XRD pattern; b) FTIR spectrum; c) XPS survey spectrum showing the C,N and O contributions ; high-resolution XPS d) C 1s and (e) O 1s spectra.

corresponding C-N-C component (287.7 eV) is observed in the C 1s spectrum (**Figure 5.2d**), where the peak at 284.8 eV is attributed to adventitious carbon. The O 1s spectrum (**Figure 5.2e**) suggests that the g-C_3N_4 also contains surface oxygen groups (C=O and C-O) formed by exposure of dangling bonds on the surface to ambient atmosphere. It is noted that both surface amino and oxygen groups are reported to bind LiPSs/Li_2S species to some extent, which adds to the advantages of the g-C_3N_4 material.[39, 135] This concept has been employed in the fabrication of the microporous oxygenated carbon nitride prepared by a completely different route, which contains about four-fold less nitrogen in the structure.[133]

The SEM image (**Figure 5.1d**) of g-C_3N_4 reveals a morphology of interconnected nanoparticles with inter-particle pores. This is confirmed by the bright and dark field TEM images (**Figure 5.1e**), where disordered pores are evident, evenly distributed over the

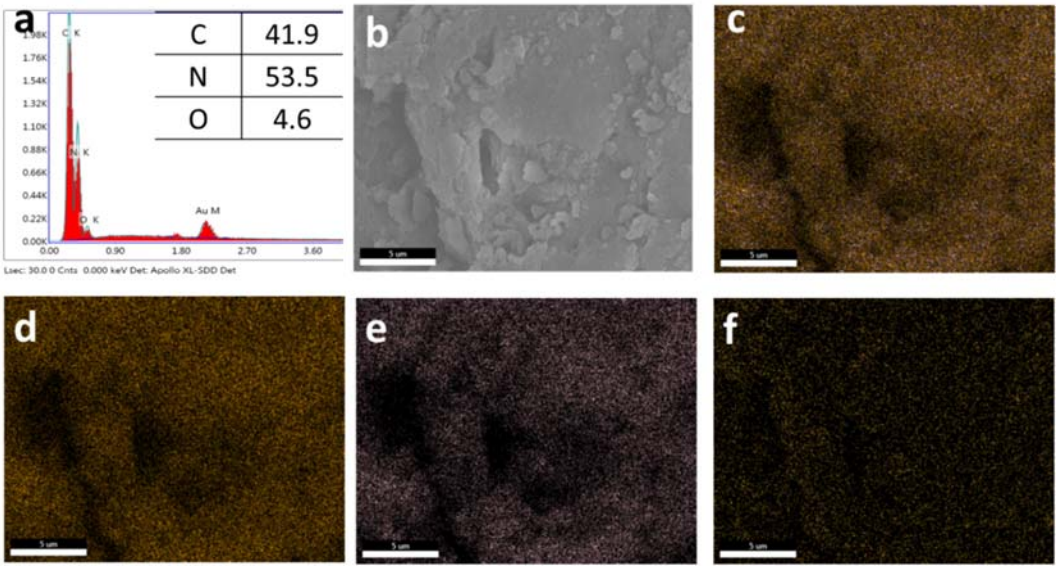

Figure 5.3 a) The EDX spectrum of g-C_3N_4 with the inset table showing the elemental composition in atomic ratio; b) the low-magnification SEM image of g-C_3N_4, showing the bulk monolith architecture; c- f) EDX mapping of the combined elements c), C d), N e) and O f) on the area in b), respectively. The scale bars are 5 µm.

framework. Nitrogen absorption/desorption measurement confirms that the nanostructured g-C_3N_4 consists of mostly mesopores (~ 5 nm), and some micropores formed by SiO_2 nanoparticle templating and NH_3 gas evolution upon condensation (**Figure 5.1c**). A high BET surface area of 615 m^2 g^{-1} with a pore volume of 0.97 cm^3 g^{-1} is achieved.

The EDX mapping (**Figure 5.3**) shows a uniform distribution of C and N, with a nitrogen concentration of 53.5 at%. This value is more than ten-fold higher than that of most reported N-doped carbons.[40,43,130] The high nitrogen concentration and surface area is crucial for interface-based LiPS binding. To illustrate this, a N-doped carbon (NdC) synthesized using a similar hard-template approach, and a commercial carbon - Vulcan carbon™ (VC) - were again used as comparisons in this study. The NdC contains pyridinic N, pyrollic N and graphitic N, with a total nitrogen concentration of 3.1 at% (**Figure 5.4a,b**). The NdC and VC

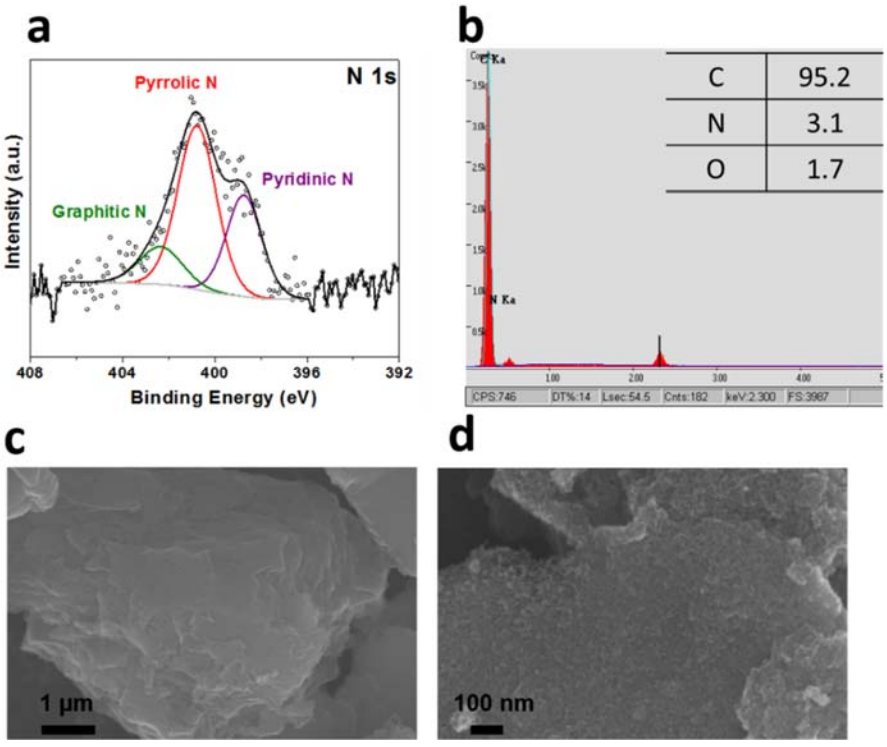

Figure 5.4 a) High-resolution XPS N 1s spectrum and b) EDX spectrum (inset: element atomic compositions), c ,d) SEM images of the as-synthesized N-doped carbon (NdC).

also exhibit nanoparticle morphology as shown in **Figure 5.4c,d**. The BET surface area (and pore volume) of NdC and VC are 922 m^2 g^{-1} (1.42 cm^3 g^{-1}) and 260 m^2 g^{-1} (0.87 cm^3 g^{-1}), respectively.

5.4 Spectroscopic Studies on the Chemical Interaction with Polysulfides

The adsorptivity of the host materials towards LiPSs was quantified using a potentiostatic titration method by measuring the residual LiPS concentration upon contact with the respective host materials in an ether-based solution. The adsorptivities of g-C_3N_4, NdC, VC, a commercial mesoporous TiO_2 (meso-TiO_2) and Super P were evaluated (**Figure 5.5a**). The NdC adsorbs twenty fold LiPS compared to that of VC or Super P (comparable to meso-TiO_2) while g-C_3N_4 adsorbs almost twice that of NdC (*i.e.*, 4.25 mg of polysulfide per 10 mg of material) even with a 33% lower surface area. This demonstrates the beneficial effect of the increased fraction of pyridinic N active sites.

The underlying principle responsible for the superior LiPS adsorptivity of g-C_3N_4 was investigated using FTIR and XPS. The spectrum of the g-C_3N_4/Li_2S_4 solid powder recovered from the titration contact experiment described above was compared to that of g-C_3N_4 and Li_2S_4 alone. Li_2S_4 exhibits a prominent FTIR peak at 1620 cm^{-1}, corresponding to a Li-S vibrational mode. The spectrum of g-C_3N_4/Li_2S_4 exhibits a slight red shift of the tri-s-triazine band that lies between 1200-1600 cm^{-1} (corresponding to the vibration of the tri-s-triazine units), that is ascribed to interaction with Li_2S_4 (**Figure 5.5b**). A new peak at 1000 cm^{-1} was observed for g-C_3N_4/Li_2S_4, suggesting the existence of interaction of the two components which can change the local symmetry and result in the enhancement (or suppression) of vibrational modes.

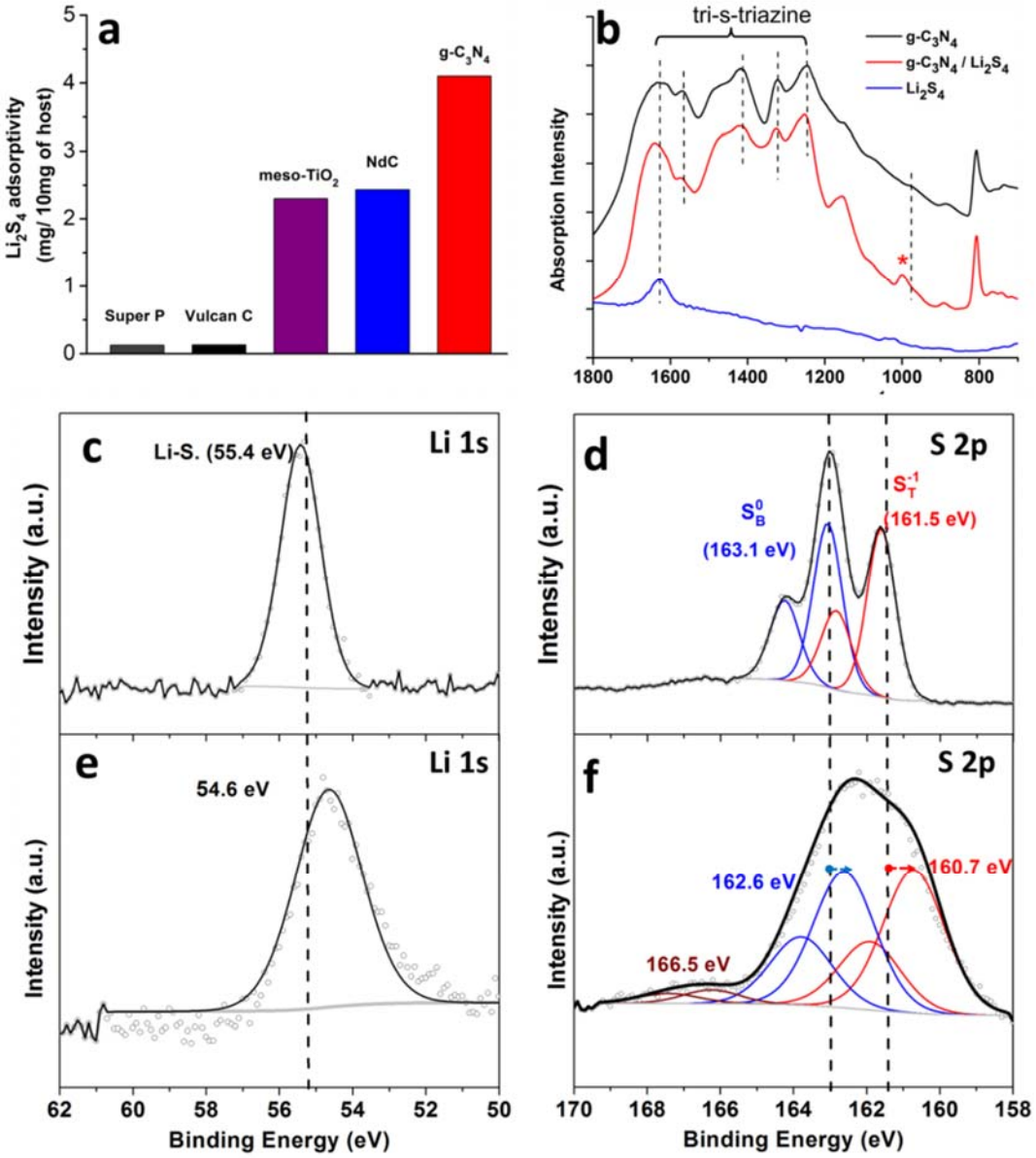

Figure 5.5 a) The polysulfide (Li_2S_4) adsorptivity of g-C_3N_4 and NdC, with comparison to Super P, VC, and a mesoporous TiO_2, as evaluated by the electrochemical titration method; b) FTIR spectrum of g-C_3N_4, g-C_3N_4 /Li_2S_4 and Li_2S_4, with the dotted lines and asterisk respectively showing the peak shifts and new peak for g-C_3N_4 /Li_2S_4; c) high-resolution XPS (c, e) Li 1s, (d, f) S 2p spectra of (c, d) Li_2S_4 and (e,f) g-C_3N_4 /Li_2S_4.

The XPS studies provide even better insight into the interaction. The Li 1s spectrum of Li_2S_4 consists of one Li-S component at 55.4 eV (**Figure 5.5c**), which shifts down to 54.6 eV upon contact with g-C_3N_4. The downward shift indicates electron transfer to Li^+ from the electron-rich pyridinic $N^{\delta-}$ groups (**Figure 5.5e**). The observed Li-N interaction is consistent with a recent report.[136] For the S 2p spectrum, Li_2S_4 shows two components that correspond to terminal sulfur S_T^{-1} and bridging sulfur S_B^0 at 161.5 eV and 163.1 eV, respectively (**Figure 5.5d**).[60] The S 2p spectrum exhibits $2p_{1/2}$ and $2p_{3/2}$ doublets due to the splitting of 2p energy levels, and only the peak positions of $2p_{3/2}$ components are cited here. Upon contact with g-C_3N_4, the S 2p spectrum shifts by more than 0.5 eV towards lower binding energy, with the S_T^{-1} affected more than the S_B^0 (**Figure 5.5f**). This shows that the terminal sulfide groups acquire a more negative charge as a result of charge polarization; a finding confirmed by first-principles calculations discussed in the next section. Very minor components at 166-169 eV in g-C_3N_4/Li_2S_4 are due to the thiosulfate and polythionate species formed by reaction between Li_2S_4 and the residual surface oxygen functional groups, as we reported for graphene oxide.[72]

5.5 Computation on the Chemical Interaction with Polysulfides

To fully understand the nature and strength of the interaction of g-C_3N_4 with LiPSs, first-principles calculations based on the DFT framework were performed. In order to quantitatively compare the substrates in terms of their ability to bind LiPSs, the g-C_3N_4 and doped/pristine carbons were respectively modeled by a monolayer 2×2 g-C_3N_4 and a 6×6 graphene supercell, creating the same substrate supercell size (only 4.0% difference).[137] The number of pyridinic N atoms per supercell was varied (0, 1, 2, 3) to model the N-doped carbon and achieve different N concentrations (0%, 1.4%, 2.9%, 4.4%, here denoted as N0C, N1C, N2C, N3C). The Li_2S_2 molecule was first used as the representative polysulfide. The number of Li_2S_2 molecules

adsorbed on the substrates was varied to quantify the Li_2S_2 binding capacity of the respective substrate. Additionally, long-chain Li_2S_4 and the end-member Li_2S (2 molecules per supercell) were also examined (see **Table 5.1**).

Table 5.1 Summary of binding energy for different polysulfides on the surface of pristine carbon (N0C), doped carbons (at different concentrations) and g-C_3N_4 (Average value of binding two polysulfide molecules per supercell is used).

$\mathbf{E_b}$ (eV)	N0C	N1C	N2C	N3C	g-C_3N_4
Li_2S	0.47	0.73	1.83	1.55	4.08
Li_2S_2	0.51	0.63	0.84	1.57	1.73
Li_2S_4	0.06	0.40	0.42	0.54	1.70

The charge density distribution maps of the host substrates are shown in the top panels of **Figure 5.6a-c** and **Figure 5.7b,c**. The pristine carbon (N0C) shows a uniform distribution of the charge over the carbon lattice (**Figure 5.6a**), whereas the pyridinic N in N-doped carbon bears negative charge (electron-rich), represented by the red electron density contour curves (**Figure 5.6b, Figure 5.7b,c**). Similarly, for all the N positions in g-C_3N_4, the N atoms bear a negative charge as expected (**Figure 5.6c**). The most stable geometrical configuration of the respective substrates - binding 2 Li_2S_2 per supercell - are representatively shown in **Figure 5.6a-c** and **Figure 5.7b,c**. The binding energy values are normalized by the number of Li_2S_2 adsorbed (**Figure 5.6d**).

There is no specific bonding of Li_2S_2 with the pristine carbon substrate (**Figure 5.6a**), consistent with its low binding energy of 0.51 eV. For both N-doped carbon N3C and g-C_3N_4,

the Li_2S_2 is bonded to the substrates *via* a favorable Li^+-$N^{\delta-}$ bond, indicated by the shortened bond distance (the average Li-N bonding is 2.14 Å and 2.06 Å, respectively, as compared to

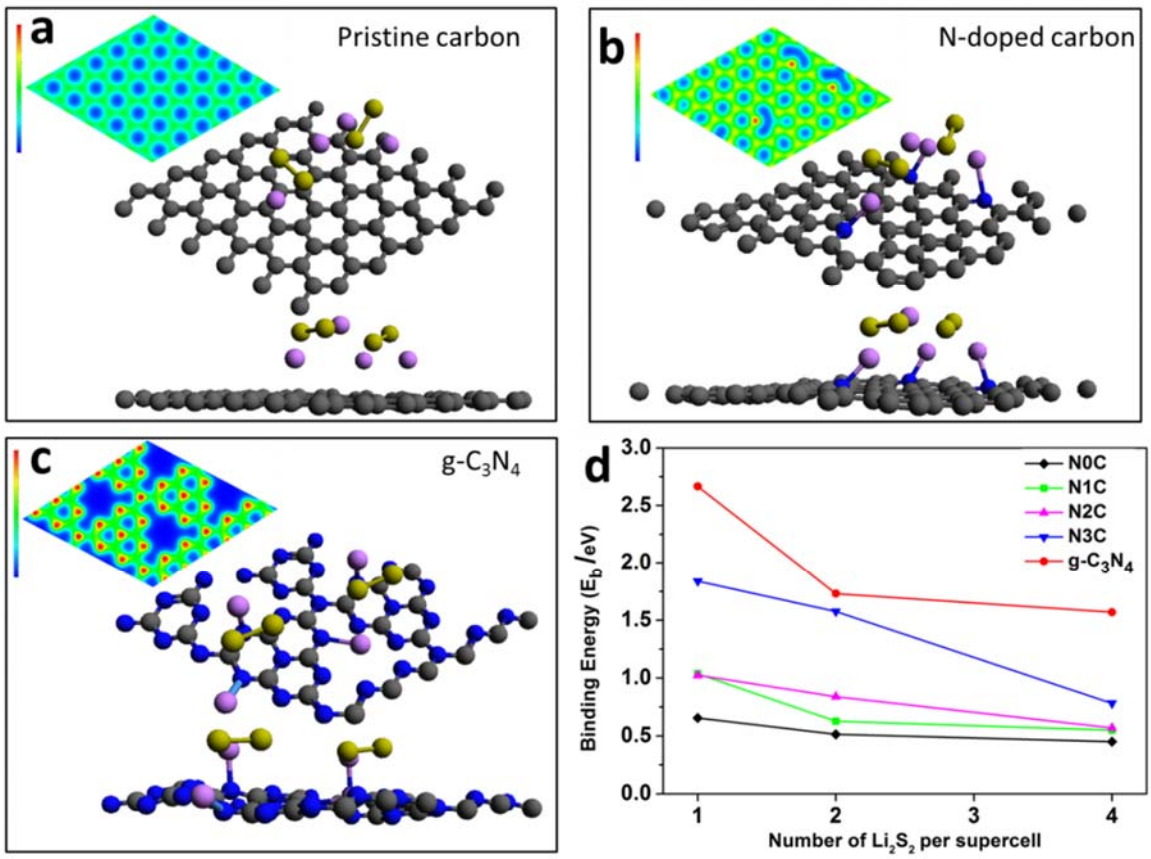

Figure 5.6 First-principles calculations representatively illustrating the most stable binding configurations, after full relaxation, of 2 Li_2S_2 molecules on a) pristine carbon, b) N-doped carbon (3 N atoms, N3C), c) g-C_3N_4 substrates (bottom panels for side views); insets on top left are the 2D deformation charge distributions of the corresponding substrates without Li_2S_2 (red for accepting electrons, blue for donating electrons). Grey, blue, purple and yellow balls represent C, N, Li and S atoms, respectively; d) the variations of the binding energy of Li_2S_2 molecules (per Li_2S_2) binding to the respective substrates, with respect to the number of Li_2S_2, as calculated by Bader charge analysis.

2.46 Å of Li-C for pristine carbon, **Figure 5.6b, c**). This is further confirmed by the geometries of g-C_3N_4 binding 1 or 4 Li_2S_2 molecules shown in **Figure 5.7e,f**. More importantly, it was clearly observed that charge transfer (by Bader charge analysis) onto the S_2^{2-} cluster occurs upon contact with the substrate (**Figure 5.7**), further lending support to the XPS S 2p studies discussed above. The calculated amount of charge transfer of Li^+ ions is too small to measure, due to the few valence electrons included in the pseudopotential models.

For general comparison, the variation of the binding energy values with respect to the N concentration in doped carbons and g-C_3N_4 is shown in **Figure 5.6d**. The superior binding ability of g-C_3N_4 is even more apparent at high concentrations of Li_2S_2. This is because g-C_3N_4 has more pyridinic N active sites available for adsorption, whereas N-doped carbon does not, as shown for the N3C binding of 4 Li_2S_2 molecules in **Figure 5.7d**. The charge transfer number for S_2^{2-} clusters shows the same trends with the binding energy values (**Figure 5.7**a).

The binding strength of the end discharge product Li_2S shows the same trend with Li_2S_2 - the binding energy increases with increasing concentration of doped N, with the g-C_3N_4 exhibiting the highest binding energy of 4.08 eV (**Table 5.1**). For the large molecule Li_2S_4, the binding energy on doped carbons is higher than that on pristine carbon, although the values for Li_2S_4 are relative lower than the respective values for Li_2S, consistent with what is reported in Ref. 107. However, due to the easy accessibility of N active sites on g-C_3N_4, the binding energy for Li_2S_4 is still as high as 1.70 eV. Thus it is believed that the high N concentration of 53.5 at% in g-C_3N_4 - along with its very high surface area - contributes to its high LiPS adsorptivity. Based on the back-of-the-envelope calculation below, it is shown that the 53.5 at% N concentration is sufficient to adsorb all the polysulfide of a sulfur cathode containing 75 wt% of sulfur.

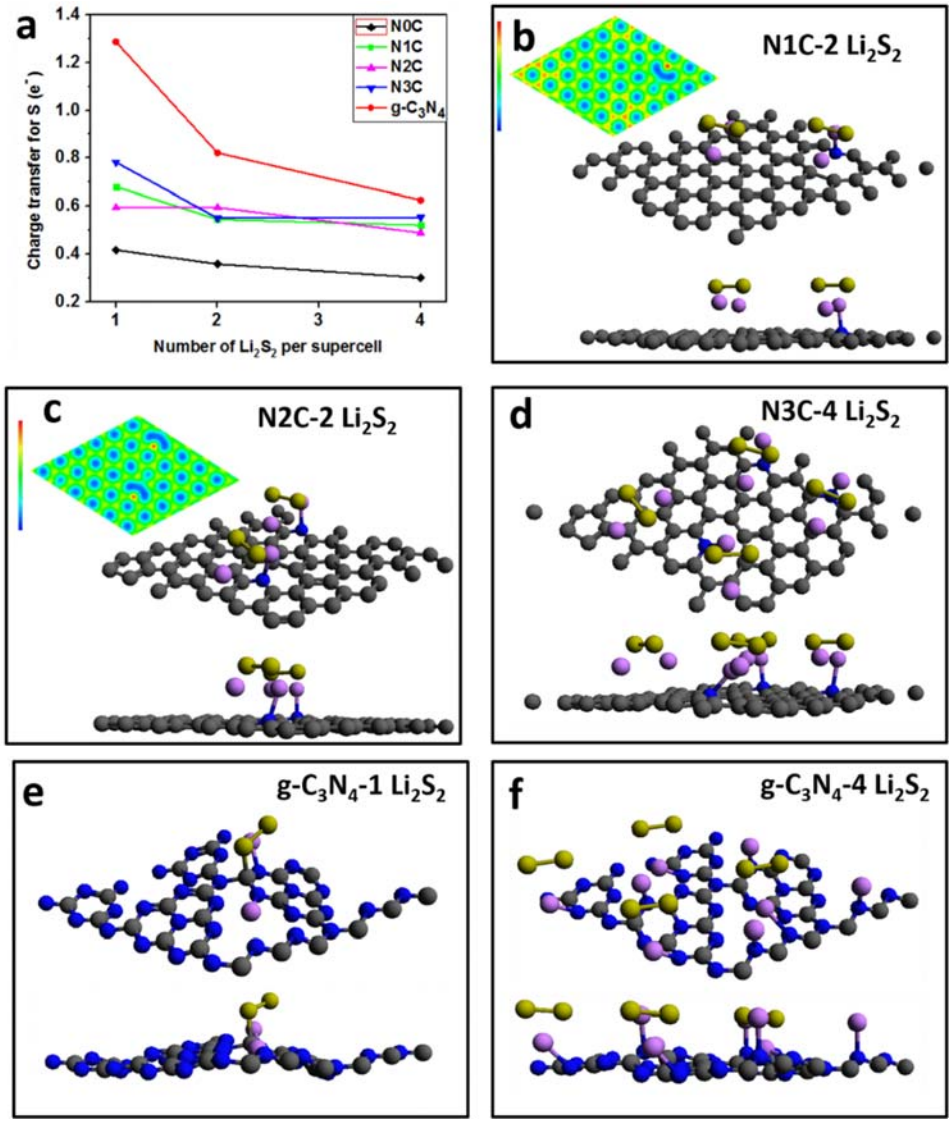

Figure 5.7 a) Plot showing the variation of charge transfer onto S_2^{2-} anion clusters (per anion) upon interaction with the respective substrates, with respect to the number of Li_2S_2 as calculated by Bader charge analysis; b-f) the most stable binding configurations of variable numbers of Li_2S_2 molecules on the respective substrates, as indicated on the top right (bottom panels for side views); Insets on top left of b, c) are the 2D deformation charge distributions of the corresponding substrates without Li_2S_2 (red for accepting electrons, blue for donating electrons).

Using the starting polysulfide Li_2S_8 as the representative, in 1 g of g-C_3N_4/S composite containing 75 wt% of sulfur, the mole of N sites is:

$$1\ \mathrm{g} * 25\% * \frac{53.5\%}{53.5\% * 14 g/mol + 41.9\% * 12 g/mol + 4.6\% * 16 g/mol} = 0.010\ mol;$$

and the mole of Li_2S_8 molecule possible generated is:

$$1\ \mathrm{g} * 75\% * \frac{1}{8 * 32\ g/mol} = 0.003\ mol;$$

Therefore, the mole of N active sites is over 3 fold greater than the maximum mole of Li_2S_8 molecules possibly generated; this shows that the N concentration of 53.5 at% is sufficient for polysulfide absorption, given the dynamic nature of polysulfide creation and consumption as redox progresses, and assuming all N sites are accessible.

5.6 Electrochemical Performances of Thin Electrodes

Sulfur electrodes were fabricated to evaluate the practical effects of high N concentration and superior LiPSs adsorptivity for the g-C_3N_4 on the cycling performance of a Li-S cells. Sulfur composites with 75 wt% sulfur were prepared by melt-diffusion method for g-C_3N_4, NdC and VC, denoted as g-C_3N_4/S75, NdC/S75 and VC/S75, respectively. TGA curve confirms the sulfur fraction (**Figure 5.8**). First, cells with a typical sulfur loading of 1.5 mg cm^{-2} and an electrolyte/sulfur ratio of 15: 1 (uL/mg) were examined in galvanostatic mode to enable comparison with previously published work; [60,62,130] higher loading cathodes are described in the next section. All Li-S cells were cycled at a slow C/20 rate for the first cycle to enable electrode conditioning prior to increasing the rate for the duration of cycling. Cells constructed with g-C_3N_4 alone as a cathode *vs.* Li metal exhibit no electrochemical redox reaction during the 1.8-3 V (*vs.* Li/Li^+) window, contributing to a negligible capacity of only ~1 mA h g^{-1}

(**Figure 5.9**). This confirms that the as-synthesized g-C_3N_4 does not participate in the redox reaction during the cycling of a Li-S cell.

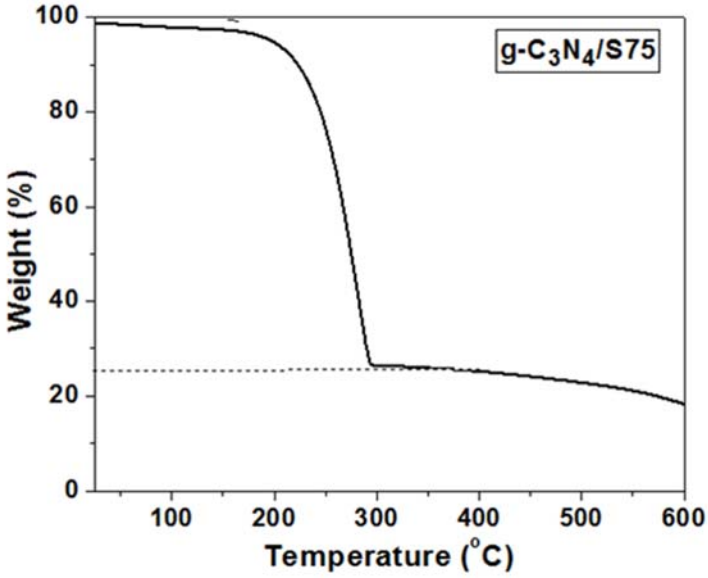

Figure 5.8 TGA curve of the g-C_3N_4/S75 composite under a N_2 atmosphere, with a ramp rate of 10 °C/min.

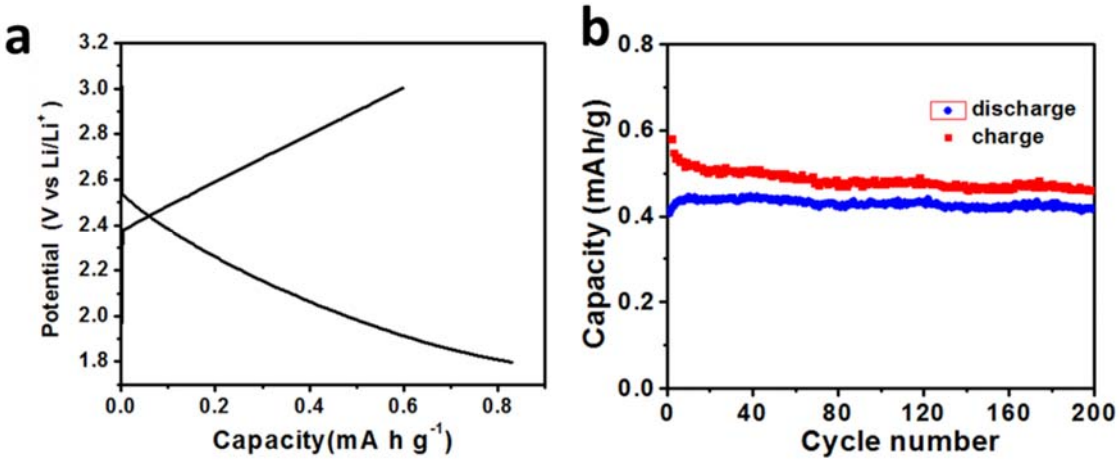

Figure 5.9 a) The voltage profile and b) cycling performance of the electrodes made from g-C_3N_4 without sulfur at a rate of 83 mA g^{-1}.

Figure 5.10a shows the first-cycle galvanostatic voltage profiles of g-C_3N_4/S75 electrode at variable rates, which exhibit typical two-plateau discharge curves. A high discharge capacity of 1170, 900, 855 and 785 mA h g^{-1} (based on the mass of sulfur) was achieved at C/20, C/5 and C/2 and C rates, respectively. The specific capacity reported here is slightly lower than for other electrodes we have reported,[60] due to the semiconducting nature of g-C_3N_4 with poor conductivity.[138] However, the addition of 15 wt% Super P carbon in the electrode guarantees good rate capability, as indicated by the negligible polarization increase upon increasing the rate.

Cycling tests at different rates (C, C/2, C/5) of the g-C_3N_4/S75 electrodes all show only a slight capacity loss over 200 cycles (**Figure 5.10b**). For example, a discharge capacity of 730 mA h g^{-1} that corresponds to 93% of the initial capacity was retained over 200 cycles at a C rate. Long-term cycling of the electrodes was carried out to demonstrate the superior life-time of g-C_3N_4 over N-doped/pristine carbon based electrodes. At a practical intermediate current density corresponding to C/2 (**Figure 5.10d**), an ultra-low capacity fade rate of 0.04% per cycle for 1500 cycles was achieved over three months cycling for the g-C_3N_4/S75 electrode at C/2, while the NdC/S75 and VC/S75 electrodes faded rapidly to low capacities of 280 mA h g^{-1} over 500 and 150 cycles, respectively.

Lower rate C/5 cycling was thus also examined (**Figure 5.10c**). The g-C_3N_4/S75 electrode retained 620 mA h g^{-1} capacity after 500 cycles, corresponding to a capacity fade rate of 0.06% per cycle, whereas NdC/S75 and VC/S75 electrode cells both experienced very rapid capacity fading. It is noted that the as-prepared g-C_3N_4/S75 electrode shows far superior cycling performance compared to the previously reported oxygenated carbon nitride-based cathodes(*i.e.* 0.10% fade per cycle over 500 cycles, with only 56 wt% sulfur content).[133]

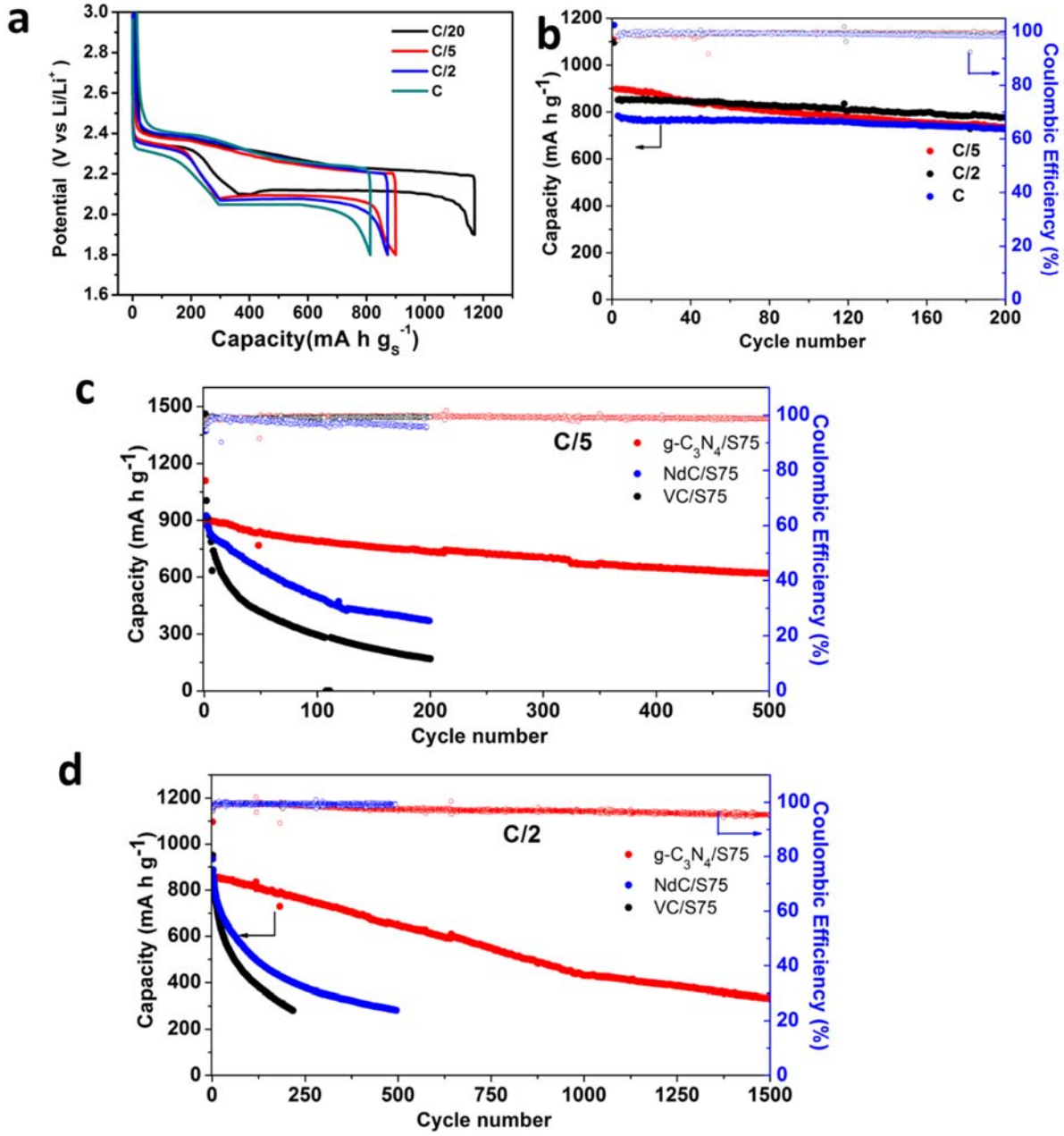

Figure 5.10 a) First-cycle voltage profiles of g-C_3N_4/S75 electrodes at various C rates; b) the discharge capacity retention of g-C_3N_4/S75 at C/5, C/2 and C rates for 200 cycles; c, d) the long-term cycling performance of g-C_3N_4/S75, NdC/S75 and VC/S75 electrodes at (c) C/5 and (d) C/2 rates. Coulombic efficiency is shown on the right y-axis.

To further probe the effectiveness of the chemical interaction of g-C_3N_4 on the inhibition of the LiPS shuttle, C_3N_4/S75 cells identical to those above were run in a $LiNO_3$-free electrolyte. **Figure 5.11** shows that almost negligible first-cycle overcharge was observed for the g-C_3N_4/S75 electrode. This is in sharp contrast to the very significant overcharge exhibited by both NdC/S75 and VC/S75 along with low coulombic efficiencies of 76% and 25%, respectively. Much higher average coulombic efficiency for the g-C_3N_4/S75 cell was obtained over 100 cycles compared to NdC/75 (~92% *vs.* ~81%), indicative of a significantly reduced polysulfide shuttle.

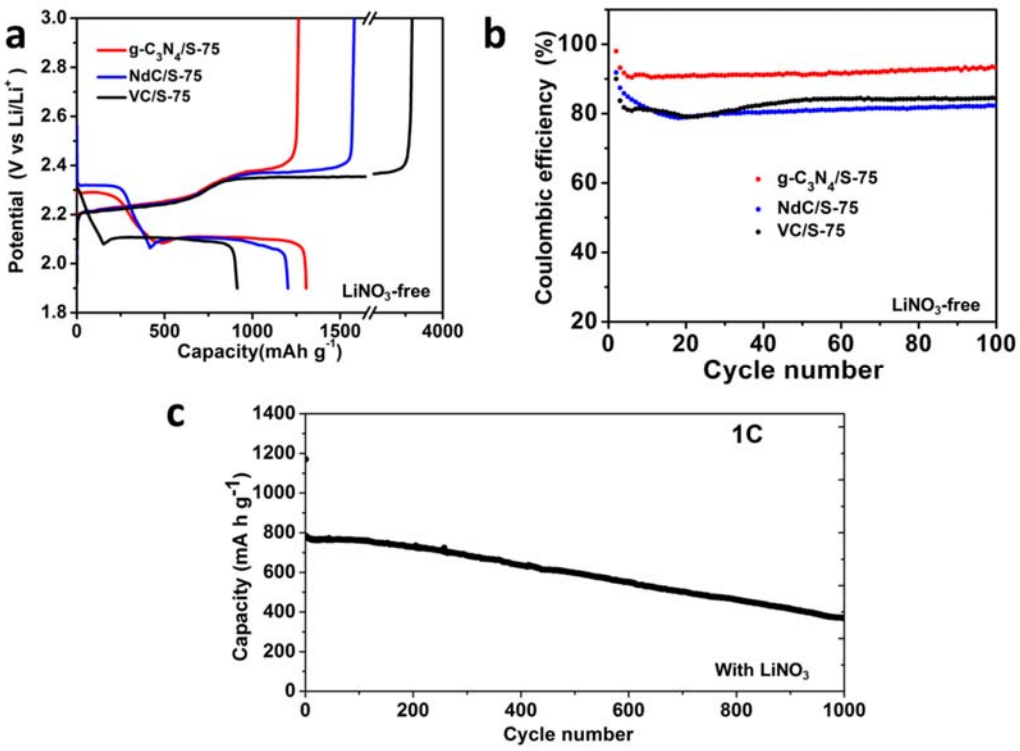

Figure 5.11 a) First-cycle voltage profiles and b) evolution of CE of sulfur cathodes in $LiNO_3$-free electrolyte. CE is calculated as the ratio of the discharge capacity of N^{th} cycle over the charge capacity of N-1^{th} cycle (the 1^{st} cycle CE is disgarded). c) High-rate cycling performance of the g-C_3N_4/S75 electrode in $LiNO_3$-containing electrolyte at 1C for 1000 cycles.

In order to evaluate the potential of g-C_3N_4/S75 electrodes in high-power energy storage applications, the electrode was also subjected to high rate cycling at a C rate (**Figure 5.11c**). A discharge capacity of 370 mA h g^{-1} was retained over 1000 cycles with a fade rate of 0.05% per cycle, indicative of very good rate capability. The morphology of an electrode after 200 cycles at discharged state was examined. No glassy Li_2S layer is evident on the cathode surface (**Figure 5.12a**), nor on the individual bulk monoliths, which is further evidence of effective confinement of polysulfides within the porous cathode.

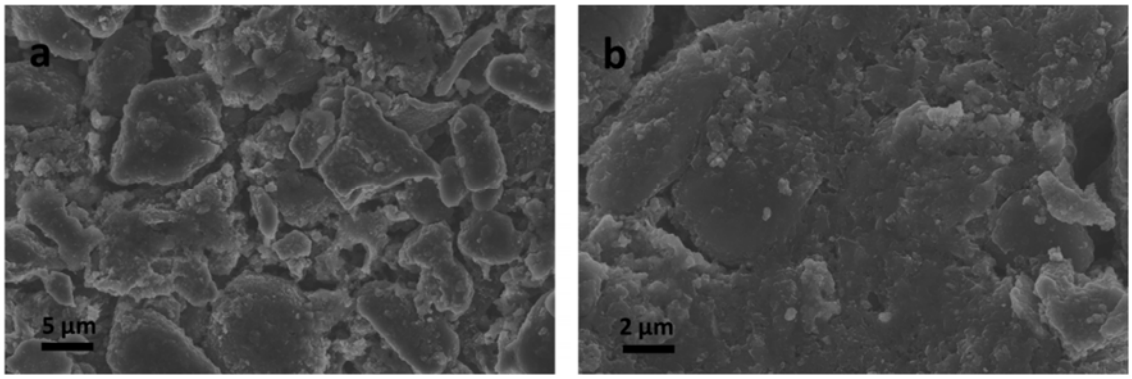

Figure 5.12 a) Low-magnification and b) high-magnification SEM images of the g-C_3N_4/S75 electrode after 200 cycles at a C rate; fully discharged status.

5.7 Electrochemical Performances for High-Loading Cathodes

Achieving high sulfur loading is critical in order for a high areal capacity and volumetric energy density.[103,139] Compared with traditional graphene nanosheets- or carbon nanospheres-based sulfur composites, the bulk monolithic architecture of g-C_3N_4 – that nonetheless still contains highly interconnected nanoporous channels – allows better particle packing, and thus thicker electrodes to be fabricated.[41,103] Here, thick electrodes were prepared at different sulfur loadings (3 - 5 mg cm^{-2}, thickness: 90 – 150 µm), with the addition of 5 wt% of graphene (total

carbon additive being 10 wt%) for slurry preparation. The graphene additive was used to create a 3D electron conducting pathway and to promote electrolyte wetting across the thick electrodes.[103] This was successful as demonstrated by the negligible variation in the voltage polarization for electrodes with different loadings (**Figure 5.13a**).

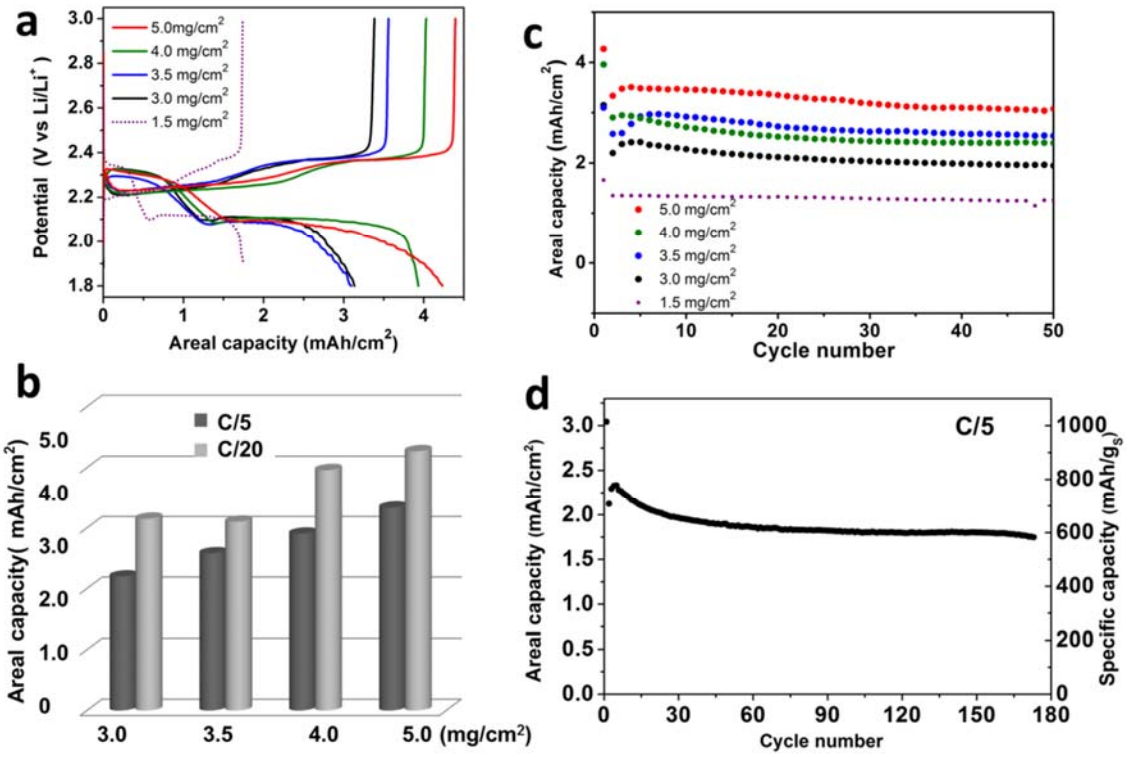

Figure 5.13 a) First-cycle voltage profiles of g-C_3N_4/S75 high-loading thick electrodes with sulfur loadings of 3 - 5 mg cm^{-2} at C/20, as compared with the 1.5 mg cm^{-2} loading electrode; b) a summary of the areal discharge capacity of g-C_3N_4/S75 thick electrodes at C/5 and C/20; c) the areal discharge capacity retention of g-C_3N_4/S75 electrodes at C/5 for 50 cycles; d) the cycling performance of a 3.0 mg cm^{-2} loaded g-C_3N_4/S75 thick electrode at C/5 (1.0 mA cm^{-2}).

All high loading cells were conditioned by cycling at C/20 for the first cycle. As shown in **Figure 5.13b**, an areal discharge capacity of 3.15 mA h cm^{-2} was achieved at C/20 for a 3.0 mg cm^{-2} electrode, which increases to 4.27 mA h cm^{-2} for the 5.0 mg cm^{-2} loading. The cycling performance for the thick electrodes at C/5 is displayed in **Figure 5.13c**, where all electrodes show very stable cycling. The longer-term cycling of the 3.0 mg cm^{-2} electrode shows extremely stable cycling following the first 20 cycles of conditioning (**Figure 5.13d**). The areal capacity of 4.27 mA h cm^{-2} (at a rate of 0.42 mA cm^{-2}) or 3.35 mA h cm^{-2} (1.67 mA cm^{-2}) reported here (**Figure 5.13b, c)** is rather high for slurry-derived electrodes, especially considering that I am able to show outstanding cycling stability over 175 cycles.

5.8 Conclusion and Thoughts

Targeting high energy density Li-S batteries with controlled polysulfide shuttling and a long cycling life, a light-weight nanoporous graphitic carbon nitride material is introduced and shows much promise as a sulfur host. In addition to low density, high-surface-area g-C_3N_4 is advantageous in containing a high N concentration of up to 53.5 at%, giving rise to its superior LiPS adsorptivity over N-doped carbons.

The nature of the interaction between g-C_3N_4 and LiPS, revealed for the first time by FTIR and XPS studies, shows a favorable Li^+-$N^{\delta-}$ interaction. First-principles calculations not only confirm this, but also provide a quantitative evaluation of the significant effect of high pyridinic N concentration on improving the LiPS adsorptivity for g-C_3N_4. The excellent long-term cycling performance was demonstrated for the g-C_3N_4/S75 electrode in a Li-S cell, with as low as 0.04% capacity fade per cycle over 1500 cycles at a C/2 rate. More importantly, high sulfur loading electrodes with up to 4.2 mA h cm^{-2} capacity and stable cycling performance were also demonstrated.

This paves the way for future exploration of new Li-S host materials embracing improved cathode architecture with these guidelines in mind. Constructing smart architecture that incorporates g-C_3N_4 and provides conductive pathways and volume accommodation is discussed in **Chapter 6**

Chapter 6 A Comprehensive Approach on Cathode towards Stable Li-S Batteries with High Energy Density

6.1 Introduction

Aside with the advances in developing host materials with chemical adsorption of LiPSs, it is now also appreciated that the low volumetric energy density of reported Li-S batteries still poses a great concern. This is due to two aspects: the low density of sulfur (2.07 mg cm^{-3}), on top of which lies a high fraction of carbon (usually > 30 wt%), and the overly high electrolyte/sulfur ratios used. Achieving high areal sulfur loading (>7 mg cm^{-2}) with low electrolyte volume is critical to maximize the energy density, but this is not the case for most reported systems to date.[140]

The challenge for high performance thick cathodes resides in all cathode components: the individualized nano-sized porous C/S composites, the PVDF binder that lacks elasticity and insufficient inter-particle conductivity.[139-142] In order to fabricate high-loading Li-S cathodes, two main approaches have been used. One is to construct 3D carbon frameworks,[43,112,143-145] and the other is to integrate the host nanomaterials before slurry processing.[41,103,146] Pure carbon 3D networks, usually composed of graphene or carbon nanofiber/tubes, with high surface area and conductivity, are reported to enable high sulfur loadings up to 21.2 mg cm^{-2}.[145] However, due to the large fraction of porous non-active carbons and the large void space inside and/or, the high areal capacity was realized at the expense of high electrolyte/sulfur ratios (µl/mg, *e.g.* 40:1,[112] 14:1,[144] 20:1[43]) necessary to fully wet the electrodes. This greatly compromises the energy density of the whole cell.

Developing thick and compact electrodes using traditional slurry-based process that fits current commercial protocols is vital for practical applications. In particular, integrating individualized nano-composites into large secondary particles is a promising route to improve inter-particle electrical connection and to construct integrated thick electrodes. This maximizes particle packing and reduces the void space, thus requiring less electrolyte. Reported carbon-based electrodes based on this principle usually lack sufficient polysulfide adsorptivity, however, which in principle aggravates polysulfide shuttling and their side reactions with the lithium.[41,103]

For slurry processed electrodes that especially experience large volume expansion, binders with sufficient adhesivity and elasticity are essential to connect individual particles and thus to fabricate compact and high areal loading electrodes. A high percentage (≥10 wt%) of binder intrinsically decreases the electrode conductivity and the ratio of active material. Few reports have been devoted to designing new binder systems for thick sulfur cathodes (and/or at a low weight percentage), aside from SBR and a polyamidoamine dendrimer reported recently. [103,147]

In this Chapter, I describe a comprehensive strategy to construct stable and high sulfur loading cathodes based on conventional slurry process, enabled by coupling multifunctional sulfur composites with an *in-situ* cross-linked polymeric binder. The process is summarized schematically in **Figure 6.1**. First, a hybrid sulfur host material with both strong chemical LiPSs adsorption and high electronic conductivity is realized by alternate stacking of two layered materials components: graphitic C_3N_4 (g-C_3N_4) and graphene. By cross-linking only 5 wt% of the CMC binder *in-situ* with the sulfur composites, crack-free high sulfur loading electrodes (up to 14.9 mg cm^{-2}) were achieved. Most importantly - owing to the compact

structure of the cathodes - an electrolyte/sulfur ratio as low as 3.5:1 (μl:mg) allows high areal capacities, up to 14.7 mA h cm^{-2} and stable cycling.

These achievements are ascribed to i) the excellent network conductivity from graphene and chemical interaction with polysulfides from g-C_3N_4, ii) a well-maintained electronic/physical connection among the sulfur composites owing to the elastomeric cross-linked binder, iii) the compact structure of electrode that requires less electrolyte. The challenges related to the lithium metal anode for ultra-high loading cathodes in Li-S batteries is also discussed in this chapter.

6.2 Experimental Approaches

6.2.1 Synthesis of Sulfur Host Materials

The graphene-C_3N_4 composite (denoted as NG-CN) was prepared by thermal treatment of the homogeneous mixture of cyanamide, graphene oxide (ACS Materials) and Ludox (AS-30, 30 wt%) silica nanoparticles. Specifically, 450 mg of cyanamide was added to 200 ml of 1 mg ml^{-1} GO aqueous solution, along with 4.3 g of AS-30 colloid solution. The mixture was sonicated for 2 hours and then stirred for 5 hours. The as-formed dispersion was heated at 105 °C for 2 hours until a thick paste formed. The paste was freeze dried to form the precursor, which was then subjected to heat treatment at 550 °C for 4 hours (4 °C min^{-1} ramping). The final product was obtained after HF (5 wt%) etching and drying at 90 °C. The g-C_3N_4 was synthesized similarly, except that no GO was used. The N-doped carbon (denoted as NdC) was synthesized in the same way as g-C_3N_4, except that polydopamine was used as the precursor, where polymerization of dopamine was achieved using tris(hydroxymethyl)-aminomethane in aqueous solution at room temperature overnight (w/w 2:1).

6.2.2 Preparation of Cathodes with Cross-Linked Binder

The NG-CN, g-C_3N_4 (and NdC) sulfur composites with 77 wt%, 75 wt% sulfur, respectively, were prepared *via* a melt-diffusion approach under ambient atmosphere at 155 $^{\circ}$C for 12 hours. The cathode slurry was prepared by mixing NG-CN/S composite with CMC, citric acid and carbon nanotubes (CNTs, diameter 8 nm), Super P with a weight ratio of 85: 4.5: 0.5: 5: 5 in a mixture solvent of H_2O and DMF (3:2, v/v). The percentage of binder is 5 wt% and the ratio of CMC to citric acid (as the cross-linker) is 9:1. Using a doctor blade, the slurry was coated on AvCarb P50 paper that has a rough surface for optimized adhesion to the active materials. The thick slurry is coated only on the top of, rather than within the current collector. The cathode was dried at room temperature for 6 hours and then at 60 ^{o}C overnight, before final treatment at 150 ^{o}C in a closed atmosphere. The thickness of the electrodes are as follows: 270, 195 and 105 μm for loadings of 14.9, 10.2 and 5.2 mg cm^{-2}, respectively, excluding the carbon paper (110 μm). The PVDF based cathode was prepared with 5 wt% of PVDF.

6.2.3 Electrochemical Measurements

A lithium foil anode and an electrolyte comprising 1 M LiTFSI and 2 wt% of $LiNO_3$ in a mixture of DME and DOL (v/v = 1:1) was used. An electrolyte/sulfur ratio of 7:1, 5:1, 4.5:1, 4:1, 3.5:1 (μl: mg) was used for the cathodes with sulfur loadings of 2.0, 5.2, 8.0, 10.0 and 14.9 mg cm^{-2}. For EIS measurements, the DC voltage was maintained at open-circuit voltage and an AC voltage of 5 mV in amplitude was applied with a frequency of 200 kHz - 20 mHz.

6.2.4 Computational Methods

First-principles calculations were performed using the plane-wave-based VASP code. PAW pseudopotentials were applied to describe electron-ion interactions, and the PBE version of the GGA was used for the electronic exchange correlation effect.86,[87] The Li_sv version PAW potential was used for Li atoms. A cut-off energy of 500 eV was used for the plane wave basis to ensure convergence. Van der Waals forces are included in the calculation. Spin-polarized calculations were employed. A double-layer graphite of a 6×6 supercell size and a 2×2 supercell layer were used for plain graphene and g-C_3N_4, respectively. For modeling NG-CN, a surface layer of g-C_3N_4 (2×2) was placed on the top of a layer of graphene (6×6), so that the sizes of the two layers are very close. A vacuum layer of 15 Å was used in the vertical direction for slab binding calculations, in order to exclude the interaction between the layer and its images. The conjugate-gradient algorithm was used for ionic relaxation. The binding energy E_{bind} of Li_2S_n on the substrates is defined as:

$$E_{bind} = (E_{sub} + E_{ps} - E_{sub+ps})$$

where E_{sub}, E_{ps} and E_{sub+ps} represent the ground-state energies of the substrate, respective polysulfide and substrate-polysulfide. A larger positive value indicates greater binding ability.

6.3 Physical Characterizations of Host Materials

Porous g-C_3N_4 materials have been reported that combine the advantages of light weight with intrinsic polarity that contributes to strong LiPSs interactions (see **Chapter 5**).[148,149] However, their semiconducting nature limits electron transport and hence sulfur utilization. Incorporating the g-C_3N_4 into a highly conductive network such as graphene can overcome this problem. Taking advantage of the fact that graphene and g-C_3N_4 both exhibit layered structures, a hybrid with alternate stacking of the two component layers was fabricated (**Figure 6.1**, step 1).[150]

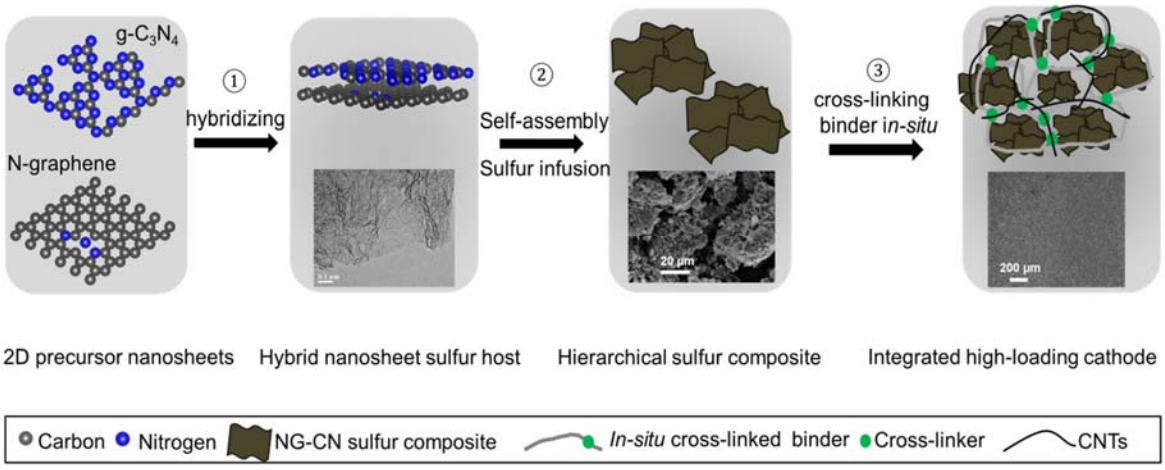

Figure 6.1 A schematic illustration of the concept of coupling hierarchical sulfur composite based on a hybrid host with *in-situ* cross-linked binder in order to fabricate stable high-loading cathodes. **Step 1** starts with hybridizing two individual 2D nanosheets (graphene and g-C_3N_4) to form the nanosheet-type host material; in **step 2**, hierarchical sulfur composites are formed as large multi-micron sized secondary particles formed as a consequence of evaporation induced self-assembly and sulfur infusion; **step 3** involves *in-situ* cross-linking of the CMC binder in the presence of the sulfur composites.

In our study, the hybrid was synthesized by thermal treatment of cyanamide and GO, which are mixed on the molecular level based on the cohesive interaction between them. Evaporation induced self-assembly of the precursor results in aggregated and micron-sized nanosheets. During heat treatment, cyanamide undergoes thermal polymerization along with the release of ammonia, which in turn initiates high temperature N doping of the graphene (NG).[151]. For comparison, pure porous g-C_3N_4 (N concentration: 53.5 at%, as in **Chapter 5**) and porous N-doped carbon (N concentration: 3.1 at%) were also synthesized.[148]

The NG-CN material exhibits a 2D nanosheet structure similar to the GO precursor, as revealed by SEM and TEM images (**Figure 6.2**). The NG-CN has a highly wrinkled structure owing to the release of ammonia gas during heat treatment. The dark-field TEM image clearly shows the porous structure resulting from the silica templating (**Figure 6.2d**). Consequently, a BET surface area of 470 m^2 g^{-1} and pore volume of 1.7 cm^3 g^{-1} (pore size ~4.5 nm) are obtained for NG-CN (**Figure 6.3**).

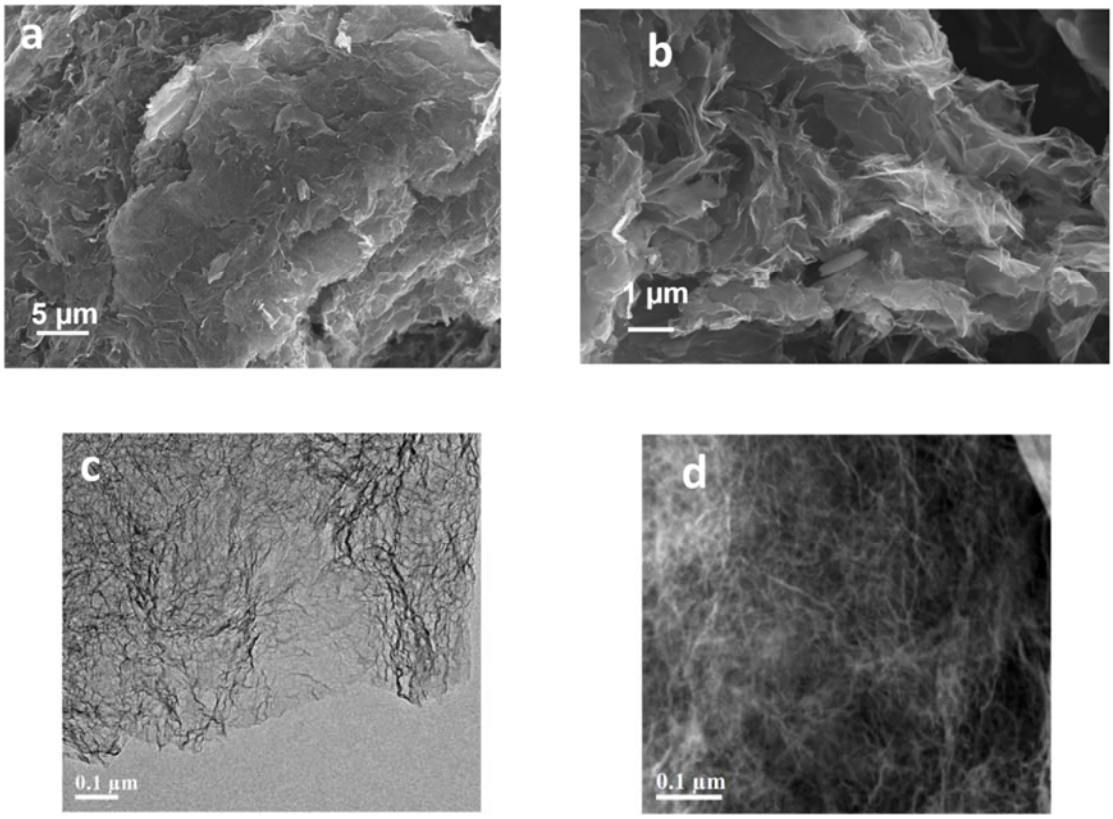

Figure 6.2. a,b) The SEM images, c) bright-field and (d) dark-field TEM images of the NG-CN.

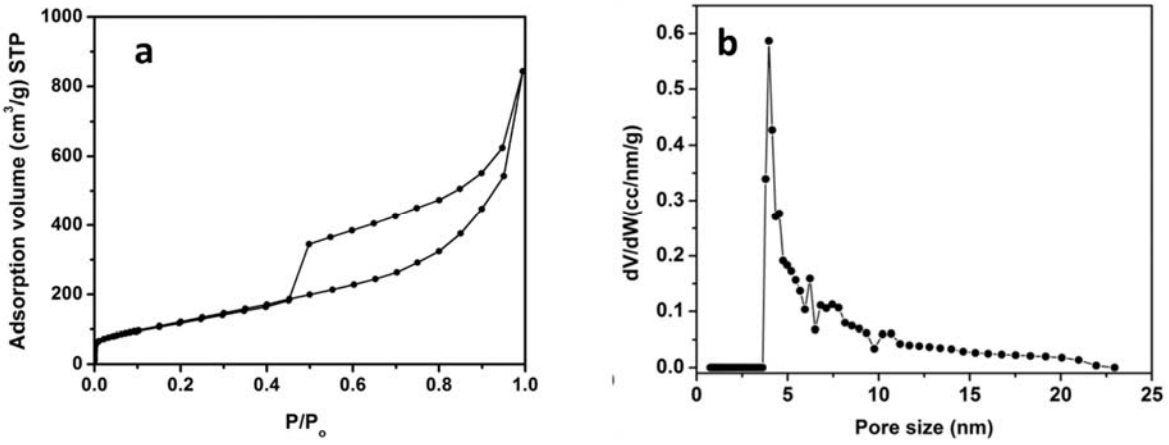

Figure 6.3 a) The N_2 adsorption/desorption isotherm and b) the pore size distribution of the NG-CN.

These properties enable high polysulfide adsorptivity (as discussed below) and homogeneous infiltration of a high fraction (77 wt%) of sulfur without the formation of large isolated sulfur particles (**Figure 6.4 a**). The weight fraction of sulfur is confirmed by TGA analysis (**Figure 6.4c**).The EDX mapping of the sulfur composite demonstrates an uniform distribution of O, S and N elements (**Figure 6.4d)**. The sulfur exists as a film layer on the surface of the hybrid host based on the similar morphology with the host itself. The possible presence in the form of small sulfur crystals can be excluded owing to the nature of melted sulfur diffusion at a high fraction (77 wt%). The SEM images show that the few-layered NG-CN nanosheets are entangled to form large secondary particles. Consequently, the melt-diffused sulfur composite shows a morphology of multi-micron-sized particles (**Figure 6.4b**). This hierarchical and interconnected architecture is important for the fabrication of thick electrodes. It not only allows improved connection between individual particles with less binder (compared to nanoparticle materials) but also ensure effective particle packing and high tap density, while moderate porosity is maintained for electrolyte penetration. [41,103]

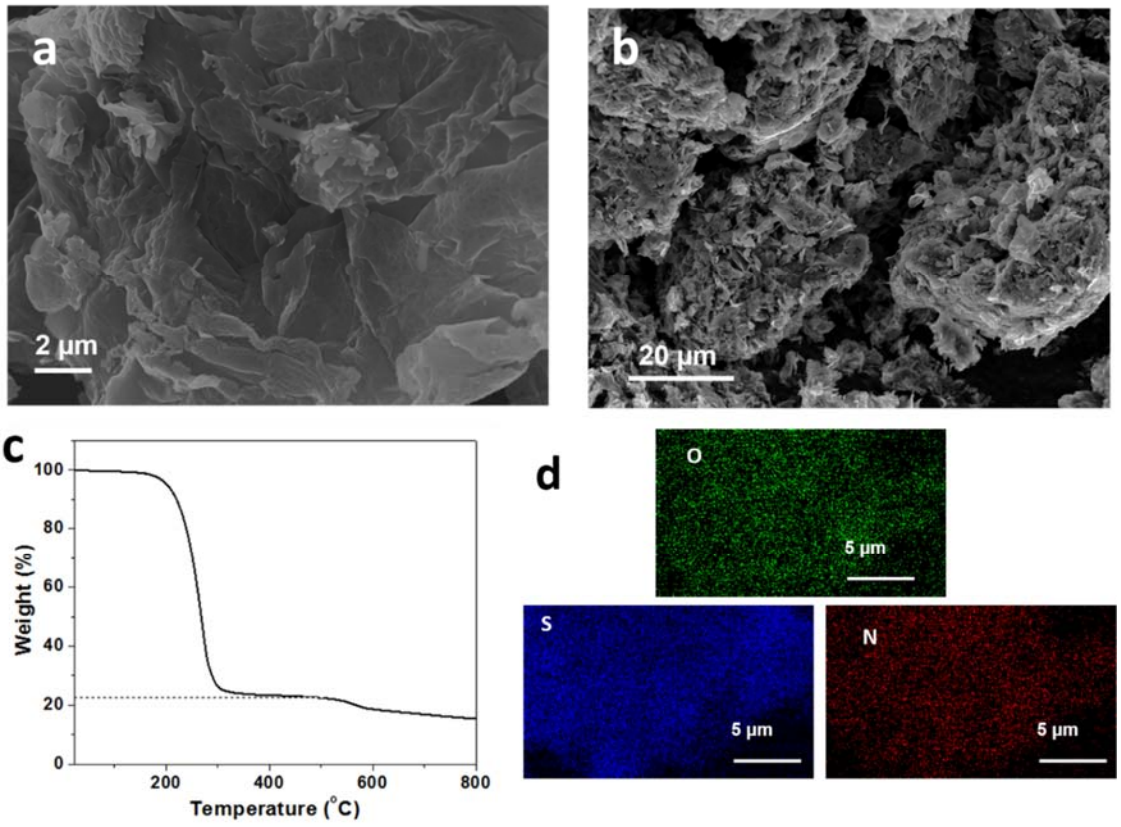

Figure 6.4 a,b) The SEM images, c) the TGA curve and d)EDX mapping (O, S, N) of NG-CN sulfur composite.

The modification of the stacking of the g-C_3N_4 layers in NG-CN is suggested by the broadening and low-angle shift of the (002) peak in the XRD pattern relative to that of g-C_3N_4, signifying a slightly increased interplanar distance (**Figure 6.5a**). The chemical environment of the NG-CN was examined by XPS and EDX. The XPS survey spectrum shows the presence of both nitrogen and oxygen with a high nitrogen concentration of 20 at% (**Figure 6.6a**), over 5-fold more than that of most reported N-doped carbons.[40,43,130]

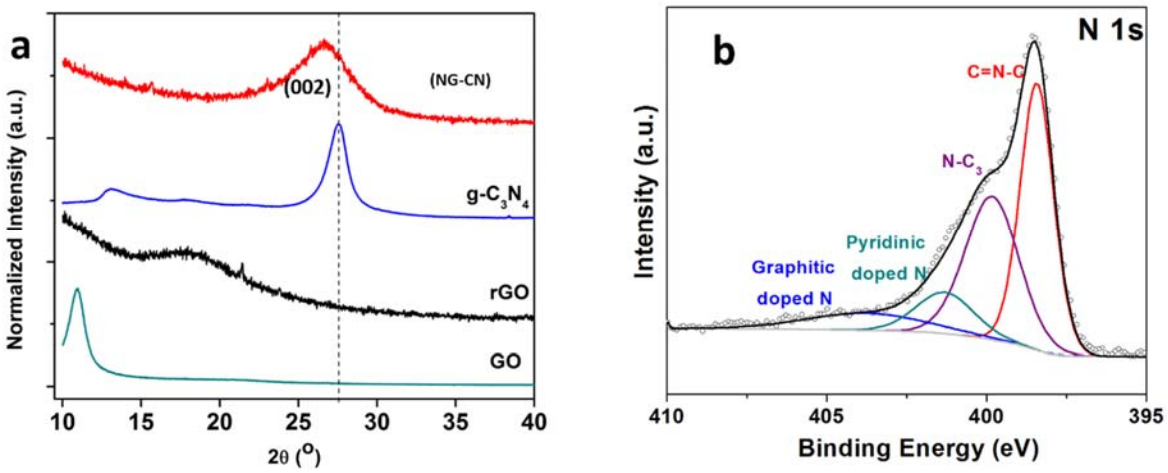

Figure 6.5 a) The XRD patterns of GO, reduced GO (rGO), g-C_3N_4 and NG-CN, and b) the high-resolution N 1s XPS spectrum of the NG-CN.

The high-resolution N 1s XPS spectrum provides detailed information on the nature of the nitrogen species (**Figure 6.5b**). The C=N-C (398.2 eV) and tertiary N (399.8 eV) moitiés from g-C_3N_4 and the other two species corresponding to pyridinic N (401.3 eV) and graphitic N (403.8 eV) in N-doped carbons were observed.[46,152,130,148,149] It confirms the formation of g-C_3N_4 and simultaneous N doping on the graphene (accounting for 20% of the nitrogen). N-doped carbons/graphenes have been reported to effectively adsorb polysulfides and here NG adds to the overall polysulfide adsorptivity. [46,130,152] Furthermore, the EDX spectrum shows a nitrogen concentration of 19 at% (**Figure 6.6b**), close to the surface-sensitive XPS results, indicating that the majority of N species are accessible for LiPS adsorption on the surface of the layers. The EDX mapping in **Figure 6.6c** shows a homogeneous distribution of N and O.

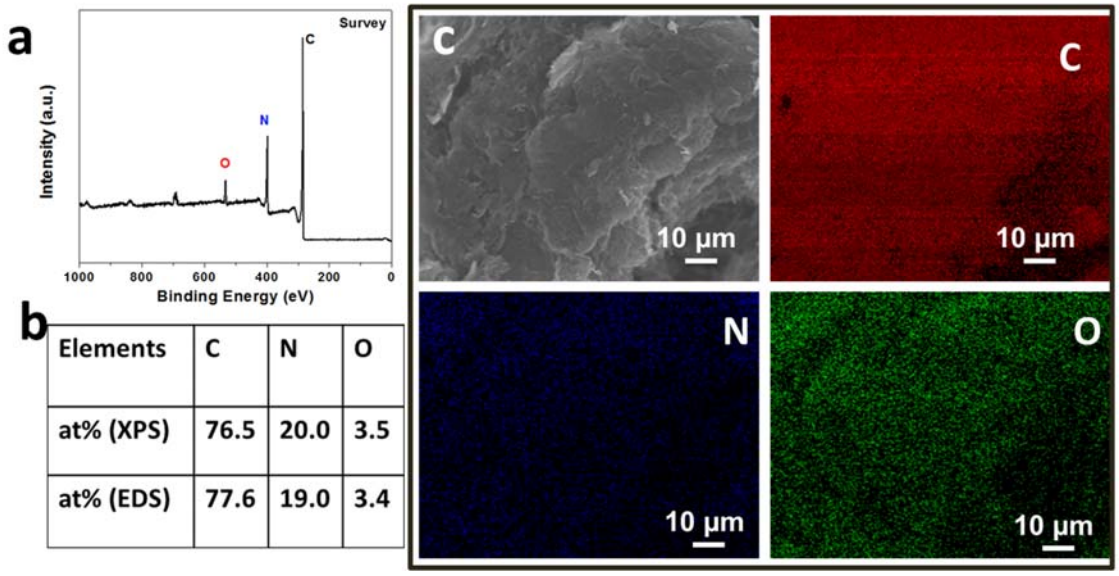

Elements	C	N	O
at% (XPS)	76.5	20.0	3.5
at% (EDS)	77.6	19.0	3.4

Figure 6.6 a) The XPS survey spectrum of NG-CN. b) The summary of atomic components (at %) of the NG-CN measured from XPS and EDX spectra. c) The SEM EDX mapping of the NG-CN (elements: C, N, O)

High electronic conductivity and high LiPS adsorptivity are two very important properties for advanced sulfur host materials. The room temperature conductivity of NG-CN is over three orders of magnitude higher than g-C_3N_4 (11.3 S/cm versus 0.012 S/cm), as measured by the four-probe method on cold-pressed pellets. The band structure of hybrid and pure g-C_3N_4 was further examined using first-principles calculations based on DFT. The g-C_3N_4 material has a band gap of 2.1 eV indicative of semiconducting behavior (**Figure 6.7a**); on the contrary, the NG-CN hybrid exhibits a metallic feature with zero band gap (**Figure 6.7b**). The downward shift of the both valence and conduction bands of the NG-CN relative to g-C_3N_4 indicates significant electron transfer between the two layer components, which enhances electron mobility.[151]

The LiPS adsorptivity of the NG-CN hybrid was quantified *via* the potentiostatic titration approach using Li_2S_4 as the representative LiPS. The data is compared with pure g-C_3N_4 (surface area: 615 m^2 g^{-1}, **Chapter 5**); porous N-doped carbon (surface area: 922 m^2 g^{-1}, **Chapter 5**);[148] and typical carbons (VC and Super P) in **Figure 6.7c**. The NG-CN adsorbs about the same amount of Li_2S_4 as g-C_3N_4, which is almost twice of N-doped carbon (owing to a much higher fraction of surface N sites) and over two orders of magnitude higher than the simple carbons.

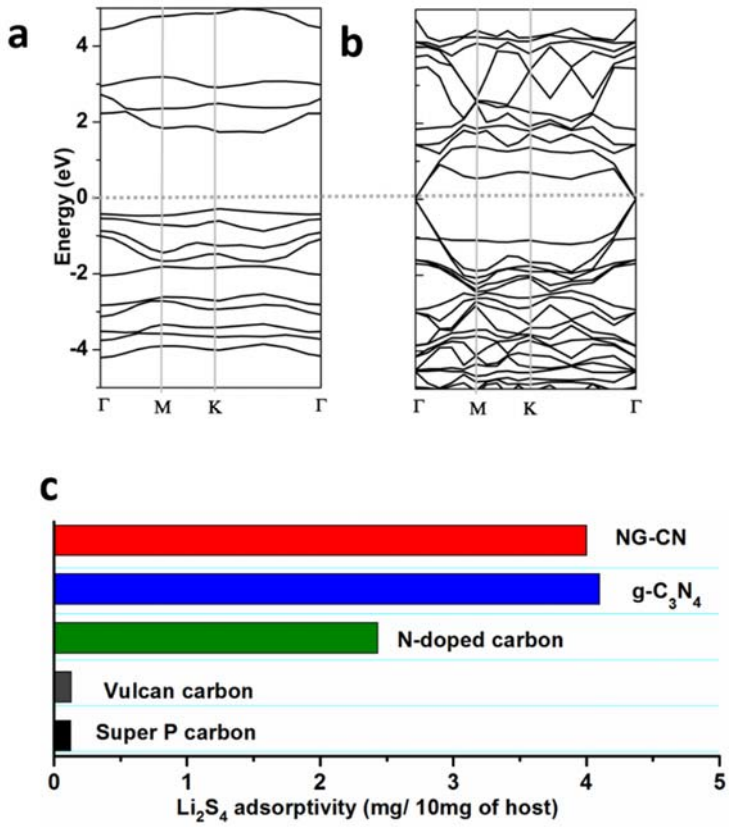

Figure 6.7 The calculated band structures of a) g-C_3N_4 and b) graphene-C_3N_4 hybrid using fully relaxed structures. c) The polysulfide (Li_2S_4) adsorptivity of the as-synthesized NG-CN compared with g-C_3N_4, porous N-doped carbon, VC and Super P.

It is noted that theoretically not all the polysulfides will be adsorbed by the NG-CN based on a sulfur fraction of 77 wt%; however, complete adsorption at one time is not required during the discharge/charge of the cell. This is because the proceeding of sulfur reduction is two successive two-phase reactions (signified by the two voltage plateaus), meaning that the formation of polysulfides from reduction of sulfur occurs along with their consumption by being further reduced to Li_2S. Therefore, there is no condition when all polysulfides are dissolved. Furthermore, depending on the amount of electrolyte added, the amount of solubilized polysulfides at a certain state varies.

6.4 Computation on Chemical Interaction with Polysulfides

To reveal the nature and strength of the interaction of the metallic NG-CN with LiPSs, first-principles calculations was carried out. Since the interaction of N-doped carbons with LiPSs has been studied in great detail, I did not attempt to simulate N-doping but instead employed a plain graphene substrate to hybridize with the g-C_3N_4 surface.[46,41] The double-layer hybrid slab was compared to plain graphite in terms of geometry and binding energy with LiPSs. The intermediate Li_2S_4, short-chain Li_2S_2 and end-product Li_2S were used to simulate LiPSs.

The fully relaxed binding geometry of the LiPSs on the NG-CN and graphite surface is shown in **Figure 6.8b-e**. As expected, there is no specific bonding between the simulated LiPSs and graphite substrate, resulting in very low binding energies (0.18, 0.94 and 0.73 eV for Li_2S, Li_2S_2 and Li_2S_4, respectively, **Figure 6.8a,b**). These arise mainly from the VDW interaction included in the calculations. However, for the graphene-CN hybrid, there is significant Li-N bonding between the Li^+ and pyridinic N (**Figure 6.8c-e**). This leads to strong interactions for Li_2S, Li_2S_2 and Li_2S_4, with binding energies of 3.18, 2.42, 1.85 eV, respectively.

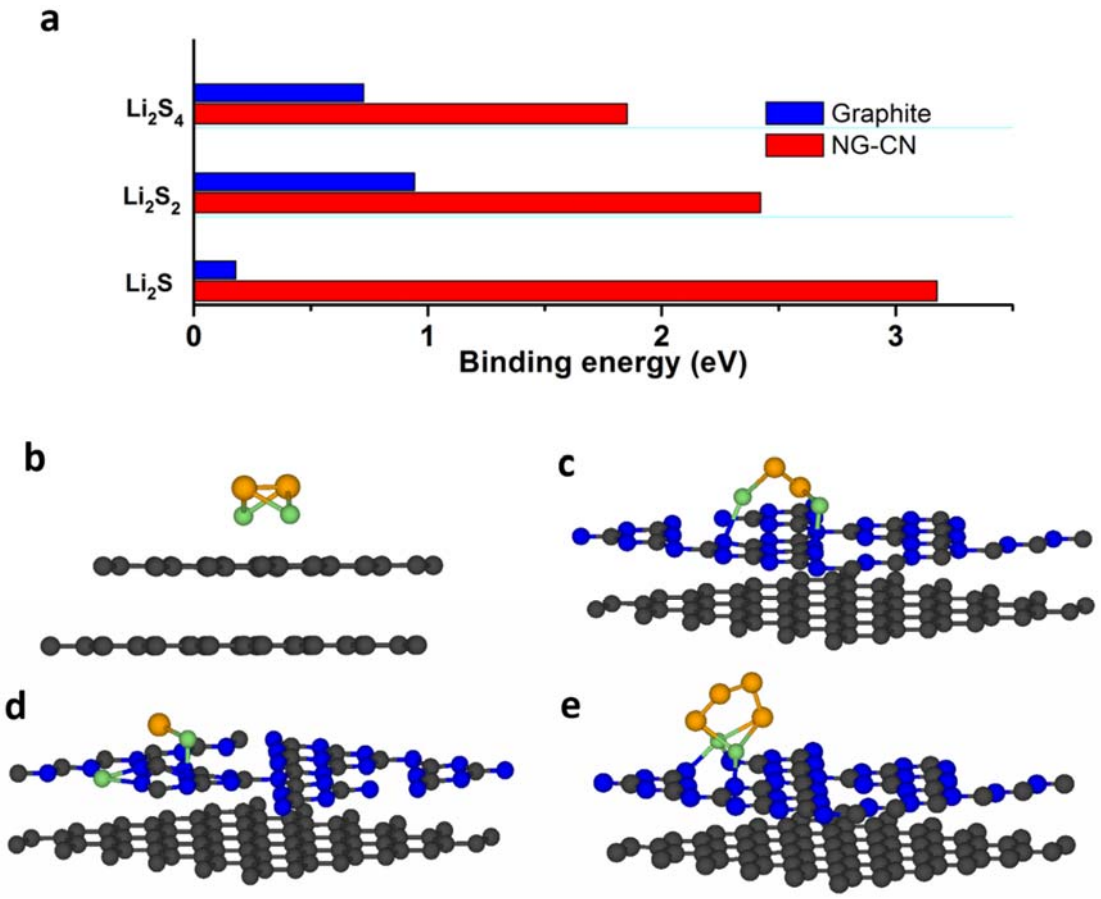

Figure 6.8 a) The summary of the calculated binding energy of Li_2S, Li_2S_2 and Li_2S_4 on NG-CN hybrid and pristine graphite substrates. b-e) The fully relaxed configurations of Li_2S_2 binding on b) graphite and c) NG-CN, and of d) Li_2S, e) Li_2S_4 binding on NG-CN. Grey, blue, green and orange balls represent carbon, nitrogen, lithium and sulfur atoms, respectively.

The higher-order LiPS experience the weakest interaction due to a lower overall fraction of positively charged Li^+ ions, as typically observed. These findings are further supported by the slightly distorted geometry of the bound LiPSs compared to the pristine molecules (**Figure 6.8**). Using Li_2S_4 as the representative polysulfide, XPS studies of the host-LiPS interaction show similar binding energy shifts in the Li 1s and $S2p_{3/2}$ spectra as we

reported for g-C_3N_4, [148] (of - 0.7 eV and - 0.5 eV respectively), indicative of Li-N bonding, and thus are not shown here.

6.5 *In-Situ* Cross-Linked Binder

High sulfur loading cathodes have been extensively reported in the past year, but most are based on sulfur or S/C composites in 3D carbon frameworks, which generally lack chemical trapping of the LiPSs. Moreover, constructing high-loading and compact cathodes on flat current collectors using traditional slurry processes is more appealing from a practical view. Inspired by binder designs for high volume expansion anode materials,[153] we cross-linked CMC binder *in situ* with the NG-CN/S composites (**Figure 6.9a**). The advantage of an *in-situ*

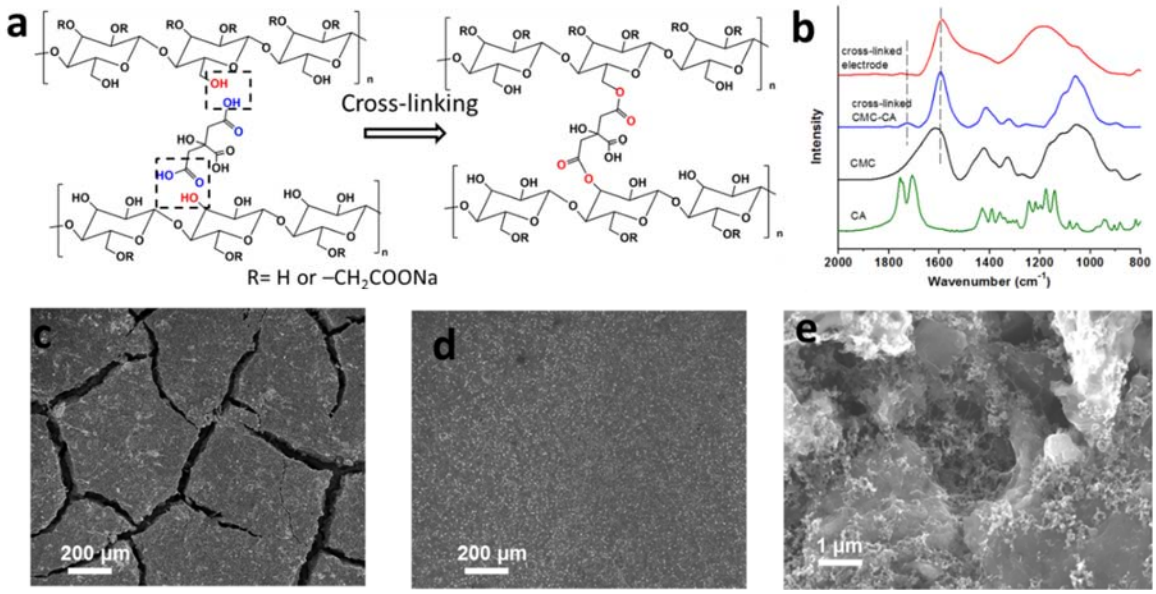

Figure 6.9. a) A schematic illustration of the cross-linking of CMC binder with CA as the linker, based on the esterification of the –OH groups in CMC and the –COOH groups in CA at 150 ºC. b) The FTIR spectra of the pristine CA, CMC, cross-linked CMC- and the in-situ cross-linked sulfur electrodes. c-e) The SEM images of the surface of sulfur cathodes fabricated using c) PVDF binder and d, e) cross-linked CMC-CA binder.

cross-linked binder to create thick electrodes is two-fold − efficient physical/electrical connection between particles and high elasticity to accommodate the large volume expansion.

To achieve this, electrodes consisting of the NG-CN/S composites, carbon additives (CNTs and Super P) and the CMC binders with citric acid (CA) were subjected to heat treatment at 150 ºC for 1 hour. In order to avoid sulfur sublimation, the reaction was conducted in a closed atmosphere. The cross-linking occurs by esterification between the –OH groups in the CMC and the –COOH in CA (**Figure 6.9a**). FTIR was conducted on the electrode, and on a reference mixture of CMC-CA (without the sulfur composite) after heat treatment (**Figure 6.9b**). Successful cross-linking is confirmed by two new peaks at 1594 cm^{-1} and 1726 cm^{-1} that correspond to the ester groups (O-C=O and C=O).[153]

SEM studies were carried out to investigate the overall and local structure of the thick cathodes (5.2 mg cm^{-2}, all mass based on sulfur) fabricated with PVDF and cross-linked CMC-CA binder. The low-magnification SEM images in **Figure 6.9c,d** clearly show large cracks in the PVDF based electrodes that are formed upon evaporation of the slurry solvent. It is believed to result fluctuating and unstable capacity retention as discussed in next section. In contrast, the cross-linked CMC-CA based electrode is flat and free of cracks as shown in the area in **Figure 6.9d** and in even larger scale. This indicates the effective connection between individual composite particles by the adhesive and elastic cross-linked CMC-CA binder. Furthermore, the high-magnification SEM image of CMC-CA based electrode in **Figure 6.9e** shows a compact structure yet with moderate porosity for electrolyte penetration. It is noted that such an integrated structure was achieved with only 5 wt% binder, increasing the overall sulfur content to 65.5 wt% in the electrode.

6.6 Electrochemistry with High Energy Density

Galvanostatic cycling was carried out to investigate the benefits on Li-S cell performance. First, electrodes with 2.0 mg cm^{-2} sulfur loading were fabricated to investigate the impact on sulfur utilization and cycling stability. As shown in **Figure 6.10a**, the PVDF based NG-CN electrode exhibits an initial capacity of 17% higher than the g-C_3N_4 electrode at a C/20 rate (1340 mA h g^{-1} *vs.* 1150 mA h g^{-1}) and also remains higher over 100 cycles at a C/2 rate (**Figure 6.10b**). This owes to the greatly improved electrode conductivity because of the hybridization of graphene within the host. The NG-CN electrode shows very stable cycling with negligible capacity fading - in contrast to that experienced by the NdC based electrodes (**Figure 6.10b**)[148] - indicative of greatly suppressed polysulfide shuttling and a stabilized cathode structure.

Based on these results, I fabricated thick NG-CN electrodes using cross-linked CMC-CA binder at varied sulfur loading between 5.2−14.9 mg cm^{-2}. Very low electrolyte/sulfur ratios (µl: mg) *e.g.*, 5:1 and 3.5:1 for the 5.2 mg cm^{-2} and 14.9 mg cm^{-2} loaded electrodes, respectively, allowed cells to operate due to their compactness and low void space. It is noted that because there is always free space in coin cells which uptakes "dead" electrolyte, extremely low total electrolyte volumes (*i.e.* 3.5:1, µl/mg) cannot be sustained in 5.2 mg cm^{-2} electrodes. Pouch cells provide a better forum to investigate extremely lean electrolyte conditions, and will serve as the protocol in future reports. All cathodes were conditioned at the same *areal* current density (0.5 mA cm^{-2}) for the first cycle before being cycled at 1.0 mA cm^{-2}. It is noted that the current density for the highest loading electrodes, *i.e.* 14.9 mg cm^{-2}, is relatively low (corresponding to ~ C/20), since higher rate would cause high polarization due to the lengthened Li^+ ion pathways.

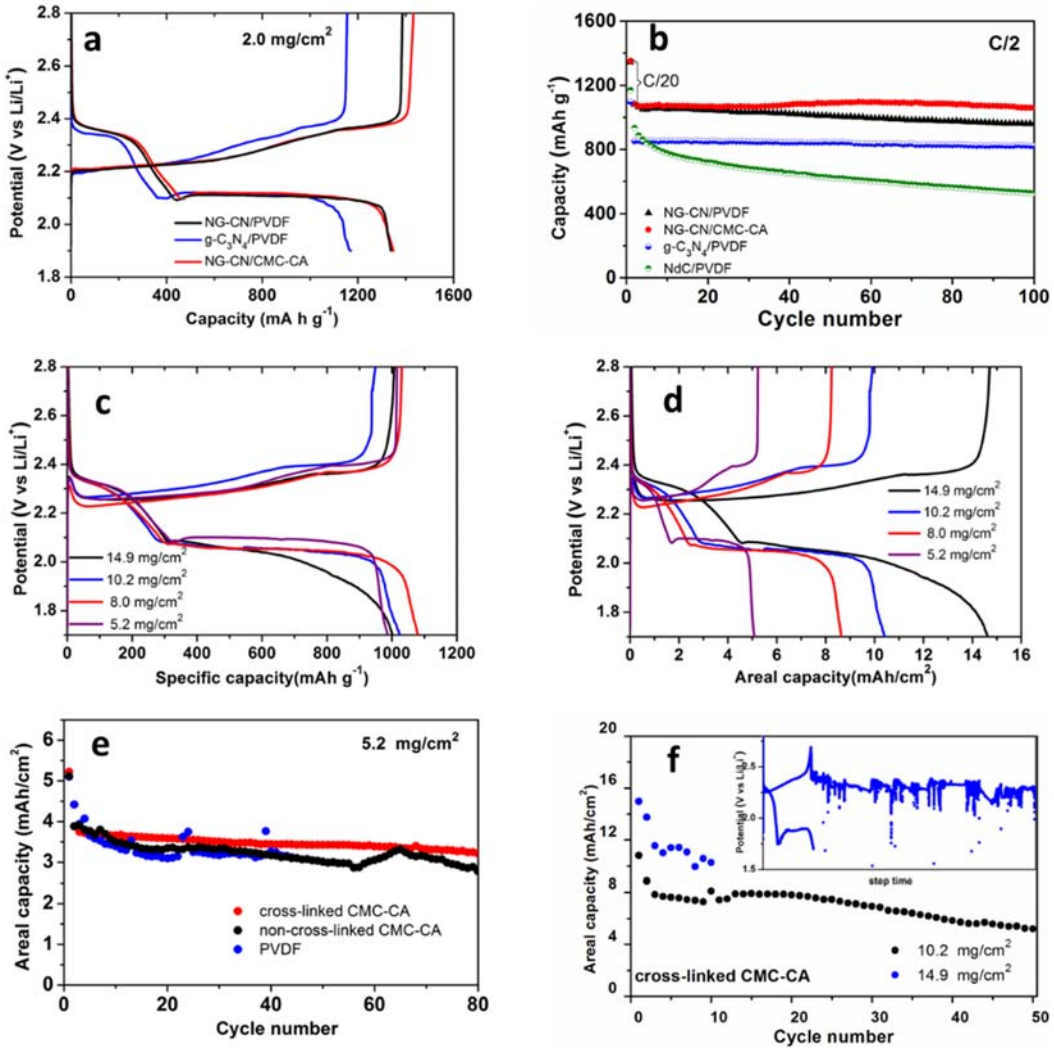

Figure 6.10 a) The voltage profiles (at C/20) and b) cycling stability (at C/2) of the different sulfur cathodes with a sulfur loading of ~2.0 mg cm^{-2}. c, d) The voltage profiles of the NG-CN/CMC-CA sulfur cathodes with varied sulfur loadings with respect to c) mass specific capacity and d) areal capacity at 0.5 mA cm^{-2}. e) The cycling stability of the NG-CN sulfur cathodes fabricated with PVDF, non- and cross-linked CMC-CA binder with sulfur loading of 5.2 mg cm^{-2} at 1.0 mA cm^{-2}. f) The cycling stability of NG-CN/CMC-CA cathodes with sulfur loadings of 10.2 and 14.9 mg cm^{-2} at 1.0 mA cm^{-2}; the inset shows the voltage profiles of the 14.9 mg cm^{-2} electrode at 11th cycle.

The voltage profiles of the cathodes at 0.5 mA cm^{-2} are shown in **Figure 6.10c**. All cathodes exhibit a typical two-plateau discharge profile, with the 14.9 mg cm^{-2} electrode exhibiting a more sloping low-voltage plateau due to increasing impedance with deep discharge. All cathodes exhibit an initial capacity between 1000 - 1100 mA h g^{-1}. The relatively smaller capacity for even a lower loaded electrode (e.g 5.2 mg cm^{-2}) is attributed to its larger sulfur-mass *specific* current and thus lower sulfur utilization. As shown in **Figure 6.10d**, an initial areal capacity of 14.70, 10.80, 8.65 and 5.15 mA h cm^{-2} was achieved for the thick electrodes with sulfur loadings of 14.9, 10.2, 8.0 and 5.2 mg cm^{-2}, respectively. The areal capacity of 14.70 mA h cm^{-2} is among the highest reported for slurry processed electrodes without carbon interlayers. Taking into account the low electrolyte/sulfur ratio, it is believed this cathode design is very promising for high energy density.

The cycling performance of the 5.2 mg cm^{-2} loaded cathodes using cross-linked CMC-CA binder is compared with those made with non-cross-linked binder (*i.e.*, no heat treatment on the cathodes) and PVDF binder in **Figure 6.10e**. The cross-linked CMC-CA based electrode shows very stable cycling over 80 cycles; the non-cross-linked electrode show fast fading over first 20 cycles followed by slight capacity fading and the PVDF electrodes shows fluctuating capacity with slow fading. The evolution of cell impedance over cycling was also monitored and shown in **Figure 6.11a**. Very stable charge-transfer impedance represented by the semicircle in the Nyquist plot is observed, suggesting effective polysulfide trapping and controlled Li_2S deposition on the NG-CN host even at high loading. This illustrates the importance of a cross-linked binder in maintaining the structure integrity and electron/ion conductivity of thick electrodes on cycling.

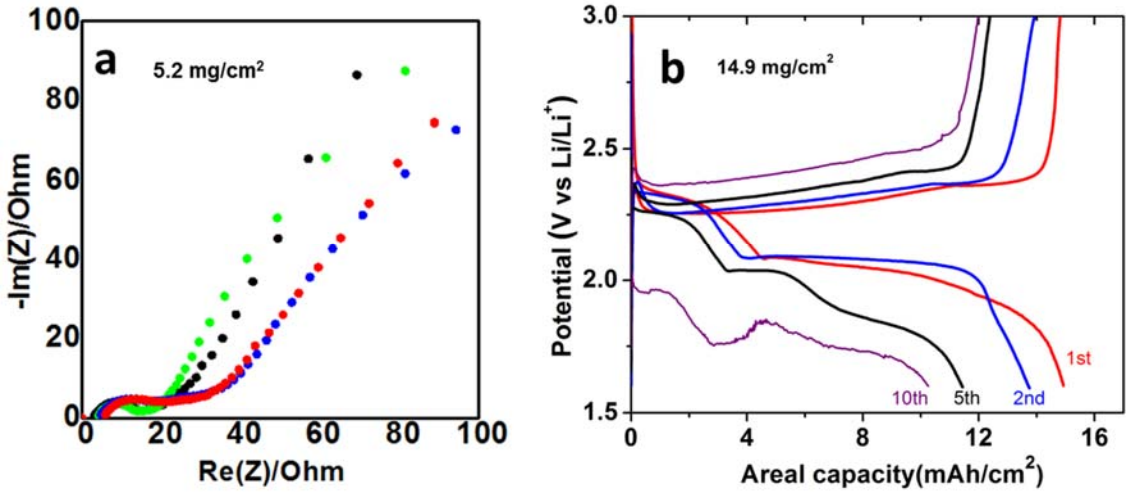

Figure 6.11 a) The Nyquist plot of the Li-S cell with the NG-CN/CMC-CA cathodes with 5.2 mg cm^{-2} sulfur loading at a fully charged state, after 1st cycle (green), 5th cycle (black), 20th cycle (blue) and 40th cycle (red). b) The voltage profiles of the Li-S cell made with the NG-CN/CMC-CA cathodes with 14.9 mg cm^{-2} sulfur loading after different numbers of cycles.

The cathode with 10.2 mg cm^{-2} loading shows a good capacity retention of 6.0 mA h cm^{-2} over 50 cycles (**Figure 6.10f**). However, the cathode with 14.9 mg cm^{-2} loading shows significant capacity fading and a short cycle life. At the 11th cycle, dendrite formation was observed as seen from the significant voltage fluctuation on charge whereupon lithium deposition occurs on the anode side (inset**, Figure 6.10f**).[154] At such high sulfur loadings, a very high areal capacity at such high current is applied on the lithium anode, which aggravates dendrite formation and impedance build-up on the anode surface. When high surface area dendritic lithium starts to form, the side reaction with polysulfides also accelerates formation of the impeding Li_2S/Li_2S_2 layer. Moreover, the accelerated side reaction of dendritic lithium with electrolyte can also lead to electrolyte depletion resulting voltage fluctuation. This is consistent with the continuous increase of the polarization as seen from the voltage profiles as a function of the cycle number (**Figure 6.11b)**. Thus it is believed that the lithium anode

corrosion becomes a dominating factor in limiting the performance of high-loading sulfur cathodes, as some recent reports have suggested.[155,156] A protected lithium metal anode that is dendrite-free and chemically stable with the organic electrolyte is required to achieve even higher areal capacity Li-S batteries.

6.7 Conclusions and Thoughts

A multifaceted approach to construct stable and high loading sulfur cathodes was shown by coupling a multifunctional and hierarchical sulfur composites with an in-situ cross-linked binder. The hybrid sulfur host characterized by alternative stacking of N-doped graphene and graphitic C_3N_4 has high conductivity and adsorptivity towards polysulfides. The hierarchical structure in the form of microsized particles adds to its advantages to build compact high loading sulfur cathodes. A cross-linked CMC binder is shown to assist the inter-particle physical binding and electrical connection, which enables compact thick electrodes with up to 14.9 mg cm^{-2} sulfur loading to be fabricated at a low electrolyte/sulfur ratio (3.5: 1, µl: mg). The cathode with 5.2 mg cm^{-2} loading shows very stable cycling over 80 cycles. Additionally, it is noted the lithium anode failure issue that must be to overcome in order to enable Li-S batteries with cathodes with even higher sulfur loadings.

Chapter 7 Sparingly Solvating Electrolytes Direct the Li-S Reaction Pathway

7.1 Introduction

Techno-economic modelling of Li-S suggests that promising materials-only fundamentals can translate to long-term goals at the systems level, assuming progress is made reducing excess material burdens.[140, 157, 158] Excess electrolyte is required in contemporary Li-S cells to overcompensate for its consumption in side reactions with lithium metal and to fully solvate the polysulfide intermediates. The fully solvating nature of conventional ether electrolytes enables facile reaction kinetics but concurrently promotes the migration of polysulfides, resulting in the isolation of active material and/or unfavorable redistribution of reactants.[159] Also, lithium metal must be protected to achieve long cycle life. The sulfur and polysulfide redistribution would limit cycle life as has been demonstrated in many other precipitation-dissolution chemistries.[160]

Sparingly solvating electrolytes are a pathway to control reactant distribution owing to the very low solubility of polysulfides in such systems, and thus their short residence time in the solvated state.[161] Many well-known precipitation-dissolution secondary electrodes operate successfully by using the sparingly solubility concept, including $Pb/PbSO_4$, Ag/AgCl, and $Fe/FeCl_2$. Unlike conventional Li-S electrolytes, sparingly solvating electrolytes also break the coupling between the quantity of electrolyte required in the cell and the reaction mechanism. Solvates, ionic liquids and super-concentrated electrolytes with reduced polysulfide solubility have been used with varying degrees of success in Li-S cells.[78,79,161-164] The electrochemistry reported in nearly all electrolytes exhibits the traditional voltage response under galvanostatic discharge. The initial capacity is delivered on a plateau in the 2.3-2.4 V vs Li/Li^+ range before

transition to a second, lower-voltage plateau around 2-2.1 V *vs* Li/Li^+.[165-167] The specific capacity associated with the transition to the second plateau varies, but often is near 300-400 mA h g^{-1}.

The solubility of polysulfides in Li-S batteries can be suppressed through properly designed electrolyte systems. One class of electrolytes with high salt concentration exhibits limited polysulfide solubility because most solvent molecules are subject to strong interactions with the Li salt, leaving minimal or none to solubilize polysulfides.[77,79] A diluent, typically a hydro-fluorinated ether (TTE),[168] is often added to reduce the undesired viscosity while maintaining or reducing polysulfide solubility further.[78,79] High concentration electrolytes based on glymes and acetonitrile exhibit good control on the polysulfide solubility and electrochemistry in Li/S batteries.[77-79,162, 169] Such systems have been comprehensively reviewed.[170,171] Another class of electrolyte composed of a mixture of a RTIL with low donor ability and LiTFSI salt also exhibits selectively low solvation for polysulfides.[75,172,173]

As introduced in **Chapter 1**, Li-S electrochemistry using an electrolyte with $ACN_2LiTFSI$ as the primary solvate and TTE as the diluent indicates a non-traditional reaction pathway.[78] It was referred to as a non-solvent, in recognition of the apparently none solubility of Li_2S_6 at room temperature. However, the electrochemistry at room temperature suffered from significant polarization (overpotential) during both discharge and charge. This Chapter demonstrates that sparingly solvating electrolytes can fundamentally redirect the reaction pathway owing to the change in relative kinetic rates for competing reactions. A greatly reduced polarization was accompanied by moderately increasing the temperature.

Dr. C. -W. Lee, Dr. K. G. Gallagher and Dr. M. Balasubramanian at Argonne National Laboratory conducted the temperature- and rate-dependent electrochemistry, GITT of the

ACN_2-LiTFSI-TTE electrolyte. Dr. S. Ha conducted the ohara cell studies. Dr. C.-W. Lee, and Dr. M. Balasubramanian largely contributed to the acquisition and analysis of the XANES data. Dr. L. Cheng, Dr. K. G. Gallagher and Dr. M. Balasubramanian contributed to the study by conducting the kinetics modelling and providing mechanism insight. I contributed to the preparation of the electrolytes for some studies, the sulfur cathodes, measurement of the polysulfide solubility, ionic conductivity, *operando* XRD, *ex-situ* SEM studies, GITT of G4 solvates.

7.2 Experiment Approaches

7.2.1 Preparation and Characterizations of the Electrolytes

LiTFSI, alumina, TEGDME (G4), tetrahydrofuran, and acetonitrile were purchased from Sigma Aldrich. The TTE, 1,1,2,2-tetrafluoroethyl 2,2,3,3-tetrafluoropropyl ether was purchased from Synquest Labs. LiTFSI was dried under vacuum overnight at 150°C. ACN and TTE were dried over alumina (activated under vacuum at ~170°C) for 24 hours to result in a water content of 0.1 and 0.6 ppm, respectively. TEGDME was dried over activated molecule sieves (4 A) for 24 hours yielding a water content of 0.6 ppm. The preparation of solvate electrolyte starts with a 2:1 molar ratio of ACN (or THF):LiTFSI. The mass-dictated volume of ACN (or THF) was mixed with the appropriate mass of salt and stirred at room temperature to yield a clear, viscous solution. Once clear, an equivalent volume of TTE was added and stirred to create a 50:50 mixture. A TEGDME solvate (G4-LiTFSI) was prepared by dissolving LiTFSI in TEGDME and TTE with a molar ratio of 1:1:4.[79] The ionic conductivity was measured over a temperature range of 27-70°C in the glovebox with a 3-star conductometer (Orion) equipped with a 2-electrode epoxy conductivity probe.

7.2.2 Electrochemistry Measurements

Unless otherwise noted, micron-sized sulfur particles (bulk sulfur) were directly used as the active material to avoid any unknown synergistic effect from a carbon structure. Positive electrodes were cast from a slurry containing 50 wt% bulk sulfur, 40 wt% conductive carbon (Timcal Super C45) and 10 wt% PVDF binder in DMF onto an Al current collector. Mesoporous CMK-3 carbon was synthesized following a previously reported approach.[19] KB (Ketjen Black) or CMK-3 sulfur composites were prepared by melt-diffusion of sulfur into the carbon at the desired mass ratio at 155 °C for 12 hours. The sulfur loading was fixed to 1.2 mg cm^{-2}.

2032 type coin cells were assembled in an argon-filled glovebox using two sheets of 2325 Celgard™ as the separator, a Li foil negative electrode, and 10 µL mg^{-1} of electrolyte. For galvanostatic experiments, the voltage window is between 1.5 to 3.0 V for 1M LiTFSI in DOL:DME (1:1) with 2% $LiNO_3$, or 1.2 to 3.0 V for others (Maccor series 4400 battery tester). The same instrument was used to perform GITT, by alternating C/10 pulses (20 min) with OCV periods (120 min).

The Ohara cell consists of a pouch with container laminates, positive and negative electrodes, and the separator sheets. The positive and negative electrode compartments were separated by a Li^+ ion conductive glass ceramic membrane (LICGC). Further details on the preparation as well as the kinetic modelling study beyond the scope of this thesis

7.2.3 Physical Characterizations of the Electrolytes

The solubility of polysulfide was measured using a UV/VIS spectrometer (Agilent 8453A). Li_2S_6 was synthesized from the reaction of sulfur and lithium superhydride following the

previously reported method.[74] The ACN-TTE solvate (or TTE, TEGDME solvate) with saturated S_8 or Li_2S_6 at 70 °C was centrifuged and the supernatant was diluted using DOL at specific ratios for UV/VIS. Standards for calibration for each system were prepared by dissolving a known amount of the solute (S_8 or Li_2S_6) in the same mixed solvent as that for sample measurement. Details are discussed in following Sections. Cycled cells were dissembled inside the glovebox and the recovered electrodes were thoroughly washed with DME and transferred to the SEM in Ar-filled vials.

7.2.4 *Operando* X-ray Diffraction Study

Operando XRD was performed using a PANalytical Empyrean diffractometer outfitted with a PIXcel detector. A home-made Swagelok-type cell with a glassy-carbon window was used. The diffraction patterns were collected using Cu-K_α radiation in Bragg–Brentano geometry. The cell was cycled at C/30 rate with a pattern collection time of 15 mins (20-55°). Patterns were group-merged by three for peak area quantification. The amount of Li_2S, α-S_8 and β-S_8 are quantified by integrating the peak area of their corresponding major peaks, (022), (222) and (200), respectively. KB with 70 wt% of hand-ground bulk sulfur was utilized as the cathodes for optimal signal acquisition and electrochemistry.

7.2.5 *Operando* X-ray Absorption Near Edge Spectroscopy

The *operando* XANES study was carried out at the sector 9-BM-B in the Advanced Photon Source using a Si(111) crystal monochromator. The instrumental resolution in the energy range near the sulfur K-edge is about 0.35 eV, with a beam size of about 200 ×200 μm. All of the XANES studies were carried out under constant helium flow in the sample chamber and the data were collected in fluorescence mode using a 4-element vortex detector. Energy

calibration was carried out using sodium thiosulfate pentahydrate, with a pre-edge feature at 2469.2 eV. The cell used to perform *operando* XANES was adapted from the 2032 coin cells using an aluminized Kapton™ window.[13] Other modifications were limited to the electrode design: 50% of bulk sulfur was mixed with 40% of conductive carbon and 10% of PVDF to reach 50 wt.% sulfur and cast onto carbon paper.

7.3 Electrochemistry of the Sparingly Solvating Electrolytes

In **Figure 7.1**, the galvanostatic behavior of Li-S cells at a C/30 rate using ACN_2LiTFSI-TTE (1:1, v:v; denoted as ACN-TTE cell) electrolyte is compared to 1M LiTFSI in DOL:DME (1:1 , v:v) with 2 wt% $LiNO_3$ electrolyte (denoted as DOL:DME cell) as a function of operating temperature and electrode architecture. In **Figure 7.1a**, the electrochemistry in the DOL:DME catholyte provides facile kinetics and reasonable sulfur utilization at 30 ˚C. In contrast, the ACN-TTE cells generally show a large overpotential and low sulfur utilization. The use of melt-infused sulfur is necessary to obtain good sulfur utilization: the bulk sulfur electrode achieves way less than the melt-infused KB/S composite electrode, due to the greater contact of insulating sulfur with the carbon and thus a larger number of triple phase junctions, as shown in **Figure 7.1a**. Studies with cells that use micron-sized bulk sulfur are expected to shed light on the nature of electrochemistry that is truly intrinsic to sulfur – thereby providing mechanistic insights of the involved reactions.

Figure 7.1b shows the voltage profile at 55 °C. The DOL:DME cell at 55 °C shows electrochemical behavior similar to that at 30 ˚C. Evidently, increasing the temperature does not fundamentally alter the behavior of the catholyte cell, but promotes the transition to solid Li_2S, thus increasing the capacity allocation in the second plateau. In sharp contrast, the electrochemistry of the ACN-TTE cell is remarkably improved at 55 ˚C. The ACN-TTE cell

at 55 °C shows minimal polarization and excellent sulfur utilization of 1435 mA h g_s^{-1}. The polarization for the ACN-TTE electrolyte at 55 °C is even lower than that observed in DOL:DME, in fact. Furthermore, the CE during cycling is almost 100%, showing suppression of the polysulfide shuttle process even though no $LiNO_3$ additive was added to passivate the

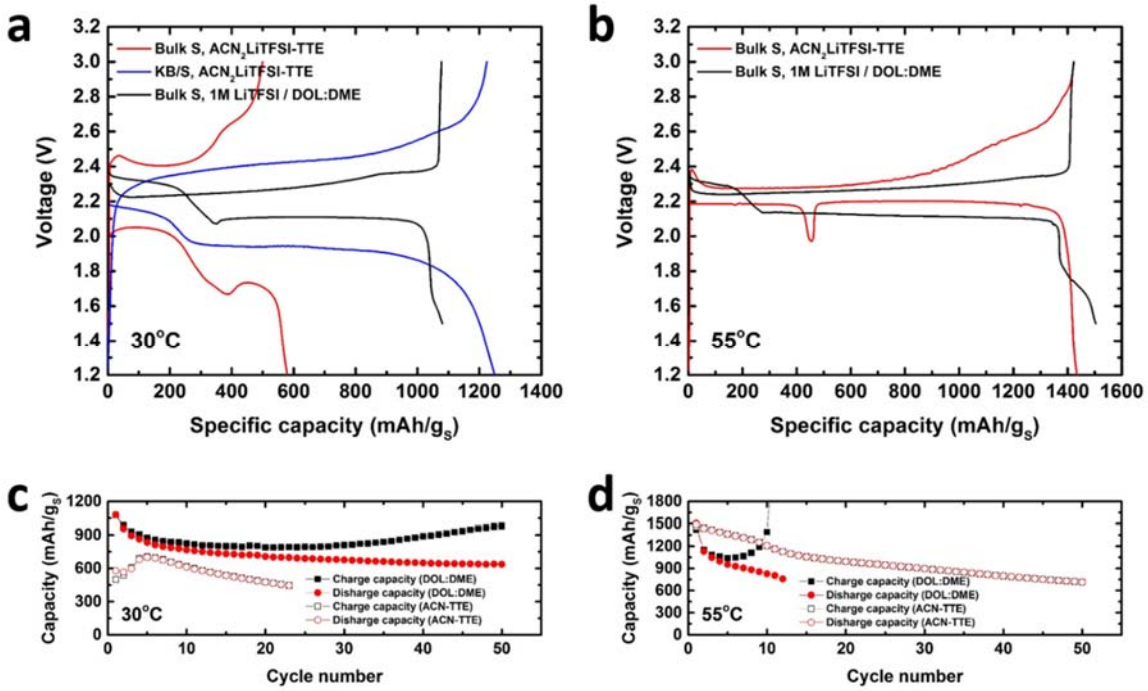

Figure 7.1 First cycle voltage profiles during galvanostatic cycling at a C/30. a) at 30 °C using bulk sulfur and KB/S electrodes in ACN-TTE compared to bulk sulfur electrode in DOL:DME and (b) at 55 °C using bulk sulfur electrodes in ACN-TTE compared with DOL:DME. The specific discharge/charge capacities over multiple cycles for bulk sulfur electrodes in ACN-HFE compared to DOL:DME (c) at 30 °C and (d) 55 °C.

negative electrode.[174] These electrochemical characteristics of the ACN solvate system are particularly noteworthy as the positive electrode uses only bulk sulfur as the active material, without any special electrode architecture.

Three additional features in the ACN-TTE sulfur electrochemistry measured at 55 ˚C are striking atypical. First, the 2.35 V plateau – characteristic of conversion of S_8 to long-chain polysulfides in conventional catholyte electrolytes – is absent in the ACN-TTE system. This fact reveals that the mechanism of sulfur reduction in the ACN solvate is different from that of conventional electrolytes.[78] Second, a noticeable voltage "dip" at *ca.*450 mA h g_s^{-1} during discharge separates the first and second plateaus. The presence of a voltage drop and the voltage recovery afterwards is often ascribed to a nucleation overpotential or supersaturation event preceding the onset of precipitation. Finally, the second plateau reveals a potential higher than that measured during the first 400 mA h g_s^{-1} of capacity. Open-circuit voltage (OCV) measurements - discussed at length later - confirm that a difference in equilibrium voltage is responsible for the voltage rise and not a kinetic factor.

Figure 7.1c,d show the capacity retention over 50 cycles of the cells utilizing ACN-TTE and DOL:DME electrolytes. As expected, the capacity retention of the DOL:DME cells are poor at the C/30 rate as a consequence of the highly active LiPS shuttle. At 55 ˚C, the LiPS shuttle effect is exacerbated and the CE quickly drops. On the other hand, ACN-TTE cells exhibit improved cycling behavior compared with DOL:DME cells, both at 30 ˚C and 55 ˚C. At 30 °C, the ACN-TTE cell requires a few initial activation cycles, but the capacity is delivered with >99% CE. At 55 ˚C, no activation is required and the ACN-TTE cell exhibits very high CE. However, capacity fade occurs, which could be related to other detrimental side reactions in addition to some crossover to the negative electrode.

To explore this, the lithium metal was isolated from the positive sulfur electrode. Our custom-made 2-compartment pouch cell incorporates an Ohara glass membrane: a single-ion conductor (denoted as Ohara-ACN cell).[175] Each compartment holds one layer of separator

wetted by electrolyte. The negative electrode compartment contained DOL:DME electrolyte interfaces with lithium. The positive electrode compartment contains ACN2LiTFSI:-TTE. The Ohara-ACN cell requires initial activation cycles, but the capacity is delivered with >99.5% of CE (**Figure 7.2**). Over 50 cycles after peak capacity, the Ohara-ACN cell shows 89% capacity

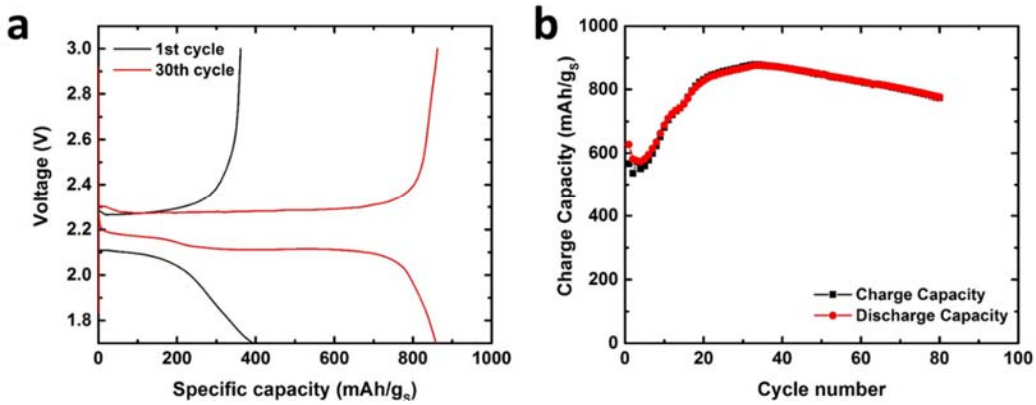

Figure 7.2 Electrochemical performance of the Ohara-ACN cell (a) voltage profile of the first cycle and 30th cycle at a rate of C/10 and (b) cycling performance over 80 cycles.

retention while the ACN-TTE cell shows only 48% capacity retention. Future studies with protected lithium electrodes would probe the underlying mechanisms at play more closely, but are beyond the scope of this thesis.

To confirm the very significant improvement found at moderate temperatures with the ACN2LiTFSI–TTE solvate electrolyte, KB/S and CMK-3/S melt-infused sulfur composites with nano-structured carboneous materials were also examined both at 30 ˚C and 55 ˚C (**Figure 7.3**). The melt-infused sulfur composites, KB/S and CMK-3/S, behave similarly at 30 ˚C, and both appear to promote greater utilization of sulfur than the simple physical mixture of bulk-sulfur and carbon black. However, all three sulfur electrodes exhibit striking similarities in the electrochemical discharge at 55 ˚C. Specifically, all cells show a plateau at the beginning of discharge, the characteristic dip at ~ 400-450 mA h g_s^{-1}, and the subsequent increase in voltage

on traversing the dip (**Figure 7.3b**). An encouraging result is that the capacity and cycling stability of bulk sulfur cells is comparable to the more elaborately architectured sulfur cathode electrodes at 55 ˚C (**Figure 7.3d**).

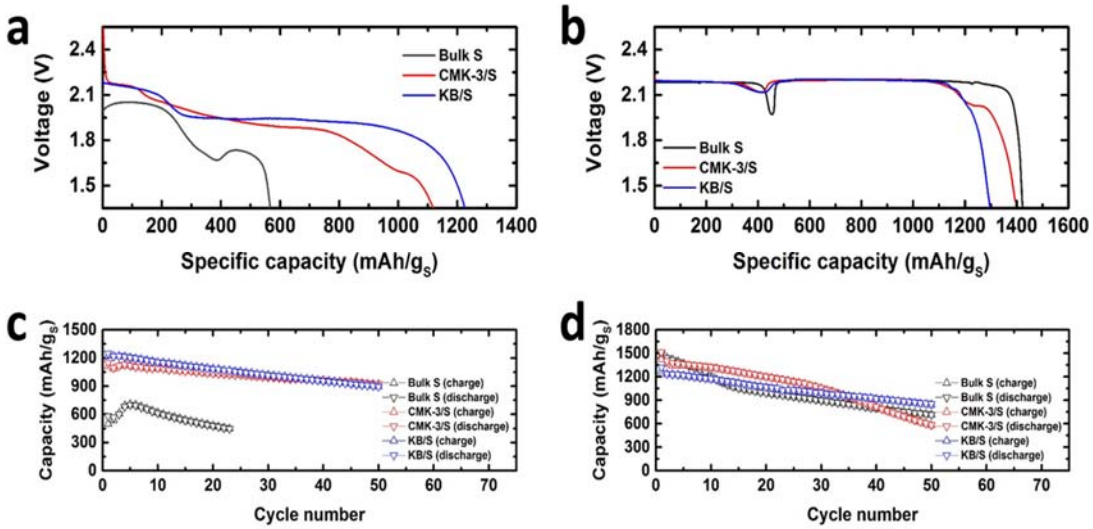

Figure 7.3 Electrochemical performance of bulk S, CMK-3/S and the KB/S nanocomposite. (a) Voltage profile of the first cycle at a C/30 rate at (a) 30 ˚C and (b) 55˚C. Cycling performance over 50 cycles at (c) 30 ˚C and (d) 55˚C.

To fully understand the effect of elevated temperature on the electrochemistry, the first cycle in separate ACN-TTE cells was measured at several temperatures, from 20°C to 70°C. **Figure 7.4a** shows the remarkable change of the system with temperature. At lower temperatures (less than 30 ˚C) a very large IR drop is observed at the start of discharge and the capacity is highly limited. At 37 °C, a significant increase in capacity is attained. The polarization in the initial discharge is reduced, a broad “dip” like feature starts to take shape, and more capacity is extractable beyond the dip albeit at a relatively low voltage of ~ 1.9 V due to severe polarization. Further increase in temperature leads to reduced polarization in both

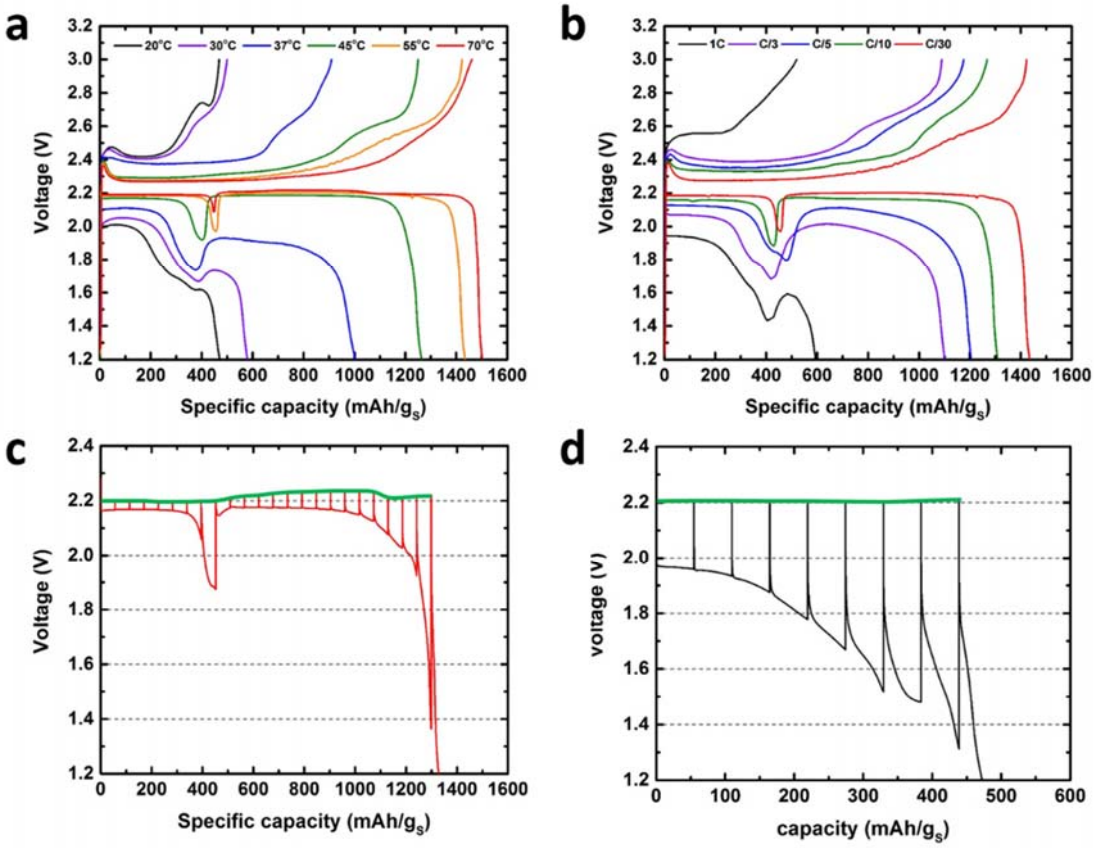

Figure 7.4 First cycle voltage profiles of bulk sulfur electrodes in separate ACN-TTE cells — (a) using C/30 rate and at indicated temperatures and (b) at a temperature of 55ºC but using various cycling rates ; GITT experiments using ACN-TTE cells at — (c) 55 °C and (d) 30 °C.

regions, before and after the dip, along with a concomitant increase in capacity. The voltage of the region beyond the dip starts to increase at 37 °C and becomes higher than the first plateau at 45 °C. Along with the activation of the reaction in the region beyond the dip, the sulfur utilization is also maximized to ~ 1503 mA h g_s^{-1} (~ 90% of the theoretical capacity) at 70 °C.

A very similar evolution of the electrochemical profile is also observed as a function of C-rate for the first cycle, illustrated in **Figure 7.4b**. This uncanny similarity - whether the

temperature or the rate of charge/discharge is changed - strongly suggests that kinetic factors affect the electrochemical response to a large extent, and particularly that of the second plateau.

As mentioned above, a small but clear increase in electrode potential occurs just past the dip. It is now shown that this does not arise from impedance contributions but is actually thermodynamic in origin. In **Figure 7.4c, d**, the GITT is used to examine the OCV (i.e. thermodynamic) of the cells using ACN-TTE electrolyte at both 55 ˚C and 30 ˚C. In the region before the dip, the quasi-equilibrium voltage attains a constant value of 2.20 V at 55 ˚C. Interestingly, the exact same OCV was obtained at 30 ˚C, which was masked during the discharge as in **Figure 7.1a** by a large overpotential (~ 200 mV larger than at 55 ˚C). As alluded to earlier, a low OCV of 2.20 V measured early in discharge points to a distinctly different reduction pathway. Additionally, the presence of a flat plateau up to *ca.*450 mA h g_s^{-1} suggests that the system exhibits classic two phase behavior; *i.e.*, direct conversion of S_8 to another product. This process is largely independent of the temperature of the reaction. The equilibrium voltage profile at 55 °C does not show the dip, indicating that the process corresponding to the dip is kinetically controlled. In the region past the dip the voltage response is complex – the OCV shows a small, continuous increase in the range of 400-1000 mA h g_s^{-1}, followed by small reduction towards the end of discharge.

To investigate how much the new Li-S cell reaction is affected by addition of TTE, the bulk sulfur electrode was examined in the solvate ACN_2LiTFSI electrolyte without TTE. In this electrolyte, the bulk sulfur electrode has almost no capacity at 30 ˚C (**Figure 7.5a**), which is ascribed to a high electrolyte viscosity that may prevent adequate wetting of the electrode. In sharp contrast, the same system at 55 ˚C shows a reasonably high capacity of ~1000 mA h g_s^{-1}, but an unstable first discharge profile, and poor reversible capacity and cycle life that are

also likely due to the high viscosity (**Figure 7.5b**). GITT dynamics comparing ACN_2LiTFSI *vs* ACN_2LiTFSI-TTE at 55 ˚C in the second plateau region are shown in **Figure 7.5c**. While the overpotential of ACN_2LiTFSI at 734 mA h g_s^{-1} is ~ 200 mV, much larger than that in ACN_2LiTFSI-TTE, the equilibrium voltage is the same in both cases. It is clear that the addition of TTE improves the kinetics without altering the inherent thermodynamics of the Li-S cell.

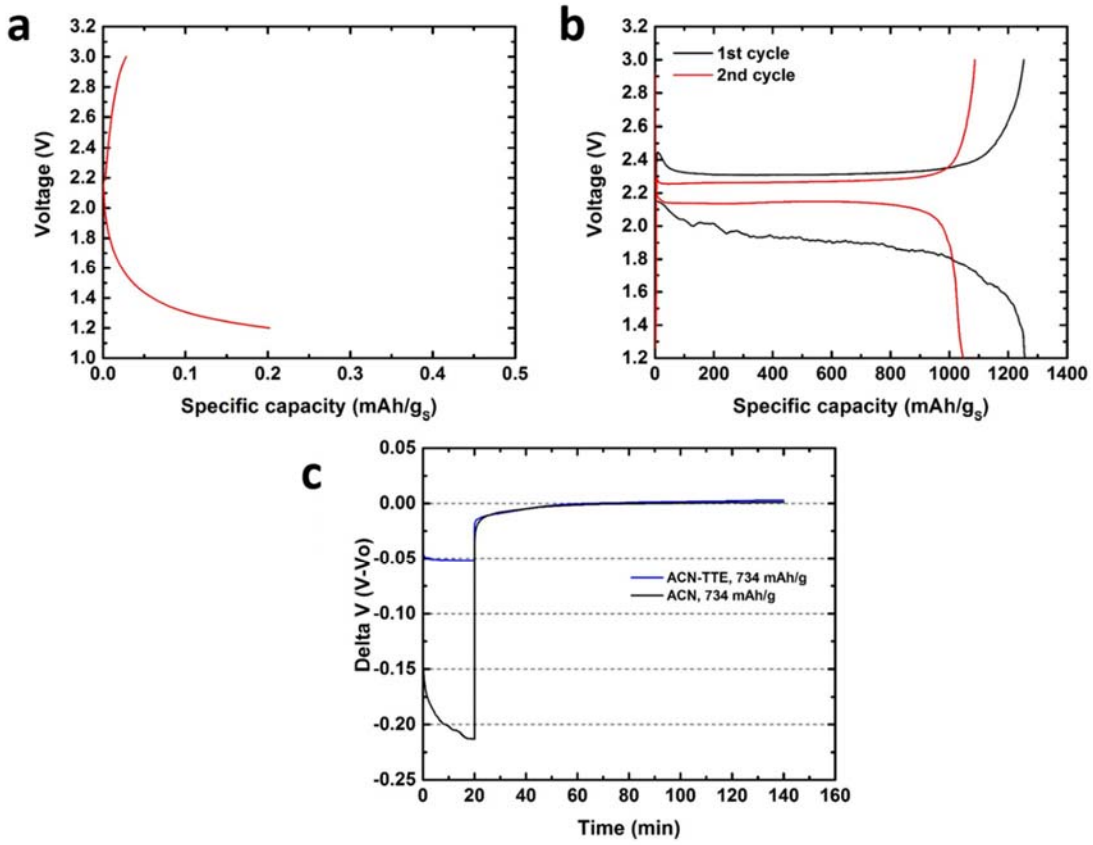

Figure 7.5 Electrochemical performance of bulk sulfur electrodes in ACN_2LiTFSI at C/30. Voltage profile of the (a) first cycle at 30 ˚C and (b) first and second cycle at 55˚C.

To investigate if the new electrochemical signature dip is a unique phenomenon of only ACN2LiTFSI, sulfur electrochemistry using 1M LiTFSI in ACN and another solvate electrolyte using THF, THF2LiTFSI-TTE was investigated. **Figure 7.6a** shows that the Li-S electrochemistry in 1M LiTFSI in ACN, using a cell with an Ohara glass membrane, matches that observed in other fully solvating systems such as DOL:DME. However, the Li-S electrochemistry measured in THF2LiTFSI-TTE closely resembled that of the ACN-TTE electrolyte (**Figure 7.6b)**. These electrolytes have a compact primary solvent molecule that has a single functional group in common which exhibits only moderate binding energy to Li^+ cations. [176] By demonstrating that both THF and ACN solvates support this new Li-S electrochemistry, it is proposed that several new electrolyte systems likely still exist to explored to examine structure-property relationships.

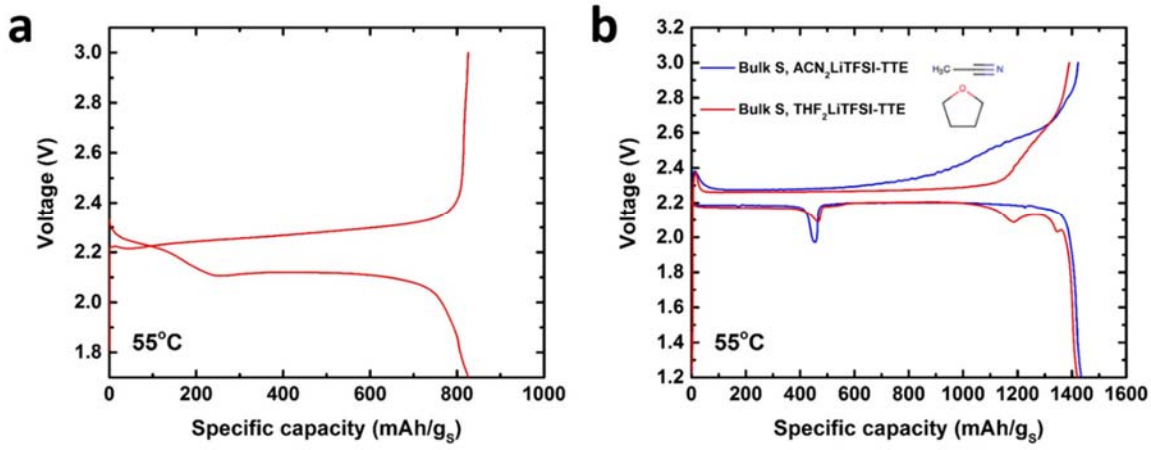

Figure 7.6 First cycle voltage profiles during galvanostatic cycling at 55 °C — (a) using 1M LiTFSI in acetonitrile in the positive electrode compartment of a cell with ohara glass membrane using C/10 rate and (b) comparison of cells with two different solvate electrolytes using a C/30 rate.

7.4 Polysulfide Solubility in Sparingly Solvating Electrolytes

As described earlier, the ACN-TTE cell shows a high capacity of ~1430 mA h g_s^{-1} at 55 ˚C, indicating a high sulfur utilization up to 86%. The enhanced sulfur utilization and lowered polarization compared to room temperature cells is significant and could be the result of enhanced reaction kinetics from increased polysulfide solvation, a solid-state reaction or other factors. To further probe the reaction mechanism, polysulfide solubility studies, structural characterization using *operando* XRD and XANES, and other physicochemical measurements were carried out. First, the ionic conductivity of ACN–TTE electrolyte increases only marginally to 2.64 mS cm^{-1} at 55 ˚C from 1.59 mS cm^{-1} at 27 °C (**Figure 7.7**). It is unlikely that such a small increase in ionic conductivity can solely explain the much improved and complex electrochemistry at moderately high temperatures.

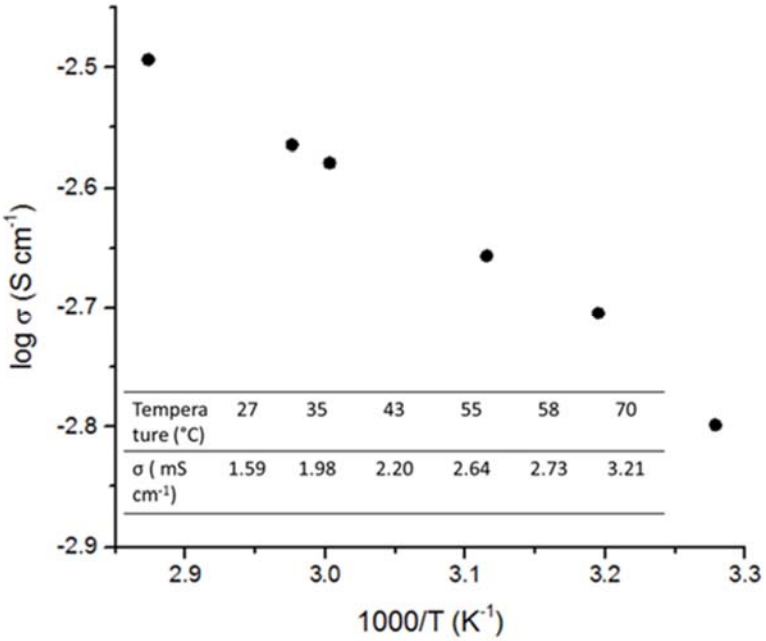

Figure 7.7 Plot and tabled data on the ionic conductivity of ACN_2-LiTFSI-TTE electrolyte at various temperatures.

I measured the solubility of elemental sulfur and polysulfides (using Li_2S_6 as the representative species) by UV-VIS spectroscopy at an elevated temperature of 70 °C. These results are shown **Table 7.1**. In all cases, the peak intensity of calibration standards (at *ca.*315 nm for Li_2S_6 and 265 nm for S_8) shows a linear relationship with respect to the concentration of solutes, in a range that includes the sample to be measured (marked as the red asterisks, **Figure 7.8e-g**). The room temperature solubility of Li_2S_6 in ACN-TTE was below the detection limit of the UV-VIS spectrometer. In contrast to the colorless solution at room temperature, the ACN-TTE electrolyte saturated with Li_2S_6 shows a pale yellow color at 70 °C, indicating some solubility (**Figure 7.8**). No precipitation occurred after the solution was cooled down to room temperature, even after two weeks.

As quantified by UV-VIS spectroscopy at 70 °C, the ACN-TTE electrolyte can dissolve 0.20 mg mL^{-1} of Li_2S_6, which corresponds to 0.2% of the total Li_2S_6 in a cell with an electrolyte to sulfur ratio of 10 µL mg^{-1} (if all the sulfur converted to Li_2S_6), or 0.02% at the target ratio of electrolyte to sulfur of 1 µL mg^{-1}. In stark contrast, G4-LiTFSI solvate solubilizes *ca.*100% of the Li_2S_8 at an electrolyte to sulfur ratio of 4 mL g^{-1}.[177] Also, sulfur exhibits one order of magnitude lower solubility (**Table 7.1**), excluding its role in enhancing the reaction kinetics.

Table 7.1 Solubility limit of S_8 and Li_2S_6 determined using UV-VIS spectroscopy at an elevated temperature of 70 °C (or RT) for different solvent/electrolytes (a: Values taken from Ref. 79)

Solubility limit (mg/ml)	TTE	ACN-TTE	G4-LiTFSI	G4-LiTFSI @ RT [a]
Li_2S_6	0.11	0.20	4.90	0.57 (Li_2S_4)
Sulphur S_8	0.013	0.035	*NA*	0.19

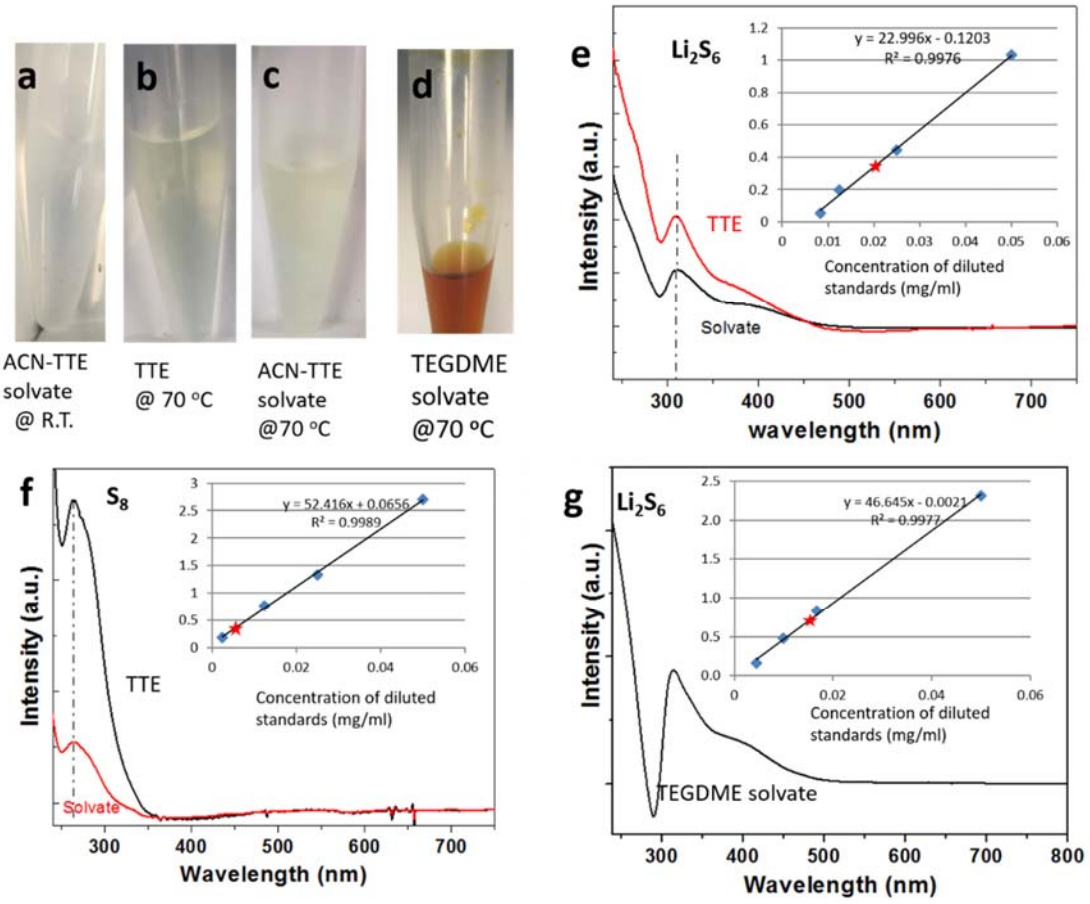

Figure 7.8 Polysulfide solubility measurement. Visual confirmation of polysulfide solubility in (a) ACN solvate at R.T. (b) TTE at 70˚C (c) ACN-TTE solvate at 70˚C and (d) TEGDME solvate at 70˚C. Representative UV-vis spectra of (e) Li_2S_6 and (f) S_8 in ACN-TTE solvate and TTE and (g) Li_2S_6 in TEGDME solvate; insets are the representative calibration curves for Li_2S_6 in ACN solvate (e), S_8 in ACN solvate, (g) Li_2S_6 in TEGDME solvate.

These results confirm ACN-TTE sparingly solvates polysulfides at elevated temperature. This small but likely essential solubility could mediate an otherwise solid-state reaction and improve the kinetics. Note that the ACN-TTE electrolyte shows almost double the solubility compared to pure TTE, indicating that the solubility is not solely attributable to the TTE solvent,

but is likely due to the altered complexing behavior of the solvate at elevated temperatures – for instance, the presence of some free ACN solvent due to a shifted equilibrium. [178]

The G4-LiTFSI solvate consisting of an equimolar ratio of TEGDME and LiTFSI, monitored using the same procedure, dissolves 25 times more Li_2S_6 (**Table 7.1**). Interestingly, however, G4-LiTFSI does not show major changes in its electrochemical properties upon increasing temperature, much in the same way that DOL:DME does not. GITT studies show the G4-LiTFSI solvate exhibits an OCV of 2.35 V in the initial discharge - characteristic of conversion of S_8 to long-chain polysulfides - followed by a second plateau of a lower voltage (**Figure 7.9**). Clearly, increasing the solubility beyond a certain range might not necessarily be beneficial and/or only increasing the solubility is not sufficient to alter the electrochemistry. Fine details of the solvate chemistry and structure may play a preeminent role in determining the nature of the solubilized intermediates. In fact, Dunning *et al*. suggest a reactant solubility of the order of 1×10^{-4} M (i.e. 0.02 mg ml^{-1} for Li_2S_6) is desired for long-lived and high-rate capability batteries based on precipitation/dissolution chemistry.[179]

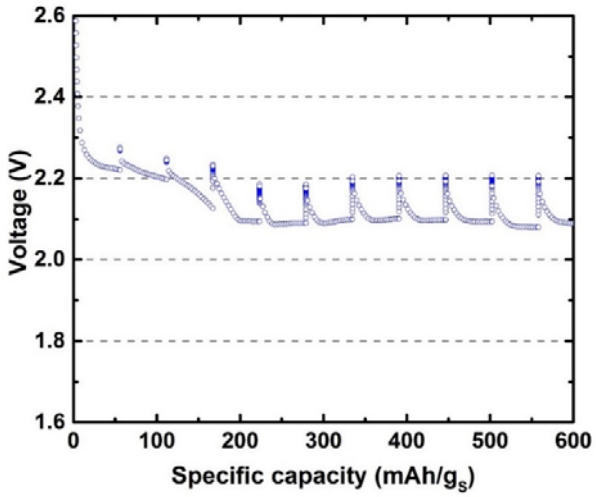

Figure 7.9 GITT experiment using the G4-LiTFSI solvate showing the OCV response in the first plateau.

7.5 *Operando* X-ray Studies on the Reaction Pathways

Operando XRD was performed to understand the time-resolved evolution of crystalline species in the sparingly solvating electrolyte system. Although the formation of crystalline Li_2S upon discharge and re-formation of sulfur were observed for both ACN-TTE and DOL:DME systems (**Figure 7.10a** and **b** respectively), their evolution of S_8/Li_2S is quite different. The individual diffraction patterns as a function of discharge/charge are shown in **Figure 7.10c** and **e**, respectively as "waterfall" plots. The evolution of elemental sulfur/Li_2S was quantified by integrating the respective major peak areas in these patterns, and are presented along with the corresponding electrochemical profiles in **Figure 7.10d** and **f.**

On discharge, compared to the DOL:DME electrolyte where rapid consumption of sulfur is completed before the supersaturation point (first purple region, **Figure 7.10d**), the ACN-TTE cell exhibits more gradual consumption of sulfur (purple region) which is complete only at the end of the second plateau (first pink region, **Figure 7.10f**). However, no other crystalline phase is detected. For ACN-TTE, after the first plateau, crystalline Li_2S starts forming before the very end of the voltage 'dip' (pink region, **Figure 7.10f**), which may indicate a nucleation overpotential for the crystallization of Li_2S. However, the voltage rise in the OCV at this point also suggests the concurrent formation of soluble longer chain polysulfides such as Li_2S_6 *via* a disproportionation reaction that forms Li_2S. In summary, the linear increase of Li_2S and an almost constant amount of sulfur over the second plateau (green region, **Figure 7.10f**) suggests a two-phase reaction to form Li_2S from the disproportionation of $Li_2S_{2\text{-}4}$ that involves sulfur. At the very end of discharge (corresponding to the third plateau in GITT study), sulfur is fully consumed resulting in the voltage drop.

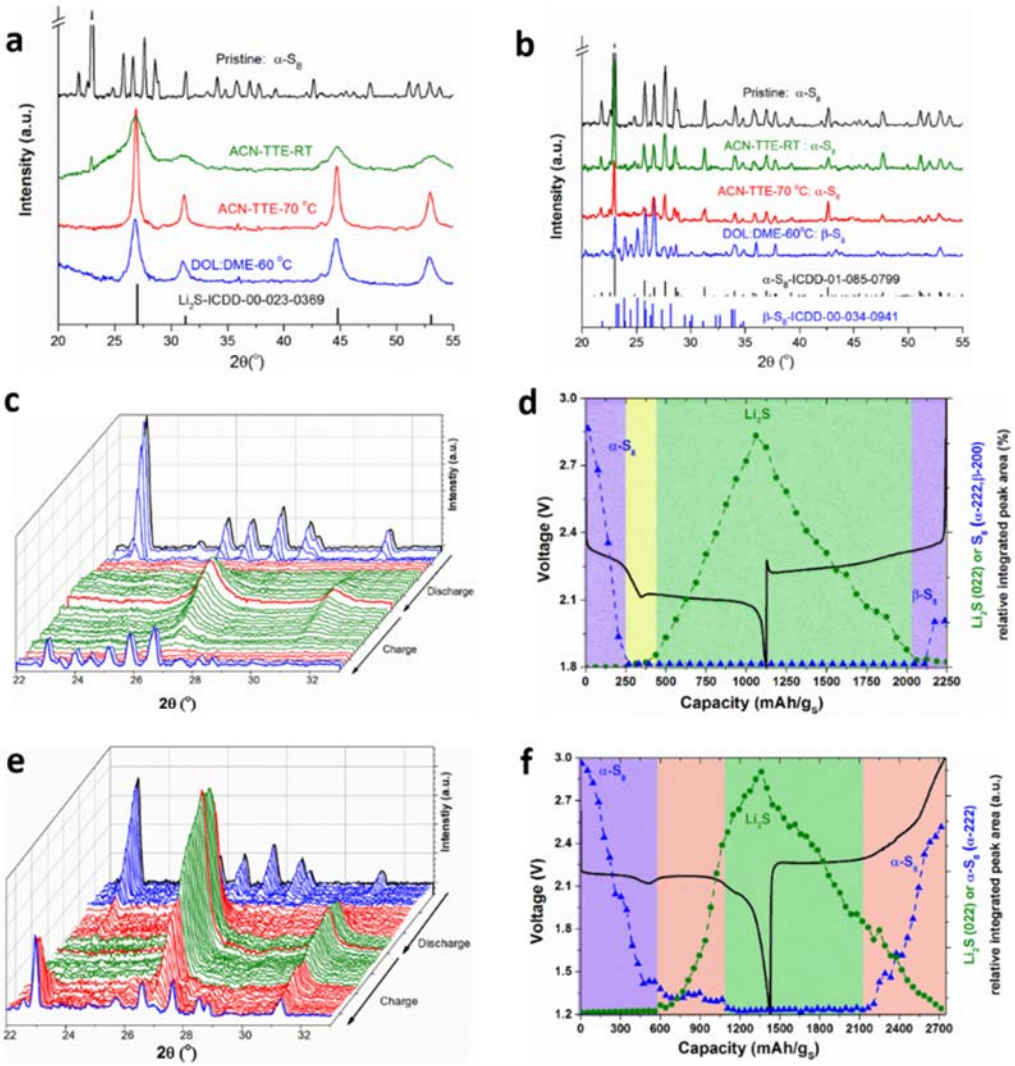

Figure 7.10 *Operando* XRD studies of the electrolytes using ground KB-S electrodes — The XRD patterns of cathodes (a) after 1st full discharge and (b) after 1st full charge in ACN-TTE and DOL:DME electrolytes at RT or elevated temperatures, along with that of the pristine electrode. (c, e) The waterfall diagrams showing the evolution of XRD patterns (22-33°) obtained *operando* as a function of discharge/charge states and (d, f) the peak-area quantified evolution of crystalline sulfur (α- or β-S_8, blue dotted lines) and Li_2S (green dotted lines) phases as a function of the capacity, during the 1st full cycle for cells in (c) the DOL:DME electrolyte at 60 °C and (e) the ACN-TTE electrolyte at 70 °C. The red patterns in the central position of (c, e) indicate the end of discharge; the colors in (d, f) code distinct stages with different compositions in terms of the presence of S_8 and Li_2S (blue: only S_8; green: only Li_2S, yellow: neither S_8 or Li_2S; red: both S_8 and Li_2S).

A salient contrasting feature of the two electrolyte systems is apparent on charge. While both commence discharge with orthorhombic α-S_8, after charge, the ACN-TTE cell maintains the α-phase. However, a metastable monoclinic β-S_8 is obtained for the catholyte DOL:DME cell, consistent with that previously reported. [16] This strongly suggests that a different conversion pathway exists for the ACN-TTE solvate, although its exact nature is still unclear. [180] Furthermore, for the DOL:DME system upon charge, sulfur formation begins only toward the final stage of charging ($S_8^{2-} \rightarrow$ β-$S_8 + 2e^-$; purple region in **Figure 7.10d**); however, sulfur forms much earlier for the ACN-TTE cell, just before the voltage rise (pink region, **Figure 7.10f**). This early onset of sulfur formation indicates a more facile oxidation of short to mid chain length polysulfide intermediates directly to sulfur. The co-presence of solid S_8 and Li_2S in ACN-TTE (the red region in **Figure 7.10f**), in contrast to their mutually exclusive presence in the DOL:DME system (purple and yellow regions in **Figure 3d**), demonstrates a quasi-solid-state reaction in the ACN-TTE system that is not dominated by polysulfide solution mediation. The S_8/Li_2S evolution at room temperature for the ACN solvate system shows a similar trend to that at elevated temperature (**Figure 7.11**), although more unreacted S_8 is present on discharge. This means that sparing solvation at elevated temperature does not affect the products of discharge/charge, but only alters the speciation pathway, as described above in the GITT studies.

In order to confirm that polysulfide species are formed prior to the 'dip', even during elevated temperature operation, *operando* XANES experiments were carried out. The data are qualitative rather than quantitative owing to spectral distortion from self-absorption of the large sulfur particles, as discussed below.

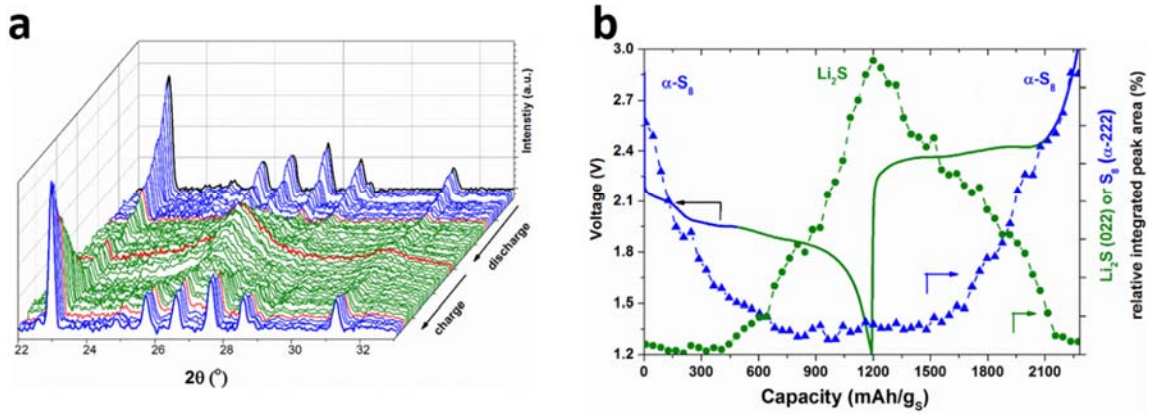

Figure 7.11 *Operando* XRD of ACN-TTE solvate at RT. (a) The waterfall plots showing the evolution of XRD patterns (22-33°) obtained *operando* as a function of discharge/charge states and (b) the peak-area quantified evolution of crystalline sulfur (α-S_8, blue dotted lines) and Li_2S (green dotted lines) phases as a function of the capacity, during 1st full cycle for the cell in the ACN-TTE solvate electrolyte. The red pattern in the center of (a) indicates the end of discharge

Figure 7.12 shows the first discharge raw XAS data performed *operando* at 60 ºC to monitor the sulfur speciation in ACN-TTE cell in the region prior to the 'dip'. The S K-edge XAS studies of this system suffers from two main complications: 1) the solvate electrolyte contains a significant amount of sulfur that contributes a large parasitic background signal. This signal can be potentially subtracted but is a source for systematic errors; 2) sulfur in the electrode is present as micrometric particles and the loading is very high. This causes severe, non-linear, self-absorption distortions of the XAS signal. The amount of distortion seen for sulfur in the starting electrode is consistent with that expected for *ca.*2 µm sulfur particles, gauged by comparing to the work of Pickering et al.[181]

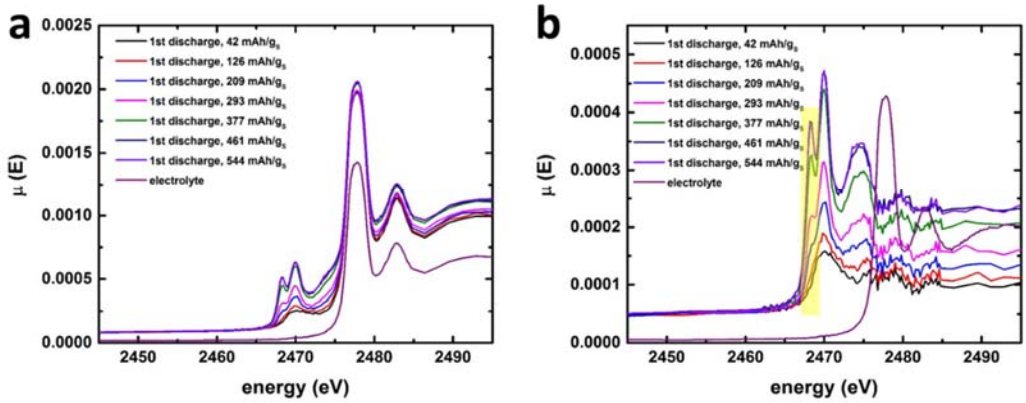

Figure 7.12 (a) Raw XANES curves prior to the 'dip' at first discharge (b) the unnormalized raw XANES curves after subtraction of the sulfur electrolyte signal with an ACN-TTE cell that uses bulk sulfur electrodes at 60 ºC

Figure 7.12b illustrates the unnormalized raw data after subtraction of the sulfur electrolyte signal. For comparison, a scaled signal of the electrolyte only is also shown. Onset of discharge leads to significant changes in the sulfur signal, with the following main findings. 1) A pre-edge peak at *ca.*2468.25 eV, representing polysulfide dianions highlighted by the yellow box, is seen early in discharge and grows significantly as discharge progresses. Given the low solubility of polysulfides in the electrolyte (**Table 7.1**), the pre-edge signal is ascribed to an amorphous or poorly crystalline polysulfide species (invisible to XRD). 2) Trisulfur radicals ($S_3^{\cdot -}$) are known to exhibit a characteristic feature *ca.*2 eV lower than that seen for dianions.[182] The absence of a clearly observable feature in that region in **Figure 7.12b** indicates that trisulfur radicals, if present, are below the detection limit. 3) The increase in pre-edge intensity is accompanied with the development of another relatively sharp feature at *ca.* 2474.75 eV. Such a feature is not seen for long-chain polysulfides and therefore provides

circumstantial evidence for the presence of medium-to-short chain polysulfides, Li_2S_n (n>4).[13,78,167,182,183]

In agreement with prior room temperature studies, lithium polysulfides are indeed generated upon the initiation of discharge (**Figure 7.12**). As mentioned earlier, XRD experiments do not identify the formation of any new crystalline phase prior to the dip in ACN-TTE cells, irrespective of the temperature at which the electrochemistry is performed. Amorphous discharge products, however, are invisible by XRD. Evidently, the early formation of Li_2S_{2-4} species results in the lower first-plateau voltage of the ACN-TTE cells.

7.6 Postmortem Imaging on the Electrodes

Ex-situ postmortem SEM studies were used to image the cathode surface morphology after first discharge and the sulfur elemental distribution on Li anodes after a full cycle. The EDX mapping of the pristine cathode shows the presence of bulk sulfur as micron-sized particles (**Figure 7.13a**). After the first discharge, the cathode run in DOL:DME shows an agglomerated layer of the discharge product (Li_2S) on the surface facing the electrolyte (**Figure 7.13b**). This is the direct consequence of the high solubility of polysulfides. However, the cathode run in the ACN-TTE electrolyte preserves the morphology of the pristine electrode without any signs of a agglomerated Li_2S layer (**Figure 7.13c**). The EDX sulfur mapping in the ACN-TTE system shows that the sulfur particles remain as distributed as in the pristine electrode, although a small reduction in the particle size compared to the pristine electrode cannot be ruled out. The Li metal anode surface was also examined after one full cycle. The pristine Li anode has a clean surface (**Figure 7.13d**). The Li anodes in the DOL:DME electrolyte show a rough surface with a porous layer, in contrast to the smooth surface exhibited for the ACN-TTE electrolyte (**Figure 7.13e,f**). Furthermore, a factor of ten less sulfur was found compared to the

DOL:DME cell (*ca.*0.4 at.% vs 3.8 at.%), as determined by EDX spectra (inset **Figure 7.13e,f**). This suggests a quasi-solid-state reaction with only minimal polysulfide shuttling.

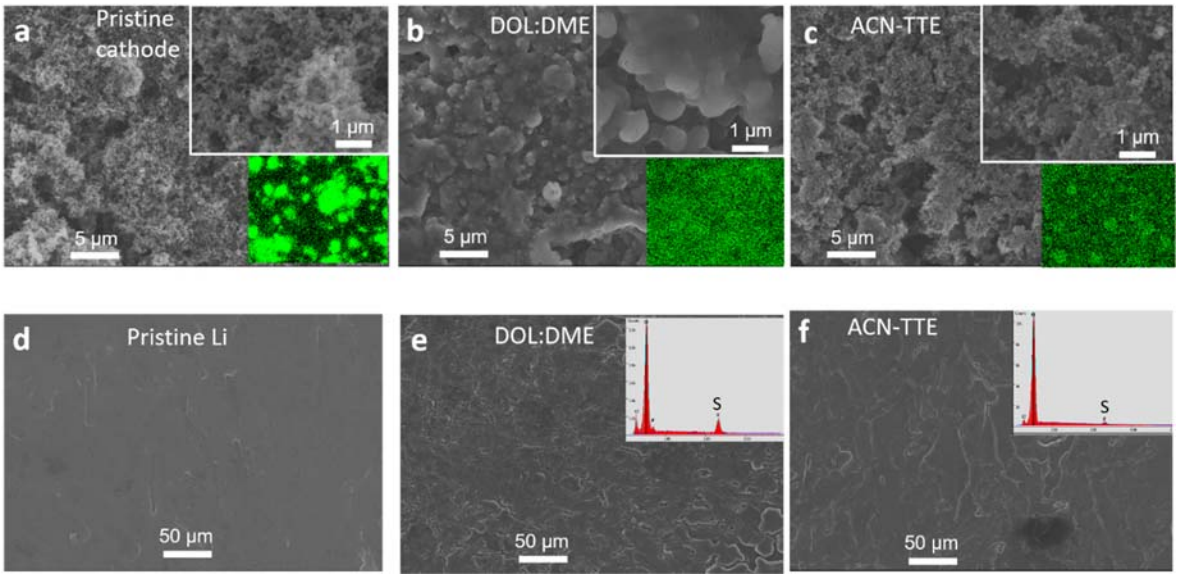

Figure 7.13 *Ex-situ* SEM images and EDX of the bulk sulfur cathodes and Li metal anodes at different states. (a-c) The SEM images (and enlarged, insets) and EDX sulfur mapping (insets) of (a) pristine cathodes, (b,c) cathodes after 1st discharge in (b) DOL:DME and (c) ACN-TTE solvate electrolytes. (d-f) The SEM images and EDX spectra (emphasizing the S signal) of the pristine Li and (e,f) Li anodes after the 1st full cycle in (e) DOL:DME and (f) ACN-TTE solvate electrolytes. Cells were cycled at 55 °C and a C/30 rate.

7.7 Proposed Reaction Pathways

Based on the observations reported above, the following reaction scheme is proposed for discussion. Clearly more work is needed for definitive proof of chemical speciation; however, it is believed the following reaction sequence on discharge is supported by the work presented herein. Only two electrochemical reactions are proposed with equilibrium potentials suggested

by observations made in the GITT study. The first reaction, **Equation 7.1**, is hypothesized to be the direct formation of a polysulfide species $Li_2S_n \cdot (4\text{-}n)S$ (i.e. Li_2S_4) in a two phase process. The nominal stoichiometry Li_2S_4 is suggested based on Faraday's law; the observation of mid to short chain polysulfides in XAS; and the absence of other crystalline species in XRD. **Equation 7.2** corresponds to the reduction of a polysulfide with some small but essential solubility in the electrolyte, here referred to as Li_2S_6, although LiS_3 is also possible. The remaining reactions are chemical in nature and do not require electron transfer to proceed. It is noted that the proposed reaction mechanism is not symmetrically reversible owing to disproportionation, as shown by the *operando* XRD.

$\frac{1}{2}S_8 + 2Li^+ + 2e^- \leftrightarrow Li_2S_4$	U = 2.2 V	(**Equation 7.1**)
$\frac{1}{2}Li_2S_6 + Li^+ + e^- \leftrightarrow Li_2S_3$	U = 2.3 V	(**Equation 7.2**)
$Li_2S_3 + Li_2S_4 \leftrightarrow Li_2S + Li_2S_6$	redox mediation	(**Equation 7.3**)
$Li_2S_3 + 1/8S_8 \leftrightarrow Li_2S_4$	S_8 consumption	(**Equation 7.4**)
$Li_2S_3 \leftrightarrow Li_2S + \frac{1}{4}S_8$	Li_2S_3 consumption	(**Equation 7.5**)

It is believed that the role of increasing temperature is to raise the concentration of a key reactant in the electrolyte, **Equation 7.2**. This increased reactant concentration may be the result of higher solubility and/or increased driving force for the cleavage of a divalent polysulfide into a monovalent radical such as shown in **Equation 7.6**.

$Li_2S_{6\,(s)} \leftrightarrow Li_2S_{6\,(l)} \leftrightarrow 2LiS_{3\,(l)}$ (**Equation 7.6**)

To examine the feasibility of the proposed scheme, a kinetic model was created and solved numerically to generate a voltage profile, track temporal speciation, and quantify reaction rates. The intermediate LiS_3 was assumed to undergo rapid chemical reaction by **Equations 7.3-7.5** to minimize the number of unknown parameters to be fit. **Figure 7.14** illustrates the results for one set of rate constants for discharge at the C/30 rate. The model is able to recreate the voltage dip and higher voltage during the middle third of discharge as reported experimentally. Herein lies the counter-intuitive nature to this new pathway, which can be described as the following. The first reaction **Equation 7.1** is more facile than the rest and thus controls the initial discharge voltage. This is readily observed in **Figure 7.1**, where less polarization is observed during the initial discharge. However, once reaction **Equation 7.1** has consumed a majority of sulfur, another reaction must carry the current or else the discharge will cease.

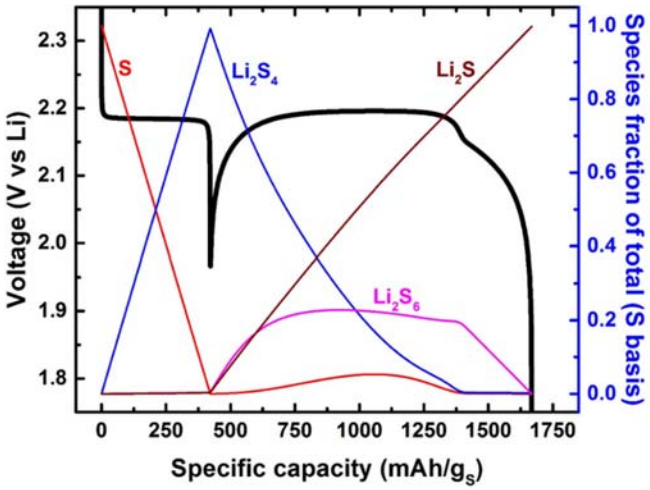

Figure 7.14 Simulated voltage curve using a kinetic model with a set of rate constants for discharge at the C/30 rate.

Our proposed scheme suggests the equilibrium established by reaction **Equation 7.2** and **7.4** will generate a very small, but finite quantity of a soluble polysulfide species from the existing Li_2S_4 generated by reaction **Equation 7.1**. These polysulfides are referred to here as Li_2S_6 but others are also possible. The dip observed during discharge is the overpotential necessary to drive reactions **Equation 7.2** and **7.3**, which then generates greater quantities of Li_2S_6 lowering the overpotential for further production. This auto-catalytic type behaviour results in a quick rise in the potential if the electrolyte can solubilize the important redox mediator. The solution concentration of the reactant is the difference between room temperature and moderate temperature electrochemistry. Once sufficient polysulfide solubility is reached, the redox mediation of S_8 and Li_2S_4 allows for high specific capacities to be accessed with minimal overpotential.

The question remains as to why **Equation 7.1** is favored in the ACN-TTE class of electrolytes over the formation of long-chain polysulfides observed in traditional catholyte electrolytes such as DOL:DME, **Equations 8.7-8**.[40]

$S_8 + 2Li^+ + 2e^- \leftrightarrow Li_2S_8$ $U^o = 2.39$ V (**Equation 7.7**)

$3/2\ Li_2S_8 + Li^+ + e- \leftrightarrow 2Li_2S_6$ $U^o = 2.37$ V (**Equation 7.8**)

It is hypothesized that the dramatically reduced solubility of polysulfides hinders the reaction kinetics of the traditional pathway to the point where **Equation 7.1** is favored. The competition between a solution pathway and a quasi-solid-state pathway likely always exists. In DOL:DME, the solution pathway kinetics are at least an order of magnitude more facile and thus the mixed potential is set by the solution pathway shown in **Equations 7.7-8**. Conversely in an electrolyte system that minimizes the solution reduction of S_8 to Li_2S_8 and all the following redox mediation, a classic two-phase reaction occurring at 2.2 V is observed.

The voltage response in the regions dominated by S and Li_2S_4 (**Figure 7.14**) suggests little dynamic change in solution concentration (i.e. rapid dissolution and precipitation at the solubility limit) or the process proceeds in the solid-state via a chemical transformation absent of concentration gradients. The term quasi-solid-state is used to describe this reaction. XRD and XAS studies leave unanswered questions to the exact speciation and mechanism. However, it is believed that this unique pathway will be more completely elucidated through future complementary *operando* experiments.

7.8 Conclusions and Thoughts

In Li-S batteries, the use of sparingly solvating electrolytes provides a unique approach to control reactant distribution and hence the electrochemistry of the cell, while suppressing the solubility of polysulfides. While such sparingly solvating systems such as the ACN_2TFSI-TTE system examined here are effectively "non-solvent" electrolytes at room temperature –which results in significant cell polarization – moderately raising the temperature promotes the solubility of key reaction intermediates. It enables operation at practical rates with minimal overpotential.

More importantly, the electrochemical profile is profoundly changed by comparison to that observed in fully solvating electrolytes such as the well-known DOL:DME system. While lithium sulfide, Li_2S, is formed on discharge and consumed on charge as proven by *operando* XRD measurements, the very low but non-negligible solubility of polysulfides in the ACN_2TFSI-TTE electrolyte fundamentally alters the pathway to form Li_2S. This gives rise to a quasi-solid state reaction and minimal polysulfide shuttling. The initial formation of intermediate-to-short chain polysulfides are also in sharp contrast to a typical solvated

electrolyte system where long-chain polysulfides are favored at the start. It is believed this owes to a change in relative kinetic rates for competing reactions, because the dramatically reduced solubility of both elemental sulfur and polysulfides hinders the reaction kinetics of the traditional pathway.

Pairing sparingly solvating electrolytes with a protected Li-metal anode is the next step in the path to mitigate the polysulfide shuttle effect, and reach a high-energy density, and long lived Li-S battery by minimizing electrolyte volume and polysulfide cross-over. More generally, however, this discovery opens the door to tailored design based on modifying the electrolyte local environment to tune and ultimately control the reaction pathway of many precipitation-dissolution chemistries.

Chapter 8 Conclusions and Future Prospects

8.1 Conclusions

This thesis presents a wide spectrum of approaches to tackle the polysulfide shuttling and to build long-lived and high energy density Li-S batteries. That includes studies on a series of sulfur host materials and a class of sparingly solvating electrolyte. The host materials for cathodes should generally be light-weight, highly polar, exhibiting chemical interaction with polysulfides and highly conductive. The sparingly solvating electrolytes are desired to possess low and controllable polysulfide solubility, high ionic conductivity and good wetting properties.

In **chapter 3**, I described a strong chemical interaction to confine LiPSs within a graphene-like Co_9S_8 nanosheet material that exhibits both metallic conductivity and hierarchical porosity. A scalable microwave solvothermal approach was utilized for the synthesis of this unique graphene-like structure. The interconnected nanosheets form 3D networks; in contrast to electrodes consisting of individualized nano-particles sulfur composite,[93] this networking structure enables high sulfur loading electrodes with stable cycling. First-principles calculations and XPS studies consistently demonstrate the coupled interaction of Co_9S_8 with Li_2S_n that relies on S_n^{2-}-$Co^{\delta+}$ and Li^{+}-$S^{\delta-}$ (of Co_9S_8) binding. It was also shown that with these intrinsic active sites, the as-synthesized Co_9S_8 exhibits far superior LiPSs adsorptivity than standard carbon materials. An ultralow capacity fading rate of 0.045% per cycle over 1500 cycles was achieved based on the Co_9S_8 based composite. Importantly, high sulfur content electrodes, up to 4.5 mg cm^{-2} loading, were shown with stable cycling over

150 cycles, demonstrating their advantage in building high energy density Li-S batteries. The significance of this study is that this concept extends to other metal sulfide/oxides, and pioneered or inspired some other studies to find the optimal metal sulfides based hosts that have both high conductivity and polysulfide adsorption, such as CoS_2, FeS_2, SnS_2.[184-187]

Utilizing metal compounds as the sulfur host materials, such as cobalt sulfides, is scientifically interesting as to strongly bind polysulfides and to control the Li_2S deposition, but they are relatively heavy and thus require high surface area, which adds to the cost. In **Chapter 4**, departing from this path, a dual-doping strategy was utilized on porous carbon using sulfur and nitrogen atoms at a relatively high doping concentration. N and S dual-doped carbon has been suggested to exhibit asymmetric charge density distribution. In this study, the interaction between LiPSs and the dual-doped carbon was examined using a combination of XPS and first-principles theoretical calculations. I demonstrate a greatly improved chemical interaction of the dual-doped carbon with LiPSs having electrophilic Li^+ and nucleophilic terminal S^-. This synergistic effect arises from N-Li and S-S interactions and leads to doubled LiPS adsorptivity over N single-doped or non-doped carbons. In addition, the dual-doped carbon exhibits a significant increase of conductivity, benefiting the power capability of a Li-S cell. This is the first time that a dual-doped carbon has been utilized as a sulfur host material with demonstrated chemisorption mechanisms, pioneering among other works on dual-doped carbons.[113,188-190] Moreover, the synthesis of mesoporous carbons typically requires the use of exotic hard templates and/or expensive surfactants as well as high-cost polymeric carbon sources involving complex procedures. However, in **Chapter 4**, a completely different route was applied to prepare this porous carbon by a low-cost biomaterial, cellulose nanocrystals. The porous structure was created based on a liquid-crystal driven self-assembly of CNCs. The dual-doped

carbon exhibits a tunable hierarchical pore structure with a high surface area. The as-made sulfur electrode was able to deliver a high capacity of 1370 mA h g^{-1} at C/20 rate and to sustain 1100 cycles with a very low capacity fading of 0.052% per cycle at 2C rate.

In **Chapter 5**, a different approach than using metal ox- or sulf-ides or doped carbon was taken by using graphitic carbon nitride (g-C_3N_4). This material incorporates multiple advantages that can be found from previously reported hosts, being light-weight, highly active polysulfide adsorption sites, high concentration of these sites (53.5 at%), although it is inferior in electronic conductivity. It has a layered structure as graphene, but is orderly composed of tri-s-triazine building blocks. The intrinsic high charge polarity of g-C_3N_4 embraces enriched LiPS binding sites, that is, pyridinic N, as quantitatively demonstrated with first-principles calculations. The nature of the interaction between g-C_3N_4 and LiPS, revealed for the first time by FTIR and XPS studies, shows a favorable Li^{+}-$N^{\delta-}$ interaction. This provides superior LiPS adsorptivity, which not only leads to controlled precipitation of the Li_2S upon reduction of LiPSs, but also of sulfur upon oxidation. Additionally, the polymeric nature of g-C_3N_4 allows for structural elasticity that benefits accommodating the volume expansion upon formation of Li_2S. Excellent long-term cycling performance of the g-C_3N_4/S75 electrode was obtained in a Li-S cell, with as low as 0.04% capacity fade per cycle over 1500 cycles at a C/2 rate. More importantly, high sulfur loading electrodes with up to 4.2 mA h cm^{-2} capacity and stable cycling performance were also demonstrated. This lays the footstone for the work in **Chapter 6**.

With a practical goal of constructing high areal loading electrodes and using a low volume of electrolyte, in **Chapter 6**, a multifaceted strategy was presented that is based on conventional slurry process, by coupling multifunctional sulfur composites with an *in-situ*

cross-linked polymeric binder. First, by alternate stacking of two layered materials components, graphitic C_3N_4 and graphene, a hybrid sulfur host material was obtained with both strong chemical LiPSs adsorption and high electronic conductivity. By cross-linking a low fraction of 5 wt% of the CMC binder *in-situ*, crack-free high sulfur loading electrodes up to 14.9 mg cm^{-2} were achieved. Most importantly, owing to the compact structure of the cathodes, an electrolyte/sulfur ratio as low as 3.5:1 (µl:mg) allows high areal capacities up to 14.7 mA h cm^{-2}.

These excellent performances benefit from i) the excellent network conductivity from graphene and chemical interaction with polysulfides from g-C_3N_4, ii) a well-maintained electronic/physical connection among the sulfur composites owing to the elastomeric cross-linked binder. However, in this work, the challenges related to the lithium metal anode for ultra-high loading cathodes in Li-S batteries are presented. In the high-loading cells, high capacity (over 10 mA h cm^{-2}) at high current (over 1 mA cm^{-2}) leads to severe lithium dendrite formation and consequently fast anode degradation and potential electrolyte dry-out. This led to fluctuating voltage and extremely fast capacity fading and eventual cell failure.

Chapter 7 presents a comprehensive study on electrolytes with sparing solubility for polysulfides. The electrochemistry of ACN_2-LiTFSI-TTE, a non-solvent electrolyte at room temperature, suffers from significant polarization. This Chapter demonstrates that by tuning the polysulfide solubility *via* temperature increase, it become a sparingly solvating electrolyte that gives rise to minimal polysulfide shuttling and a quasi-solid state reaction. This can redirect the reaction pathway owing to the change in relative kinetic rates for competing reactions between solid-liquid transition and solid-solid transition. The electrochemical profile is profoundly changed with respect to fully solvating catholyte cells. As proven by *operando*

XRD measurements, the pathways to form Li_2S and sulfur are altered, from the reduction of sulfur/polysulfides and oxidation of polysulfides, respectively. The initial formation of intermediate-to-short chain polysulfides are in sharp contrast to a typical solvated electrolyte where long-chain polysulfides are favored at the start. A greatly reduced polarization by moderately increasing the cell temperature was also realized. This discovery should inspire further studies into modifying the electrolyte local environment to tune the reaction pathway of precipitation-dissolution electrochemistry.

8.2 Future Prospects

This thesis, along with many other exciting reports in the literature as introduced in **Chapter 1**, has shown great improvement in the cycling life of a Li-S battery. These cathodes expand over a wide spectrum of materials, metal oxides/sulfides, porous doped carbons and carbon nitride and their composites. There has been a great addition to these classes of materials in recent literatures as shown in the **Chapters 3-7**. The verification and understanding of the chemical interaction of various host materials with polysulfides by spectroscopic and theoretical studies, the deposition behavior of discharged/charged products, catalytic reduction/oxidation of the products comprise the most important contribution of this thesis to the Li-S research community. Excellent cycling behavior up to over 1000 cycles or longer has been achieved in this thesis and other literature reports. This has been a great improvement over the achievements made a decade ago. It appears that the commercialization of Li-S batteries is getting closer than ever before.

The problems from the practical points of view, however, are now widely recognized by the Li-S research community. First, the electrolyte volume for the widely reported catholyte-type Li-S cells is generally in the very high range of 10-30 μl/mg of sulfur, which is due to two

facts: i) the kinetics of catholyte relies on great or even full dissolution of polysulfides and ii) the highly porous carbon hosts requires large electrolyte volume for effective wetting. This range is way higher than what is being applied currently in commercial Li-ion cells (1-2 μl/mg of active materials), which means the weight percentage of active components in Li-S batteries made in such ways would be much lower, compromising the specific energy and energy density. Therefore, compact electrodes using lower fractions of highly porous carbons and less void space, but still possessing good diffusion kinetics are desired.

New approaches on optimizing the electrolytes are promising solutions. Sparing solvating electrolytes, as discussed in **Chapter 7**, which decouples the electrolyte volume with sulfur loading are options worth further exploring. On the other hand, electrolytes using solvents with even greater polysulfide solvating power (than glymes) should in principle allow less electrolyte to be used, while with good kinetics which is another promising direction to work on. Attention is needed to the protection of anode for the candidates of these electrolytes.

Pertinent to the first problem is the low areal sulfur loading of reported cathodes, which has been generally lower than 2 mg cm^{-2}. Although recent reports have shown higher areal loading even up to 21 mg cm^{-2}, the cycling behavior is worse than the low loading ones, and only up to 100 cycles have been reported. Although the exact failure mechanism is not clear yet, one of the reasons is the degrading cathode structure with undermined Li^+ diffusion/electron conducting pathways caused by the uncontrolled deposition of Li_2S/S_8 and volume expansion/extraction at high loadings. Another major reason accounting for this is the degradation of the Li metal anode from the dendrite formation that tends to occur at such high areal capacity and current. It is known that the dendritic Li anode suffers from severe parasite

reactions with the electrolyte, high porosity and pulverization, increasing impedance and accelerates the electrolyte drying out at the same time.

Further reports on the Li-S batteries should include the relevant experimental parameters, such as electrolyte volume and sulfur loading. The exact cell failure mechanism needs to be thoroughly studied by *ex-situ* or *operando* microscopy studies, EIS and other electrochemical techniques. The other challenge is the safety concern of using Li metal in the cell. Proper protection of the Li anode, or replacing it with other high-capacity lithiated anode, such as Si, Ge alloys is promising. Only when these practical problems are tackled can the Li-S battery technology come into large-scale commercialization.

References

1 J. A. Turner, *Science*, **285**, 687 (1999).

2 J. B. Goodenough, K.-S. Park, *J. Am. Chem. Soc*., **135**, 1167 (2013).

3 K. Brandt, *Solid State Ionics*, **69**, 173 (1994).

4 B. L. Ellis, K. T. Lee, L. F. Nazar, *Chem. Mater*., **22**, 691 (2010).

5 L. F. Nazar, M. Cuisinier, Q. Pang, *MRS Bull*., **39**, 436 (2014).

6 D. Kundu, T. Elahe D. Victor, L. F. Nazar, *Angew. Chem. Int.Ed.* **54**, 3431 (2015).

7 N. S. Choi, Z. Chen, S. A. Freunberger, X. Ji, Y. K. Sun, K. Amine, G. Yushin, L. F. Nazar, J. Cho, P. G. Bruce, *Angew. Chem. Int. Ed.*, **51**, 9994 (2012).

8 M.S. Whittingham, *Chem. Rev.,* **104**, 4271 (2004).

9 S. Evers, L. F. Nazar, *Acc. Chem. Res*., **46**, 1135 (2012).

10 A. Manthiram, Y. Fu, Y.-S. Su, *Acc. Chem. Res*., **46**, 1125 (2012).

11 A. Rosenman, E. Markevich, G. Salitra, D. Aurbach, A. Garsuch, F. F. Chesneau, *Adv. Energy Mater*, 1500212 (2015).

12 Q. Pang, X. Liang, C.Y. Kwok, L.F. Nazar, *Nat. Energy*, **1,** 16132 (2016).

13 M. Cuisinier, P.-E. Cabelguen, S. Evers, G. He, M. Kolbeck, A. Garsuch, T. Bolin, M. Balasubramanian, L.F. Nazar, *J. Phy. Chem. Lett. 4*, 3227(2013)

14 M.U. Patel, I. Arcon, G. Aquilanti, L. Stievano, G. Mali, R. Dominko, *Chemphyschem*. 15, 894 (2014).

15 M.U. Patel, R. Demir-Cakan, M. Morcrette, J.M. Tarascon, M. Gaberscek, R. Dominko, *ChemSusChem* **6**, 1177 (2013).

16 S. Waluś, C. Barchasz, R. Bouchet, J.C. Leprêtre, J.F. Colin, J.F. Martin, E. Elkaïm, C. Baehtz, F. Alloin, *Adv. Energy Mater.*, **5**, 0165 (2015).

17 J. Nelson, S. Misra, Y. Yang, A. Jackson, Y. Liu, H. Wang, H. Dai, J.C. Andrews, Y. Cui, M.F. Toney, *J. Am. Chem. Soc.* **134**, 6337 (2012).

18 R. Cao, W. Xu, D. Lv, J. Xiao, J.G. Zhang, *Adv. Energy Mater.*, **5**, 2273 (2015).

19 X. Ji, K. T. Lee, L. F. Nazar, *Nat. Mater*, **8**, 500 (2009).

20 G. He, S. Evers, X. Liang, M. Cuisinier, A. Garsuch, L. F. Nazar, *ACS Nano*, **7**, 10920 (2013).

21 N. Jayaprakash, J. Shen, S. S. Moganty, A. Corona, L.A. Archer, *Angew. Chem. Int. Ed*., **50**, 5904 (2011).

22 F. Bottger-Hiller, P. Kempe, G. Cox, A. Panchenko, N. Janssen, A. Petzold, T. Thurn-Albrecht, L. Borchardt, M. Rose, S. Kaskel, C. Georgi, H. Lang, S. Spange, *Angew. Chem. Int. Ed.*, **52**, 6088 (2013).

23 J. Schuster, G. He, B. Mandlmeier, T. Yim, K. T. Lee, T. Bein, L. F. Nazar, *Angew. Chem. Int. Ed*., **51**, 3591 (2012).

24 L. Sun, M. Li, Y. Jiang, W. Kong, K. Jiang, J. Wang, S. Fan, *Nano Lett*., **14**, 4044 (2014).

25 R. Elazari, G. Salitra, A. Garsuch, A. Panchenko, D. Aurbach, *Adv. Mater*., **23**, 5641 (2011).

26 G. Zheng, Y. Yang, J. J. Cha, S. S. Hong, Y. Cui, *Nano Lett*., **11**, 4462 (2011).

27 S. Xin, L. Gu, N. H. Zhao, Y. X. Yin, L. J. Zhou, Y. G. Guo, L. J. Wan, *J. Am. Chem. Soc*., **134**, 18510 (2012).

28 Z. Li, Y. Jiang, L. Yuan, Z. Yi, C. Wu, Y. Liu, P. Strasser, Y. Huang, *ACS Nano*, **8**, 9295 (2014).

29 S. Evers, L. F. Nazar, *Chem. Commun.*, **48**, 1233 (2012).

30 H. Wang, Y. Yang, Y. Liang, J. T. Robinson, Y. Li, A. Jackson, Y. Cui, H. Dai, *Nano Lett*., **11**, 2644 (2011).

31 Y. Yang, G. Yu, J. J. Cha, H. Wu, M. Vosgueritchian, Y. Yao, Z. Bao, Y. Cui, *ACS Nano*, **5**, 9187 (2011).

32 Y.-S. Su, A. Manthiram, *Chem. Commun.,* **48**, 8817 (2012).

33 S.-H. Chung, P. Han, R. Singhai, V. Kalra, A. Manthiram, *Adv. Energy. Mater.,* **5**, 1500738 (2015).

34 D.-W. Wang, Q. Zeng, G. Zhou, L. Yin, F. Li, H.-M. Cheng, I. R. Gentle, G. Q. M. Lu, *J. Mater. Chem. A*, **1**, 9382 (2013).

35 Y. Yang, G. Zheng, Y. Cui, *Chem. Soc. Rev*., **42**, 3018 (2013).

36 L. Ji, M. Rao, H. Zheng, L. Zhang, Y. Li, W. Duan, J. Guo, E. J. Cairns, Y. Zhang, *J. Am. Chem. Soc*., **133**, 18522 (2011).

37 L. Zhang, L. Ji, P. A. Glans, Y. Zhang, J. Zhu, J. Guo, *Phys. Chem. Chem. Phys*., **14**, 13670 (2012).

38 M. K. Song, Y. Zhang, E. J. Cairns, *Nano Lett.* **13**, 5891 (2013).

39 G. Zhou, L.-C. Yin, D.-W. Wang, L. Li, S. Pei, I. R. Gentle, F. Li, H.-M. Cheng, *ACS Nano*, **7**, 5367 (2013).

40 J. Song, T. Xu, M. L. Gordin, P. Zhu, D. Lv, Y.-B. Jiang, Y. Chen, Y. Duan, D. Wang, *Adv. Funct. Mater.,* **24**, 1243 (2013).

41 J. Song, M. L. Gordin, T. Xu, S. Chen, Z. Yu, H. Sohn, J. Lu, Y. Ren, Y. Duan, D. Wang, *Angew. Chem. Int. Ed.*, **54**, 4325 (2015).

42 W. Zhou, C. Wang, Q. Zhang, H. D. Abruña, Y. He, J. Wang, S. X. Mao, X. Xiao, *Adv. Energy Mater.*, 1401752 (2015).

43 G. Zhou, Y. Zhao, A. Manthiram, *Adv. Energy Mater.*, 1402263 (2015).

44 Y. Qiu, W. Li, W. Zhao, G. Li, Y. Hou, M. Liu, L. Zhou, F. Ye, H. Li, Z. Wei, S. Yang, W. Duan, Y. Ye, J. Guo, Y. Zhang, *Nano Lett.*, **14**, 4821 (2014).

45 C. Wang, K. Su, W. Wan, H. Guo, H. Zhou, J. Chen, X. Zhang, Y. Huang, *J.Mater. Chem. A*, **2**, 5018 (2014).

46 H.-J. Peng, T.-Z. Hou, Q. Zhang, J.-Q. Huang, X.-B. Cheng, M.-Q. Guo, Z. Yuan, L.-Y. He, F. Wei, *Adv. Mater. Interfaces*, **1**, 1400227 (2014).

47 G. Zheng, Q. Zhang, J. J. Cha, Y. Yang, W. Li, Z. W. Seh, Y. Cui, *Nano Lett.*, **13**, 1265 (2013).

48 L. Ma, H. Zhuang, Y. Lu, S. S. Moganty, R. G. Hennig, L. A. Archer, *Adv. Energy Mater.*, **4**, 1400390 (2014).

49 Z. Wang, Y. Dong, H. Li, Z. Zhao, H. Bin Wu, C. Hao, S. Liu, J. Qiu, X. W. Lou, *Nat. Commun*, **5**, 5002 (2014).

50 M.-S. Song, S.-C. Han, H.-S. Kim, J.-H. Kim, K.-T. Kim, Y.-M. Kang, H.-J. Ahn, S. X. Dou, J.-Y. Lee, *J. Electrochem. Soc.*, **151**, A791 (2004).

51 Y. J. Choi, B. S. Jung, D. J. Lee, J. H. Jeong, K. W. Kim, H. J. Ahn, K. K. Cho, H. B. Gu, *Phys. Scripta*, **129**, 62 (2007).

52 X. Ji, S. Evers, R. Black, L. F. Nazar, *Nat. Commun.*, **2**, 325 (2011).

53 S. Evers, T. Yim, L. F. Nazar, *J Phys. Chem. C*, **116**, 19653 (2012).

54 K. T. Lee, R. Black, T. Yim, X. Ji, L. F. Nazar, *Adv. Energy Mater.,***2**, 1490 (2012).

55 Z. Wei Seh, W. Li, J. J. Cha, G. Zheng, Y. Yang, M. T. McDowell, P. C. Hsu, Y. Cui, *Nat. Commun.*, **4**, 1331 (2013).

56 H. Kim, J. T. Lee, D.-C. Lee, A. Magasinski, W.-i. Cho, G. Yushin, *Adv. Energy Mater.*, **3**, 1308 (2013).

57 Z. Xiao, Z. Yang, L. Wang, H. Nie, M. Zhong, Q. Lai, X. Xu, L. Zhang, S. Huang, *Adv. Mater.*, **27**, 2891 (2015).

58 B. Ding, L. Shen, G. Xu, P. Nie, X. Zhang, *Electrochim. Acta*, **107**, 78 (2013).

59 Q. Li, Z. Zhang, K. Zhang, L. Xu, J. Fang, Y. Lai, J. Li, *J. Solid State Electrochem.*, **17**, 2959 (2013).

60 Q. Pang, D. Kundu, M. Cuisinier, L. F. Nazar, *Nat. Commun.*, **5**, 4759 (2014).

61 Q. Pang, Nanostructured Non-Carbonaceous Materials for Improvement of Sulfur Cathode in Lithium-Sulfur Battery, *University of Waterloo Master Thesis* (2014).

62 X. Tao, J. Wang, Z. Ying, Q. Cai, G. Zheng, Y. Gan, H. Huang, Y. Xia, C. Liang, W. Zhang, Y. Cui, *Nano Lett.*, **14**, 5288 (2014).

63 J. Zheng, J. Tian, D. Wu, M. Gu, W. Xu, C. Wang, F. Gao, M. H. Engelhard, J. G. Zhang, J. Liu, J. Xiao, *Nano Lett.* **14**, 2345 (2014).

64 W. Xia, A. MA hmood, R. Zou, Q. Xu, *Energy Environ. Sci*., **8**, 1837 (2015).

65 J. Zhou, X. Yu, X. Fan, X. Wang, H. Li, Y. Zhang, W. Li, J. Zheng, B. Wang, X. Li, *J. Mater. Chem. A*, **3**, 8272 (2015).

66 J. Zhou, R. Li, X. Fan, Y. Chen, R. Han, W. Li, J. Zheng, B. Wang, X. Li, *Energy Environ. Sci*., **7**, 2715 (2014).

67 Z. Zhao, S. Wang, R. Liang, Z. Li, Z. Shi, G. Chen, *J. Mater. Chem. A*, **2**, 13509 (2014).

68 R. Demir-Cakan, M. Morcrette, F. Nouar, C. Davoisne, T. Devic, D. Gonbeau, R. Dominko, C. Serre, G. Ferey, J. M. Tarascon, *J. Am. Chem. Soc.*, **133**, 16154 (2011).

69 Z. Wang, X. Li, Y. Cui, Y. Yang, H. Pan, Z. Wang, C. Wu, B. Chen, G. Qian, *Crystal Growth Design,* **13**, 5116 (2013).

70 X. Liang, A. Garsuch, L. F. Nazar, *Angew. Chem. Int. Ed*., **54**, 3907 (2015).

71 X. Liang, Y. Rangom, C. Y. Kwok, Q. Pang, L. F. Nazar, *Adv. Mater.* 29, 1603040 (2017).

72 X. Liang, C. J. Hart, Q. Pang, A. Garsuch, T. Weiss, L. F. Nazar, *Nat. Commun*., **6**, 5682 (2015).

73 E. Wiberg, Holleman-Wiberg: Inorganic Chemistry, Academic Press, New York, NY USA (2001).

74 C.J. Hart, M. Cuisinier, X. Liang, D. Kundu, A. Garsuch, L.F. Nazar, *Chem. Commun.*, **51**, 2308 (2015).

75 J.-W. Park, K. Ueno, N. Tachikawa, K. Dokko, M. Watanabe, *J. Phys. Chem. C,* **117**, 20531 (2013).

76 N. Tachikawa, K. Yamauchi, E. Takashima, J.W. Park, K. Dokko, M. Watanabe, *Chem. Commun.,* **47**, 8157 (2011).

77 L. Suo, L. Y.S. Hu, H. Li, M. Armand, L. Chen, *Nat. Commun.* **4**, 1481 (2013).

78 M. Cuisinier, P.E. Cabelguen, B.D. Adams, A. Garsuch, M. Balasubramanian, L.F. Nazar, *Energy Environ. Sci.,* **7**, 2697 (2014).

79 K. Dokko, N. Tachikawa, K. Yamauchi, M. Tsuchiya, A. Yamazaki, E. Takashima, J.W. Park, K. Ueno, S. Seki, N. erizawa, M. Watanabe, *J. Electrochem. Soc.* **160**, A1304 (2013).

80 E.G. Moroni, G. Kresse, J. Hafner, *J. Phys. Conden. Matter,* **11**, L35 (1999).

81 J.P. Perdew, K. Schmidt, K. *AIP Conference Proceedings,* **577**, 1(2001).

82 G. Zhou, L. Li, C. Ma, S. Wang, Y. Shi, N. Koratkar, W. Ren, F. Li, H.-M. Cheng, *Nano Energy*, **11**, 356 (2015).

83 E. Talaie, P. Bonnick, X. Sun, Q. Pang, X. Liang, L.F. Nazar, *Chem. Mater.*, **29**, 90 (2017).

84 M. Safari, C. Y. Kwok, L. F. Nazar. *ACS Cent. Sci.*, **2**, 2374 (2016).

85 R. Ortega, A. Carmona, I. Llorens, P.L. Solari, *J. Anal. At. Spectrom.,* **27,** 2054 (2012).

86 G. Kresse, J. Furthmüller, *Phys. Rev. B,* **54**, 11169 (1996).

87 G. Kresse, J. Furthmüller, *Comput. Mater. Sci.* **6**, 15 (1996).

88 Y. V. Mikhaylik, J. R. Akridge, *J. Electrochem. Soc.* **151**, A1969 (2004).

89 Y. Diao, K. Xie, S. Xiong, X. Hong, *J. Electrochem. Soc.*, **159**, A421 (2012).

90 R. Elazari, G. Salitra, Y. Talyosef, J. Grinblat, C. Scordilis-Kelley, A. Xiao, J. Affinito, D. Aurbach, *J. Electrochem. Soc.*, **157**, A1131 (2010).

91 S. Zhang, S. Tsuzuki, K. Ueno, K. Dokko, M. Watanabe, *Angew. Chem. Int. Ed.* **54**,1302 (2015).

92 A. Garsuch, S. Herzog, L. Montag, A. Krebs, K. Leitner, *ECS Electrochem. Lett.* **1**, A24 (2012).

93 Z. W. Seh, J. H. Yu, W. Li, P. C. Hsu, H. Wang, Y. Sun, H. Yao, Q. Zhang, Y. Cui, *Nat. Commun.,* **5**, 5017 (2014).

94 R. C. Hoodless, R. B. Moyes, P. B. Wells, *Catal. Today,* **114**, 377 (2006).

95 D. M. Pasquariello, R. Kershaw, J. D. Passaretti, K. Dwight, A. Wold, *Inorg. Chem.* **23**, 872 (1984).

96 Q. Wang, L. Jiao, Y. Han, H. Du, W. Peng, Q. Huan, D. Song, Y. Si, Y. Wang, H. Yuan, *J. Phys. Chem. C,* **115**, 8300 (2011).

97 Y.O. Chen, Y.A. Chang, *Metall. Trans. B*, **9**, 61(1978).

98 N. Kumar, N. Raman, A. Z. Sundaresan, *Anorg. Allg. Chem*., **640**, 1069(2014).

99 Z. Wang, L. Pan, H. Hu, S. Zhao, *CrystEngComm.,* **12**, 1899(2010).

100 R. Jin, R. Liu, Y. Xu, G. Li, G. Chen, *J. Mater. Chem. A,* **1**, 7995(2013).

101 I. Bilecka, M. Niederberger, *Nanoscale*, **2**, 1358(2010).

102 G.B. Zeng, R. Caputo, D. Carriazo, L. Luo, M. Niederberger, *Chem. Mater*., **25**, 3399 (2013).

103 D. Lv, J. Zheng, Q. Li, X. Xie, S. Ferrara, Z. Nie, L. B. Mehdi, N. D. Browning, J.-G. Zhang, G. L. Graff, J. Liu, J. Xiao, *Adv. Energy Mater.,* **5**, 02290 (2015).

104 C. J. Hart, M. Cuisinier, X. Liang, D. Kundu, A. Garsuch, L. F. Nazar, *Chem. Commun.*, **51**, 2308(2015).

105 R. A. Sidik, A. B. Anderson, *J Phy. Chem. B*, **110**, 936 (2006).

106 L. Wang, T. Zhang, S. Yang, F. Cheng, J. Liang, J. Chen, *J. Energy. Chem*., **22**,72 (2013).

107 Q. Zhang, Y. Wang, Z. W. Seh, Z. Fu, R. Zhang, Y. Cui, *Nano Lett.,* **15**, 3780 (2015).

108 Z. Wang, L. Pan, H. Hu, S. Zhao, *CrystEngComm,* **12**, 1899(2010).

109 Z. Li, W. Li, H. Xue, W. Kang, X. Yang, M. Sun, Y. Tang, C.-S. Lee, *RSC Adv.,* **4**, 37180 (2014).

110 Q. Zhao, X. Hu, K. Zhang, N. Zhang, Y. Hu, J. Chen, *Nano Lett.,* **15**, 721(2015).

111 Z. Li, J. Zhang, X. W. D. Lou, *Angew. Chem. Int. Ed.,* **54**, 12886 (2015).

112 Q. Sun, X. Fang, W. Weng, J. Deng, P. Chen, J. Ren, G. Guan, M. Wang, H. Peng, *Angew. Chem. Int. Ed.,* **127**, 10685 (2015).

113 G. Zhou, E. Paek, G. S. Hwang, A. Manthiram, *Nat. Commun.,* **6**, 7760 (2015).

114 Z. Lin, Z. Liu, N. J. Dudney, C. Liang, *ACS Nano,* **7**, 2829 (2013).

115 J. Hassoun, B. Scrosati, *Adv. Mater.,* **22**, 5198 (2015).

116 M. Cuisinier, P.-E. Cabelguen, B. Adams, A. Garsuch, M. Balasubramanian, L.F. Nazar, *Energy Environ. Sci.,* **7**, 2697 (2014).

117 C. Tang, Q. Zhang, M.-Q. Zhao , J.-Q. Huang , X.-B. Cheng , G.-L. Tian , H.-J. Peng , F. Wei, *Adv. Mater*., **26**, 6100 (2015).

118 J. Liang, Y. Jiao, M. Jaroniec, S. Z. Qiao, *Angew.Chem. Int. Ed.,* **51**, 11496 (2012).

119 H. Zhu, Z. Jia, Y. Chen, N. Weadock, J. Wan, O. Vaaland, X. Han, T. Li, L. Hu, *Nano Lett.,* **13**, 3093 (2013).

120 Y. Habibi, L. A. Lucia, O. J. Rojas, *Chem. Rev.,* **110**, 3479 (2010).

121 J. Tang, M. F. X. Lee, W. Zhang, B. Zhao, R. M. Berry, K. C. Tam, *Biomacromolecules,* **15**, 3052 (2014).

122 J. Tang, Y. Song, R. M. Berry, K. C. Tam, *RSC Adv.,* **4**, 60249 (2014).

123 W. Ai, Z. Luo, J. Jiang, J. Zhu, Z. Du, Z. Fan, L. Xie, H. Zhang, W. Huang, T. Yu, *Adv. Mater.,* **26**, 6186 (2014).

124 J. Tang, Y. Song, R. M. Berry, K. C. Tam, *RSC Adv.,* **4**, 60249 (2014).

125 J. A. Kelly, M. Giese, K. E. Shopsowitz, W. Y. Hamad, M. J. MacLachlan, *Acc. Chem. Res.,* **47**, 1088 (2014).

126 R. Silva, J. Al-Sharab, T. Asefa, *Angew. Chem. Int. Ed.*, **124**, 7283 (2012).

127 K. E. Shopsowitz, J. A. Kelly, W. Y. Hamad, M. J. MacLachlan, *Adv. Funct. Mater.,* **24**, 327 (2014).

128 X. Li, X. F. Li, M. N. Banis, B. Q. Wang, A. Lushington, X. Y. Cui, R. Y. Li, T. K. Sham, X. L. Sun, *J. Mater. Chem. A,* **2**, 12866 (2014).

129 Z. W. Seh, H. Wang, P.-C. Hsu, Q. Zhang, W. Li, G. Zheng, H. Yao, Y. Cui, *Energy Environ. Sci.*, **7**, 672 (2015).

130 Q. Pang, J. Tang, H. Huang, X. Liang, C. Hart, K.C. Tam, L.F. Nazar, *Adv. Mater.*, **27**, 6021 (2015).

131 A. Thomas, A. Fischer, F. Goettmann. M. Antonietti, J.O. Müller, R. Schlögl, J.M. Carlsson, *J. Mater. Chem., **18***, 4893 (2014).

132 S. Cao, J. Low, L. Yu, M. Jaroniec, *Adv. Mater.,* **27**, 2150 (2015).

133 J. Liu, W. Li, L. Duan, X. Li, L. Ji, Z. Geng, K. Huang, L. Lu, L.Zhou, Z. Liu, W. Chen, L. Liu, S. Feng Y. Zhang, *Nano Lett.,* **15**, 5137 (2015).

134 J. Sun, J. Zhang, M. Zhang, M. Antonietti, X. Fu X. Wang, X. *Nat. Commun.,* **5**, 1139 (2012).

135 Z. Wang, Y. Dong, H. Li, Z. Zhao, H. Wu, C. Hao, S. Liu, J. Qiu X.W. Lou, *Nat. Commun.,* **5**, 5002 (2014).

136 K. Park, J.H. Cho, J.H. Jang, B.C. Yu, A.T. De La Hoz, K.M. Miller, C.J. Ellison, J.B. Goodenough, *Energy Environ. Sci.*, **8**, 2389 (2015).

137 A. Du, S. Sanvito, Z. Li, D. Wang, Y. Jiao, T. Liao, Q. Sun, Y.H. Ng, Z. Zhu, R. Amal, S.C. Smith, *J. Am. Chem. Soc.*, *134*, 4393 (2012).

138 Y. Zhang, T. Mori, J. Ye, M. Antonietti, *J. Am. Chem. Soc*., **132**, 6294 (2012).

139 S. Urbonaite, T. Poux, P. Novák, *Adv. Energy Mater.,* **5**, 00118 (2015).

140 D. Eroglua, K. R. Zavadila, K.G. Gallagher. *J. Electrochem. Soc.,* **162**, A982 (2015).

141 M.A. Pope, I.A. Aksay, *Adv. Energy Mater.*, **5**, 00124 (2015).

142 L. Borchardt, M. Oschatz, S. Kaskel, *Chem. Eur. J.,* **22**, 7324 (2016).

143 Z. Yuan, H. Peng, J. Huang, X. Liu, D. Wang, X. Cheng, Q. Zhang, *Adv. Func. Mater*., **24**, 6105 (2014).

144 L. Qie, A. Manthiram, *Adv. Mater,.* **27**, 1694 (2015).

145 R. Fang, S. Zhao, P. Hou, M. Cheng, S. Wang, H.-M. Cheng, C. Liu, F. Li, *Adv. Mater.*, **28**, 3374 (2016).

146 X. Ye, J Ma, Y.S. Hu, H. Wei, F. Ye, *J. Mater. Chem. A*, **4**, 775 (2016).

147 P. Bhattacharya, M.I. Nandasiri, D. Lv, A.M. Schwarz, J.T. Darsell, W.A. Henderson, D.A. Tomaliac, J. Liu, J.-G. Zhang, J. Xiao, *Nano Energy*, **19**, 176 (2016).

148 Q. Pang, L.F. Nazar, *ACS Nano*, **10***,* 4111 (2016).

149 J. Liu, W. Li, L. Duan, X. Li. L. Ji, Z. Geng, K. Huang, L. Lu, L. Zhou, Z. Liu, W. Chen, L. Liu, S. Feng, Y. Zhang, *Nano Lett.*, **15**, 5137 (2015).

150 A. Du, S. Sanvito, Z. Li, D. Wang, Y. Jiao, T. Liao, Q. Sun, Y.H. Ng, Z. Zhu, R. Amal, S.C. Smith, *J. Am. Chem. Soc.*, **134**, 4393 (2012).

151 Y. Zheng, Y. Jiao, Y. Zhu, L.H. Li, Y. Han, Y. Chen, A. Du, M. Jaroniec, S.Z. Qiao, *Nat. Commun.*, **5**, 3783 (2014).

152 J. Song, Z. Yu, M.L. Gordin, D. Wang, *Nano Lett.*, **16**, 864 (2016).

153 J. Song, Z. Yu, M.L. Gordin, X. Li, H. Peng, D. Wang, *ACS Nano*, **9**, 11933 (2015).

154 Y. Liu, D Lin, Z. Liang, J. Zhao, K. Yan, Y. Cui, *Nat. Commun.*, **7**, 10992 (2016).

155 L. Qie, C. Zu, A. Manthiram, *Adv. Energy Mater.,* **5**, 02459 (2015).

156 R. Cao, W. Xu, D. Lv, J. Xiao, J.G. Zhang, *Adv. Energy Mater.*, **5**, 02273 (2015).

157 Y. Diao, K. Xie, S. Xiong, X. Hong, *J. Electrochem. Soc.*, **159**, A421 (2012).

158 M. Hagen, D. Hanselmann, K. Ahlbrecht, R. Maça, D. Gerber, J. Tübke, *Adv. Energy Mater.*, **5**, 1401986 (2015).

159 Y. V. Mikhaylik, J. R. Akridge, *J. Electrochem. Soc.*, **151**, A1969 (2004).

160 X. Yu, H. Pan, Y. Zhou, P. Northrup, J. Xiao, S. Bak, M. Liu, K.-W. Nam, D. Qu, J. Liu, T. Wu, X.-Q. Yang, *Adv. Energy Mater.*, **5**, 1500072 (2015).

161 L. Cheng, L. A. Curtiss, K. R. Zavadil, A. A. Gewirth, Y. Shao, K. G. Gallagher, *ACS Energy Lett.*, **1**, 503 (2016).

162 K. Ueno, J. W. Park, A. Yamazaki, T. Mandai, N. Tachikawa, K. Dokko, M. Watanabe, *J. Phys. Chem. C*, **117**, 20509 (2013).

163 D. M. Seo, O. Borodin, S.-D. Han, P. D. Boyle, W. A. Henderson, *J. Electrochem. Soc.*, **159**, A1489 (2012).

164 Y. Yamada, K. Furukawa, K. Sodeyama, K. Kikuchi, M. Yaegashi, Y. Tateyama, A. Yamada, *J. Am. Chem. Soc.*, **136**, 5039 (2014).

165 H. Yamin, A. Gorenshtein, J. Penciner, Y. Sternberg, E. Peled, *J. Electrochem. Soc.*, **135**, 1045 (1988).

166 S.-E. Cheon, K.-S. Ko, J.-H. Cho, S.-W. Kim, E.-Y. Chin, H.-T. Kim, *J. Electrochem. Soc.*, **150**, A796 (2003).

167 Y.-C. Lu, Q. He, H. A. Gasteiger, *J. Phys. Chem. C*, **118**, 5733 (2014).

168 W. Weng, V. G. Pol, K. Amine, *Adv. Mater.*, **25**, 1608 (2013).

169 E. S. Shin, K. Kim, S. H. Oh, W. I. Cho, *Chem. Commun.*, **49**, 2004 (2013).

170 Y. Yamada, A. Yamada, *J. Electrochem. Soc.*, **162**, A2406 (2015).

171 S. Zhang, K. Ueno, K. Dokko, M. Watanabe, *Adv. Energy Mater.*, **5**, 1500117 (2015).

172 L. Yuan, J. Feng, X. Ai, Y. Cao, S. Chen, H. Yang, *Electrochem. Commun.*, **8**, 610 (2006).

173 J.W. Park, K. Yamauchi, E. Takashima, N. Tachikawa, K. Ueno, K. Dokko, M. Watanabe, *J. Phys. Chem. C,* **117**, 4431 (2013).

174 S. S. Zhang, *J. Electrochem. Soc.*, **159**, A920 (2012).

175 N. Gotoh, M. Hayasaka, U.S. Patent 5028567 A, Jul 2, (1991).

176 M. Okoshi, Y. Yamada, A. Yamada , H. Nakai, *J. Electrochem. Soc.*, **160**, A2160 (2013).

177 S. Zhang, K. Ueno, K. Dokko, M. Watanabe, *Adv. Energy Mater.*, **5**, 1500117 (2015).

178 K. A. See, H.-L. Wu, K. C. Lau, M. Shin, L. Cheng, M. Balasubramanian, K.G. Gallagher, L. A. Curtiss, A.A. Gewirth, *ACS App. Mater. Interfaces*, **8**, 34360 (2016).

179 P. Ruetschi, *J. Power Sources*, **2**, 3 (1997).

180 M. A. Lowe, J. Gao, H. D. Abruna, *RSC Adv.*, **4**, 18347 (2014).

181 I. J. Pickering, G. N. George, E. Y. Yu, D. C. Brune, C. Tuschak, J. Overmann, J. T. Beatty, R. C. Prince, *Biochemistry*, **40**, 8138 (2001).

182 M. Cuisinier, C. Hart, M. Balasubramanian, A. Garsuch, L.F. Nazar, *Adv. Energy Mater.*, **5**, 1401801 (2015).

183 P. Kumar, R. Nagarajan, R. Sarangi, *J. Mater. Chem. C*, **1**, 2448 (2013).

184 Z. Yuan, H.-J. Peng, T.-Z. Hou, J.-Q. Huang, C.-M. Chen, D.-W. Wang, X.-B. Cheng, F. Wei, Q. Zhang, *Nano Lett.*, **16**, 519 (2016).

185 Z. Ma, Z. Li, K. Hu, D. Liu, J. Huo, S. Wang, *J. Power Sources*, **325**, 71 (2016).

186 S. S. Zhang, D. T. Tran, *J. Mater. Chem. A*, **4**, 4371 (2016).

187 X. Li, Y. Lu, Z. Hou, W. Zhang, Y. Zhu, Y. Qian, J. Liang, Y. Qian, *ACS Appl. Mater. Interfaces*, **8**, 19550 (2016).

188 F. Wu, J. Li, Y. Tian, Y. Su, J. Wang, W. Yang, N. Li, S. Chen, L. Bao, *Sci. Rep.*, **5**, 13340 (2015).

189 Z. Yang, D. Yu, S. Wang, H. Cheng, J. Yu, *RSC Adv.*, **5**, 78017(2016).

190 W. Ai, W. Zhou, Z. Du, Y. Chen, Z. Sun, C. Wu, C. Zou, C. Li, W. Huang, T. Yu *Energy Storage Mater.,* **6** 112(2017).